Doctoral Thesis

Flow-Induced Vibration of a Spherical Body

Rajamuni Dewayalage
Methma Madushankani Rajamuni

BSc (Hons) in Engineering and MSc in Applied Mathematics

A Thesis submitted for the degree of Doctor of Philosophy at Monash University (2018)

Department of Mechanical and Aerospace Engineering

This thesis is dedicated to

My loving parents Leelasena and Karunawathi,

and

My dear husband Sanath Darshana.

Copyright Notices

Declaration of Authorship

I, Rajamuni Dewayalage Methma Madushankani Rajamuni, hereby declare that this thesis contains no material which has been accepted for the award of any other degree or diploma at any university or equivalent institution and that, to the best of my knowledge and belief, this thesis contains no material previously published or written by another person, except where due reference is made in the text of the thesis.

This thesis includes two original manuscripts that have been published in peer reviewed journals, and one manuscript that has been submitted for publication. The core theme of the thesis is 'Flow-induced vibration of a spherical body'. The ideas, development and writing up of all the papers in the thesis were the principal responsibility of myself, the student, working within the Department of Mechanical and Aerospace Engineering under the supervision of Prof Mark Christoper Thompson and Prof Kerry Hourigan.

The inclusion of co-authors reflects the fact that the work came from active collaboration between researchers and acknowledges input into team-based research.

I have not renumbered sections of submitted or published papers in order to generate a consistent presentation within the thesis. In the case of Chapters 4 and 5, my contribution to the work involved is described in the following table on Page viii.

Student signature: [redacted] Date: 11 September 2018

The undersigned hereby certify that the above declaration correctly reflects the nature and extent of the student's and co-authors' contributions to this work. In instances where I am not the responsible author I have consulted with the responsible author to agree on the respective contributions of the authors.

Main Supervisor signature: [redacted] Date: 11 September 2018

Thesis Chapter	**Publication Title**	**Status**	**Nature and % of student contribution**	**Co-author names, nature and % of contribution**	**Co-authors(s), Monash student Y/N**
4	Transverse flow-induced vibration of a sphere	Published (JFM 2018)	85% – Concepts, solver development, conducting simulations, analysing results and manuscript authoring.	Mark C Thompson: 8% – Concepts, research advises, and reviewing the manuscript. Kerry Hourigan: 7% – Concepts, research advise, and reviewing the manuscript.	N
5	Vortex-induced vibration of a transversely rotating sphere	Published (JFM 2018)	85% – Concepts, conducting simulations, analysing results and manuscript authoring.	Mark C Thompson: 8% – Concepts, research advises, and reviewing the manuscript. Kerry Hourigan: 7% – Concepts, research advise, and reviewing the manuscript.	N

Mistakes are wonders.

Sometimes they bring a shame exposing our illiteracy,

impatient, carelessness or stupidity,

while they are powerful enough to teach us valuable lessons.

They also come with a price,

which can be paid by the money, time or lives.

Abstract

This thesis investigates the flow-induced vibration of a sphere over a wide range of flow and vibration parameters. In particular, different modes of sphere vibration were studied numerically for both elastically mounted and tethered cases. In addition, the effects of sphere transverse rotation on the vortex-induced vibration were investigated over a broad range of rotation rates. Consequently, this thesis consists of three main sections. The first section, using simultaneous displacement, force measurements and wake characteristics, investigates the response of an elastically mounted sphere for the classic case where the motion of the sphere is restricted to move in a direction transverse to the freestream. The second section extends this study by investigating effects of the transverse rotation on the vortex-induced vibration of a sphere. Finally, the third section investigates the characteristics of different modes of sphere vibration using a tethered sphere.

Despite the large volume of research has been conducted on FIV, most of these studies were based on two-dimensional bodies like cylinders. Comparatively a fewer studies have been conducted with three-dimensional bodies. Therefore, this study is aimed to enhance the understanding of an intrinsically three-dimensional body, especially under forced rotation, which will enhance our understanding of flow-induced vibration for more complex cases. A non-deformable mesh was chosen for the simulations by modelling the flow in a non-inertial reference frame, attached to the centre of the sphere. Two new Fluid-Structure Interaction (FSI) solvers were implemented in OpenFOAM to efficiently solve the coupled fluid-structure systems for elastically mounted and tethered cases.

Two sets of simulations were conducted by fixing the Reynolds number at $Re = 300$ and 800 with an elastically mounted sphere. A periodic Vortex-Induced Vibration (VIV) response was observed over mode I and II regimes. In contrast to previous experimental observations, the amplitude of mode II was similar to that of mode I for low Reynolds numbers. Two trails of interlaced hairpin loops were observed in the wake. At higher reduced velocities, at $Re = 300$ the sphere vibrated with a small amplitude, while mode IV type intermittent bursts of vibration were identified at $Re = 800$. The effect of Reynolds number on flow-induced vibration is found to be significant in the laminar regime.

The effects of sphere transverse rotation on VIV is investigated at $Re = 300$ for rotation rates $\alpha \in [0,\ 2.5]$. Under forced rotation, the sphere oscillated about a new

time-mean position. Rotation also resulted in a decreased oscillation amplitude and a narrowed synchronisation range. VIV was suppressed completely for higher rotation rates ($\alpha > 1.3$). The symmetric wake observed for zero-rotation case deflected to the advancing side under rotation,s as a result of the Magnus effect. This symmetry breaking appears to be associated with the reduction in the observed amplitude response and the narrowing of the synchronisation range.

Three sets of simulations were conducted at $Re = 500$, 1200, and 2000 with a tethered sphere. Similar to the elastically mounted sphere, a periodic VIV response was observed at the modes I and II regimes. As the Reynolds number increased, the response amplitude increased, especially over the mode II regime, and the sphere response was closer to previous experimental observations. Similar to the $Re = 800$ case with an elastically mounted sphere, the sphere showed mode IV type intermittent bursts beyond the mode II regime, without an intervening mode III, for all three Reynolds numbers considered. However, mode III was observed for a very heavy tethered sphere. Mode III, which can be categorised as movement induced vibration, appears to occur due to the high inertia of the system. It can also be identified as a weak response that is sensitive to the parameter values and disturbances. The low-frequency modes III and IV responses seem to originate from the wake pattern found for the static sphere.

List of publications

Journal Articles

Rajamuni, M. M., Thompson, M. C. & Hourigan, K. 2018 Transverse flow-induced vibrations of a sphere. *Journal of Fluid Mechanics* **837**, 931–966.

Rajamuni, M. M., Thompson, M. C. & Hourigan, K. 2018 Vortex-induced vibration of a transversely rotating sphere. *Journal of Fluid Mechanics* **847**, 786–820.

Rajamuni, M. M., Thompson, M. C. & Hourigan, K. 2018 Vortex dynamics and vibration modes of a tethered sphere. *Journal of Fluid Mechanics.* (submitted)

Rajamuni, M. M., Thompson, M. C. & Hourigan, K. 2018 Vortex-induced vibrations of a sphere close to a free surface. *Journal of Fluid Mechanics.* (in draft)

Conference papers

Rajamuni, M. M., Thompson, M. C. & Hourigan, K. 2016 Vortex induced vibration of rotating spheres. 20th *Australasian Fluid Mechanics Conference Perth, Australia,* 5–8 *December.*

Rajamuni, M. M., Thompson, M. C. & Hourigan, K. 2018 An efficient FSI solver for multiple-degree-of-freedom flow-induced vibration. 30th *International Conference of Parallel Computational Fluid Dynamics, Indianapolis, Indiana, USA,* 14–17 *May.*

Rajamuni, M. M., Thompson, M. C. & Hourigan, K. 2018 Flow-induced vibration of a sphere. 7th *Conference on Bluff Body Wakes and Vortex-Induced Vibrations, Carry-le-Rouet (Marseille), France,* 3–6 *July.*

Acknowledgments

PhD is a long and lonely journey with full of challenges. There are many people who were with me providing assistance and support from the worst to the best moments over my candidature. I take this opportunity to sincerely thank all of them.

It is a great pleasure to express my earnest gratitude and appreciation to my supervisors Prof. Mark Christoper Thompson and Prof. Kerry Hourigan for giving me the opportunity to carry out this research study as a part of the FLAIR group. With enormous effort, they guided me, corrected my mistakes, and helped me to succeed. Their continuous encouragements, directions and patience profoundly impacted on my PhD and the completion of this thesis. Furthermore, I would like to appreciate their financial support provided for attending conferences and present my research work.

I am grateful to Prof. John Sheridan, who introduced me to my supervisors. My sincere thankfulness goes to PhD progress review examiners; Prof. Kris Ryan, Dr Martin Griffith and Dr Jisheng Zhao for their support, suggestions and encouragements.

I gratefully acknowledge the support from Australian Research Council Discovery Grants DP150102879 and DP170100275, and computing time from the National Computational Infrastructure (NCI), and the Pawsey Supercomputing Centre. I received a Faculty of Engineering International Postgraduate Research Scholarship (FEIPRS) for my course fees and a Monash Graduate Scholarship (MGS) for the living expenses, and therefore I would like to thank Faculty of Engineering and Monash University Institute of Graduate Research for their financial support.

I would like to thank the Department of Mechanical and Aerospace Engineering's staff, especially Stelios Konstantinidis, Fiona Pyrczak, Bill Belbin, Bev Pearce, Jacelyn Tan, and Nancy Hawe, for their support. I am happy to acknowledge the Department of Mechanical and Aerospace Engineering, the Department of Electrical and Computer Systems Engineering, and the School of Mathematical Sciences for giving me opportunities to work as a Teaching Associate throughout my PhD to improve my teaching skills.

I must thank Sri Lankan government for providing me free education up to my Bachelor's degree. Also, I like to thank Texas Tech University for giving me a chance to get a Masters degree and offering me a Teaching Assistantship. I can't imagine coming here without those supports.

I am grateful to dear friend Anchal Sareen for her support and voluminous fruit-

ful discussions on flow-induced vibration. I would also like to thank my colleagues: Shantanu Bhat, Farah Houdroge, Lawrence Wong, Shian Mike Chi, James Venning, Sewminda Kalana Samarasinghe, Abdul Mateen Qadri, Dhiraj Kumar Singh, Sengupta Sourav, Atul Soti, Sarang Kulkarni, Binbin Chen, and Shevarjun Senthil for making this journey possible by countless supports and cheer ups.

Earnest blessings I receive from my family energised me and let this thesis be possible. I am thankful to my loving family: Manatunga Dewage Karunawathi, Chaminda Christeen Rajamuni, Rasika Priyadarshani, Dinidi Nimesha, Dilini Nihinsa, Amandina, Kahagalage Piyadasa, and Barlasooriya Arachchighe Indrani, including my late father, Rajamuni Dewayalage Leelasena for endless supports and encouragements and for being with me.

Last, but not least, I extend my heartfelt gratitude to my dear husband, Sanath Darshana. Your love, appreciation, support and harmony continue to strengthen me, and inspire me. Thank you.

Nomenclatura

English Symbols

A	Sphere response amplitude
$\boldsymbol{a_c}$	Acceleration of the sphere in Cartesian coordinates, $\boldsymbol{a_c} = M\boldsymbol{a_s}$
$\boldsymbol{a_s}$	Acceleration of the sphere in spherical coordinates
A^*	Non-dimensional sphere response amplitude, $A^* = A/D$
A_x^*	Non-dimensional sphere response amplitude in the streamwise direction, $A_x^* = \sqrt{2}X_{rms}/D$
A_y^*	Non-dimensional sphere response amplitude in the lateral direction, $A_y^* = \sqrt{2}Y_{rms}/D$
A_z^*	Non-dimensional sphere response amplitude in the transverse direction, $A_z^* = \sqrt{2}Z_{rms}/D$
B	Buoyancy force, $B = \frac{4}{3}\pi(D/2)^3\rho(1-m^*)g$
c	Structural damping constant
$\boldsymbol{C}$	Companion matrix
$\overline{C}_d$	Time-averaged drag coefficient
$\overline{C}_l$	Time-averaged lift coefficient
C_a	Added mass coefficient, $C_a = 0.5$ for a sphere
C_d	Drag coefficient, $C_d = 2F_d/(\rho U^2 S)$
C_{ly}	Lift coefficient in the y direction, $C_{ly} = 2F_{ly}/(\rho U^2 S)$
C_{lz}	Lift coefficient in the z direction, $C_{lz} = 2F_{lz}/(\rho U^2 S)$
C_l	Lift coefficient
C_{sp}	Number of cells in the sphere boundary
D	Diameter of the sphere

$\boldsymbol{e_r}$	Unit vector in the radial direction
$\boldsymbol{e_\phi}$	Unit vector in the polar direction
$\boldsymbol{e_\theta}$	Unit vector in the azimuthal direction
f	Sphere response frequency
$\boldsymbol{f_l}$	Flow-induced integrated vector force acting on the sphere due to the pressure and viscous shear forces
f^*	Frequency ratio, $f^* = f/f_n$
F_d	Drag force (force in the x direction)
f_n	Natural frequency of the system
F_p	Potential force component
F_t	Total fluid forces acting on the sphere, $F_t = F_p + F_v$
F_v	Vortex force component
F_{ly}	Lift force in the y direction
F_{lz}	Lift force in the z direction
F_l	Lift force
f_s	Vortex shedding frequency
f_{vo}	Static body vortex shedding frequency
Fr	Froude number, $Fr = U/\sqrt{gD}$
G	Mapping between $\boldsymbol{x_i}$ and $\boldsymbol{x_{i+1}}$, $\boldsymbol{x_{i+1}} = G\boldsymbol{x_i}$
g	Gravitational acceleration
I	Inertia of the tethered sphere at the base of the tether, $I = m(D^2/10 + L^2)$
$\boldsymbol{i}$	Unit vector in the x direction
$\boldsymbol{j}$	Unit vector in the y direction
k	Spring constant
$\boldsymbol{K}$	Matrix created with the vectors of flow field, $\boldsymbol{K} = (\boldsymbol{x_1}\ \boldsymbol{x_2},\ \ldots, \boldsymbol{x_{m-1}})$
$\boldsymbol{k}$	Unit vector in the z direction

KM	Koopman mode
L	Tether length
l^*	Non-dimensional tether length, $l^* = L/D$
M	Mapping of the spherical coordinate system ($\boldsymbol{e_r}$ $\boldsymbol{e_\theta}$ $\boldsymbol{e_\phi}$) to the Cartesian coordinate system ($\boldsymbol{i}$ $\boldsymbol{j}$ $\boldsymbol{k}$)
m	Mass of the sphere
m^*	Mass ratio of the sphere, $m^* = m/m_f \equiv \rho_s/\rho$
m^*_{crit}	Critical mass ratio
M^{-1}	Inverse of the mapping M
m_f	Mass of fluid displaced by the sphere
N_r	Number of nodes in the radial direction of a square frustum
P	Fluid pressure
p	Kinematics fluid pressure, $p = P/\rho$
$\boldsymbol{r_s}$	Position of the sphere in spherical coordinates
Re	Reynolds Number, $Re = UD/\nu$
S	Reference surface area, $S = \pi(D/2)^2$
S_n	Non-dimensional natural frequency, $S_n = f_n D/U$
St	Strouhal number, $St = f_{vo} D/U$
T	Tension of the tether
t	Time
T_c	Period of the sphere oscillation, $T_c = 1/f$
U	Free-stream velocity of the flow
$\boldsymbol{u}$	Fluid velocity vector
U^*	Reduced velocity, $U^* = U/f_n D$
$\widehat{\boldsymbol{v}}_{\boldsymbol{i}}$	Rescaled i^{th} Ritz vector, $\widehat{\boldsymbol{v}}_{\boldsymbol{i}} = \boldsymbol{K}\widehat{\boldsymbol{z}}_{\boldsymbol{i}}$
$\widehat{\boldsymbol{z}}_{\boldsymbol{i}}$	Scaled version of $\boldsymbol{z_i}$, $\widehat{\boldsymbol{z}}_{\boldsymbol{i}} = \beta_i \boldsymbol{z_i}$, where β_i is the ith element of the vector $\boldsymbol{\beta}$

$\boldsymbol{v_c}$	Velocity of the sphere in Cartesian coordinates, $\boldsymbol{v_c} = M\boldsymbol{v_s}$
$\boldsymbol{v_i}$	i^{th} Koopman mode (or i^{th} Ritz vector)
$\boldsymbol{v_s}$	Velocity of the sphere in spherical coordinates
X	Sphere displacement in the x direction
x	Streamwise direction
$\boldsymbol{x_i}$	i^{th} flow field vector
Y	Sphere displacement in the y direction
y	Lateral direction
$\ddot{\boldsymbol{y}}_{\boldsymbol{s}}$	Acceleration vector of the solid
$\dot{\boldsymbol{y}}_{\boldsymbol{s}}$	Velocity vector of the solid
$\boldsymbol{y_s}$	Displacement vector of the solid
Z	Sphere displacement in the z direction
z	Transverse direction
$\boldsymbol{z_i}$	i^{th} eigenvector of C
$\boldsymbol{Z}$	Matrix of Ritz vectors, $\boldsymbol{Z} = (\boldsymbol{z_1}\ \boldsymbol{z_2},\ \ldots, \boldsymbol{z_{m-1}})$
Z_{max}	Maximum sphere displacement in the z direction
Z_{rms}	Root mean square value of the sphere displacement in the z direction

Greek Symbols

α	Rotation rate (speed of the sphere surface normalized by the free stream velocity), $\alpha = \omega D/2U$
δl	Cell thickness of the sphere boundary
δt	Time step
γ	Relaxation parameter
λ_A	Periodicity of the sphere displacement, $\lambda_A = \sqrt{2}Z_{rms}/Z_{max}$
μ	Dynamic viscosity
ν	Kinematic viscosity, $\nu = \mu/\rho$

ω	Angular velocity of the sphere
ϕ	Tether angle from z direction (polar angle)
ϕ_t	The phase between the sphere displacement and the total force
ϕ_v	The phase between the sphere displacement and the vortex force
ψ	$4/(3Fr^2)$
ρ	Density of the fluid
ρ_s	Density of the sphere
τ	Non-dimensional time, $\tau = tU/D$
θ	Tether angle from x-z plan (azimuthal angle)
ζ	Damping ratio, $\zeta = c/(2\sqrt{mk})$
$\boldsymbol{\beta}$	$\boldsymbol{Z^{-1}e_1}$, where $e_1 = (1\ 0\ 0 \ldots\ 0)$
$\boldsymbol{\eta}$	Outward unit normal vector
$\dot{\boldsymbol{\omega}}$	Angular acceleration vector of the sphere, $\dot{\boldsymbol{\omega}} = \boldsymbol{a_s}/L$
$\boldsymbol{\omega}$	Angular velocity vector of the sphere
$\ddot{\phi}$	Second derivative of ϕ w.r.t. time
$\dot{\phi}$	First derivative of ϕ w.r.t. time
$\ddot{\theta}$	Second derivative of θ w.r.t. time
$\dot{\theta}$	First derivative of θ w.r.t. time
$\overline{\theta}_l$	Time-averaged layover angle
$\boldsymbol{\nabla\cdot}$	Divergence operator
$\boldsymbol{\nabla}$	Gradient operator
$\boldsymbol{\nabla}^2$	Laplacian operator
λ_i	i^{th} eigenvalue of C (or i^{th} Ritz value)
θ_l	Layover angle (the angle of the tether to the lateral direction)

Contents

List of Figures

List of Tables

It is better to conquer yourself than to win a thousand battles. Then the victory is yours. It cannot be taken from you, not by angels or by demons, heaven or hell.

Lord Buddha

1. Introduction

Fluids and structures are everywhere, so the interaction between them can be expected to occur any time somewhere in the world, even at the time I am writing this thesis. We all have witnessed Fluid-Structure Interaction (FSI) at least once, for example, oscillation of long flag poles, chimney stacks and wire cables. Although FSI seems to be gentle and harmless in some situations, it can result in fatigue structural damage. The collapsing of the Tacoma Narrows Bridge in 1940 as a result of large-scale oscillations caused by natural winds is one of the most renowned examples of damage due to induced oscillations. FSI is of practical significance for many Engineering fields. Therefore, it has been an important research topic in fluid dynamics for many years.

Flow-induced vibration (FIV) of a structure is one of the most important types of fluid-structure interaction problems. It is a vibration phenomenon of solid structures induced by the flow of the surrounding fluid. When a fluid flows past a bluff solid structure, a large amplitude fluctuation pressure force can develop near the rear of the structure, which leads to the formation of a wake with alternately shedding vortices. FIV is primarily excited by the wake formed behind the structure. *Vortex-induced vibration*, or (VIV), is a category of FIV, occurring through the synchronisation of structural vibration with the wake unreadiness. In particular, a structure experiences large amplitude VIV for the cases where the vortex shedding frequency is locked-in to the natural frequency of the system. VIV occurs only in a discrete range of flow speeds, and the amplitudes are limited to the order of magnitude of one characteristic length (i.e. the diameter of the sphere). This is a self-limited vibration state that can be sustained over a lengthy period. *Galloping* is another category of FIV, occurring through the aerodynamic instabilities under certain conditions of the fluid-structure system. Galloping can arise for any light-weight structure exposed to a flow. A variety of structures are potentially unstable owing to aerodynamic galloping. In contrast to VIV, galloping occurs for all flow speeds past a critical value and it is not self-limited, with a much larger amplitude developing. Both VIV and galloping can cause fatigue damage or failure of a structure and therefore they are crucial considerations for the design of many engineering systems. Some examples are bridges, chimney stacks, aircraft, ground vehicles, submarines, tethered structures and offshore structures. Hence, it is important to have a better understanding of FIV and the methods of controlling it.

The most popular geometries used for fundamental FSI studies are cylinders and

spheres. In the case of flow past a circular (or square) cylinder, a huge volume of research has been undertaken, due to its intrinsic engineering importance and due to the simplicity of setting up such arrangements both experimentally and computationally. In contrast, comparatively fewer studies have been conducted on the flow past a sphere (or spheroid). Thus, the wake of a sphere is less well understood, compared with the wake of a cylinder. However, versatile applications exist on FIV of a sphere, for example, tethered bodies such as buoys, underwater mines, tethered balloons, and towed objects behind vessels.

Key features of FIV of a sphere were initially revealed through the series of experimental investigations conducted by Williamson & Govardhan (1997); Govardhan & Williamson (1997); Jauvtis *et al.* (2001) and Govardhan & Williamson (2005) using tethered and elastically-mounted spheres. The sphere was also found to show a VIV behaviour with a large oscillation amplitude, similar that found for a cylinder. The reduced velocity, $U^* \equiv UD/f_n$, which is a non-dimensionalisation of the upstream velocity, U, based on the natural frequency of the system, f_n, was identified to be more suitable than the Reynolds number for FIV of a sphere; here, D is the diameter of the sphere. The nature of FIV of a sphere was significantly different to that of a cylinder, as their wake patterns are different. Four distinct modes of sphere vibrations (named as modes I-IV) were identified with varying characteristics in terms of sphere oscillation amplitude and phase, and wake structures.

The first two modes (modes I and II) were identified as vortex-induced vibration responses as the sphere vibration was synchronised with both vortex shedding frequency and the natural frequency of the system. The sphere response amplitude is found to vary smoothly, as the vibration transitions from mode I to mode II. These two modes were observed in the range of $5 \lesssim U^* \lesssim 10$ for a variety of mass ratios ($\equiv$ density ratio of the sphere and fluid). Govardhan & Williamson (2005) observed a reduction in the vibration amplitude and narrowing of the synchronisation regime as the mass ratio increased. Mode I is found to be more robust as it is a consequence of natural resonance. Most of the previous FIV studies of a sphere were experimental and those studies were performed in the turbulence regime due to the experimental limitations. Only a few computational studies were reported on FIV of a sphere over the modes I and II regimes, and their findings in the laminar regime slightly deviated from the experimental observations. Therefore, this computational study is focused on enhancing the understanding of modes I and II, especially the effect of Reynolds number over the range $Re = [300, 2000]$ using both elastically-mounted and tethered spheres.

As the reduced velocity increased beyond the mode II regime, after a de-synchronisation regime, the sphere again showed another periodic vibration state for $U^* \in [20, 40]$ (Jauvtis *et al.* 2001). This was designated as mode III. It was an unexpected finding and was difficult to explain from the classic lock-in theories, as the vortex shedding frequency

was three to eight times higher than the sphere vibration frequency. Even though mode III is not a VIV response, Govardhan & Williamson (2005) argued that it is indeed a *Movement-induced vibration* response. Mode III was only found for heavy spheres, and as a consequence, the sphere vibration frequency was identical to the system's natural frequency. Jauvtis *et al.* (2001) found an intermittent bursts of vibration for $U^* > 100$, and this state was named as mode IV. In this mode, the maximum oscillation amplitude was found to show a linearly increasing trend as the reduced velocity increased. Mode IV cannot be considered a movement induced vibration as it shows similarities to the galloping behaviour. The low-frequency vibration modes III and IV are less examined and their nature is not well understood. Hence, this study also aims to extend the understanding of mode III and IV regimes.

Effects of sphere rotation on its flight have been investigated for centuries. Benjamin Robinson and Heinrich Gustav Magnus were the first to observe a transverse force applied on the sphere when it propagates with a transverse rotation. This phenomenon is known as *Magnus effect*. Magnus identified that the rotational motion of the sphere is responsible for this transverse force (Magnus force). It was found that the magnitude of the Magnus force increases with the rotation rate. Moreover, in the laminar regime, the flow underwent a series of different transitions between steadiness and unsteadiness as the rotation rate was increased. Interestingly, the flow past a rotating sphere has many practical applications. In sports such as cricket, football, tennis, and netball, where the trajectory of the ball depends on the transverse rotation of the ball Goff & Carré (2010). Engineering applications can be found in particle transport processes (Torobin & Gauvin 1960; White & Schulz 1977), combustion systems (Pearlman & Sohrab 1997; Dgheim *et al.* 2012), and saltation of particles White & Schulz (1977), where the particles are modelled as rotating spheres. However, the influence of transverse rotation on the flow-induced vibration was not examined until the very recent experimental study of Sareen *et al.* (2018*a*) from our group. They observed a reduction in the oscillation amplitude and narrowing of the synchronisation regime as the rotation rate increased over the modes I and II regimes for turbulence flows. However, there is much more to explore on the effect of forced rotation on VIV of a sphere, especially the wake structures and force measurements. The present study also aims to reinforce the knowledge on the competition between the Magnus effect and the vortex-induced vibration of a sphere in the laminar regime, numerically.

1.1. Structure of the thesis

Apart from the Introduction, there are six chapters in this thesis. Each chapter begins with a brief introduction of the content and ends with a brief summary highlighting the key discussion and findings. The thesis is structured as follows:

Chapter 2: A brief review of the literature is presented illustrating the current state of the knowledge of vortex-induced vibration of a sphere, highlighting the key finding and disclosing the gaps and unanswered areas.

Chapter 3: The numerical methodology is presented discussing the problems formulation, numerical approach and validation studies.

Chapter 4: The results of the flow-induced vibration of an elastically-mounted sphere is presented. The effect of Reynolds number on FIV of a sphere is discussed analyzing the sphere response amplitude, force measurements and wake structures.

Chapter 5: Effects of the sphere transverse rotation on the vortex-induced vibration of an elastically-mounted sphere are presented by discussing the sphere response, forces exerted on the sphere and vortical wake structures.

Chapter 6: Flow-induced vibration of a tethered sphere is investigated and the results are compared with previous experimental studies. A detailed discussion on different modes of sphere vibration is also provided.

Chapter 7: A comprehensive conclusion of the thesis is given summarising the key findings of the previous chapters. Future works are also discussed at the end of the chapter.

I have never met a man so ignorant that I couldn't learn something from him.

Galileo Galilei

2. Literature Review

A huge amount of research has been undertaken over past decades advancing the knowledge of *Flow-Induced Vibration* (FIV) of structures, as it is practically important to a variety of Engineering fields. Due to the complexity and non-linearity of FIV problems, it is impossible to find an analytical solution. Therefore, fundamentals of FIV have been disclosed extensively through experimental and numerical studies with generic bluff bodies. The textbooks by Blevins (1977) and Naudascher & Rockwell (2005) and the comprehensive reviews of Bearman (1984); Parkinson (1989); Sarpkaya (2004); Williamson & Govardhan (2004, 2008); Wu *et al.* (2012) provide a detailed introduction to the field. Most FIV studies have been based on cylindrical structures, although spherical bodies are equally important. This chapter presents a brief review of the literature on the state of art of flow-induced vibration of spheres, describing the fundamentals and related topics to the research presented in this thesis. Vortex-induced vibration (VIV) of the generic three-dimensional bluff body, the sphere, will be examined and discussed in detail to explore the fundamentals of the field. In addition, the current state of knowledge on the effects of transverse rotation on a bluff body in a uniform fluid flow is also presented.

Prior to investigating the interaction of the fluid flow and the sphere, it is essential to understand the nature of the problem for the case when the sphere is held stationary. The chapter begins by reviewing the flow past a stationary sphere in § 2.1, including discussions on different flow regimes, fundamental aspects of vortex shedding and fluid forces exerted on the sphere. Following this, § 2.2 presents studies on effects of transverse rotation of the sphere describing the forces applied on it and wake patterns as a function of Reynolds number and rate of rotation. The current state of knowledge on flow-induced vibration of a sphere is presented in § 2.3. This section mainly deals with the sphere responses (i.e. the amplitude, frequency and phase responses), force measurements and wake structures of elastically-mounted and tethered spheres under various flow conditions. In addition, previously identified different modes of sphere vibration are also discussed. Next, the current state of limited knowledge built on the combined effect of constant rotation and vortex-induced vibration is discussed in § 2.4. Finally, a summary of the chapter and research questions are given in § 2.5.

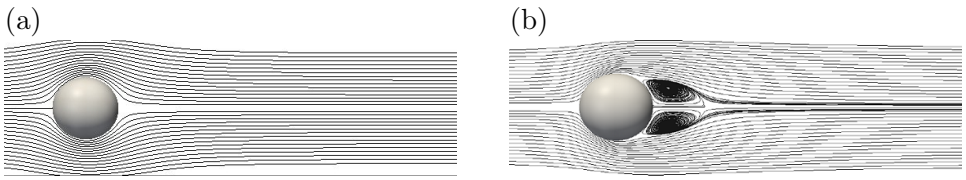

Figure 2.1.: Streamlines of Axisymmetric steady flow; (a) Creeping flow, $Re < 24$, visualized at $Re = 10$ and (b) Separated axisymmetric steady flow, $25 < Re < 210$, visualized at $Re = 100$.

2.1. Flow past a stationary sphere

The Reynolds number, Re, which measures the ratio of inertial to viscous forces, is the key non-dimensional parameter governing the flow state. For fluid-structure interaction of a sphere, the Reynolds number is generally defined as

$$Re = \frac{UD}{\nu},$$

where U is the free-stream velocity of the fluid, D is the diameter of the sphere, and ν is the kinematic viscosity of the fluid. In general, but not exclusively, experimental studies have been conducted for higher Reynolds numbers while numerical studies have tended to focus on lower Reynolds numbers. Results from both approaches are presented here.

The flow of a viscous fluid past a stationary isolated sphere is considered first, as it provides a baseline study for wake states. Several notable research studies have been conducted previously at various Reynolds numbers. Flow transitions have been mapped depending on the structure of the wake as a function of Reynolds number. In this section, we present some results from relevant studies according to the flow regimes in detail.

2.1.1. Axisymmertic steady flow

When a sphere is placed in a steady flow at low Reynolds numbers, the fluid creeps smoothly around the sphere surface without separating from it, as shown in figure 2.1 (a). In addition, the flow streamlines appear identical upstream and downstream of the sphere. Creeping flows are also known as Stoke flows. For $Re < 1$, the advective inertial forces are smaller and negligible compared to the viscous forces. Therefore, the complex Navier-Stokes equations can be approximated by a set of linear equations as proposed by Stokes (1851). This enables one to obtain an analytical solution and calculate the forces applied on the sphere. However, as the Reynolds number increased, the inertial effect cannot be neglected and the full Navier-Stokes equations need to be considered.

Taneda (1956) photographically studied the wake produced by a sphere moving in a tank of water at Reynolds number between 5 and 300. He observed that as Re was

increased from 5, the flow that was initially attached to the sphere started to separate at $Re \approx 24$, creating a recirculation bubble behind the sphere near the stagnation point. This first flow transition to separated flow was also observed by Dennis & Walker (1971) semi-analytically, and by Masliyah & Epstein (1970); Johnson & Patel (1999) numerically. The recirculation bubble behind the sphere take a 'toroidal' form which is axisymmetric with respect to the streamwise centreline of the sphere, and the flow has a fixed separation line encircling the sphere (see figure 2.1 (b)). As the Reynolds number increased, Taneda observed that the size of the recirculation bubble grows at a rate close to the logarithmic of Reynolds number, and become more and more elongated in the streamwise direction. Johnson & Patel (1999) found that this toroidal vortex behind the sphere was balanced by the viscous forces, as opposed to radial pressure gradients.

As the Reynolds number increases close to 130, Taneda observed a faint periodic pulsative motion with a very long period occurring at the rear of the vortex ring. However, the flow was perfectly laminar until $Re = 200$. Magarvey & Bishop (1961) studied falling droplets of an immiscible fluid in a number of different liquid-liquid systems and reported a closed recirculation region immediately behind the sphere. They observed a tail lift by the passing drop with a single thread and categorized this axisymmetric regime as a *single threaded* wake. This regime was found to be continued until the Reynolds number reach approximately 210.

The drag coefficient is found to be approximately inversely proportional to the Reynolds number up to $Re = 100$ (Kawaguti 1955; Masliyah & Epstein 1970). Over the range of $Re \in (20,\ 210)$, Jones *et al.* (2008) observed that the drag coefficient, $C_d = \frac{F_d}{\frac{1}{2}\rho U^2(\pi(D/2)^2)}$, dropped from 2.7 to 0.7 with an exponentially decreasing trend, resembling the results of Tabata & Itakura (1998) and Clift *et al.* (2005), where F_d is the drag force and ρ is the density of the fluid.

2.1.2. Non-axisymmetric steady flow

As the Reynolds number increased further, the flow loses it axisymmetry and undergoes a transition. The flow does remain steady despite the transition, as first observed by Magarvey & Bishop (1961). Past research studies found that this transition occurs at $Re \approx 210$ (Magarvey & Bishop 1961; Magarvey & MacLatchy 1965; Johnson & Patel 1999; Natarajan & Acrivos 1993; Tomboulides *et al.* 1993; Wu & Faeth 1993; Thompson *et al.* 2001). The stability analysis of Natarajan & Acrivos (1993) referred to this transition as a regular bifurcation, due to the fact that the flow remains steady. This bifurcation was found to be supercritical by the computational study of Thompson *et al.* (2001) using the Landau model.

The nature of the flow in this regime consists of an interesting wake configuration of twin vortex trails. They are equal in strength and opposite in sign. Magarvey &

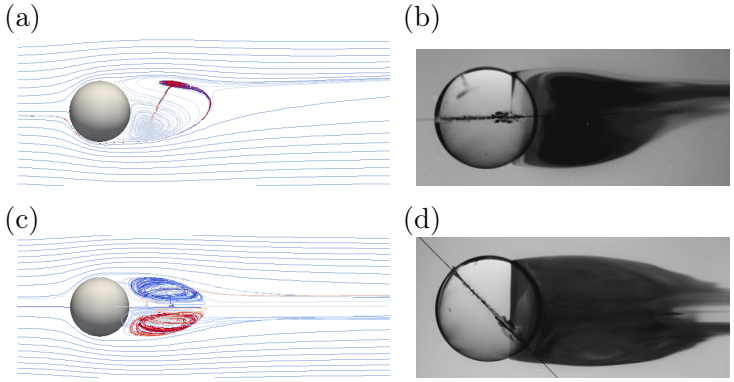

Figure 2.2.: Streamlines coloured by the intensity of rotation of the flow ((a) and (c)) and the flow visualization by Johnson & Patel (1999) ((b) and (d)) of the planar-symmetric steady flow, $210 < Re < 270$, visualized at $Re = 250$: (a) and (b) in the plane of symmetry, (c) and (d) in the plan perpendicular to the plane of symmetry, which passes through the centre of the sphere.

Bishop (1961) referred to this spectacular structure observed behind the falling droplets for $210 < Re < 270$ as a *double threaded* wake. These vortex trails (or vortex tubes) are oriented in the streamwise direction with an offset from the streamwise centreline (see figure 2.2 (a) and (b)). Even though the flow no longer possesses axial symmetry, the flow exhibits planar symmetry with respect to a plane passing through the streamwise centreline of the sphere as shown in figure 2.2 (c) and (d). The orientation of the plane is arbitrary and will only depend on random external influences, such as perturbation due to model support in an experimental situation, or boundary conditions or grid asymmetry in numerical simulations.

Johnson & Patel (1999), who studied flow past a sphere for Reynolds number up to 300 by both experiments and numerical simulations, found that the regular transition is associated with an azimuthal instability of the low-pressure core of the pre-transition toroidal vortex. They argued that this instability grows, as the viscous effect of the toroidal vortex becomes less important. Based on that, they proposed a mechanism to describe this regular transition, which can be described as follows. The azimuthal pressure gradient resulting from the instability distorts the axisymmetric toroidal vortex. As figure 2.2 (a) shows, the toroidal vortex appears to be tilted and its size is clearly not constant in the azimuthal direction. Additionally, the toroidal core is been opened up, allowing entrainment and release of fluid. The release of wake fluid occurs through two trails, in agreement with the double threaded twin trails observed in previous experimental studies.

As the flow loses its axial symmetry, the sphere experiences a lateral (lift) force, F_l, which was not found for axisymmetric flows. Magarvey & MacLatchy (1965) observed

the presence of this force by noting a deviation of the flight of the liquid drops from the vertical lines. More recently, the presence of a lateral force has been verified by several numerical simulations. Gushchin *et al.* (2002) performed direct numerical simulations and found a finite value for the lift force at $Re = 210.5$ although this lift force was zero for $Re = 210$. Consistently, Johnson & Patel (1999) observed a lift force as soon as the flow entered this regime. Moreover, they found that the lift force grew quickly within a couple of Reynolds numbers and showed an increasing trend toward the end of the regime at $Re \approx 270$.

2.1.3. Unsteady flow

2.1.3.1. Planar-symmetric unsteady flow

Simulations of Thompson *et al.* (2001) noted that toward the end of the steady regime, the trails of the twin vortex tubes described above kink together several diameters down-stream of the sphere. The trails have come closer together at a point, before moving apart again. This kinking was more prominent as the Reynolds number increased and showed a possibility of shedding a vortex and a transition to an unsteady wake. In experiments, the twin vortex trails were found to show an unsteady undulation of long wavelength, as the Reynolds number increase closer to the transition (Magarvey & Bishop 1961; Sakamoto & Haniu 1990; Ormières & Provansal 1999; Schouveiler & Provansal 2002). This pre-transitional unsteadiness of the wake only lasts for a narrow range of Reynolds numbers, and later leads to a three-dimensional pattern of periodic vortex shedding.

Various experimental and numerical investigations have observed that the flow transition to unsteadiness occurs in the range of $270 < Re < 300$. The experimental study of Magarvey & Bishop (1961) found that the wake becomes unsteady and consists of series of interconnected vortex loops above $Re = 290$. However, the experimental study of Sakamoto & Haniu (1990) on flow past a sphere observed an unsteady wake beyond $Re = 300$, while Wu & Faeth (1993) reported vortex shedding over $Re = 280$. The stability analysis of Natarajan & Acrivos (1993) predicted a value of $Re \approx 277$ for the transition, while Ghidersa & Dušek (2000) and Thompson *et al.* (2001) predicted it occurs approximately at $Re = 272$ using the Landau model. The stability analyses indicated that the Hopf bifurcation is also supercritical, similar to the normal bifurcation (Natarajan & Acrivos 1993; Thompson *et al.* 2001; Schouveiler & Provansal 2002).

The transition from a steady flow to a time-periodic flow is the most important transition in the sphere wake with respect to the flow-induced vibration. After this transition, the onset of laminar vortex shedding occurs. Several experimental and computational studies reported shedding of time-periodic vortex loops behind the sphere, as shown in figure 2.3. This periodic shedding induces a periodic force on the sphere. The transverse

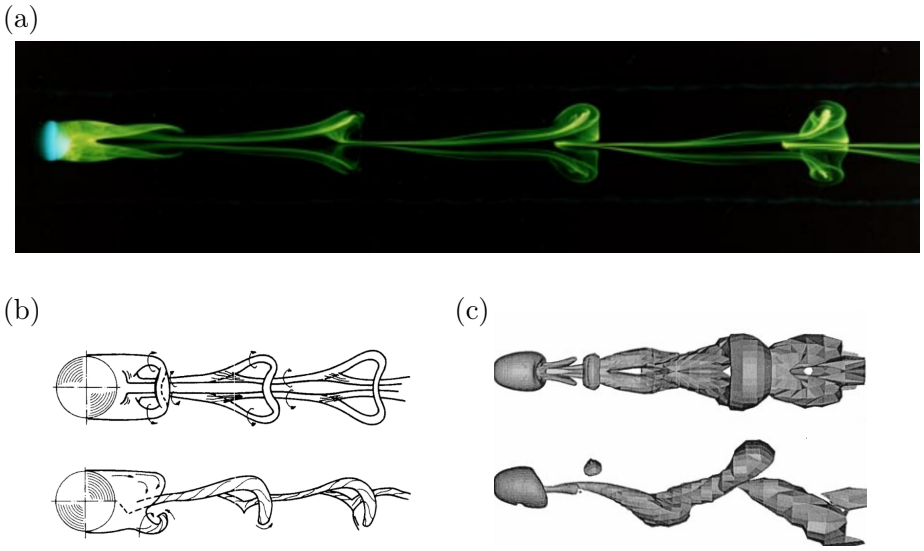

Figure 2.3.: Unsteady wake behind the sphere; (a) dye visualization of Leweke *et al.* (1999) at $Re = 320$, (b) schemetics of the wake observed by Achenbach (1974), and (c) vortical structures of Johnson & Patel (1999) at $Re = 300$.

component of the force is directly responsible for the excitation of sphere vibration when it was mounted with elastic supports or using a tether.

The structure and the orientation of the vortices shed behind the sphere show differences to those behind a cylinder, which is the $2D$ counterpart of the sphere. As the sphere is the most fundamental $3D$ shape, a vortex sheds like a hairpin, which is indeed three–dimensional. In addition, these vortex loops are interconnected and oriented in the streamwise direction, in contrast to the transversely oriented vortices of the wake behind a cylinder. Figure 2.3 (b) shows the schematic of this $3D$ wake formation observed by Achenbach (1974) from two directions perpendicular to one another. The diagram shows the directions and circulations of the flow using arrows. Although the flow is unsteady, it shows a symmetry with respect to a plane similar to the double-threaded steady wake, as shown in the figure. This planar symmetry of the wake has been observed by many researchers, and Mittal (1999), who developed an accurate Fourier–Chebyshev spectral collocation method to study flow past spheroids, found that the symmetry plane remained fixed, and the orientation of the plane was arbitrary.

For a sphere that is held rigidly fixed in a uniform flow, many experimental studies reported one-sided vortex shedding behind the body (Achenbach 1974; Sakamoto & Haniu 1990; Leweke *et al.* 1999; Ormières & Provansal 1999); an example of this is shown in figure 2.3 (a). Consistently, numerical studies of Tomboulides *et al.* (1993) and Johnson & Patel (1999) on flow past a rigidly mounted sphere observed that vortices

only shed from one side of the sphere, although a two-sided vortex structure was observed a couple of diameters downstream (see figure 2.3 (c)). However, in contrast to this one-sided wake configuration of a flow past a solid sphere, the wake behind freely falling drops, studied by Magarvey & Bishop (1961); Magarvey & MacLatchy (1965), were two-sided. As a liquid drop has the freedom to move sideways as it descends, vortex loops were shed from opposite sides of the drop. This indicates that if a degree of freedom is given to a rigidly mounted sphere in a uniform flow, it may excite vibration vigorously.

When the sphere is held fixed, Mittal (1999) and Johnson & Patel (1999) found that the vortex shedding induces a lift force on the sphere. The orientation of the lift force was lined up with the plane of symmetry of the wake. Mittal (1999) noted that the lift force was about an order of magnitude smaller than the drag force. Despite the fact that the size of the lift force was smaller, it was highly periodic as the vortex shedding was periodic. Moreover, Johnson & Patel (1999) reported that the lift force fluctuated with a magnitude one order higher than that of the drag force. These observations also lead to a prediction of vortex-induced vibration of a free sphere.

Sakamoto & Haniu (1990) calculated the vortex shedding frequency based on the fluctuating velocity detected by a hot-wire probe mounted in the wake behind the sphere. The frequency of the vortex shedding, f_{vo}, can be expressed as a non-dimensional quantity, called Strouhal number, $St = f_{vo}D/U$. Sakamoto & Haniu observed that St was scattered with an increasing trend from $St \approx 0.15$ to ≈ 0.17, as the Reynolds number increased until the symmetry of the flow loses around $Re \approx 420$. However, the numerically calculated values for the St based on lift and drag forces were slightly lower than the experimental values; both Johnson & Patel (1999) and Tomboulides *et al.* (1993) found that $St \approx 0.137$ at $Re = 300$.

2.1.3.2. Irregular unsteady flow

Magarvey & Bishop (1961) and Sakamoto & Haniu (1990) observed that the regular vortex shedding described above began to be generated irregularly and the shedding direction oscillated intermittently from left to right beyond $Re \approx 420$, as shown in figure 2.4. Sakamoto & Haniu (1990) observed a transition region for a narrow range of Reynolds number ($420 < Re < 480$), for which both regular and irregular vortex shedding occurred intermittently. After this range, vortex shedding was always irregular in its strength and frequency. Sakamoto & Haniu proposed that this irregularity of the vortex formation was perhaps due to the supply, storage, and emission of energy within the vortex formation region becoming imbalanced. They found that the vortex shedding frequency increased linearly with increasing Reynolds number in this regime as well.

In line with experimental findings, the numerical studies of Mittal (1999); Tomboulides & Orszag (2000); Mittal *et al.* (2002) also observed this breakdown of planar symmetry of the wake. The investigation of Mittal *et al.* (2002) of the irregular regime quanti-

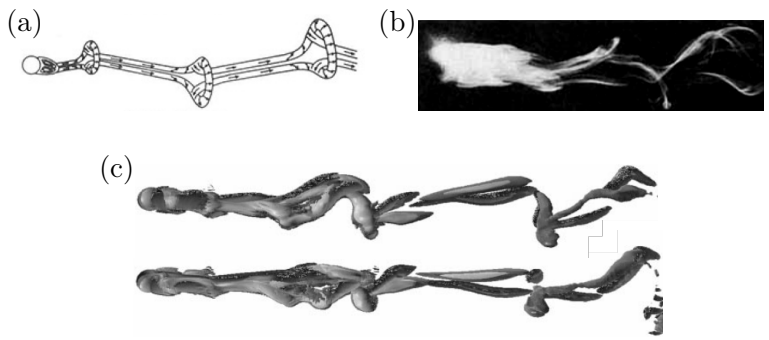

Figure 2.4.: Irregular wake behind the sphere; (a) a schematics of the wake observed by Sakamoto & Haniu (1990), (b) the dye visualization of the wake by Sakamoto & Haniu (1995) at $Re = 650$, (c) the iso-surface of the streamwise vorticity observed by Tomboulides & Orszag (2000) in two planes perpendicular to each other at $Re = 500$.

tatively showed that the shedding was not completely random and that there was a preferred azimuthal orientation. However, there was a significant cycle-to-cycle variation in the orientation of the loops about this preferred orientation. Their observations led to a conclusion that the wake was most likely to be planar symmetric in the time-averaged sense. They also found that as the Reynolds number increased, the preference for any particular orientation diminished. This may be mainly due to the wake becoming chaotic at higher Reynolds numbers, as described in the next section.

2.1.3.3. Chaotic flow

When the Reynolds number exceeds approximately 800, the hairpin vortices begin to change from the laminar to turbulent structures. Figure 2.5 (a) shows the chaotic wake observed by Sakamoto & Haniu (1990, 1995) at $Re = 1350$. As can be seen, the flow separates from the sphere surface and forms a vortex tube which extends for a couple of diameters. Further downstream, the wake consists of several small vortex loops showing the effect of turbulence. The numerical studies of Tomboulides & Orszag (2000) and Mittal *et al.* (2002) also reported a similar observation, as shown in figure 2.5 (c). Although the wake is distorted, hairpin loops were clearly recognizable up to supercritical Reynolds numbers ($Re \approx 3.7 \times 10^5$), as shown in the schematic of figure 2.5 (b) (Taneda 1978; Sakamoto & Haniu 1990, 1995; Mittal *et al.* 2002). For $3.8 \times 10^5 < Re < 10^6$, the experimental study of Taneda (1978) found that the wake behind the sphere consisted of a pair of streamwise line vortices. He also found that for all Reynolds numbers ranging from 400 to 10^6, the sphere wake was not axisymmetric, which showed an evidence of randomly oriented side force applying on the sphere.

In this section, we discuss the literature on flow past a rigid and stationary sphere.

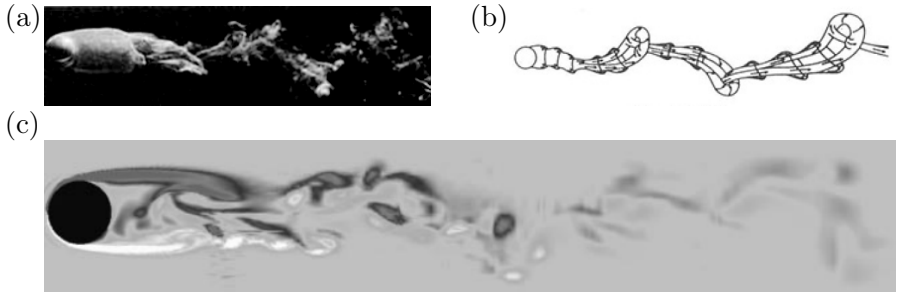

Figure 2.5.: Chaotic wake behind the sphere; (a) the dye visualization of the wake by Sakamoto & Haniu (1995) at $Re = 1350$, (a) the schematics of the wake observed by Sakamoto & Haniu (1990), and (c) the iso-contours of azimuthal vorticity observed by Tomboulides & Orszag (2000) at $Re = 1000$.

As the Reynolds number increases from zero, the flow undergoes several transitions. Flow regimes have been identified primarily according to the wake characteristics. In summary, the flow that was attached to the surface of the sphere at low Reynolds numbers separates and forms an axisymmetric wake, with a toroidal vortex core behind the sphere, as Re reaches ≈ 24. Later, this toroidal core deforms and creates a double threaded wake behind the sphere at a Reynolds number of ≈ 210. This steady regime continues until $Re \approx 270$. Then, the flow becomes unsteady with the onset of vortex shedding. Vortex loops are oriented in the streamwise direction and planar symmetric with respect to a plane, similar to the double-threaded wake. As the Reynolds number reaches ≈ 420, the symmetry of the flow is lost and vortex loops shed irregularly. The flow becomes chaotic as the laminar hairpin structures become turbulent for $Re > 800$.

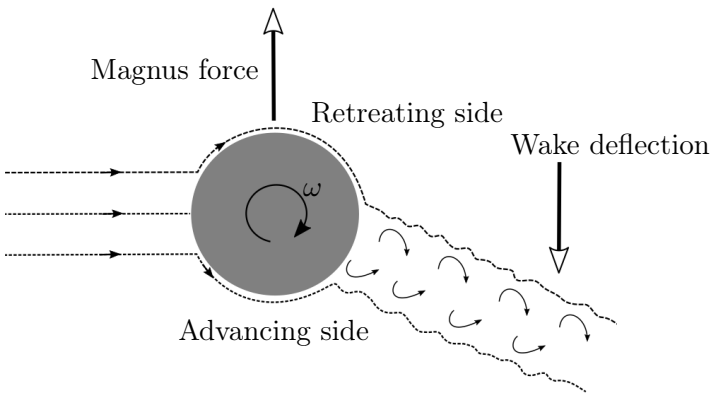

Figure 2.6.: Schematic of the Magnus effect of a rotating sphere.

2.2. Flow past a rotating sphere

Although there are impressive engineering and sports applications of flows past rotating spheres as mentioned in chapter 1, only a few studies have been conducted on the effect of rotation on the flow. One contributing factor is that there are inherent difficulties in measuring forces and satisfactorily limiting flow contamination from mounts in experimental studies, whilst numerical models require substantially increased resolution to capture the thin boundary layer. Thus, the characteristics of the flow past a rotating sphere are less well understood compared with those for a stationary sphere. However, studies are needed to further understand the characteristics of the flow and widen the applications. In this section, we present the current knowledge on the forces and wakes of rotating spheres.

2.2.1. Flow past a transversely rotating sphere

Early research studies carried out by Benjamin Robin (1707–1751) observed that the flight of solid balls underwent an unexpected drift when fired from smooth-bore guns. With his ballistic experiments, he confidently concluded that this drift was due to the whirling motion of the bullets (Robin 1972; Johnson 1986). About a century later, in laboratory experiments, Heinrich Gustav Magnus (1802-1870) proved that the rotational motion of the solid was responsible for the transverse force that deflected the flight path (Magnus 1853). Hence, later this phenomenon was named the *Magnus effect*, although sometimes it is also referred to as the *Robin-Magnus effect*. Figure 2.6 displays this phenomenon of wake deflection leading to a transverse force (Magnus force) on a solid sphere. The sphere surface motion is in the flow direction on the retreating side of the sphere and opposite towards the advancing side. This causes deflection of the fluid flow on the advancing side, and hence induces a force on the retreating side, as shown in figure 2.6.

When a rigidly mounted sphere is undergoing a forced rotation, in addition to the Reynolds number, the parameter called the *rotation rate* is also required to fully describe the nature of the problem. For a transversely rotating sphere, the non-dimensional rotation rate, α, can be defined as the maximum speed of the surface of the sphere normalised by the freestream speed ($\alpha = \omega D/2U$, where ω is the angular velocity of the sphere). In this section, first, we will review the literature on the effects of rotation on the lift and drag forces induced on the sphere, and later, we will discuss the issues of transverse rotation on the flow.

2.2.1.1. Effects of rotation on the lift and drag forces

Effects of particle rotation on fluid forces have been investigated both experimentally and numerically, as well as theoretically. The early research study of Rubinow & Keller (1961) derived an expression for the lift force acting on a transversely rotating sphere for the Stokes regime ($Re \leq 1$ and $\alpha = \omega\ D/2U \leq 0.01$), based on the Stokes and Oseen approximation. They found that the drag force was not affected by the sphere rotation and the lift coefficient, $C_l = \frac{F_l}{\frac{1}{2}\rho U^2(\pi(D/2)^2)}$, could be expressed as $C_l = 2\alpha$. The computational study of You *et al.* (2003) investigated the effect of rotation at low Reynolds numbers ($Re < 64.5$) and high rotation rates ($\alpha < 5$). At $Re = 0.5$, they observed that C_l increased linearly with increasing α, supporting Rubinow & Keller formula. In addition, they found that the lift coefficient decreased with decreasing rotation rate or increasing Reynolds number.

At moderate Reynolds numbers, several notable studies have focused on deriving an expression for the lift and drag forces (Oesterlé & Dinh 1998; Kurose & Komori 1999; You *et al.* 2003; Niazmand & Renksizbulut 2003). The experimental study of Oesterlé & Dinh (1998) proposed an empirical correlation to estimate the lift coefficient from the rotation rate and Reynolds number, $C_l \approx 0.45 + (2\alpha - 0.45)e^{(-0.075\ \alpha^{0.4} Re^{0.7})}$, in the parameter ranges, $1 < \alpha < 6$ and $10 < Re < 140$. Their results seem to indicate that the influence of rotation rate on lift force is negligible for $Re > 100$. In their conclusion, they stated that empirical values of forces are not very accurate and numerical simulations are essential for further validations. The force coefficients calculated by the numerical study of You *et al.* (2003) were slightly different to those of Oesterlé & Dinh (1998), although the trend lines were similar.

The problem of rotating spherical particles in a linear shear flow has also received attention in the literature. Salem & Oesterle (1998) numerically investigated the effects of both sphere rotation and the shear rate for $Re < 40$. For low Reynolds numbers, they found that the drag force was slightly affected by the shear rate, but was not altered by the rotation rate, consistent with the observation of Rubinow & Keller (1961). For higher Reynolds numbers, they did not compute the forces; however, they proposed an expression for the torques exerted on a rotating particle in a shear flow for the

angular speed range, $-2 < \omega < 2$. Kurose & Komori (1999) also conducted a similar investigation for a wide range of Reynolds numbers, $1 < Re < 500$, different shear rates, and rotation rates ranging from 0 to 0.25. They observed a slight increment in the drag force as the rotation rate increased at a fixed Reynolds number, and this effect was more noticeable for $Re > 200$. Furthermore, the lift coefficient in a uniform unsheared flow appeared to increase with increasing rotation rate. However, they found that the lift coefficient tended to approach a constant value for $Re > 200$ for a given rotational rate.

Niazmand & Renksizbulut (2003) numerically studied the effect of sphere rotation on the uniform flow up to $Re = 300$ over the rotation rate range, $0 < \alpha < 1$. Their results of lift coefficient were in a good agreement with Kurose & Komori (1999). They also reported that C_l increased with rotation rate monotonically. Based on their result, they found that the relationship, $C_l = 0.11(1+\alpha)^{3.6}$, holds for the lift coefficient. At a given rotation rate, as the Reynolds number increased, they observed that C_l increases and then becomes constant, consistent with the results of Oesterlé & Dinh (1998); Kurose & Komori (1999) and You *et al.* (2003).

In more recent studies, Giacobello *et al.* (2009) and Kim (2009) investigated the flow past a transversely rotating sphere at $Re = 100$, 250, 300, for $0 \leq \alpha \leq 1$ and $0 \leq \alpha \leq 1.2$, respectively. Their studies revealed that both drag and lift coefficients increased with the rotation rate for all three Reynolds numbers considered. The force coefficients they calculated were also in good agreement with Kurose & Komori (1999) and Niazmand & Renksizbulut (2003). Dobson *et al.* (2014) studied the flow at those Reynolds numbers over the rotation rates $1.25 \leq \alpha \leq 3$. They reported that both lift and drag force coefficients slightly decreased as α increased beyond 2.

A number of experimental studies concerning the forces acting on a rotating sphere at high Reynolds numbers have been reported. Barkla & Auchterlonie (1971) conducted experiments on the lift and drag forces of a rotating sphere in the Reynolds number range, $1500 < Re < 3000$, and found that the lift coefficient is proportional to the rotation rate for the range, $2 < \alpha < 4$ ($C_l = (0.16 \pm 0.04)\alpha$). Tsuji *et al.* (1985) estimated C_l on a rotating sphere by studying the trajectories of the sphere impinging on an inclined plate. They also found a linear relationship between the lift coefficient and the rotation rate, $C_l = (0.4 \pm 0.1)\alpha$, for $550 < Re < 1600$ and $\alpha < 0.7$. The dependency of lift coefficient on the Reynolds number was found to become small for higher Reynolds numbers.

In some specific conditions, a rotating sphere is found experience a lift force in the direction opposite to that predicted by the Magnus effect. This is known as the *inverse Magnus effect* (Maccoll 1928; Davies 1949; Taneda 1957; Tanaka *et al.* 1990; Aoki *et al.* 2003; Muto & Oshima 2012; Kim *et al.* 2014). This counterintuitive phenomenon only occurs around the critical Reynolds numbers and low rotation rates. In the critical flow regime, Muto & Oshima (2012) observed that the lift coefficient became negative at

a relatively low rotational speed and then changed to positive as the rotational speed increased. Moreover, they revealed that only in the critical flow regime showed a trace of inverse Magnus effect, while both subcritical and supercritical flow regimes followed the regular Magnus effect. The numerical investigation of Kim *et al.* (2014) was focused on elucidating when and why the inverse Magnus effect occurs. They identified that the inverse Magnus effect is caused by the difference in the boundary-layer growth and separation along the advancing and retreating sphere surfaces. They also propose a model to predict when the inverse Magnus effect can occur, so that one can avoid it.

2.2.1.2. Effect of rotation on the flow

As described earlier, when the sphere is under a forced rotation, a deflection of the wake to the advancing side of the sphere was observed. Even though most studies on flow past a rotating sphere were focused on force measurements, a couple of studies were dedicated to examining the wake as well (Salem & Oesterle 1998; Niazmand & Renksizbulut 2003; Kim 2009; Giacobello *et al.* 2009; Poon *et al.* 2010, 2013, 2014; Dobson *et al.* 2014). This section presents findings of these studies organized according to the different flow regimes that were discussed in § 2.1 for a non-rotating sphere.

Effect of sphere rotation on the axisymmetric and steady flow

The study of Salem & Oesterle (1998) on the axisymmetric flow regime of a stationary sphere found that the toroidal vortex behind the sphere disappears in case of sphere rotation. Moreover, they observed only one stagnation point, which was displaced slightly away from the sphere surface due to the thin rotating fluid layer created near the sphere surface, as a result of the no-slip condition. With the presence of a sphere rotation, Niazmand & Renksizbulut (2003) also reported a similar observation of a deflected wake to the advancing side, as shown in figure 2.7. Although the flow lost it axisymmetry, it posed a symmetry with respect to the plane transverse to the axis of rotation which goes through the centre of the sphere, resembling the planar-symmetric steady wake of a stationary sphere. As shown in figure 2.7, a small recirculation zone is present behind the sphere at low rotation rates. The size of the circulation zone is small when compared to the case of zero-rotation, and it becomes smaller and eventually disappears as the rotation rate increased. Both Niazmand & Renksizbulut (2003) and Kim (2009) reported that this circulation zone was completely absent for $\alpha \geq 0.5$ at $Re = 100$.

Introduction of the sphere rotation forces the wake to form a double-threaded wake structure, similar to that of a stationary sphere above the regular transition ($210 < Re < 270$). Giacobello *et al.* (2009) observed that the uniformly developed shroud envelope for the zero-rotation case, distorts with the presence of rotation, causing it to grow over the advancing side and to diminish over the retreating side of the sphere

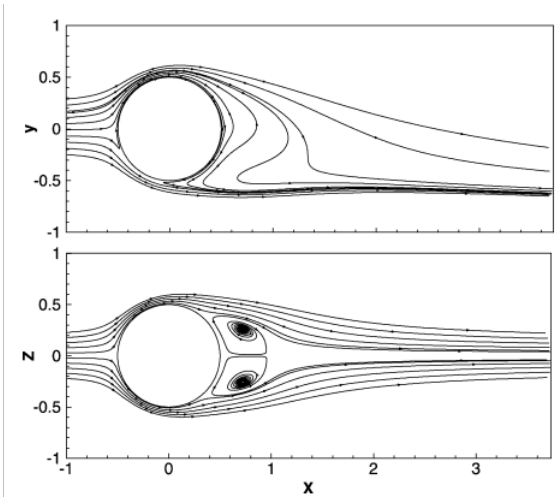

Figure 2.7.: Streamline showing the loss of axisymmetry of the flow when the sphere is under a force rotation at $Re = 100$ and $\alpha = 0.25$ from Niazmand & Renksizbulut (2003).

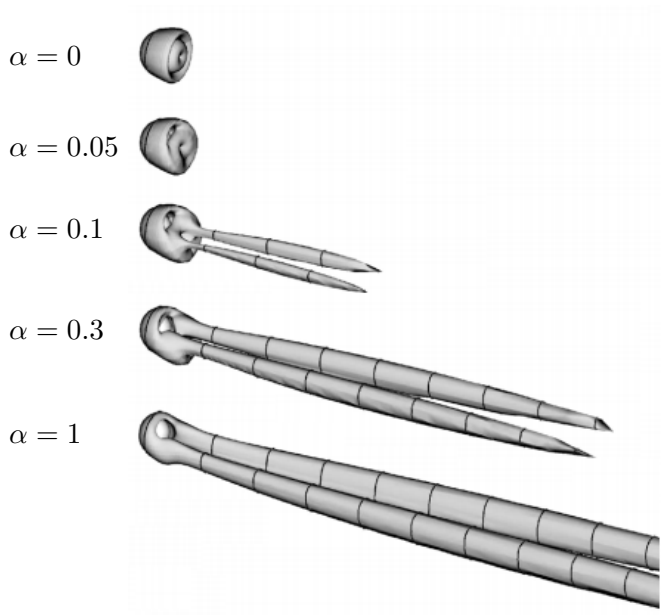

Figure 2.8.: Wake structure observed by Giacobello *et al.* (2009) at $Re = 100$ at different rotation rates. As a rotation is imposed on the sphere, the axisymmetric wake transits to a double threaded steady wake.

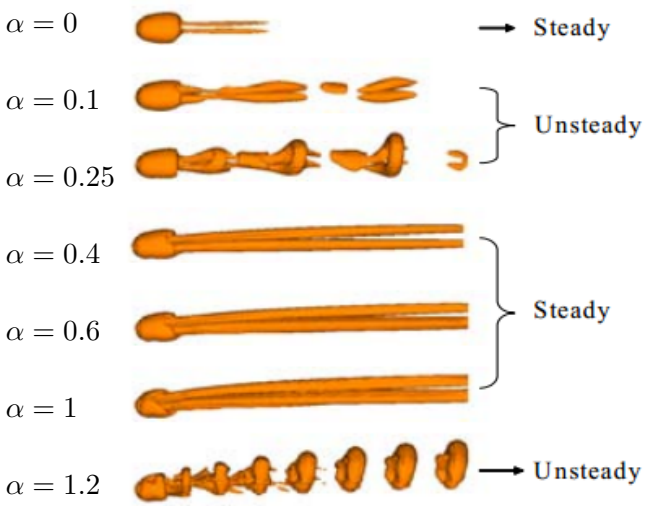

Figure 2.9.: Wake structure observed by Kim (2009) at $Re = 250$ for different rotation rates. The wake undergoes a series of transitions between steadiness and unsteadiness with increasing rotation rate.

as shown in figure 2.8. As the rotation rate increased, the double-threaded structure became stronger and elongated in the streamwise direction, indicating an increase in their rotational strength (Giacobello *et al.* 2009; Kim 2009).

Effect of sphere rotation on the planar-symmetric and steady flow

The studies of Giacobello *et al.* (2009) and Kim (2009) at $Re = 250$, representing the planar-symmetric and steady regime of the wake of a stationary sphere ($210 < Re < 270$), have observed a series of wake transitions between steadiness and unsteadiness, as shown in figure 2.9. They reported that the twin vortex trails observed for the zero-rotation case became stronger with the introduction of sphere rotation, as for the $Re = 100$ case. When the rotation rate reached approximately 0.1, the flow underwent a transition to an unsteady wake. As the rotation rate increased further, the onset of vortex shedding occurred in the form of hairpin loops similar to those observed for a stationary sphere above the Hopf bifurcation ($270 < Re < 420$). Vortex loops were shed from one side of the sphere and they were planar-symmetric with respect to a plane orthogonal to the axis of sphere rotation. However, the flow was unsteady only for a narrow range of rotation rates. At higher rotation rates, $0.4 < \alpha \leq 1$, vortex shedding was completely suppressed and flow returned back to the double-threaded steady wake.

As the rotation rate passed the unity, the flow again transited to an unsteady wake (Kim 2009; Dobson *et al.* 2014). However, the vortical structure was recognizably dissimilar from the regular vortex shedding of a sphere, as shown in the figure 2.9 at

$\alpha = 1.2$. In addition, the vortex shedding frequency was more than double the regular shedding frequency. By analysing the streamlines and particle traces, Kim claimed that this secondary vortex shedding observed at higher rotation rates was due to the roll-up of vorticity along the shear-layer separating from the advancing side of the sphere. This regime is known as *shear-layer instability regime*.

The computational study of Dobson *et al.* (2014) examined the nature of the wake at higher rotation rates, $1.25 < \alpha < 3$. At $Re = 250$ and $\alpha = 2$, they observed a double threaded wake near the sphere while the wake further downstream was unsteady with vortex loops. It was identified as a shear layer instability, although the vortex formation frequency was halved compared to that of the shear-layer instability regime. Moreover, oscillation magnitudes of the force coefficients were decaying, indicating a possibility of a steady wake at the asymptotic state. Therefore, their claim on the extension of shear-layer instability regime to larger rotation rates is debatable. As the rotation rate increased further, Dobson *et al.* (2014) reported that the flow entered into a different regime beyond the shear-layer instability regime. They named it the *separatrix regime* as they found an existence of a separatrix at $0.2D$ from the sphere, which isolates the free stream flow from the surface driven boundary layer due to the sphere rotation. In this regime, they observed a double threaded wake structure which oscillates slightly as it convects downstream.

Effect of sphere rotation on the unsteady flow

To investigate the effect of rotation on the unsteady vortex shedding regime, $270 < Re < 420$, both Giacobello *et al.* (2009) and Kim (2009) chose a Reynolds number of 300, as did Niazmand & Renksizbulut (2003). At $Re = 300$, as the rotation rate increased from zero, vortex shedding continued. All three studies reported that the shedding frequency increased linearly with increasing rotation rate. This unsteady vortex shedding was identical to that observed at $Re = 250$ and low rotation rates. As the rotation rate increased, a series of transitions between steadiness and unsteadiness was found to occur, similar to the $Re = 250$ case, following the same order. The flow became steady with a double-threaded wake around $\alpha = 0.4$. As the rotation rate increased beyond 0.8, the flow entered into the shear-layer instability regime, with one-sided loops. Kim (2009) found that this unsteadiness persisted until $\alpha = 1.2$. The wake in the shear-layer instability regime also maintained a planar symmetry. The symmetry breaking perturbation test of Giacobello *et al.* (2009) revealed that this plane of symmetry was physical. Dobson *et al.* (2014) reported that the flow switched into the separatrix regime after the shear-layer instability regime for $\alpha > 2$.

The investigation of Poon *et al.* (2014) on flow past a rotating sphere in the Reynolds number range, $500 < Re < 1000$, and for rotation rates, $0 < \alpha < 1.2$, revealed a

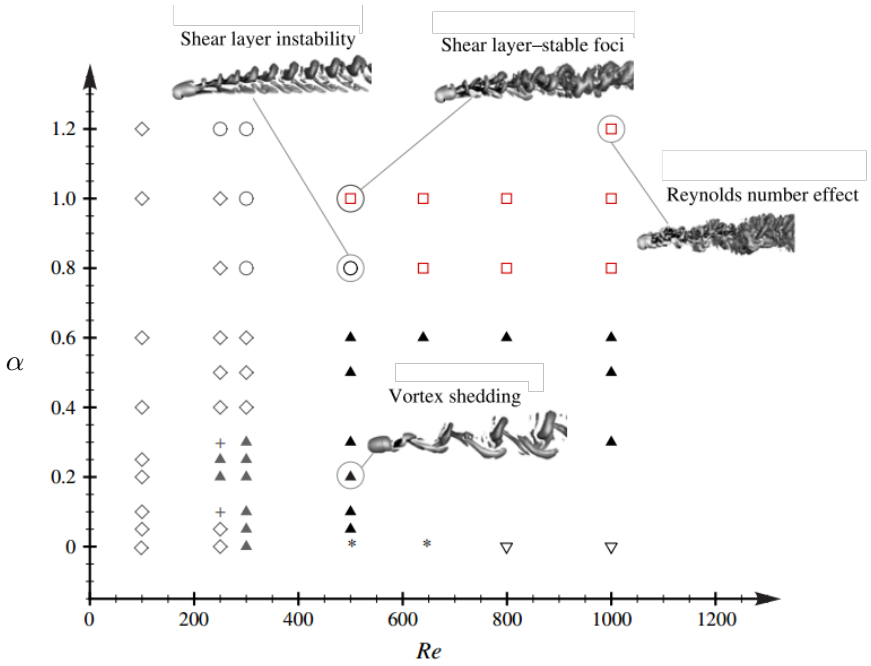

Figure 2.10.: Different flow regimes of a transversely rotating sphere generated by Poon *et al.* (2014) with the results of Giacobello *et al.* (2009) and Kim (2009); ⋄ steady flow; + oscillation vortex thread; ▲ vortex shedding; ◯ shear layer instability; ▽ turbulent flow with laminar boundary layer; □ shear layer stable foci.

new flow regime, namely the *shear layer stable foci regime*. This name is given as they observed a stable focus near the onset of shear layer instability that resulted in a highly unsteady flow. A summary of flow regimes mapped by Poon *et al.* (2014) together with the results of Giacobello *et al.* (2009) and Kim (2009) according to the Reynolds number and the rotation rate is shown in figure 2.10. As shown in the figure, the shear layer stable foci regime was observed at $Re = 500$ and $\alpha = 1$, and also for $640 < Re < 1000$ and $\alpha \geq 0.8$. They found that the stable focus became more pronounced as the rotation rate increased. Poon *et al.* also studied the nature of the flow at $Re = 500$ and 1000 for increasing rotation rate. At $Re = 500$ and zero rotation, vortices were shed from the sphere in random directions as discussed in § 2.1.3.2. The introduction of transverse rotation regulated the vortex shedding process, where the vortex loops rolled up to the advancing side of the sphere, being orthogonal to the streamwise direction. However, they found that the flow became chaotic as it entered the shear layer stable foci regime. A similar observation was found at $Re = 1000$ as well.

2.2.2. Flow past a streamwise rotating sphere

Compared with the flow past a sphere rotating in the transverse direction, even less research has been carried out on spheres rotating in other directions. Kim & Choi (2002)

investigated the characteristics of the flow past a sphere rotating in the streamwise direction at $Re = 100$, 250 and 300 for $0 \leq \alpha \leq 1$. Perhaps not surprisingly, the time-averaged lift force vanished with streamwise rotation at $Re = 250$ and 300, which was, of course, non-zero under zero rotation. The drag force increased with rotation rate, similar to the case with transverse rotation. They observed that the wake structures behind the sphere were modified significantly with rotation and the flow became *frozen* at some rotation rates. Poon *et al.* (2010) and Poon *et al.* (2013) studied the effect of the rotating axis angle at $Re = 100$, 250 and 300 for $0 \leq \alpha \leq 1$. They found that the wake structure strongly depended on the rotation rate and the axis angle at $Re = 250$ and 300, while the flow was always steady at $Re = 100$.

In this section, we have reviewed the findings on flow past a rotating sphere. As a transverse rotation is imposed on the sphere, a lift force is found to be applied on the retreating side of the sphere, deflecting the wake to the advancing side. Several studies were focused on deriving an expression for the Magnus force in terms of the Reynolds number and rotation rate. The lift force is found increase and then approach a constant value with increasing rotation rate, as well as with increasing Reynolds number. The drag force is also found to increase with increasing rotation rate beyond the Stokes regime. Wake structures behind the sphere have been greatly influenced by the sphere rotation. Three new wake regimes, namely, shear layer instability regime, separatrix regime and shear layer stable foci regime, have been discovered. Wake structure of the flow strongly depends on Reynolds number and the rotation rate, as shown in figure 2.10 by the parameter map generated by Poon *et al.* (2014) together with the results of Giacobello *et al.* (2009) and Kim (2009).

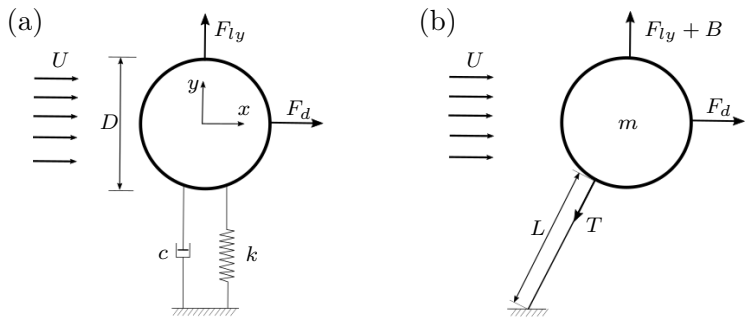

Figure 2.11.: Schematics of flow-induced vibration for (a) an elastically-mounted sphere and (b) a tethered sphere. Note that U is the free-stream velocity, m and D are the mass and the diameter of the sphere, respectively, c is the structural damping, k is the spring constant, F_{ly} is the lift force in y direction, F_d is the drag force, B is the buoyancy force, L is the tether length and T is the tension of the tether.

2.3. Flow-induced vibration of a sphere

As § 2.1 discussed, the fluctuating pressures generated by vortex shedding exerts fluctuating force components on the sphere. Both lift and drag forces fluctuate at the vortex-shedding frequency (Johnson & Patel 1999). If the sphere is flexible, elastically-mounted or supported with a tether as shown in figure 2.11, then these fluctuating forces can excite the body to vibrate. The vibration that occurs through the synchronization of the structural response with the wake unsteadiness is known as *Vortex-Induced Vibration*, or VIV. This occurs when the vortex shedding frequency, f_s, is close enough to the natural frequency of the system, f_n. In addition to VIV, structural vibration can also be excited due to the intrinsically unstable nature of the system, like movement-induced vibration or galloping.

The field of FIV has been continuously developing over the last few decades through experimental and computational studies. However, the majority of them were based on cylindrical structures, albeit that the FIV of spherical structures is equally important. As the sphere wake differs from the cylinder wake, the nature of FIV of spherical bodies diverges from that of cylindrical bodies. In this section, we will discuss the current state of art of FIV of a sphere, highlighting the major findings including similarities and dissimilarities of FIV of a circular cylinder.

The majority of early studies of tethered spheres have concerned the effect of surface waves on tethered buoyant spheres. For an example, the investigation of Harleman & Shapiro (1960) and Shi-Igai & Kono (1969) employed 'Morison's equation' and empirically obtained drag and inertial coefficients to predict the flow-induced vibration of the sphere as a forced vibration problem. The coupling of wave motion and the sphere dynamics yielded a complicated equation for which the underlying physics is difficult

to understand. Gottlieb (1997) investigated the response of a non-linear small-body ocean-mooring system excited by finite-amplitude waves and restrained by a massless elastic tether. He determined the stability of periodic motion numerically using Floquet analysis and found that the bifurcation structure includes ultra-subhamonic and quasi-periodic responses. The hydrodynamic dissipation mechanism was found to control stability thresholds, whereas the convective nonlinearity governed the evolution to chaotic system response.

2.3.1. Sphere response

Vortex-induced vibration of a tethered sphere in a uniform flow was first studied by Williamson & Govardhan (1997) and Govardhan & Williamson (1997) experimentally. They discovered that a tethered sphere vibrates vigorously at a saturation amplitude of close to two diameters peak-to-peak. The transverse oscillation frequency was half that of the streamwise oscillation frequency, despite the fact that the natural frequency of a tethered body is independent of the direction. This led the sphere to follow a path in the shape of a 'figure eight', with streamwise amplitude of 0.4 diameters. The streamwise amplitude was found to decrease with the increasing mass ratio, resulting in the typical sphere trajectory changing from a 'figure eight' to a 'crescent' shape (Govardhan & Williamson 1997, 2005; Jauvtis *et al.* 2001). Moreover, the streamwise amplitude was negligibly small for $m^* > 6$. Govardhan & Williamson (1997) observed an excellent collapse of data over a range of different mass ratios (the density ratio between the sphere and fluid, m^*) and tether length ratios (the ratio between tether length and the sphere diameter, l^*) when plotting the sphere response amplitude versus reduced velocity, $U^* = U/(f_n D)$, rather than versus Reynolds number. This is not quite surprising as the structural vibration is closely related to the system's natural frequency and past VIV studies have also used it.

Govardhan & Williamson (1997) observed a local peak in the amplitude response curve when the r.m.s. value of the amplitude was used instead of the maximum amplitude. This peak appeared around $U^* \sim 6$. It was further found that the sphere vibration frequency, f, matched the system's natural frequency, f_n, and the vortex shedding frequency of the static sphere, f_{vo}. Indeed, this is a vortex-induced vibration response caused by resonance and is known as *mode I* vibration. After mode I, as the reduced velocity was increased, Jauvtis *et al.* (2001) and Govardhan & Williamson (2005) observed another periodic VIV response known as *mode II* vibration. The amplitude of mode II was about twice that of mode I. The transition between these two modes was quite clear from the amplitude response curve which has a local peak at mode I, for very light tethered bodies ($m^* < 1$), as shown in figure 2.12 (a). However, for elastically-mounted higher-mass-ratio spheres and heavy tethered spheres, the transition between modes I

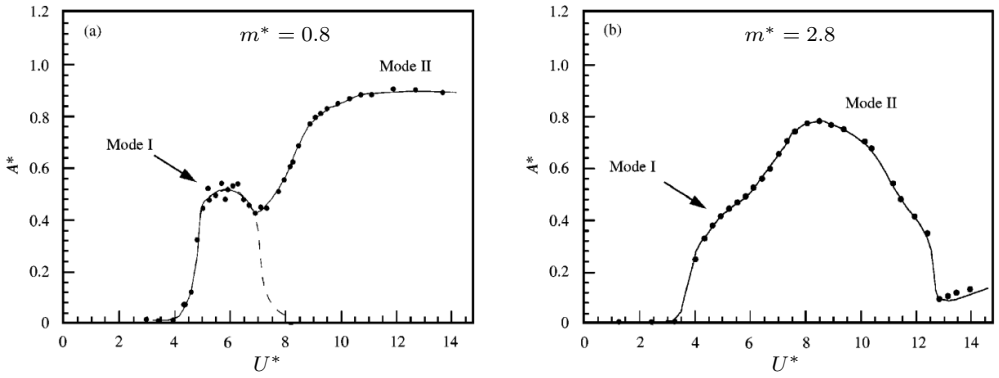

Figure 2.12.: Variation of sphere response amplitudes, A^*, over the modes I and II regimes for (a) a light sphere of $m^* = 0.8$ and (b) a heavy sphere of $m^* = 2.8$ by Jauvtis *et al.* (2001). The sphere response amplitude varies smoothly from mode I to mode II. At mode I, a local peak in the amplitude response curve appears only for light tethered spheres ($m^* < 1$).

and II was more continuous in the amplitude response curve as shown in figure 2.12 (b).

For the VIV of a cylinder, two or three distinct branches have been observed in the vibration amplitude response curve $A^*(U^*)$ depending on the combined mass-damping parameter, $m^*\zeta$, where ζ is the damping ratio. For high values of $m^*\zeta$, Feng (1968) observed two branches in the response curve, namely the *initial* and *lower* branches. He found that the transition between these two branches was hysteretic. Khalak & Williamson (1999) observed another branch in the response curve that lies in between these two branches with low $m^*\zeta$, namely the *upper* branch. The amplitude they observed on the upper branch was much higher than on the initial and lower branches. Moreover, they showed that the transition between the initial and upper branches was hysteretic and the transition between upper and lower involved intermittent switching. One major dissimilarity of VIV of a sphere and a cylinder is that the response amplitude transits smoothly from mode I to mode II for a sphere, while the amplitude jumps suddenly from one branch to another for a cylinder.

The experimental study of Govardhan & Williamson (2005) investigated modes I and II vibration states extensively using both elastically-mounted and tethered spheres. They identified that mode II was also a VIV response for which the sphere vibrates in synchrony with the vortex shedding. To study the difference between modes I and II, Govardhan & Williamson (2005) plotted the sphere response amplitude as a function of $(U^*/f^*)St \equiv f_s/f_{vo}$, where $f^* = f_s/f_n$ and $St = f_{vo}D/U$. For small-mass-ratio tethered spheres, the response amplitude was found clustered around $(U^*/f^*)St = 1$ and 1.6 in mode I and mode II, respectively, showing a clear transition. However, for higher-mass-ratio spheres, the response curve was smooth when plotted against

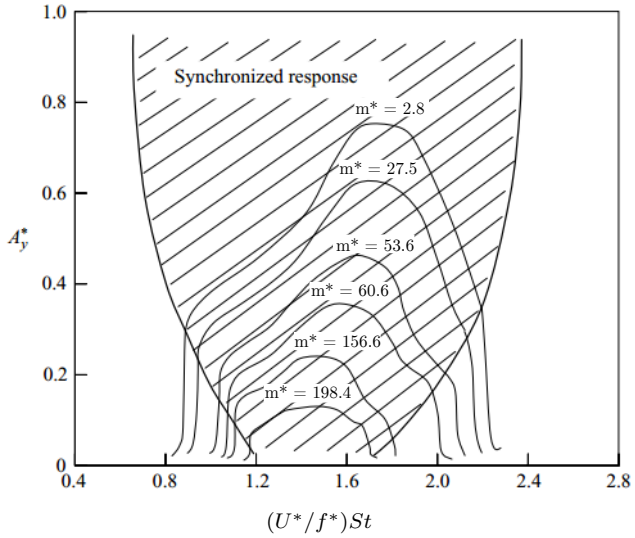

Figure 2.13.: Synchronized response regime from Govardhan & Williamson (2005) for increasing amplitude plots: $(m^* + Ca)\zeta = 0.333$, 0.290, 0.261, 0.190, 0.151, 0.029; $m^* = 198.4$, 156.6, 60.6, 53.6, 27.5, 2.8, where Ca is the added mass coefficient.

$(U^*/f^*)St$.

Govardhan & Williamson identified a maximum saturated response of around 0.9 diameters from their Griffin plot (the plot of peak amplitude response as a function of the mass–damping, $(m^* + C_a)\zeta$, where C_a is the added mass coefficient). Moreover, they showed that the sphere response was reasonably independent of the Reynolds number from 2000 to 12000. Both mass and structural damping have direct influences on VIV. Govardhan & Williamson reported that when the mass ratio and mass-damping parameter systematically decreased then the synchronization regime widened, while the response amplitude increased, as shown in figure 2.13. Nevertheless, they mentioned that the body response for a tethered sphere (xy motion) and a hydroelastic sphere (y-only) compares well for similar mass-damping parameters.

Jauvtis *et al.* (2001) experimentally found another periodic large amplitude vibration state beyond mode II regime, with heavy spheres of mass ratios, $m^* = 28$, 80 and 940. It was an unexpected finding which appeared in the reduced velocity range, $20 < U^* < 40$, and was named *mode III* (see figure 2.14). For a tethered sphere, mode III appeared after a desynchronization region, but for an elastically-mounted one degree of freedom sphere, transition from mode II to mode III was continuous (Govardhan & Williamson 2005). It was difficult to explain the cause of mode III using classic lock-in theories, since the principal vortex shedding frequency was found to be 3 to 8 times higher than the sphere vibration frequency. In addition, such a vibration state has not been found for a cylinder. Later, Govardhan & Williamson (2005) classified mode III as a Movement-Induced Excitation. However, the nature of mode III vibration state has

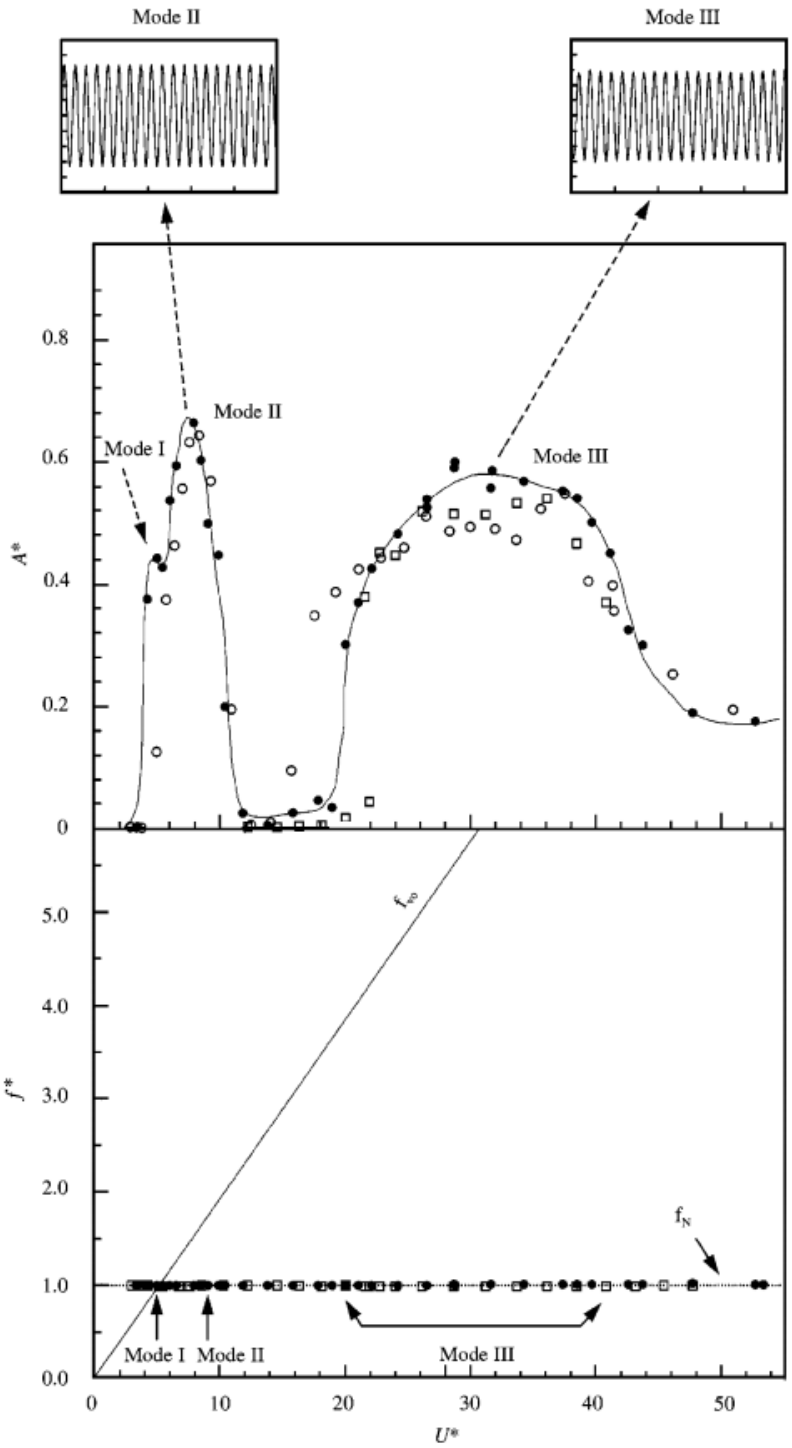

Figure 2.14.: Amplitude, A^*, and frequency, f^*, responses over a large range of U^*, showing the very broad regime of periodic mode III oscillations ($20 < U^* < 40$) from Jauvtis *et al.* (2001); • $m^* = 80$ ($12\ in \times 12\ in$ wind tunnel); ◯ $m^* = 80$ ($18\ in \times 18\ in$ wind tunnel); and □ $m^* = 940$ ($18\ in \times 18\ in$ wind tunnel).

not been examined in details and further investigations are required to enhance the understanding of this mode.

Subsequently, Jauvtis *et al.* (2001) found another vibration state after mode III for $U^* > 100$ with a sphere of $m^* = 80$, which is known as *mode IV*. In this mode, the sphere showed intermittent bursts of vibrations, in contrast to periodic vibrations for the first three modes. Despite being an aperiodic vibration, interestingly, the main frequency component was close to the natural frequency of the system. Moreover, it was observed that the response amplitude increased with increasing reduced velocity. Even less attention was given to mode IV and the mechanism responsible for this galloping type intermittent vibration state still remains unknown to the research community.

Hout *et al.* (2010) identified three bifurcation regions for the VIV of a heavy ($m^* = 7.87$) tethered sphere in the reduced velocity range, $2.8 \leq U^* \leq 31$. The sphere remained stationary in the first regime while it showed large amplitude periodic oscillations in the second regime, similar to modes I and II observed by Jauvtis *et al.* (2001) and Govardhan & Williamson (2005). In the third bifurcation regime, the sphere showed less periodic and smaller amplitude vibrations. For VIV of a cylinder, it has been discovered that a critical mass ratio, m^*_{crit}, exists, below which a large amplitude response will persist up to infinite reduced velocity (Govardhan & Williamson 2000, 2002). Using the effective added mass, Govardhan & Williamson (2005) estimated that m^*_{crit} is approximately 0.6 for a sphere. Eshbal *et al.* (2012) investigated the VIV of a light tethered sphere with $m^* = 0.392 < m^*_{crit}$, for the Reynolds number range, $430 \leq Re \leq 1925$. As U^* increased, they observed a continuously increasing trend in the r.m.s. amplitudes after the first bifurcation, as expected.

Coulombe-Pontbriand & Nahon (2009) investigated the dynamics of spherical aerostat on a single tether in the supercritical Reynolds number range ($Re > 3.7 \times 10^5$). Their experiments demonstrated that a tethered sphere in a turbulent flow will strongly oscillate. The amplitude of the transverse oscillation was found to increase with the increasing $U^* \in [5,\ 40]$ but was independent of the tether length. They also performed numerical simulations based on a prior model created by Lambert (2002), and found a good agreement between numerical and experimental results.

Mi & Gottlieb (2015) derived a Lagrangian-based model to estimate both structural and aeroelastic parameters, of lighter-than-air spheres, via asymptotic analysis of internal resonance conditions between the transverse wake frequency and its structural counterpart. Validation of the model was demonstrated by comparison of results with those of Govardhan & Williamson (1997) and Coulombe-Pontbriand & Nahon (2009). Mi & Gottlieb (2016) derived a nonlinear initial boundary value problem for a planar multi-tethered spherical aerostat system and observed superharmonic periodic, period-doubled, quasiperiodic and chaotic-like frequency responses. Mi & Gottlieb (2017) improved the model developed by Mi & Gottlieb (2015) to the multi-tether framework

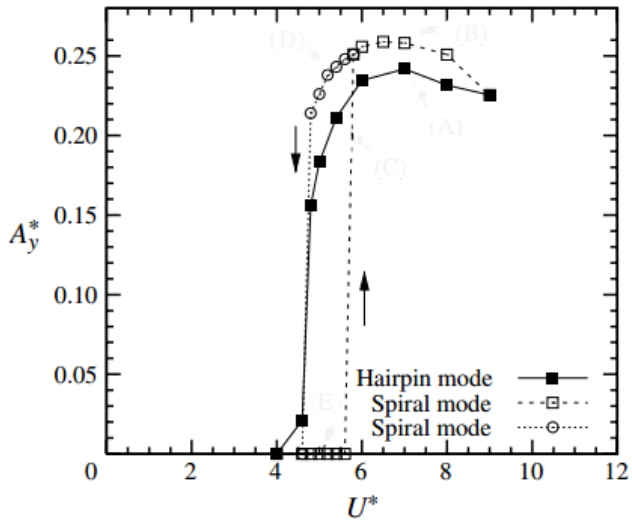

Figure 2.15.: The VIV response observed by Behara *et al.* (2011) at $Re = 300$ with a 3 DOF elastically-mounted sphere. Two distinct sphere vibration modes (hairpin and spiral) appear at the same reduced velocities; ■ hairpin mode; □ and ○ spiral mode obtained for increasing and decreasing U^*, respectively.

incorporating the rotational degrees-of-freedom to describe complete rigid-body dynamics.

Recently, a few computational studies have also reported VIV of a sphere at low Reynolds numbers (Pregnalato 2003; Provansal *et al.* 2003; Lee *et al.* 2008, 2013; Behara *et al.* 2011; Behara & Sotiropoulos 2016). The combined numerical and experiment studies of Lee *et al.* (2008, 2013) investigated the VIV of a neutrally buoyant ($m^* = 1$) tethered sphere, which may be considered as locally planar for small vibration amplitudes relative to the tether length. Neutral buoyancy was chosen to eliminate the effect of gravity. They found seven different broad and relatively distinct sphere oscillation and wake states over the Reynolds number range, $50 < Re < 12000$. Provansal *et al.* (2003) examined the trajectories of a heavy ($m^* = 2.433$) tethered sphere and found a periodic VIV response. Hysteresis was observed in the transition to synchronized vibration. They reported that the trajectory of the sphere could be elliptic, quasi-circular, or even straight (planar), depending on the initial conditions. However, this study was limited to the reduced velocity range, $0 < U^* < 5$. Pregnalato's (2003) investigation of VIV of a tethered sphere at Reynolds number 500 observed modes II-IV vibrations characterised by Jauvtis *et al.* (2001). Two different mass ratios ($m^* = 0.8$ and 0.082) were used in this study. For $m^* = 0.8$, mode II was observed in the reduced velocity range, $5 < U^* < 10$, while modes III and IV appeared for $U^* > 10$. However,, for $m^* = 0.082$, mode IV vibration did not appear in the reduced-velocity range studied ($0 < U^* < 20$) which led to a suspicion of the existence of a critical mass.

The computational study of Behara *et al.* (2011) investigated VIV of an elastically-mounted sphere with 3 DOF at Reynolds number $Re = 300$ and reduced mass, $m_r = 2$ ($m^* = 3.8197$). Over the reduced velocity range, $4 \leq U^* \leq 9$, they observed two distinct sphere vibration modes at the same reduced velocities, each corresponding to a distinct type of wake structure, namely *hairpin* and *spiral* modes, as shown in figure 2.15. For the hairpin mode, the sphere vibrated in a linear path in the transverse plane, while for the spiral mode the sphere moved on a circular orbit. Furthermore, for the spiral mode, they observed hysteresis in the response amplitude at the beginning of the synchronization regime. More recently, Behara & Sotiropoulos (2016) extended this study by expanding the U^* range and increasing the Reynolds number up to 1000 at $U^* = 9$. They identified that the hairpin mode is unstable and merges with the spiral mode at $U^* = 9$. Moreover, the sphere response was found to be strongly dependent on the Reynolds number.

2.3.2. Force measurements

Williamson & Govardhan (1997) and Govardhan & Williamson (1997) reported that the sphere oscillation increased the drag force and the tether angle by the order of 100% over that predicted using the drag measurement of a stationary sphere by Wieselsberger (1922). Consistently, Coulombe-Pontbriand & Nahon also found that there was a substantial increment in the drag coefficient in their study of a spherical aerostat due to the balloon's large oscillations, surface roughness, and wind turbulence. The numerical study of Behara *et al.* (2011) also reported an increment in the drag force as the sphere began to vibrate. Similar to their amplitude response curve, two branches were found in the plot of drag coefficient which corresponds to hairpin and spiral modes. In each case, the drag coefficient increased as soon as the sphere began to vibrate and that increment decreased with increasing U^*. Moreover, the spiral mode showed hysteresis at the beginning of the transition to VIV.

To examine the difference between modes I and II, Govardhan & Williamson (2005) studied the variation of fluid force as the sphere transitioned from mode I to mode II. The total fluid force, F_t, acting on the body can be conveniently be split into two components, a 'potential force' component (F_p) related to the potential added mass and a 'vortex force' component (F_v) related to the dynamic vorticity (Lighthill 1986). For a cylinder, Govardhan & Williamson (2000) observed a shift in the total phase, ϕ_t (the phase between the sphere displacement and the total force), or the vortex phase, ϕ_v (the phase between the sphere displacement and the vortex force), as the vibration state transitions from one branch to another. Analogously, Govardhan & Williamson (2005) showed that vortex phase was approximately 90° higher for mode II compared to mode I, while the total phase remains almost constant over both modes I and II regimes, as shown in figure 2.16. Hout *et al.* (2010) also found that phase at which vortices were

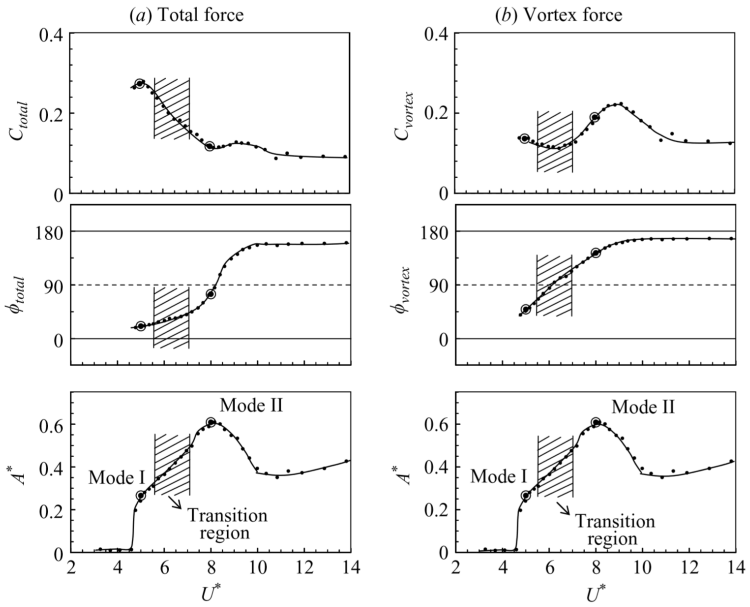

Figure 2.16.: Force and phase angle variation with U^*: (a) total force; (b)vortex force from Govardhan & Williamson (2005). The ⊙ symbols on the plots indicate locations in the heart of mode I and mode II regimes, outside the transition region between the two modes ($m^* = 31$, $(m^* + Ca)\zeta = 0.15$).

shed increased with increasing U^* in the second bifurcation region of periodic vibration.

2.3.3. Wake structures

Govardhan & Williamson (2005) observed a chain of two-sided hairpin vortex loops in the wake for both modes I and II with the aid of digital particle image velocimetry (DPIV), as shown in figure 2.17. They observed a development of a vortex ring at the head of the vortex loop, due to the pinching off and vortex reconnection of the two sides of the loop. Moreover, they claimed that it presumably resembles the $2P$ mode of counter-rotating vortex pair formation in the case of the vibrating cylinder observed in the upper and lower branches (Williamson & Roshko 1988). Govardhan & Williamson reported that the sphere vibration locks the vortex formation in a particular preferred orientation, maintaining a planar symmetry with the (horizontal) plane containing the principal body displacement, unlike the azimuthal wandering of the wake structures behind static spheres (observed for $Re > 420$, as discussed in § 2.1.3).

As discussed in § 2.3.2, Govardhan & Williamson (2005) found that the vortex phase increased as the sphere transit from mode I to mode II. Consistently, they observed that the timing of vortex shedding relative to the sphere motion changed once it passed from mode I to mode II. Similarly, Hout *et al.* (2010) observed that the place where the vortex pinch-off occurs depends on the reduced velocity. They reported that increasing

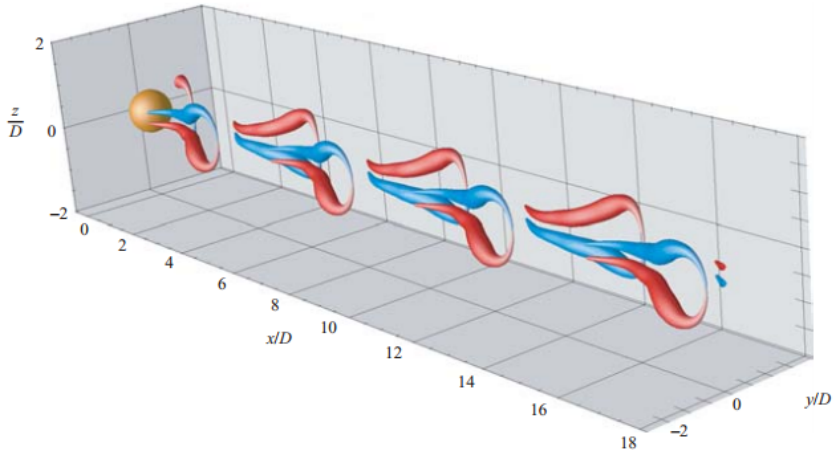

Figure 2.17.: Three-dimensional patio-temporal reconstruction of the sphere wake from the measured time sequence of streamwise vorticity at mode I by Govardhan & Williamson (2005).

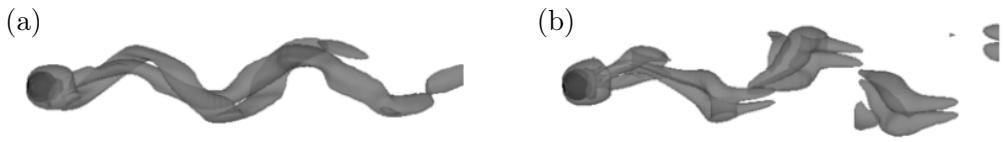

Figure 2.18.: Instantaneous wake structures observed by Behara *et al.* (2011) (a) spiral mode and (b) hairpin mode at $U^* = 7$, $Re = 300$, $m_r = 2$.

or decreasing U^* caused earlier or later pinch-off relative to the location it occurred at the peak amplitude of region II, respectively.

Hout *et al.* (2010) also discovered shedding of hairpin vortices on alternating sides of the sphere having horizontal plane of symmetry. They characterized the near wake spatial-temporal vortex pattern by a saw-tooth of counter-rotating vortices. As discussed earlier, when the sphere is mounted with elastic supports in all three spatial directions, Behara *et al.* (2011); Behara & Sotiropoulos (2016) observed that the sphere can also move in a circular trajectory in addition to the linear trajectory. In this case, they observed a counter-rotating streamwise spiralling wake behind the sphere which led to calling it the spiral mode, see figure 2.18 (a). In the other case, where the sphere moved in a linear path, they observed regularized two-sided hairpin loops, as shown in figure 2.18 (b). Behara & Sotiropoulos (2016) reported that the spiral mode they observed at $U^* = 9$ and $Re = 300$ and 400, transitioned to the hairpin mode at $Re = 500$ and continued up to $Re = 1000$.

The experimental study of Brücker (1999) examined freely rising air bubbles in water and found three different types of bubble motion; spiralling, zigzagging, and rocking, during their rise. Their results showed that zigzagging motion was coupled to a generation of two-sided hairpin loops, while the spiraling bubble created a twisted pair of

streamwise vortices that were wound like a helix, resembling the spiral wake observed by Behara *et al.* (2011); Behara & Sotiropoulos (2016). Horowitz & Williamson (2010) experimentally studied the dynamics and vortex formation modes of spheres rising or falling freely through a fluid. They found that falling spheres ($m^* > 1$) always moved without vibration. A rising sphere was found to vibrate only if its mass ratio was below a critical value (0.4 for the range, $260 < Re < 1550$ and 0.6 for $Re > 1550$). They did not observe a helical or spiral trajectory. They reported that wakes comprised single-sided and double-sided periodic sequences of vortex rings, named as R and $2R$ modes. In addition, in the zigzag regime, they discovered a new $4R$ mode, in which four vortex rings are created per cycle of oscillation.

This section was devoted to the discussion of the literature on the flow-induced vibration of a sphere. In summary, four different sphere vibration modes, modes I-IV, were identified based on the sphere response, forces applied on it and wake characteristics. Mode I, is the resonance state. A sphere shows mode II type vibration after mode I with comparatively larger amplitudes. The transition between mode I and II is continuous, and both modes I and II are highly periodic vortex-induced vibrations. Mode III is also periodic and has observed in the reduced velocity range, $20 < U^* < 40$. In contrast to the first three modes, mode IV is an intermittent burst of vibration and has been observed for $U^* > 100$. Two-sided hairpin type wakes were observed for both modes I and II. For mode III, long vortex loop structures were observed in the wake. The last two vibration modes that occur at low frequencies have not been well examined and more research is needed.

2.4. Effect of the body rotation on the VIV

VIV of a rotating cylinder

Even though the body rotation directly influences the forces exerted on it and the wake structure, as discussed in § 2.2, the effects of solid rotation on VIV has not been examined up until very recently. The computational studies of Bourguet & Jacono (2014) and Zhao *et al.* (2014) were the first investigations on flow-induced vibration of a rotating cylinder, conduced at $Re = 100$ and $Re = 150$, respectively. Both of these studies observed that the peak oscillation amplitude increased and the synchronization regime, defined as the reduced velocity range where large vibrations close to the natural frequency are observed, widened as the rotation rate increased. Bourguet & Jacono (2014) found that the synchronization regime narrowed beyond $\alpha = 3.5$ and vibration was completely suppressed for $\alpha \geq 4$. They also discovered two new vortex shedding patterns; $T + S$ (a triplet with a single vortex per cycle) and U pattern (transverse undulation of the spanwise vorticity layers without vortex detachment). Zhao *et al.* (2014) reported that when a two degree of freedom is given to the cylinder, its responses at $\alpha = 0.5$ and 1 were significantly different from that at $\alpha = 0$.

The experimental study of Seyed-Aghazadeh & Modarres-Sadeghi (2015) on VIV of a rotating cylinder ($350 \leq Re \leq 1000$) also revealed that the synchronization regime became narrower at high rotation rates, and oscillations suppressed beyond $\alpha = 2.4$. However, they reported that the rotation of the cylinder does not show a significant influence on the response amplitude, in contrast to the results of Bourguet & Jacono (2014) and Zhao *et al.* (2014). More recently, Wong *et al.* (2017) conducted experiments to investigate the characteristics of FIV of a transversely rotating circular cylinder over the Reynolds number range, $1100 < Re < 6300$. They also observed a significant structural vibration up to $\alpha = 3.5$. They reported that the oscillation amplitude increased with the rotation rate for $\alpha \leq 2$ prior to a sharp decreasing trend for higher α values. Interestingly, $\alpha \approx 2$ corresponds to the rotation rate beyond which vortex shedding ceases for a static cylinder (Mittal & Kumar 2003; Kang *et al.* 1999). However, Bourguet & Jacono (2014) reported an increasing trend of amplitudes even beyond $\alpha = 2$. Zhao *et al.* (2018) experimentally studied the in-line FIV of a rotating circular cylinder and found VIV synchronisation and rotation-induced galloping responses. The amplitude in the VIV synchronisation region was found to increase up to$\sim 0.5D$, while it could grow up to $1.56D$ in the rotation-induced galloping region.

VIV of a rotating sphere

The experimental study of Sareen *et al.* (2018*a*), published recently, is the only in-

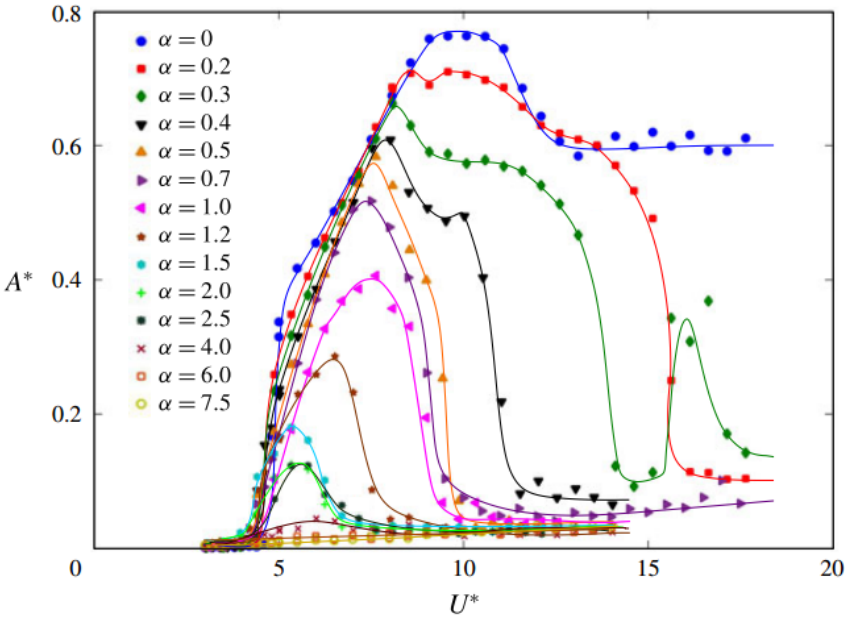

Figure 2.19.: The sphere response amplitude, A^*, as a function of reduced velocity, U^*, for different rotation rates, α, from Sareen *et al.* (2018*a*). The sphere response amplitude decreases and the synchronisation regime narrows with the increasing rotation rate.

vestigation on the effect of sphere rotation on VIV, to the author's knowledge. They examined the cross-flow VIV of a transversely rotating sphere over the reduced velocity range, $0 < U^* < 18$, corresponding to a Reynolds number range of $5\,000 < Re < 30\,000$, and for rotation rates of $0 < \alpha < 7.5$. The vibration amplitude exhibited a monotonically and gradually decreasing trend as the imposed rotation rate was increased from 0 to 6, beyond which the body vibration was insignificant, as shown in figure 2.19. Moreover, Sareen *et al.* found that the synchronisation regime narrowed as the rotation rate increased, leading the peak saturation amplitude to occur at a progressively lower reduced velocity. Indeed, these are in contrast with the observations for the VIV of a rotating cylinder, for which the oscillation amplitude increased and syncronisation regime broadened initially with increasing α before the suppression of VIV by narrowing the synchronization regime (Bourguet & Jacono 2014; Zhao *et al.* 2014; Wong *et al.* 2017). Sareen *et al.* (2018*a*) reported that the imposed rotation not only reduced vibration amplitudes, but also made the body vibration less periodic.

The range of reduced velocity chosen for Sareen *et al.* study covers both modes I and II regimes for a zero-rotation sphere. They reported that both modes I and II type vibration persisted even under the influence of imposed sphere rotation. The variation of the vortex phase was similar to that of the zero-rotation case, where ϕ_v increased gradually from low values in mode I to almost 180° as the system underwent a continuous transition to mode II.

Sareen *et al.* (2018*a*) visualized the flow behind the sphere using both Hydrogen-

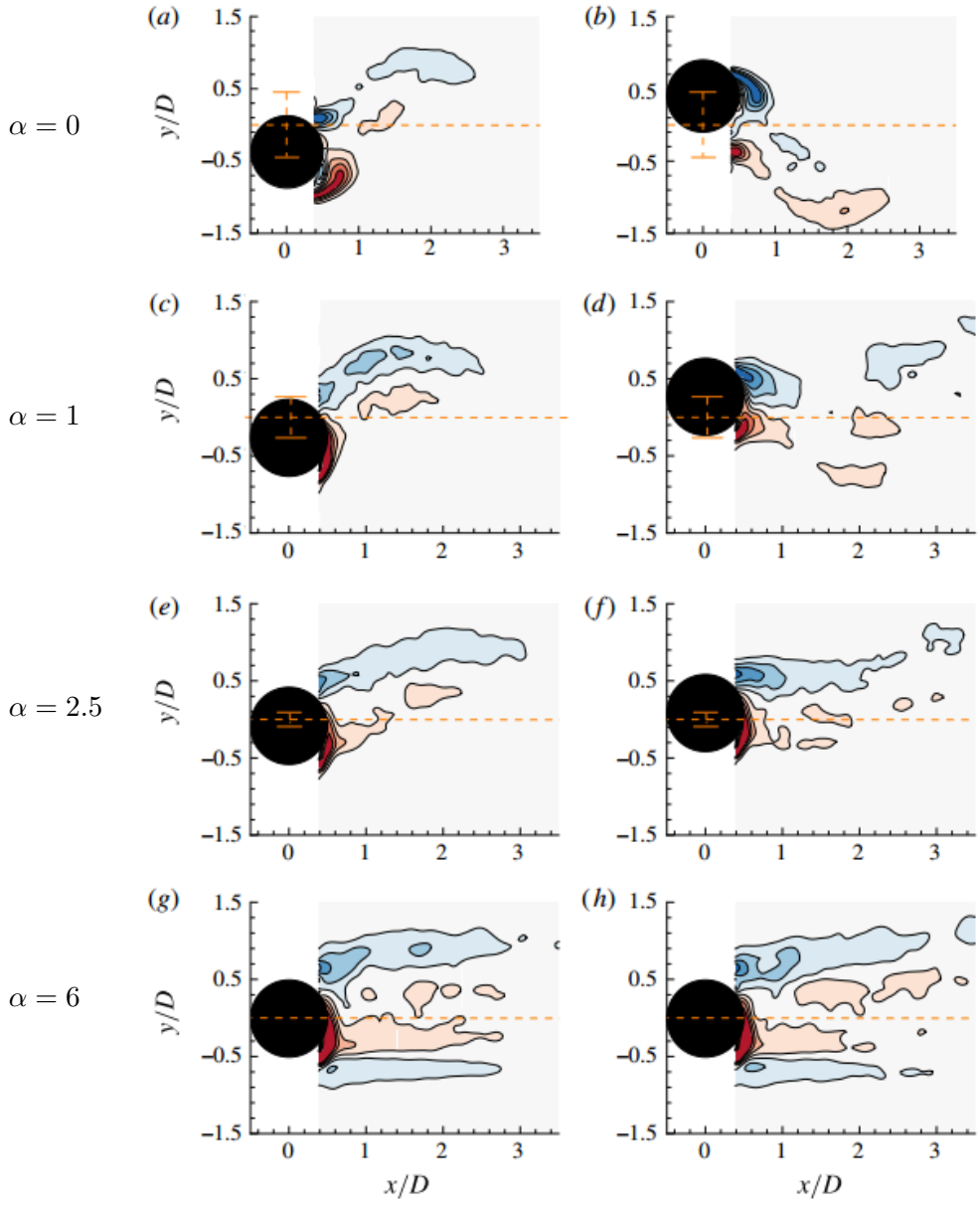

Figure 2.20.: Equatorial near-wake vorticity maps obtained from phase–averaged PIV at $U^* = 6$ by Sareen *et al.* (2018*a*). Panels (a,c,e,g) show images corresponding to when the sphere is at its lowest position, and (b,d,f,h) when it is at its highest position.

bubble visualisation and particle image velocimetry (PIV) performed in the equatorial plane (see figure 2.20). They observed that the mean wake deflected toward the advancing side of the sphere with increasing rotation rate due to the Magnus effect. Consequently, large-scale one-sided vortex shedding occurred at higher rotation rates. They claimed that the lack of an oscillating force acting on the sphere led to near–suppression of the VIV.

2.5. Chapter summary and research questions

The preceding review of the literature indicates the limited knowledge built on the flow-induced vibration of a sphere. In contrast to the FIV of a cylinder, only a few investigations was devoted to exploring the fundamentals of FIV of a sphere. Moreover, the majority of these studies were experimental studies, conducted at higher Reynolds numbers. A couple of computational studies investigated the characteristics of FIV of a sphere. Nevertheless, there exist limitations to those studies, and some questions remain unanswered. A summary of the literature is listed below by highlighting the gaps in knowledge and stating the proposed research questions to answer them.

1. The experimental studies of Govardhan & Williamson (1997); Williamson & Govardhan (1997); Jauvtis *et al.* (2001); Govardhan & Williamson (2005) on the flow-induced vibration of a sphere identified four different vibration modes (modes I-IV), based on the characteristics of the flow and sphere response. The first two modes (observed over $U^* \sim 5 - 10$) are self-limited vortex-induced vibration responses. Mode III is also a self-limited vibration state but not a VIV, as the vortex shedding frequency is $3 \sim 8$ times higher than the sphere vibration frequency. In contrast to the first three modes, mode IV (observed for $U^* > 100$) is not a self-limited vibration state. Modes I and II have been developed more attention in the literature. Govardhan & Williamson (2005) revealed that the effect of the Reynolds number is negligible over the range, $2000 < Re < 12000$, while the impact of the mass ratio is significant over the range $0.1 < m^* < 1000$ in modes I and II regimes. The majority of studies were based on tethered spheres, albeit there are some dissimilarities between VIV of a tethered sphere and an elastically-mounted sphere. Behara *et al.* (2011); Behara & Sotiropoulos (2016) have conducted the only computational studies on VIV of an elastically-mounted sphere (with 3 DOF) in the laminar regime. There were substantial differences between their amplitude response curve to that of the experiments at higher Reynolds numbers. Moreover, only the modes I and II regimes were considered in these studies, and the effect of Reynolds number on VIV was not well examined. Therefore, the first question for research is: *How does the flow-induced vibration of an elastically-mounted sphere over the reduced velocity range* $3 \leq U^* \leq 100$ *at low Reynolds numbers differ from the experimental studies at higher Reynolds numbers?*

2. Despite the fact that sphere rotation greatly influences the forces applied on it and the wake, the consequences of sphere rotation on the VIV has not been examined until the very recent experimental study of Sareen *et al.* (2018*a*). They explored the effect of sphere rotation over the modes I and II regimes, corresponding to the Reynolds numbers $5000 < Re < 3000$, for $0 < \alpha < 7.5$. They observed

a decrement in the amplitude and narrowing of the synchronization regime as the rotation rate increased. Moreover, oscillations were insignificant for $\alpha > 6$. However, the nature of the problem at low Reynolds numbers is not known yet. In the laminar regime, for the non-VIV sphere, it was found that the flow undergoes a couple of transitions between the steadiness and the unsteadiness as the rotation rate increased. As a result, the behaviour of the sphere at low Reynolds numbers may be different from that observed in experiments, as was found for the VIV of a cylinder. Therefore, the second question for research is: *What are the effects of imposed transverse rotation on the vortex-induced vibration of an elastically-mounted sphere over the rotation rates,* $0 < \alpha < 2.5$ *at low Reynolds numbers?*

3. Mode III, which was named as a movement-induced vibration by Govardhan & Williamson (2005), and an intermittent burst of mode IV vibration states observed at low frequencies are difficult to explain by the classic lock-in theories. Moreover, their nature is not well understood. Pregnalato (2003) undertook the only computational study devoted to the VIV of a tethered sphere in the laminar regime. However, due to the computational constraints, insufficient investigation has been reported on the low-frequency regimes. Therefore, to enhance the understanding of modes of sphere vibration, the third question for research is: *What is the nature of the flow-induced vibration of a tethered sphere over the Reynolds number range,* $500 < Re < 2000$*?*

Numerical investigations are required to answer these research questions and broaden the understanding of flow-induced vibration of a sphere. Initially, the flow-induced vibration of an elastically mounted sphere will be investigated. Then, the effect of the imposed transverse rotation of the sphere on VIV will be examined. Finally, the flow-induced vibration of a tethered sphere will be studied to enhance the knowledge on different modes of sphere vibration. Prior to the discussion of results, the numerical approach will be presented in chapter 3.

> If you want your children to be intelligent, read them fairy tales. If you want them to be more intelligent, read them more fairy tales.
>
> Albert Einstein

3. Numerical Methodology

This chapter presents a basic overview of the numerical methods used for the simulations conducted for this thesis. The overview given here is not exhaustive, and it should be noted that the main focus of the thesis was not the development of computational methods, but the fluid mechanics of flow-induced vibration.

The widely used open-source computational fluid dynamics (CFD) package OpenFOAM (https://openfoam.org) was utilised for the numerical simulations. The chapter begins with a brief overview of OpenFOAM in § 3.1 including topics on setting up a case in OpenFOAM, discretization of the fluid dynamics equations and the algorithm used by the fluid solver for non-FIV simulations. With this established, the numerical approach used for FIV of an elastically-mounted body is described in § 3.2. Here, the newly developed fluid-structure solver in the case of an elastically-mounted body is discussed in detail. Following this, the numerical approach used for a tethered sphere is presented in § 3.3, detailing the FSI solver developed to treat a tethered body, and the methods of calculating the natural frequency of the system and the reduced velocity. § 3.4 provides a brief introduction to the dynamic mode decomposition technique, which is later used to analyse the wake undergoing different vibration modes. Grid and domain details are presented in § 3.5, which describes the grid generation process and boundary conditions. Finally, the results from a series of validation studies are given in § 3.6. Results confirming the accuracy of the solutions achieved in both space and time are presented. These tests provide confidence in the predictions of this thesis.

3.1. Simulations in OpenFOAM

OpenFOAM is an open-source CFD package released by OpenCFD Ltd and distributed freely via https://www.openfoam.com for Linux operating systems. OpenFOAM has the facility of performing simulations on multiple processors in parallel. In the present study, simulations were performed in parallel on the Magnus supercomputer at the Pawsey supercomputing centre though computer-time allocation merit grants $n67$ and $d71$.

OpenFOAM is a framework for developing application executables that use packaged functionality contained within a collection of approximately 100 C+ libraries (The-OpenFOAM-Foundation 2018). OpenFOAM comes with approximately 250 pre-built applications that fall into *solver* and *utility* categories. *Solvers* are designed to solve a

specific problem in continuum mechanics while *utilities* are designed to perform tasks that involve data manipulation. OpenFOAM solvers are capable of handling a wide range of problems in fluid dynamics. Users can develop new solvers, utilities and libraries with some pre-requisite knowledge of the underlying method, physics and programming techniques involved.

OpenFOAM comes with both pre- and post-processing environments. The interface to the pre- and post-processing are themselves OpenFOAM utilities, thereby ensuring consistent data handling across all environments. OpenFOAM has limited graphical interface. Therefore the utility *paraFoam* provides possibilities of visualizing the grid and the obtained results by connecting to the data analysis and visualization application ParaVIEW.

3.1.1. File structure of an OpenFOAM case

Typically, an OpenFOAM case contains mainly three types of directories, namely the *constant* directory, the *system* directory and *time* directories, as shown in figure 3.1. Only a brief description of the file system is given below, and readers are referred to the OpenFOAM user guide (The-OpenFOAM-Foundation 2018) for more details.

The constant directory

The constant directory contains the full description of the case grid in a subdirectory called *polyMesh*. The constant directory also contains the files specifying physical and turbulent properties for the application concerned, *e.g.* the file *transportProperties* which contains the transport properties. Since only the laminar condition is considered for the present simulations, the value of the kinematic viscosity of the fluid was the only content of the *transportProperties* file.

The system directory

The system directory contains the files associated with the control parameters and solution procedures. It should contain at least the *controlDict*, *fvSchemes* and *fvSolution* files. The *controlDict* file specifies the control parameters including the start/end time, the time step and parameters for data output. The *fvSchemes* determines the discretization schemes used in the solution, while the *fvSolution* determines the equation solver algorithms, tolerances and other algorithm controls. The discretization schemes and the equation solver algorithms used for the present simulations are discussed in detail in § 3.1.4 and § 3.1.5, respective.

The files: *decomposeParDict*, *forceCoeffs* and *mapFields* were also used for the present simulations. The *decomposeParDict* file determines the parameters for decomposing the

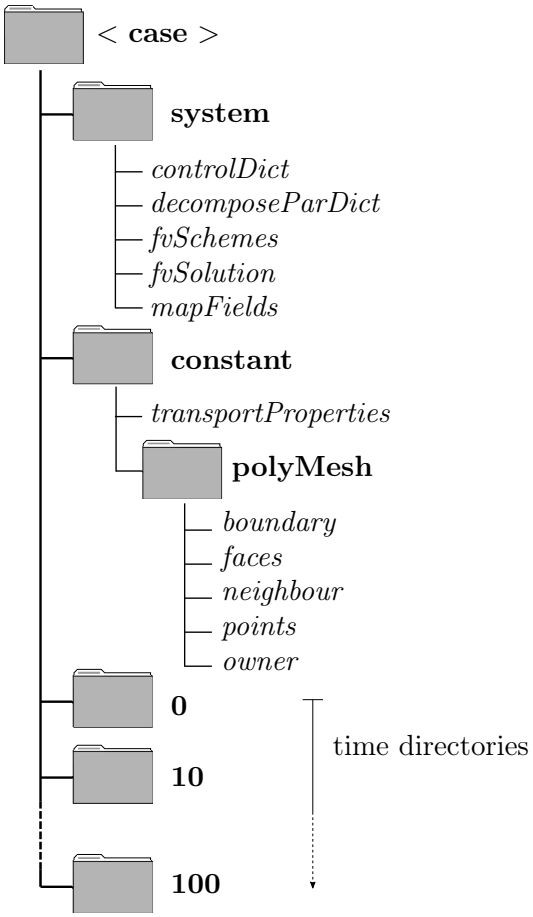

Figure 3.1.: The file system of an OpenFOAM case. Reproduced from (The-OpenFOAM-Foundation 2018, fig 4.1, section 4.1) and modified.

grid into separate domains to run the case in parallel on multiple processors. The *forceCoeffs* file determines the parameters required to calculate force measurements and force coefficients. Once *forceCoeffs* is included in the *controlDict* file, as shown in appendix A, OpenFOAM writes the forces and force coefficients to a file in a directory called *postProcessing*. The *mapFields* file was used when it required to map the field data from a coarse grid to a finer grid.

The time directories

A case directory contains individual files for each time instance. The name of each time directory is based on the simulated time at which the data is written, *e.g.* for the initial time $t = 0$, the time directory is named as '0'. A time directory contains individual files of data for particular fields, e.g. velocity and pressure fields. The field

data can either be initial values and boundary conditions prescribed by the user, or results written to a file by OpenFOAM. It is always required to initialize the fields even when the solution does not strictly require it, as in steady-state problems.

3.1.2. Governing equations

The numerical approach for any computational study strictly depends on the assumptions made. There are three main assumptions made regarding the fluid in the systems considered in this thesis.

First, the fluid is assumed to be a continuum. This assumption makes it possible to consider a fluid as a collection of infinitesimal control volumes, which are small in comparison to the characteristic length scale of the system, but large in comparison to the molecular length scale. In those control-volume elements, macroscopic (observed/measurable) properties such as density, pressure, temperature, and bulk velocity are taken to be well-defined. This assumption only becomes invalid for supersonic flows, or molecular flows on the nano-scale level.

Second, the fluid is assumed to be incompressible: *i.e.* the fluid cannot be compressed with the application of an external pressure. With this assumption, the material derivative of the density vanishes, as does the divergence of the fluid velocity. It is typically valid for flows where the Mach number, Ma, which is the ratio between the velocity of the flow and the velocity of sound in the fluid, is smaller than ~ 0.3, since the effect is proportional to Ma^2. This condition is applicable in the many current engineering applications, especially to those in water. Also, the fluid is assumed to be isothermal, so that (temperature-induced) density gradients play no part in the flow dynamics.

Third, the fluid is assumed to be Newtonian. This means that the viscous stresses arising from its flow, at every point, are linearly proportional to the local strain rate. This proportionality constant is the dynamic viscosity, μ, of the fluid. Sir Isaac Newton showed that many familiar fluids such as water and air have this property.

The equations that govern the bahaviour of such a Newtonian fluid with the incompressibility constraint are the Navier-Stokes equations,

$$\frac{\partial \mathbf{u}}{\partial t} = -(\mathbf{u}\cdot\boldsymbol{\nabla})\mathbf{u} - \frac{1}{\rho}\boldsymbol{\nabla}P + \frac{\mu}{\rho}\boldsymbol{\nabla}^2\mathbf{u}, \tag{3.1}$$

and the continuity equation,

$$\nabla\cdot\mathbf{u} = 0. \tag{3.2}$$

Here, $\mathbf{u} = \mathbf{u}(x,y,z,t)$ is the velocity vector of the fluid at a given location and at a given time, P is the pressure, ρ is the fluid density, assumed constant. Given constant density, it is usual to eliminate explicit reference to the density by introducing the kinematic pressure $p = P/\rho$, and the kinematic viscosity $\nu = \mu/\rho$. Equation 3.1 gives the rate of change of the momentum (per unit mass) of the fluid flow. The terms on the right of

this equation account for the effects of convection, pressure, and diffusion on momentum transport.

OpenFoam facilitates simulations in the dimensional form. For the present direct numerical simulations, the only fluid property that is required to be specified is the kinematic viscosity, ν, which can be obtained by $\nu = UD/Re$, where U is the freestream velocity.

3.1.3. The fluid solver for non-VIV simulations

OpenFOAM has a wide range of standard solvers designed for applications in different categories of continuum mechanics. Flow in the laminar regime has been considered for the thesis. The pre-built *icoFoam* solver is considered to be appropriate for the present simulations, as it is a transient solver for the incompressible, laminar flow of Newtonian fluids. The *icoFoam* solver was implemented according to the PISO (Pressure Implicit with Splitting of Operator) algorithm introduced by Issa (1986). This algorithm approximates the spatially and temporally discretized fluid equations with an order of accuracy $O(\delta t^2)$, with δt the time step. The widely used PISO algorithm is generally stable and relatively easy to implement.

The PISO algorithm integrates the Navier-Stokes equations forward in time using a predictor step followed by several corrector steps. In the predictor step, the discretized momentum equation (we will refer to this as *the velocity equation*) is solved implicitly for a new velocity field with the previous pressure and velocity fields. An equation is derived combining the discretized continuity equation and momentum equations (we will refer to this as *the pressure equation*). In the corrector step, a velocity field and a pressure field are found that are able to satisfy both the continuity and the momentum equations. This is done by first solving the above-mentioned pressure equation for the pressure (with the velocity found in the predictor step or the previous corrector step), and then solving the momentum equation for the velocity. At the end of the time step, the velocity and the pressure fields found from the last corrector step are taken as the new velocity and pressure fields. Appendix B describes the PISO algorithm used in the *icoFoam solver* in more detail, while appendix C shows the actual *icoFoam.C* file used to compile the *icoFoam* solver. Issa (1986) shows that this algorithm needs, at least, two corrector steps to achieve the desired accuracy. He showed that with two corrector steps, the velocity and pressure can be approximated to orders of accuracy $O(\delta t^4)$ and $O(\delta t^3)$, respectively. Adding another corrector step would increase the accuracy of the approximations, but it will unnecessarily increase the computational time, because the order of accuracy of the algorithm is only $O(\delta t^2)$. Therefore, we used only two corrector steps in all of our simulations.

3.1.4. Numerical discretization

OpenFOAM is developed based on finite-volume method (FVM), similar to many computational fluid dynamics packages, as this method is easy to formulate. The finite-volume method is a numerical technique that transforms the partial differential equations into a system of discrete algebraic equations, analogous to the finite-difference (FD) and finite-element (FE) methods. The finite-volume method relies on a control volume approach. In general, the finite-volume approach is based on conservation of some quantity, *i.e.*, what goes into the control volume through the sides accumulates in the control volume. In this method, the governing equations are integrated over all finite volumes of the computational domain.

The finite-volume method requires a spatial domain to discretize, breaking it into a number of cells or control volumes. The cells are contiguous, *i.e.* they do not overlap and they completely fill the domain. Dependent variables are principally stored at cell centroids, although they may be stored in cell faces or vertices. In OpenFOAM, there is no limitation on the number of faces that bound a cell, nor any restriction on the alignment of faces. This kind of grid setup is often referred to as an *arbitrarily unstructured* grid. Thus, it provides considerable freedom in grid generation and manipulation, especially when the geometry is complex or changes over time.

OpenFOAM offers the freedom of choosing appropriate discretization schemes from a wide selection, for each and every term in the governing equations. This is done through the *fvSchemes* file in the *system* directory. Equations 3.1 and 3.2 were spatially and temporally discretized using different schemes, as tabulated in table 3.1. The time-derivative term, $\partial \boldsymbol{u}/\partial t$, was discretized based on the backward Euler approach, which is implicit and second order accurate. The gradient (∇) and Laplacian (∇^2) operators were discretized by the second-order Gauss scheme using linear interpolation. The divergence ($\nabla\cdot$) operator was also discretized similarly but with the *Gamma*= 0.5 interpolation scheme. To calculate the surface normals for the Laplacian, a blend of the corrected (which is unbounded, second-order and conservative) and uncorrected (bounded, first-order and non-conservative) schemes were used with a blend factor of 0.5.

3.1.5. Solution and algorithm controls

The velocity equation mentioned in the predictor step was solved using a Preconditioned (Bi-) Conjugate Gradient (PBiCG) iterative method preconditioned with a Diagonal Incomplete-Lower-Upper (DILU) decomposition. The pressure equation defined in a corrector step was solved using a Preconditioned Conjugate Gradient (PCG) iterative method preconditioned with the Diagonal Incomplete Cholesky (DIC) decomposition. It is possible to use the simpler Conjugate Gradient method with the DIC preconditioner for the pressure equation (see the equation B.5), since the Laplacian operator yields

Terms and operators	Numerical schemes	Interpolation
Divergence	Gauss	Gamma V 0.5
Gradient	Gauss	linear
Laplacian	Gauss	linear
Interpolation		linear
Surface normal gradient		limited 0.5
Time derivative	Backward Euler	

Table 3.1.: Numerical schemes used in the discretization.

a symmetric and positive definite matrix when discretized. However, the discretized velocity equation will not be symmetric due to the nonlinear convection term, thus dictating the use of the Bi-conjugate gradient method with the DILU preconditioner.

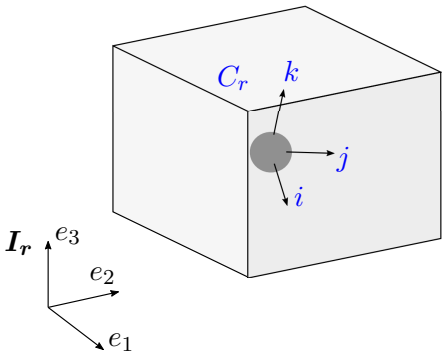

Figure 3.2.: The fixed frame I_r $(e_1,\ e_2,\ e_3)$ and the moving frame C_r $(i,\ j,\ k)$. The fluid body was modeled in the moving reference frame C_r, which is attached to the centre of the sphere, rather than the absolute reference frame I_r.

3.2. Numerical approach: FIV of an elastically-mounted sphere

In flow-induced vibration problems, the solid body has the freedom of moving in response to the forces acting on it. To account for the motion of the solid, a dynamic grid technique or immersed boundary method can be used. OpenFOAM facilitates solving fluid-structure interaction problems though dynamic grid techniques, in which the grid is deformed according to the solid motion during each time step. Ding *et al.* (2013); Habchi *et al.* (2013); Wu *et al.* (2014) provide some examples of researches who utilised OpenFOAM based in those techniques for FIV problems. Nevertheless, these dynamic grid techniques or immersed boundary methods are computationally expensive, given a fixed geometry.

A single-body FIV problem, such as the present cases, can be solved efficiently without using a dynamic grid technique. Instead of deforming the grid, the coupled solid motion and fluid equations can be solved in a body-fixed reference frame with a non-deformable grid, as used by Blackburn & Henderson (1996); Leontini *et al.* (2006*a*,*b*, 2013). This technique is considerably more efficient than a dynamic grid technique. Therefore, a new solver was developed to solve the coupled FSI system for an elastically-mounted sphere. The FSI system and the FSI solver are discussed in detail in the following two subsections.

3.2.1. Governing equations

To avoid mesh deformation, the fluid flow was modelled in the moving reference frame attached to the centre of the sphere (see figure 3.2). This is a non-inertial reference frame, since it accelerates according to the motion of the sphere. Therefore, (momentum)

Navier-Stokes equations given in equation 3.1 need to be adjusted accordingly. This can be done by adding the acceleration of the frame, which is indeed the acceleration of the sphere, to the momentum equations, as a source term. For an elastically-mounted rigid-body, the motion of the solid body was assumed to behave as a spring-mass-damper system, while the fluid was assumed incompressible and viscous.

The coupled fluid-solid system can be described by the Navier-Stokes equations given by equations (3.3), and the continuity equation given by (3.4), together with the governing equation for the motion of the sphere by equation (3.5):

$$\frac{\partial \boldsymbol{u}}{\partial t} + (\boldsymbol{u} \cdot \boldsymbol{\nabla})\boldsymbol{u} \;=\; -\boldsymbol{\nabla} p \;+\; \nu\, \boldsymbol{\nabla}^2 \boldsymbol{u} \;-\; \ddot{\boldsymbol{y}}_{\boldsymbol{s}}, \tag{3.3}$$

$$\boldsymbol{\nabla} \cdot \boldsymbol{u} \;=\; 0, \tag{3.4}$$

$$m\, \ddot{\boldsymbol{y}}_{\boldsymbol{s}} \;+\; c\, \dot{\boldsymbol{y}}_{\boldsymbol{s}} \;+\; k\, \boldsymbol{y}_{\boldsymbol{s}} \;=\; \boldsymbol{f}_{\boldsymbol{l}}. \tag{3.5}$$

Here, $\boldsymbol{y}_{\boldsymbol{s}}$, $\dot{\boldsymbol{y}}_{\boldsymbol{s}}$, and $\ddot{\boldsymbol{y}}_{\boldsymbol{s}}$ are the sphere displacement, velocity, and acceleration vectors, respectively. In addition, m is the mass of the sphere, c is the damping constant, k is the structural spring constant, and $\boldsymbol{f}_{\boldsymbol{l}}$ is the flow-induced integrated vector force acting on the sphere due to kinematic pressure and viscous shear forces acting on the body surface.

3.2.2. The fluid-structure solver

A new solver (named *vivIcoFoam*) was created to solve the fluid-structure coupled system defined by the equations (3.3) - (3.5) for laminar flows. This solver is based on the pre-built OpenFOAM solver, *icoFoam*, that we discussed in § 3.1.3. In this solver, the coupled fluid-structure system is solved using a predictor-corrector iterative method, which predicts the solid motion and corrects it in several corrector iterations. At the end of each iteration, the fluid equations given in equation (3.3 and 3.4) are solved with the predicted or subsequently corrected solid acceleration, and the fluid forces induced on the solid are calculated. Details of the predictor and corrector iterations at the $(n+1)^{th}$ time step are as follows.

The predictor iteration: Initially, the sphere acceleration, $\ddot{\boldsymbol{y}}_{\boldsymbol{s}}$, is predicted explicitly using the third-order polynomial extrapolation

$$\ddot{\boldsymbol{y}}_{\boldsymbol{s}}^{(n+1)} \;=\; 3\, \dot{\boldsymbol{y}}_{\boldsymbol{s}}^{(n)} \;-\; 3\, \dot{\boldsymbol{y}}_{\boldsymbol{s}}^{(n-1)} \;+\; \dot{\boldsymbol{y}}_{\boldsymbol{s}}^{(n-2)}. \tag{3.6}$$

Then, the sphere velocity, $\dot{\boldsymbol{y}}_{\boldsymbol{s}}$, and displacement, $\boldsymbol{y}_{\boldsymbol{s}}$, are estimated by integrating the predicted $\ddot{\boldsymbol{y}}_{\boldsymbol{s}}$ and estimated $\dot{\boldsymbol{y}}_{\boldsymbol{s}}$ by a third-order Adams-Moulton method by

$$\dot{\boldsymbol{y}}_{\boldsymbol{s}}^{(n+1)} \;=\; \dot{\boldsymbol{y}}_{\boldsymbol{s}}^{(n)} \;+\; \frac{\delta t}{12} \left(5\, \ddot{\boldsymbol{y}}_{\boldsymbol{s}}^{(n+1)} \;+\; 8\, \ddot{\boldsymbol{y}}_{\boldsymbol{s}}^{(n)} \;-\; \ddot{\boldsymbol{y}}_{\boldsymbol{s}}^{(n-1)}\right) \tag{3.7}$$

and

$$\boldsymbol{y_s}^{(n+1)} = \boldsymbol{y_s}^{(n)} + \frac{\delta t}{12}\left(5\,\dot{\boldsymbol{y}}_{\boldsymbol{s}}^{(n+1)} + 8\,\dot{\boldsymbol{y}}_{\boldsymbol{s}}^{(n)} - \dot{\boldsymbol{y}}_{\boldsymbol{s}}^{(n-1)}\right), \tag{3.8}$$

respectively, where δt is the time step. Finally, the fluid equations are solved with the predicted $\ddot{\boldsymbol{y}}_{\boldsymbol{s}}$, and the fluid force exerted on the sphere is calculated for the coming corrector iteration.

A corrector iteration: Initially, the corrected value of $\ddot{\boldsymbol{y}}_{\boldsymbol{s}}$ is calculated by solving the solid motion equation (3.5) with the values of $\boldsymbol{y_s}$, $\dot{\boldsymbol{y}}_{\boldsymbol{s}}$, and $\boldsymbol{f_l}$ calculated in the predictor or the previous corrector iteration by

$$\ddot{\boldsymbol{y}}_{\boldsymbol{s}}^{(n+1)} = -\frac{c}{m}\,\dot{\boldsymbol{y}}_{\boldsymbol{s}}^{(n+1)} - \frac{k}{m}\,\boldsymbol{y_s}^{(n+1)} + \frac{1}{m}\,\boldsymbol{f_l}^{(n+1)}. \tag{3.9}$$

Then, the corrected values of $\dot{\boldsymbol{y}}_{\boldsymbol{s}}$ and $\boldsymbol{y_s}$ are updated using equations (3.7) and (3.8) with the corrected $\ddot{\boldsymbol{y}}_{\boldsymbol{s}}$. Finally, the fluid equations are solved with the corrected $\ddot{\boldsymbol{y}}_{\boldsymbol{s}}$, and the fluid force exerted on the sphere is calculated. Several corrector steps are performed until the magnitudes of the fluid force and the solid acceleration converge to within a prescribed error bound, typically $\epsilon = 0.001$. This value was chosen for simulations since it was found that further decreasing ϵ does not increase the accuracy of the solution. Tests were performed to ensure that the chosen bound was sufficient to provide converged flow solutions. Typically, the FSI solver required 3 corrector steps. In most cases the number of corrector steps was less than 10, with the upper limit set to 15.

The temporal accuracy of the overall FSI solver is second-order, although the solution process for the solid motion is third-order accurate. This is because the PISO algorithm itself is of second-order accuracy. It is recalled that the fluid domain was modelled in a moving frame-of-reference. This motion is acknowledged through the outer domain velocity boundary conditions (except the outlet boundary). In this thesis, all the outer boundaries, except the outlet where a pressure condition is enforced, have a velocity condition prescribed on them. Once the predictor-corrector iterative process has completed, the velocity at the inlet boundaries is updated according to the velocity of the solid, $\dot{\boldsymbol{y}}_{\boldsymbol{s}}$, before proceeding to the next time step.

Implementation of *vivIcoFoam* solver in OpenFOAM

The web page, https://openfoamwiki.net/index.php, describes how to develop a new OpenFOAM solver, by providing an example of 'how to add temperature to *icoFoam*'. The *vivIcoFoam* solver was implemented in OpenFOAM following those steps. Appendix D describes the steps of developing the *vivIcoFoam* solver in more detail, while

appendix E shows the *vivIcoFoam.C* file and header files used to compile the solver. Therefore, only a brief overview of the solver is given below.

This solver was developed such that it can be used for both $2D$ simulations (such as cylindrical bodies) and $3D$ simulations. In addition, the solid motion can be restricted to the lift direction or can be allowed to move in all three directions. The solid motion parameters and other algorithm control settings should be prescribed in the *solidMotionData* file, which is in the *system* directory of a case, (see appendix F for a sample of this file). The solver calculates the mass of the solid, m, the damping constant, c, and the spring constant, k, according to the values given for the non-dimensional parameters: mass ratio m^*, damping ratio ζ, and reduced velocity U^*, by

$$m = \frac{4}{3}\rho\pi(D/2)^3 m^*,$$
$$c = 4\pi m\zeta/U^*$$

and

$$k = 4\pi^2 m/(U^*)^2.$$

This solver is designed to be used for a rectangular fluid domain. The solver reads the names of the boundary patches from the *boundaryToUpdate* file in the *constant* directory. A sample of this file can be found in appendix F. This file also declares the type of the simulation, *i.e.* $2D$ or $3D$, to recognize the inlet patches that need to be updated. The solver updates the velocity of the inlet boundaries and the pressure gradient of the solid boundary at the end of each time step, as detailed in § 3.5.1. The solver writes the solid motion data (displacement, velocity and acceleration of the solid) together with the force coefficients to a csv file in the case directory. The name of this file has the time-tag appended, at which the simulation is started, for example if it was started from $t = 0$ then the name of the data file is *solidDisplacmentData-0.csv*.

Only the asymptotic state of a simulation was used for the analyses presented in this thesis. Sometimes, simulations need a long time to reach the asymptotic state. However, there is a run-time limitation of a maximum of 1 day on the Magnus supercomputer. Therefore, in such a case, it is required to restart from the previously stopped time. In these circumstances, the *vivIcoFoam* solver writes the necessary solid-motion data of the last three time steps to an OpenFOAM file called *lastMotionData* in the *system* directory (a sample of this file also given in appendix F). The solver updates this file at the time it writes the results for the fluid to a *time* directory.

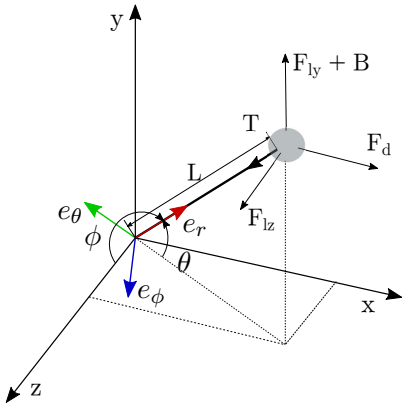

x - freestream direction
θ - tether angle from xz plan
ϕ - tether angle from z direction
F_d - drag force
F_{ly} - lift force in the y direction
F_{lz} - lift force in the z direction
B - buoyancy force
T - tension of the tether
L - tether length

Figure 3.3.: Schematic of the tethered sphere. Two coordinate systems were used to model the system; Cartesian coordinate, $< i, j, k >$, and spherical coordinates, $< e_r, e_\theta, e_\phi >$.

3.3. Numerical approach: FIV of a tethered sphere

3.3.1. Problem formulation

Figure 3.3 shows a schematic of the system, which is simply a tethered sphere in a uniform flow field. The tether was assumed to be massless. This is compatible with experimental studies that choose a tether whose mass is negligible compared to the mass of the sphere (Govardhan & Williamson 1997, 2005; Williamson & Govardhan 1997). Moreover, the tether was assumed to be rigid and inextensible, *i.e.* there was no radial movement along the tether axis. This assumption is found to be justified, as experimentally, there appeared to be very little movement in the radial direction. This assumption restricts the motion of the sphere to a spherical manifold whose radius is the tether length. Moreover, with this holonomic constraint, the number of equations required to describe the sphere dynamics reduces to two, even though the sphere has three degrees of freedom. Moreover, the tethered sphere undergoes pure rotation around the base point of the tether. Therefore, a 3D Rotation Group SO(3) can also be used to obtain the equations of motion of the sphere, as used by Rajamuni *et al.* (2014). However, for simplicity, Newtonian Mechanics principles were used here, as described below.

To derive the equations of motion of the sphere, a spherical coordinate system was employed with unit vectors, $\boldsymbol{e_r}$, $\boldsymbol{e_\theta}$, and $\boldsymbol{e_\phi}$, as shown in figure 3.3. However, the Navier-Stokes equations were derived with a Cartesian coordinate system with unit vectors $\boldsymbol{i}$, $\boldsymbol{j}$, $\boldsymbol{k}$ in the x, y, and z directions, respectively. The mapping between these two coordinate systems is bijective and can be elaborated with parameters, $\theta \in [0, 2\pi)$ and $\phi \in [0, \pi]$ as:

$$M : \begin{pmatrix} \boldsymbol{e_r} \\ \boldsymbol{e_\theta} \\ \boldsymbol{e_\phi} \end{pmatrix} = \begin{pmatrix} \cos\theta\sin\phi & \sin\theta\sin\phi & \cos\phi \\ -\sin\theta & \cos\theta & 0 \\ \cos\theta\cos\phi & \sin\theta\cos\phi & -\sin\phi \end{pmatrix} \begin{pmatrix} \boldsymbol{i} \\ \boldsymbol{j} \\ \boldsymbol{k} \end{pmatrix}, \tag{3.10}$$

$$M^{-1} : \begin{pmatrix} \boldsymbol{i} \\ \boldsymbol{j} \\ \boldsymbol{k} \end{pmatrix} = \begin{pmatrix} \cos\theta\sin\phi & -\sin\theta & \cos\theta\cos\phi \\ \sin\theta\sin\phi & \cos\theta & \sin\theta\cos\phi \\ \cos\phi & 0 & -\sin\phi \end{pmatrix} \begin{pmatrix} \boldsymbol{e_r} \\ \boldsymbol{e_\theta} \\ \boldsymbol{e_\phi} \end{pmatrix}, \tag{3.11}$$

where θ is the angle of tether to the xz plane and ϕ is the angle of the tether to the z direction. In spherical coordinates, the position of the sphere, $\boldsymbol{r_s}$, can be expressed as $\boldsymbol{r_s} = L\ \boldsymbol{e_r}$, where L is the length from bottom of the tether to the centre of the sphere. Then, the velocity, $\boldsymbol{v_s}$, and the acceleration, $\boldsymbol{a_s}$, of the sphere can be obtained by differentiating the position and the velocity of the sphere w.r.t. time, as given in equations (3.12) and (3.13), respectively.

$$\boldsymbol{v_s} = L\left(\dot{\theta}\sin\phi\ \boldsymbol{e_\theta} + \dot{\phi}\ \boldsymbol{e_\phi}\right). \tag{3.12}$$

$$\boldsymbol{a_s} = L\ \left(-(\dot{\theta}^2\sin^2\phi + \dot{\phi}^2)\ \boldsymbol{e_r} + (\ddot{\theta}\sin\phi + 2\dot{\theta}\dot{\phi}\cos\phi)\ \boldsymbol{e_\theta} + (-\dot{\theta}^2\sin\phi\cos\phi + \ddot{\phi})\ \boldsymbol{e_\phi}\right). \tag{3.13}$$

Forces acting on the sphere are of three types: a structural force T (the tension in the tether); a buoyancy force, B; and the fluid forces F_d, F_{ly} and F_{lz}, which denote the components in the streamwise (x), lateral (y) and transverse (z) directions, respectively (see figure 3.3). In spherical coordinates, the summation of all forces can be written as:

$$\begin{aligned} \sum \boldsymbol{F} \quad = \quad & (F_d\cos\theta\sin\phi + (F_{ly}+B)\sin\theta\sin\phi + F_{lz}\cos\phi - T)\ \boldsymbol{e_r} \\ & - (F_d\sin\theta - (F_{ly}+B)\cos\theta)\ \boldsymbol{e_\theta} \\ & + (F_d\cos\theta\cos\phi + (F_{ly}+B)\sin\theta\cos\phi - F_{lz}\sin\phi)\ \boldsymbol{e_\phi}. \end{aligned} \tag{3.14}$$

Once the sphere acceleration and forces acting on it are known, the equations of motion can be easily obtained by the angular momentum balance, that is $I\dot{\boldsymbol{\omega}} = \sum \boldsymbol{r_s}\times\boldsymbol{F}$, where $I = m(D^2/10+L^2)$ is the inertia of the sphere at the base of the tether, $\dot{\boldsymbol{\omega}} = \boldsymbol{a_s}/L$ is the angular acceleration of the sphere and m and D are the mass and diameter of the sphere, respectively. The component equations are

$$m(D^2/10 + L^2)(\ddot{\theta}\sin\phi + 2\dot{\theta}\dot{\phi}\cos\phi) = -L\,(F_d\sin\theta - (F_{ly}+B)\cos\theta) \tag{3.15}$$

and

$$m(D^2/10+L^2)(\ddot{\phi}-\dot{\theta}^2\sin\phi\cos\phi) = L\left(F_d\cos\theta\cos\phi + (F_{ly}+B)\sin\theta\cos\phi - F_{lz}\sin\phi\right). \quad (3.16)$$

The above two dynamics equations can be converted into a matrix form by rearranging the terms as

$$\begin{pmatrix}\ddot{\theta}\\ \ddot{\phi}\\ 0\end{pmatrix} = \frac{L}{m\left(\frac{D^2}{10}+L\right)}\begin{pmatrix}-\sin\theta/\sin\phi & \cos\theta/\sin\phi & 0\\ \cos\theta\cos\phi & \sin\theta\cos\phi & -\sin\phi\\ 0 & 0 & 0\end{pmatrix}\begin{pmatrix}F_d\\ F_{ly}+B\\ F_{lz}\end{pmatrix} + \begin{pmatrix}-2\dot{\theta}\dot{\phi}\cot\phi\\ \dot{\theta}^2\sin\phi\cos\phi\\ 0\end{pmatrix}. \quad (3.17)$$

At this point, it is important to note that there is a singularity associated with $\phi = 0$. However, it is not a problem for the current simulations, since ϕ can never be 0 because the buoyancy force is much higher than the fluid forces and therefore, the tether can never be aligned to the transverse direction (z direction).

The Newtonian fluid is assumed incompressible and viscous, and modelled in a Cartesian coordinate system whose origin is the centre of the sphere. As discussed in § 3.2 this is a non-inertial reference frame. Therefore, the acceleration of the frame ($\boldsymbol{a_s}$, given in equation 3.13) should be included in the momentum equation. However, since this equation is in spherical coordinates, it is necessary to first convert it into Cartesian coordinates, which can be easily done by the mapping, M, given in equation (3.10). Let $\boldsymbol{a_c}$ is the acceleration of the frame once it is converted into Cartesian coordinates, then

$$\boldsymbol{a_c} = M\boldsymbol{a_s}. \quad (3.18)$$

Finally, the coupled fluid-solid system can be described by the fluid equations given in (3.19) and (3.20) and the sphere motion equations given in (3.17) together with equations (3.10), (3.13), and (3.18):

$$\frac{\partial \boldsymbol{u}}{\partial t} = -(\boldsymbol{u}\cdot\boldsymbol{\nabla})\boldsymbol{u} - \boldsymbol{\nabla}p + \nu\,\boldsymbol{\nabla}^2\boldsymbol{u} - \boldsymbol{a_c}, \quad (3.19)$$

$$\boldsymbol{\nabla}\cdot\boldsymbol{u} = 0. \quad (3.20)$$

As a reminder, here p is the kinematic pressure, i.e., the static pressure divided by the density.

3.3.2. FSI solver for a tethered sphere

As described above, a new fully coupled solver (named *tetheredVivIcoFoam*) was developed, based on the pre-built *icoFoam* solver for laminar flows, to solve the coupled fluid-solid system defined by equations (3.17)-(3.2) for a tethered sphere. Similar to the solver we previously developed for the FIV of an elastically-mounted solid body in § 3.2, this solver employs a predictor-corrector iterative method. The solid motion was first predicted explicitly in the predictor iteration and then corrected as necessary with

several corrector iterations. Once the solid motion is obtained (from the predictor or a corrector iteration), the Navier-Stokes equations were solved using the PISO algorithm by treating the acceleration of the frame as a source term. This iterative process for the $(n+1)^{th}$ time step can be elaborated as follows:

The predictor iteration: Initially, the angular accelerations of the sphere, $(\ddot{\theta} \quad \ddot{\phi})^T$, are predicted explicitly using a third-order polynomial interpolation by

$$\begin{pmatrix} \ddot{\theta} \\ \ddot{\phi} \end{pmatrix}^{(n+1)} = 3 \begin{pmatrix} \ddot{\theta} \\ \ddot{\phi} \end{pmatrix}^{(n)} - 3 \begin{pmatrix} \ddot{\theta} \\ \ddot{\phi} \end{pmatrix}^{(n-1)} + \begin{pmatrix} \ddot{\theta} \\ \ddot{\phi} \end{pmatrix}^{(n-2)} . \tag{3.21}$$

Then, the angular velocities, $(\dot{\theta} \quad \dot{\phi})^T$, and tether angles, $(\theta \quad \phi)^T$, are estimated using a third-order Adams-Moulton method, by integrating the angular accelerations and angular velocities to obtain

$$\begin{pmatrix} \dot{\theta} \\ \dot{\phi} \end{pmatrix}^{(n+1)} = \begin{pmatrix} \dot{\theta} \\ \dot{\phi} \end{pmatrix}^{(n)} + \frac{\delta t}{12} \left(5 \begin{pmatrix} \ddot{\theta} \\ \ddot{\phi} \end{pmatrix}^{(n+1)} + 8 \begin{pmatrix} \ddot{\theta} \\ \ddot{\phi} \end{pmatrix}^{(n)} - \begin{pmatrix} \ddot{\theta} \\ \ddot{\phi} \end{pmatrix}^{(n-1)} \right) \tag{3.22}$$

and

$$\begin{pmatrix} \theta \\ \phi \end{pmatrix}^{(n+1)} = \begin{pmatrix} \theta \\ \phi \end{pmatrix}^{(n)} + \frac{\delta t}{12} \left(5 \begin{pmatrix} \dot{\theta} \\ \dot{\phi} \end{pmatrix}^{(n+1)} + 8 \begin{pmatrix} \dot{\theta} \\ \dot{\phi} \end{pmatrix}^{(n)} - \begin{pmatrix} \dot{\theta} \\ \dot{\phi} \end{pmatrix}^{(n-1)} \right) , \tag{3.23}$$

respectively. Then, the acceleration of the sphere, $\boldsymbol{a_s}^{(n+1)}$, is obtained by equation (3.13) and converted it into Cartesian coordinates, $\boldsymbol{a_c}^{(n+1)}$, using the mapping given in equation (3.10). At the end of the predictor step, the Navier-Stokes equations given in equations (3.19) and (3.20) are solved with the predicted $\boldsymbol{a_c}^{(n+1)}$ and the forces exerted on the sphere, $(F_d \quad F_{ly} \quad F_{lz})^{(n+1)}$, are calculated.

A corrector iteration: Initially, angular accelerations of the sphere, $(\ddot{\theta} \quad \ddot{\phi})^T$, are corrected by equation (3.17) with the values obtains for θ, ϕ, $\dot{\theta}$, $\dot{\phi}$, F_d, F_{ly} and F_{lz} at the predictor iteration (or at the last corrector iteration). Then, the corrected angular accelerations are relaxed to improve the convergence characteristics by

$$\begin{pmatrix} \ddot{\theta} \\ \ddot{\phi} \end{pmatrix}^{(n+1)'} = \begin{pmatrix} \ddot{\theta} \\ \ddot{\phi} \end{pmatrix}^{(n+1)*} + \gamma \left(\begin{pmatrix} \ddot{\theta} \\ \ddot{\phi} \end{pmatrix}^{(n+1)**} - \begin{pmatrix} \ddot{\theta} \\ \ddot{\phi} \end{pmatrix}^{(n+1)*} \right) , \tag{3.24}$$

where γ is the relaxation parameter, and $*$ and $**$ represents the angular accelerations calculated in the previous and the current iterations, respectively. The method becomes unstable, especially for small mass ratio spheres in the absence of any relaxation. The

convergence of the method can be improved by the choice of γ, depending on the parameter combination. Once the angular accelerations are corrected and relaxed, the angular velocities and tether angles are calculated, similar to the predictor step. With these newly calculated values, the sphere acceleration (in Cartesian coordinates) is calculated and the Navier-Stokes equations are solved. Finally, the fluid forces exerted on the sphere are calculated to use in the next corrector iteration. This iterative process is terminated once the magnitude of the fluid forces and sphere angular accelerations are converged within the given tolerance limit, $\epsilon = 0.001$. This value was chosen for simulations since it was found that further decreasing ϵ did not increase the accuracy of the solution.

As described in the previous section, the fluid flow is modelled in the moving frame which is attached to the centre of the sphere. This motion is acknowledged through the outer domain velocity boundary conditions (expect the outlet boundary). Similar to the elastically mounted case, all the outer boundaries, except the outlet where a pressure condition is enforced, have velocity prescribed on them. Once the predictor-corrector iterative process is completed, the velocity boundary conditions are updated according to the sphere velocity, $\boldsymbol{v_c} = M\boldsymbol{v_s}$.

3.3.3. The natural frequency

As discussed in § 2.3, the reduced velocity, $U^* = U/(f_n D)$, is identified as a suitable parameter for FIV problems, as it is a function of the system's natural frequency. In experiments, a range of reduced velocity is obtained by increasing the flow velocity, U. Since the Reynolds number is also a function of the flow velocity, it is impractical to increase the reduced velocity by fixing the Reynolds number. This is an undesirable side-effect that appears in experiments. However, when performing simulations, it is desirable to fixed the Reynolds number at a suitable value. This limits the number of varying parameters for each set of simulations. Moreover, if the Reynolds number is increased then the laminar flow transitions to turbulence by introducing small scales of motion. To accurately predict these small scales, a finer mesh density is required. However, this increases the computational cost considerably.

Williamson & Govardhan (1997) obtained an expression for the non-dimensional natural frequency of the tethered sphere system as

$$S_n \approx \left(\frac{1}{2\pi}\right) \frac{1}{Fr\sqrt{l^*}} \sqrt{\frac{1-m^*}{C_a + m^*}}, \tag{3.25}$$

where C_a is the added mass coefficient (0.5 for a sphere). The mass ratio, m^*, and the tether length ratio, $l^* = L/D$, are desired to be kept constant for a particular set of simulations. Therefore, it is possible to obtain a range of natural frequencies (reciprocal of the reduced velocity) by varying the Froude number, Fr, numerically. The Froude

number is a non-dimensional number defined as the ratio of the flow inertia to the gravitational force ($Fr = U/\sqrt{gD}$, where g is the gravitational force). Furthermore, it is conceivably possible to investigate numerically as $U^* \to \infty$, whereas the reduced velocity range is limited experimentally to the flow velocity accessible in the flow facility. For this thesis, three sets of simulations were performed by fixing the Reynolds number at $Re = 500$, 1200 and 2000 with a tethered sphere. Studying the cases for the Reynolds numbers $Re = 1200$ and 2000, which are closer to the experimental studies of Govardhan & Williamson (1997); Williamson & Govardhan (1997); Jauvtis *et al.* (2001); Govardhan & Williamson (2005) provide additional insight into those studies, while the case of $Re = 500$ will provide an understanding of the problem in the laminar regime.

3.3.4. Calculation of the reduced velocity

To obtain a range of reduced velocities, it is required to calculate the natural frequency of the tethered system accurately, which is the focus of this section.

Let $(X,\ Y,\ Z)^T$ be the position of the sphere in Cartesian coordinates. Then, the equation of motion of the tethered sphere can be obtained by the linear momentum balance (see figure 3.3) as

$$m \begin{pmatrix} \ddot{X} \\ \ddot{Y} \\ \ddot{Z} \end{pmatrix} = \begin{pmatrix} F_d \\ F_{ly} + B \\ F_{lz} \end{pmatrix} - T \begin{pmatrix} \sin\phi\cos\theta \\ \sin\phi\sin\theta \\ \cos\phi \end{pmatrix}. \tag{3.26}$$

However, $(\sin\phi\cos\theta,\ \sin\phi\sin\theta,\ \cos\phi)^T$ is the unit vector along the tether, $\boldsymbol{e_r}$, and can be expressed as $(X, Y, Z)^T/L$. Hence, the equations of motion can be rearranged into

$$m \begin{pmatrix} \ddot{X} \\ \ddot{Y} \\ \ddot{Z} \end{pmatrix} + \frac{T}{L} \begin{pmatrix} X \\ Y \\ Z \end{pmatrix} = \begin{pmatrix} F_d \\ F_{ly} + B \\ F_{lz} \end{pmatrix}. \tag{3.27}$$

From these equations, it is clear that the natural frequency of the system is identical in all three directions and is given by

$$f_n = \frac{1}{2\pi}\sqrt{\frac{T}{mL}}. \tag{3.28}$$

This can be written in the non-dimensional form as

$$S_n = \frac{f_n D}{U} = \frac{1}{2\pi}\sqrt{\frac{D^2 T}{U^2 mL}}. \tag{3.29}$$

Since the sphere is assumed to have no motion in the direction of the tether, the tension of the tether can be obtained simply from the force balance as

$$T = \sqrt{F_d^2 + (F_{ly} + B)^2 + F_{lz}^2}, \tag{3.30}$$

assuming the centrifugal force is negligible, consistent with a large tether length ratio. With this expression for T, equation (3.29) can be written in the non-dimensional form as

$$S_n = \frac{1}{2\pi}\sqrt{\frac{\sqrt{C_d^2 + \{C_{ly} + (1-m^*)\psi\}^2 + C_{lz}^2}}{(4/3)(m^* + C_a)l^*}}, \tag{3.31}$$

where $\psi = 4/(3Fr^2)$. For a stationary sphere, the time-averaged lateral (y) and transverse (z) forces are negligible compared to the drag force. Moreover, $(1-m^*)\psi$ is much greater then C_{ly} over the entire reduced velocity range investigated for the mass ratios of interest in this study ($m^* = 0.8$ and 80). Hence, 3.31 can be simplified to

$$S_n \approx \frac{1}{2\pi}\sqrt{\frac{\sqrt{C_d^2 + \{(1-m^*)\psi\}^2}}{(4/3)(m^* + C_a)l^*}}. \tag{3.32}$$

The reduced velocity, U^*, is defined as the inverse of the natural frequency, S_n, leading to

$$U^* = 2\pi\sqrt{\frac{(4/3)(m^* + C_a)l^*}{\sqrt{C_d^2 + \{(1-m^*)\psi\}^2}}}. \tag{3.33}$$

For all of the numerical results presented in chapter 6, equation 3.33 has been used to calculate the reduced velocity. A range of U^* is obtained by varying ψ. In experiments, since the gravitational acceleration is constant, C_d is negligible compared to the buoyancy force component therefore S_n given in equation 3.25 is valid. In contrast, in this numerical study, the buoyancy term is of the same order of magnitude as the drag coefficient for higher reduced velocities. Therefore, it is required to use equation 3.33 instead of equation 3.25.

3.4. Dynamic mode decomposition

Dynamic mode decomposition (DMD) is also used as part of the analysis to characterise the wake behind the sphere. DMD is a numerical procedure introduced by Schmid & Sesterhenn (2008) for extracting the dynamic periodic features of a flow. This method involves spectral analysis of Koopman operator. For a given sequence of time-resolved flow field measurements, in this thesis, the case consisting of a set of velocity fields at fixed time increments, DMD computes a set of approximations to the Koopman modes, also called Ritz vectors, with associated eigenvalues, called Ritz values. Ritz vectors are the eigenfunctions of the Koopman operator, each of which is associated with a fixed oscillation frequency specified by the argument of the associated eigenvalue. A Koopman mode may grow or decay exponentially in time, according to the magnitude of the corresponding eigenvalue. In particular, this analysis is useful to extract the dominant frequencies belonging to the sequence of fields and the corresponding periodic spatially-varying modes, which may be localised in different regions of space. The approach used in the thesis closely follows that of Rowley *et al.* (2009); Schmid (2010, 2011), so only a very brief outline is given here.

Let $\boldsymbol{x_1}$, $\boldsymbol{x_2}$, $\ldots$, $\boldsymbol{x_m}$ represent a set of column vectors of the field data (e.g. velocity field), collected at equal time intervals δt. It is assumed to have a linear mapping, G, that connects the flow field $\boldsymbol{x_i}$ to the subsequent flow field $\boldsymbol{x_{i+1}}$, *i.e.*

$$\boldsymbol{x_{i+1}} = G\boldsymbol{x_i}. \tag{3.34}$$

This mapping is also considered to remain constant over the duration of sampling period. Following the Krylov technique, in particular, the Arnoldi approach, $\boldsymbol{x_m}$ can be expressed as a linearly independent combination of previous snapshots, *i.e.*

$$G\boldsymbol{x_{m-1}} \equiv \boldsymbol{x_m} = c_1\boldsymbol{x_1} + c_2\boldsymbol{x_2} + \ldots + c_{m-1}\boldsymbol{x_{m-1}} \equiv \boldsymbol{K}\boldsymbol{c}, \tag{3.35}$$

where $\boldsymbol{K} = (\boldsymbol{x_1}\ \boldsymbol{x_2}\ \ldots\ \boldsymbol{x_{m-1}})$ and $\boldsymbol{c} = (c_1\ c_2\ \ldots\ c_{m-1})^T$. This leads to the following matrix equation

$$\boldsymbol{GK} \equiv \begin{pmatrix} \boldsymbol{x_2} & \boldsymbol{x_3} & \ldots & \boldsymbol{x_m} \end{pmatrix} = \begin{pmatrix} \boldsymbol{x_1} & \boldsymbol{x_2} & \ldots & \boldsymbol{x_{m-1}} \end{pmatrix} \begin{pmatrix} 0 & 0 & \ldots & 0 & c_1 \\ 1 & 0 & \ldots & 0 & c_2 \\ 0 & 1 & \ldots & 0 & c_3 \\ \vdots & & \ddots & & \vdots \\ 0 & 0 & \ldots & 1 & c_{m-1} \end{pmatrix} \equiv \boldsymbol{KC}. \tag{3.36}$$

The matrix $\boldsymbol{C}$ is called the *Companion matrix*, which is the equivalent low dimensional representation of the field data. Since the vectors $\boldsymbol{x_1}$, $\ldots$, $\boldsymbol{x_m}$ are known, the coefficients, c_1, $\ldots$, c_{m-1} can be easily obtained by the QR factorization or Singular Value

Decomposition. Let $\boldsymbol{z_i}$ and λ_i be the ith eigenvector and eigenvalue of $\boldsymbol{C}$, respectively. Then, the Koopman modes (Ritz vectors) of the data set can be obtained by

$$\boldsymbol{v_i} = \boldsymbol{K}\boldsymbol{z_i}, \tag{3.37}$$

and the Ritz values are directly the eigenvalues of the Companion matrix. Note that both the Ritz vectors and values consist of complex conjugate pairs.

The field at any discrete time t_k can be reconstructed using the Ritz vectors and values. However, the Ritz vectors should be obtained from the properly re-scaled eigenvalues for the reconstructions. Let $\hat{\boldsymbol{z}}_{\boldsymbol{i}} = \beta_i \boldsymbol{z_i}$ be the scaled version of $\boldsymbol{z_i}$ using the ith element of the vector $\boldsymbol{\beta} = \boldsymbol{Z^{-1}}\boldsymbol{e_1}$, where $\boldsymbol{Z} = [\boldsymbol{z_1}\ \boldsymbol{z_2}\ \ldots\ \boldsymbol{z_{m-1}}]$ and $\boldsymbol{e_1} = (1\ 0\ \ldots\ 0)^T$. If $\hat{\boldsymbol{v}}_{\boldsymbol{i}} = \boldsymbol{K}\hat{\boldsymbol{z}}_{\boldsymbol{i}}$ is the scaled Ritz vector, then the field at any discrete time t_k can be reconstructed by

$$\boldsymbol{x_k} = \sum_{i=1}^{m-1} \lambda_i^k \hat{\boldsymbol{v}}_{\boldsymbol{i}}. \tag{3.38}$$

If the sequence of fields is strictly periodic, so that $\boldsymbol{x_m} = \boldsymbol{x_1}$, then the above expansion is equivalent to a Fourier decomposition.

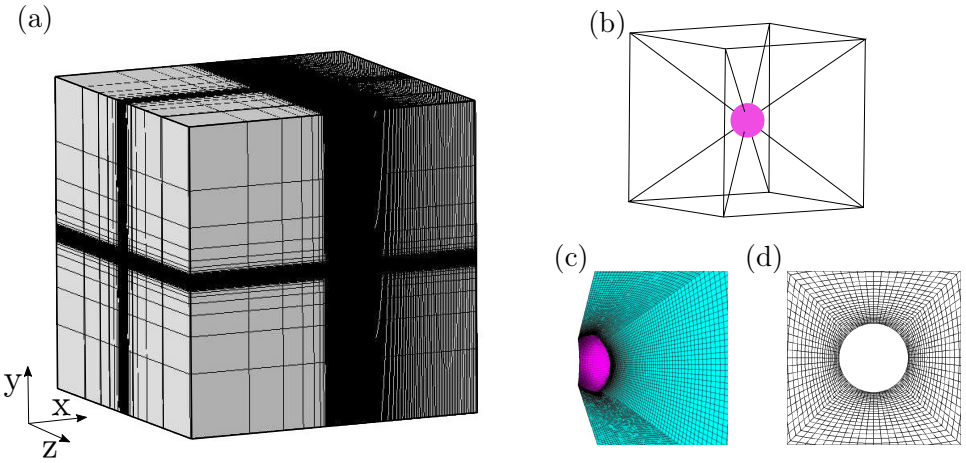

Figure 3.4.: The hexahedral grid computational domain: (a) isometric view; (b) cubic block placed around the sphere, which was decomposed into 6 square frustums; (c) isometric view of the grid in a square frustums near the sphere surface; and (d) grid near the sphere surface in x-y plane.

3.5. Grid and domain details

A cubical domain with a side length of $100D$ was chosen for the fluid flow with the sphere (of diameter $D = 1\ m$) at its centre. A hexahedral grid was generated using Ansys-ICEM-CFD for the fluid domain. The grid was saved in the Fluent format as a *.msh* file, after specifying the boundary conditions. Then, it was converted to the OpenFOAM format using the OpenFOAM utility called *fluentMeshToFaom*. Figure 3.4 shows a typical grid used for simulations presented in this thesis. A cubic block with a side length of $5D$ was placed around the sphere to achieve greater resolution near the sphere (see figure 3.4 (b)). This cube was first decomposed into six square frustums. The grid was concentrated toward the sphere surface by assigning exponentially distributed grid points in the radial direction of each square frustum (see figure 3.4 (c) and (d)). Uniformly distributed grid points were assigned in the other two directions of each square frustum. A large number of grid points were assigned in the downstream direction to reasonably resolve the wake structures.

Five successively finer grids were constructed to analyse the dependency of the computed solution on the grid refinement (see § 3.6). The first four grids were generated by fixing the number of cells in the sphere boundary, $C_{sp} = 7350$, as shown in table 3.2. Grid 1 contains $\backsimeq 0.79$ million cells whose cell thickness at the sphere boundary, δl, is $0.011D$. Grid 2 was created by decreasing δl to $0.004D$. This yielded $\backsimeq 1.25$ million cells, with approximately 10-16 cells within the boundary layer before flow separation. This grid is fine enough for the studies presented in this thesis. However, a few more grids were generated to confirm that the solution is insensitive to further refinement of the grid. Grid 3 was generated by decreasing δl further down to $0.002D$, but with

Grid	C_{sp}	N_r	δl	No. cells
Grid 1	7 350	70	$0.011D$	0.79×10^6
Grid 2	7 350	100	$0.004D$	1.25×10^6
Grid 3	7 350	100	$0.002D$	1.25×10^6
Grid 4	7 350	200	$0.002D$	1.96×10^6
Grid 5	18 150	100	$0.004D$	2.57×10^6

Table 3.2.: Details of the computational grids: C_{sp} is the number of cells in the sphere surface, N_r is the number of nodes in the radial direction of a square frustum and δl is the minimum thickness of the cells (in the radial direction) at the sphere boundary in each grid.

same number of cells as Grid 2 to obtain more concentration toward the sphere boundary. Grid 4 was generated by doubling the number of nodes in the radial direction of a square frustum, N_r, with the same δl as Grid 3 (see table 3.2). This increased the number of cells to $\backsimeq$ 1.96 million. Finally, to analyse the effect of grid refinement in the tangential direction, Grid 5 was generated by increasing the number of cells in the sphere boundary, C_{sp}, to 18 150 with $\delta l = 0.004D$, which is same δl as Grid 2.

3.5.1. Boundary conditions

The cubical fluid domain has two types of outer boundaries: inlet and outlet. Five faces of the cube were treated as inlets and the velocity was prescribed on them. For an FIV simulation, which uses either the *vivIcoFoam* or *tetheredVivIcoFoam* solvers, the motion of the reference frame was taken into account through these inlets by updating the frame velocity at each time step, as described in § 3.2 and § 3.3. The remaining face of the cube is the outlet over which a zero pressure is imposed. The inner boundary (sphere boundary) is treated as a wall and assumed to have no-slip and no-penetration boundary conditions. The flow is assumed in the x direction with an upstream velocity of $U = 1m/s$; the boundary conditions for pressure and velocity at each boundary are tabulated in table 3.3.

For the results presented in chapter 5 with a transversely rotating sphere, a rotating wall velocity is prescribed on the sphere boundary using the *rotatingWallVelocity* utility. When the sphere is under a forced rotation, the normal pressure gradient at the sphere surface is in general non-zero. Therefore, it was calculated by taking the inner product of the momentum equation 3.3 (or 3.19 for a tethered sphere) and the outward unit normal vector, $\boldsymbol{\eta}$, as follows

$$\boldsymbol{\nabla} p \cdot \boldsymbol{\eta} \;=\; \big(-(\boldsymbol{u} \cdot \boldsymbol{\nabla})\boldsymbol{u} \;+\; \nu \boldsymbol{\nabla}^2 \boldsymbol{u} \;-\; \ddot{\boldsymbol{y}}_{\boldsymbol{s}} \big) \cdot \boldsymbol{\eta}. \tag{3.39}$$

Boundary	Velocity, $\boldsymbol{u}$	Pressure, p
Inlet	$\boldsymbol{u} = (U\ 0\ 0) - \dot{\boldsymbol{y}}_{\boldsymbol{s}}$	$\boldsymbol{\nabla} p \cdot \boldsymbol{\eta} = 0$
Sphere	$\boldsymbol{u} = (0\ 0\ 0)$	$\boldsymbol{\nabla} p \cdot \boldsymbol{\eta} = 0$
Outlet	$\boldsymbol{\nabla} \boldsymbol{u} \cdot \boldsymbol{\eta} = 0$	$p = 0$

Table 3.3.: Boundary conditions: U is the upstream velocity; $\boldsymbol{\eta}$ is the outward normal vector at a corresponding boundary; and $\dot{\boldsymbol{y}}_{\boldsymbol{s}}$ is the velocity of the sphere.

The FSI solver (*vivIcoFoam* or *tetheredVivIcoFoam*) calculates the normal pressure gradient at the sphere surface, after finding the acceleration of the solid body by the predictor or a corrector iteration, and updated before the fluid equations are solved.

	$Re = 300$		
Study	$\overline{C}_d$	$\overline{C}_l$	St
Present study	0.665	0.070	0.137
Constantinescu & Squires (2000)	0.665	0.065	0.136
Giacobello *et al.* (2009)	0.658	0.067	0.134
Johnson & Patel (1999)	0.656	0.069	0.137
Kim *et al.* (2001)	0.657	0.067	0.137
Kim (2009)	0.658	0.067	0.134
Poon *et al.* (2010)	0.658	0.067	0.134

Table 3.4.: Comparison of computed time-averaged drag coefficient, $\overline{C}_d$, time-averaged lift coefficient, $\overline{C}_l$, and Strouhal number, St, at $Re = 300$ with other numerical studies.

3.6. Numerical sensitivity and validation studies

3.6.1. Validation studies

3.6.1.1. Flow past a stationary sphere

The flow past a rigidly mounted sphere was investigated at $Re = 300$, 500 and 1000. The computed values for the time-averaged drag and lift coefficients, $\overline{C}_d$ and $\overline{C}_l$, respectively, and the Strouhal number, St, are listed in tables 3.4-3.6. As the lift coefficient is negligible at $Re = 1000$, a secondary Strouhal number is calculated instead of $\overline{C}_l$. As can be seen, the present results closely match values calculated in other studies (Clift *et al.* 2005; Giacobello *et al.* 2009; Johnson & Patel 1999; Kim *et al.* 2001; Kim 2009; Morsi & Alexander 1972; Mittal 1999; Poon *et al.* 2009, 2010, 2014; Roos & Willmarth 1971; Sakamoto & Haniu 1990; Tomboulides & Orszag 2000).

3.6.1.2. Flow past a transversely rotating sphere

Flow past a rigidly mounted and transversely rotating sphere was studied at $Re = 300$ for the rotation rate of $0 \leq \alpha \leq 3$. The time-averaged drag coefficient, $\overline{C}_d$, showed an increasing trend with α up to $\alpha \approx 1.75$ and then a decreasing trend. The time-averaged lift coefficient, $\overline{C}_l$, increased with increasing α and became flat for $\alpha \geq 1.25$. The values calculated for both $\overline{C}_d$ and $\overline{C}_l$ were in good agreement with the results in the literature (Giacobello *et al.* 2009; Kim 2009; Poon *et al.* 2010; Dobson *et al.* 2014), see section 3.1 of chapter 5 for more detail. The flow underwent a series of transitions between 'steadiness' and the 'unsteadiness', as the rotation rate was increased. The wake structures observed at low rotation rates matched well with other research studies. However, our results at higher rotation rate were slightly different from others. The reason for that is discussed in detail in section 3.1 of chapter 5, together with some plots of the wake.

	$Re = 500$		
Study	$\overline{C}_d$	$\overline{C}_l$	St
Present	0.57	0.06	0.18
Clift *et al.* (2005)	0.56	-	
Morsi & Alexander (1972)	0.55	-	
Mittal (1999)	0.57	-	-
Poon *et al.* (2014)	0.56	0.05	0.15
Roos & Willmarth (1971)	0.547	-	-
Sakamoto & Haniu (1990)	-	-	0.18
Tomboulides & Orszag (2000)	-	-	0.167

Table 3.5.: Comparison of computed time-averaged drag coefficient, $\overline{C}_d$, time-averaged lift coefficient, $\overline{C}_l$, and Strouhal number, St, at $Re = 500$ with other studies.

	$Re = 1000$		
Study	$\overline{C}_d$	St-1	St-2
Present	0.49	0.19	0.33
Morsi & Alexander (1972)	0.46	-	-
Poon *et al.* (2014)	0.46	0.185	0.33
Poon *et al.* (2009)	0.46	0.2	0.34
Roos & Willmarth (1971)	0.472, 0.483	-	-
Sakamoto & Haniu (1990)	-	0.2	-
Tomboulides & Orszag (2000)	-	0.2	0.35

Table 3.6.: Comparison of computed time-averaged drag coefficient, $\overline{C}_d$, and Strouhal numbers, St-1 and St-2, at $Re = 1000$ with other studies.

3.6.1.3. FIV of an elastically-mounted sphere

To validate the *vivIcoFoam* solver developed for FIV simulations, a set of simulations were conducted on VIV of a circular cylinder with parameters chosen from Leontini *et al.* (2006*b*). As section 3.2 of chapter 4 and section 3.2 of chapter 5 describe, the results computed for the maximum amplitude, the peak lift coefficient, frequency ratio, and the averaged phase angle are in a good agreement with Leontini *et al.* (2006*b*). This study provides confidence in the new solver.

3.6.2. Grid-independence analysis

3.6.2.1. FIV of an elastically-mounted sphere

To study the sensitivity of the solution to grid refinement, two grid independence analyses were conducted at $Re = 300$ and $U^* = 7$, and $Re = 800$ and $U^* = 6$, as described in section 3.3 of chapter 4. In both of these cases, a large amplitude VIV response was observed. The results obtained for the r.m.s. value of the response amplitude, time-averaged drag coefficient, the r.m.s. values of the fluctuating components of the drag and lift coefficients and the frequency ratio were in a good agreement for grids 2, 3 and 5 (see section 3.3 of chapter 4 for more detail). Therefore, grid 2, being the smallest grid, was used to obtain the results presented in chapter 4.

Grid 2 was used for the study presented in chapter 5 as well. To verify this grid is fine enough to resolve the flow in FIV simulations of transversely rotating spheres, a grid sensitivity analysis was performed at $Re = 300$, $\alpha = 1.5$ and $U^* = 6$ as well. In this case, the flow was steady. Therefore, the time-averaged sphere position, time-averaged drag and lift coefficients were calculated. As table 2 of chapter 5 shows, the results obtained for grids 2, 3 and 5 agree well with each other (see section 3.3 of chapter 5). This provides an additional validation on grid refinement.

3.6.2.2. FIV of a tethered sphere

The sensitivity of the solution to the spatial resolution was investigated at $Re = 1200$ and $m^* = 0.8$ for $U^* = 6.5$ and 9. These two reduced velocities were chosen to represent modes I and II states, respectively. The r.m.s. of the response amplitude, A^*, the time-averaged drag coefficient, $\overline{C}_d$, the Strouhal number, St, and the frequency ratio, $f^* = f/f_n$, were calculated with each grid, and the results are tabulated in table 3.7. As can be seen, the results match reasonably well with each other for all five grids at both reduced velocities, as a result of employing finer grids in each case. The percentage error difference of all of the quantities for the different grids is at most 3%. Grid 3 was chosen for the simulations, as it is concentrated nodes toward the sphere and better captured the boundary layers.

3.6.3. Time step dependence

To achieve temporal accuracy and numerical stability, the Courant condition needs to be satisfied, *i.e.* the time step, δt, should be selected such that the Courant number is less than unity. The Courant number is defined for one cell as

$$Co = \frac{\delta t |\boldsymbol{u}|}{\delta x}, \tag{3.40}$$

where $|\boldsymbol{u}|$ is the magnitude of the velocity through that cell and δx is the cell size in the direction of the velocity. The smallest cell thickness of the grid is $0.002D$ for a cell at

	$U^* = 6.5$				$U^* = 9$			
Grid	A^*	$\overline{C}_d$	St	f^*	A^*	$\overline{C}_d$	St	f^*
Grid 1	0.56	0.73	0.15	0.96	0.83	0.83	0.12	1.05
Grid 2	0.57	0.73	0.15	0.96	0.83	0.81	0.12	1.05
Grid 3	0.57	0.73	0.15	0.96	0.83	0.82	0.12	1.05
Grid 4	0.58	0.73	0.15	0.96	0.83	0.82	0.12	1.05
Grid 5	0.57	0.73	0.15	0.96	0.81	0.81	0.12	1.05

Table 3.7.: The sensitivity of the spatial resolution of the flow parameters of vortex-induced vibration of a tethered sphere at $Re = 1200$ and $m^* = 0.8$ for $U^* = 6.5$ (mode I) and 9 (mode II). The oscillation amplitude of the sphere, A^*, the time-mean drag $\overline{C}_d$, Strouhal number, St, and the ratio of vortex shedding frequency to the natural frequency, $f^* = f/f_n$, are listed.

	$(\alpha, U^*) = (0, 7)$					$(\alpha, U^*) = (1.5, 6)$		
Time step	A^*	$\overline{C}_d$	$C_{d,rms}$	$C_{l,rms}$	f/f_n	$\overline{Y}/D$	$\overline{C}_d$	$\overline{C}_l$
$0.005D/U$	0.37	0.80	0.05	0.11	0.93	0.14	1.04	0.60
$0.0025D/U$	0.38	0.80	0.05	0.11	0.93	0.14	1.05	0.60

Table 3.8.: The sensitivity of the temporal resolution of the flow parameters of vortex-induced vibration of a rotating sphere at $(\alpha, U^*) = (0, 7)$ and $(1.5, 6)$, $Re = 300$ and $m^* = 2.865$. The oscillation amplitude of the sphere, A^*, the time-mean sphere displacement, $\overline{Y}/D$, the time-mean drag and lift coefficients, $\overline{C}_d$ and $\overline{C}_l$, the r.m.s. values of fluctuation component of the drag and lift coefficients, $C_{d,rms}$ and $C_{l,rms}$, and the ratio of vortex shedding frequency to the natural frequency, f/f_n, are listed.

the sphere surface. Thus, the time step should be less than $0.002D/|\boldsymbol{u}|$, to satisfy the Courant condition for the entire grid. As the cell velocities at the sphere boundary are $\lll U$, $\delta t = 0.005D/U$ was used as the time step for the majority of simulations. To verify this chosen time step is small enough for the simulations, two sets of simulations were conducted at $(\alpha, U^*) = (0, 7)$ and $(1.5, 6)$, $Re = 300$ and $m^* = 2.865$ by halving the time step, as shown in table 3.8. The results obtained for $\delta t = 0.0025D/U$ do not significantly vary from the values calculated for $\delta t = 0.005D/U$, providing a validation of the temporal accuracy.

3.7. Summary

In this chapter, we demonstrate the numerical methodology used for the results presented in this thesis. In summary, the CFD package OpenFOAM was utilised for the simulations. It was identified that solving the fully coupled fluid-structure system with a non-deformable mesh is more computationally efficient than using a dynamic grid technique or immersed boundary method. Therefore, two new fluid-structure interaction solvers were developed for the FIV problems, depending on the mounting method of the solid body (with elastic supports or using a tether). Five finer grids were generated using the Ansys ICEM CFD package and converted to the OpenFOAM format. Results were found to be independent of the grids. The values calculated for the time-mean drag and lift coefficients, and the Strouhal number, for the non-FIV simulations agreed well with the results of previous studies. In addition, the new solvers were validated for use with the FIV simulations.

Be the change that you wish to see in the world.

Mahatma Gandhi

4. Flow-induced vibration of an elastically-mounted sphere

In the field of flow-induced vibration, a concrete understanding has been developing on spherical bodies. The contribution of the experimental studies conducted at greater Reynolds numbers is considerably higher compared to the numerical studies focused on low Reynolds numbers. As a result, there exist a lot of unanswered FIV problems associated with low Reynolds number flows, especially with elastically-mounted spheres. The experimental study of Govardhan & Williamson (2005) revealed that the effect of Reynolds number on the FIV of a sphere was negligible over the range $2000 < Re < 12000$. However, the sphere responses observed by the computational studies of Behara *et al.* (2011) and Behara & Sotiropoulos (2016) at $Re = 300$ were significantly different from the experimental observations of Govardhan & Williamson (1997); Williamson & Govardhan (1997); Jauvtis *et al.* (2001); Govardhan & Williamson (2005). In addition, the majority of studies were based on a tethered sphere, although there are some dissimilarities between the FIV of a tethered sphere and an elastically-mounted sphere. Thus, to enhance the knowledge of FIV, this chapter presents the investigation of flow-induced vibration of a sphere mounted with elastic supports in a direction transverse to the free stream. The content of the chapter is the following Journal of Fluid Mechanics article reproduced with the permission

Rajamuni, M. M., Thompson, M.C. & Hourigan, K. 2018 Transverse flow-induced vibrations of a sphere. *Journal of Fluid Mechanics* **837**, 931–966.

We found that the characteristics of the FIV of a sphere are highly dependent on the Reynolds number, as well as the reduced velocity, with the two sets of simulations conducted at $Re = 300$ and 800 over the reduced velocity ranges $3.5 \leq U^* \leq 100$ and $3 \leq U^* \leq 50$, respectively. Over the modes I and II ranges, the sphere showed a periodic vibration response at each Reynolds number. Here, the sphere response amplitude increased and the synchronization regime widened as the Reynolds number increased from 300 to 800. The sphere response at $Re = 800$ was more similar to that observed in the experimental studies. The sphere response at higher reduced velocities was completely different at these two Reynolds numbers. The sphere showed intermittent bursts of vibration at $Re = 800$ for $U^* > 14$, while it vibrated with a small amplitude at $Re = 300$

over the ranges, $13 \leq U^* \leq 16$ and $26 \leq U^* \leq 100$ through a new time-mean position. This indicates that the effect of Reynolds number is even higher in the low frequencies.

J. Fluid Mech. (2018), *vol.* 837, *pp.* 931–966. © Cambridge University Press 2018 931
doi:10.1017/jfm.2017.881

Transverse flow-induced vibrations of a sphere

Methma M. Rajamuni[1,†], Mark C. Thompson[1] and Kerry Hourigan[1]

[1]Fluids Laboratory for Aeronautical and Industrial Research (FLAIR), Department of Mechanical and Aerospace Engineering, Monash University, Clayton, Victoria 3800, Australia

(Received 8 January 2017; revised 21 November 2017; accepted 4 December 2017)

Flow-induced vibration of an elastically mounted sphere was investigated computationally for the classic case where the sphere motion was constrained to move in a direction transverse to the free stream. This study, therefore, provides additional insight into, and comparison with, corresponding experimental studies of transverse motion, and distinction from numerical and experimental studies with specific constraints such as tethering (Williamson & Govardhan, *J. Fluids Struct.*, vol. 11, 1997, pp. 293–305) or motion in all three directions (Behara *et al.*, *J. Fluid Mech.*, vol. 686, 2011, pp. 426–450). Two sets of simulations were conducted by fixing the Reynolds number at $Re = 300$ or 800 over the reduced velocity ranges $3.5 \leqslant U^* \leqslant 100$ and $3 \leqslant U^* \leqslant 50$ respectively. The reduced mass of the sphere was kept constant at $m_r = 1.5$ for both sets. The flow satisfied the incompressible Navier–Stokes equations, while the coupled sphere motion was modelled by a spring–mass–damper system, with damping set to zero. The sphere showed a highly periodic large-amplitude vortex-induced vibration response over a lower reduced velocity range at both Reynolds numbers considered. This response was designated as branch A, rather than the initial/upper or mode I/II branch, in order to allow it to be discussed independently from the observed experimental response at higher Reynolds numbers which shows both similarities and differences. At $Re = 300$, it occurred over the range $5.5 \leqslant U^* \leqslant 10$, with a maximum oscillation amplitude of $\approx 0.4D$. On increasing the Reynolds number to 800, this branch widened to cover the range $4.5 \leqslant U^* \leqslant 13$ and the oscillation amplitude increased (maximum amplitude $\approx 0.6D$). In terms of wake dynamics, within this response branch, two streets of interlaced hairpin-type vortex loops were formed behind the sphere. The upper and lower sets of vortex loops were disconnected, as were their accompanying tails. The wake maintained symmetry relative to the plane defined by the streamwise and sphere motion directions. The topology of this wake structure was analogous to that seen experimentally at higher Reynolds numbers by Govardhan & Williamson (*J. Fluid Mech.*, vol. 531, 2005, pp. 11–47). At even higher reduced velocities, the sphere showed distinct oscillatory behaviour at both Reynolds numbers examined. At $Re = 300$, small but non-negligible oscillations were found to occur (amplitude of $\approx 0.05D$) within the reduced velocity ranges $13 \leqslant U^* \leqslant 16$ and $26 \leqslant U^* \leqslant 100$, named branch B and branch C respectively. Moreover, within these reduced velocity ranges, the centre of motion of the sphere shifted from its static position. In contrast, at $Re = 800$, the sphere showed an aperiodic intermittent mode IV vibration state immediately beyond branch A, for $U^* \geqslant 14$. This vibration state was designated as the intermittent branch. Interestingly, the dominant frequency of the sphere vibration was close to the natural

† Email address for correspondence: methma.rajamuni@monash.edu

frequency of the system, as observed by Jauvtis *et al.* (*J. Fluids Struct.*, vol. 15(3), 2001, pp. 555–563) in higher-mass-ratio higher-Reynolds-number experiments. The oscillation amplitude increased as the reduced velocity increased and reached a value of $\approx 0.9D$ at $U^* = 50$. The wake was irregular, with multiple vortex shedding cycles during each cycle of sphere oscillation.

Key words: aerodynamics, computational methods, flow–structure interactions

1. Introduction

Over many years, considerable research effort has been directed to examining the nature of fluid–structure interaction (FSI). This is due to its practical importance to many fields where coupled interactions between a fluid flow and solid-body motion can occur. One of the most crucial phenomena associated with FSI is flow-induced vibration (FIV), which is the oscillatory response of a coupled fluid–structure system due to fluid forcing. Vortex-induced vibration, or VIV, is a category of FIV, occurring through the synchronization of structural vibration with wake unsteadiness, typically vortex shedding. Fatigue damage, or even catastrophic structural failure, can result from FIV. Thus, for structural design, it is always important to consider such possible resonant interactions. Aircraft, marine vessels, submarines, ground vehicles, chimneys and bridges are good examples of relevant engineering systems. Fundamental understanding of VIV has been revealed through experimental and numerical research studies for generically shaped bodies, with major findings summarized in, e.g., Parkinson (1989), Sarpkaya (2004), Williamson & Govardhan (2004, 2008) and Wu, Ge & Hong (2012). While most research conducted has been based on cylindrical structures, especially circular cylinders, numerous applications involve three-dimensional body shapes, including spherical bodies.

Key features of VIV of a sphere were revealed through experiments by Williamson & Govardhan (1997). They found that a tethered sphere oscillates strongly at a transverse saturation amplitude of close to two diameters peak to peak. In line with previous studies of VIV of a circular cylinder, they recognized that plotting the amplitude response versus the reduced velocity, $U^* = U/f_nD$, where U is the free-stream velocity, f_n is the natural frequency of the system and D is the sphere diameter, was more suitable for interpreting and classifying the behaviour than using the amplitude response versus the Reynolds number. They observed that the transverse oscillation is dominant compared with the streamwise oscillation and that the streamwise oscillation frequency is twice that of the transverse oscillation. They also observed that there were two different modes of oscillation, namely modes I and II. Both two modes appeared within the reduced velocity range $U^* \sim 5$–10, and the body oscillation frequency, f, was close to the static body vortex shedding frequency, f_{vo} ($f_{vo}/f \sim 1$); this clearly indicated that these vibrations were induced from vortex shedding behind the sphere. However, there was no clear boundary between mode I and mode II in the amplitude response diagram of VIV of a sphere, contrary to the amplitude response of a cylinder, which has distinct initial, upper and lower branches. Later, the question of how mode II differed from mode I was answered by Govardhan & Williamson (2005) by examining the vortex phase, ϕ_{vo}. The vortex phase is the phase difference between the vortex force on the sphere and the sphere displacement. They found that there was approximately a 90° phase shift between modes I and II.

In addition to the first two modes of vibration observed with light spheres ($m^* < 1$, where m^* is the density ratio between solid and fluid) by Williamson & Govardhan (1997), Jauvtis, Govardhan & Williamson (2001) found that there existed another mode of vibration (mode III) which appeared within the reduced velocity range $U^* \sim 20$–40 for heavy (tethered) spheres ($m^* \gg 1$). For mode III vibration, it was found that the principal vortex shedding frequency was three to eight times higher than the sphere vibration frequency. Therefore, they stressed that this vibration phenomenon was difficult to explain by classical 'lock-in' theories. Later, Govardhan & Williamson (2005) argued that, in the absence of any body vibration in mode III, there would be no fluid forcing at the natural frequency of the system. However, if the body were to be perturbed, it could generate a self-sustaining vortex force that could amplify, leading to body vibrations of large amplitudes. They categorized mode III as 'movement-induced excitation' (Naudascher & Rockwell 2012). Jauvtis *et al.* (2001) also observed another mode of regular vibration, mode IV, as the reduced velocity was further increased to the range $U^* > 100$. In this mode, the sphere oscillation frequency was not regular and periodic as it was in the first three modes, but, interestingly, the main frequency component was very close to the natural frequency.

Govardhan & Williamson (2005) used digital particle image velocimetry (DPIV) to observe the formation of a chain of hairpin-type vortex loops on both sides of the wake behind the sphere for both modes I and II. Furthermore, they observed a change in the timing of vortex shedding relative to body motion once it passed from mode I to II, consistent with their observation of a change of vortex phase between these modes. They identified that for a sphere undergoing VIV, there was a preferred orientation of the loops to maintain a symmetry with the plane containing the principal transverse vibrations. For mode III vibrations, they observed a two-sided chain of trailing vortex pairs locked to the body oscillation frequency. In related work, Brücker (1999) investigated the nature of freely rising air bubbles in water. The bubbles showed spiralling, zigzagging and rocking motions during their rise in water according to the diameters of the bubbles. For a zigzagging bubble, an alternate oppositely oriented hairpin-type wake structure was observed, similar to the observation of Govardhan & Williamson (2005) for mode I and II vibrations. For a spiralling bubble, a steady wake was observed, which wound in a helical path.

Pregnalato (2003) numerically investigated the FIV of a tethered sphere at a Reynolds number of 500 for two mass ratios, $m^* = 0.082$ and $m^* = 0.8$. He observed three modes of vibration, corresponding to the last three modes of vibration characterized by Jauvtis *et al.* (2001). In the study of Pregnalato (2003), the sphere exhibited mode II vibration in the reduced velocity range $U^* = 5$–10, and mode III vibration for $U^* > 10$ for both mass ratios. Mode II and III vibrations were highly sinusoidal, similarly to the experimental studies. He observed mode IV vibration with the higher mass ratio, $m^* = 0.8$, sphere. However, for the low mass ratio, mode IV was not observed, regardless of the reduced velocity. Recently, Lee, Hourigan & Thompson (2013) studied VIV of a neutrally buoyant ($m^* = 1$) tethered sphere constrained to move on a spherical surface, which may be considered as locally planar for small vibration amplitudes relative to the tether length. This was a combined numerical and experimental study, covering the Reynolds number range $Re = 50$–12 000. They distinguished seven broad and relatively distinct sphere oscillation regimes and characteristic wake structures.

Behara, Borazjani & Sotiropoulos (2011) investigated VIV of a sphere through numerical simulations. As distinct from the current study, the sphere was mounted

on elastic supports, allowing movement in all three spatial directions, with the Reynolds number set to $Re = 300$, reduced mass $m_r = 2$, for the reduced velocity range $U^* = 4$–9. They observed two distinct branches of the response curve in the synchronization regime, each corresponding to a distinct type of wake structure, identified as hairpin and spiral vortices. The oscillation amplitude was lower in the hairpin branch compared with the spiral branch. When the wake was in the hairpin shedding mode, the sphere moved along a linear path in the transverse plane, while when spiral vortices were being shed, the sphere vibrated on a circular orbit. Furthermore, under VIV on the spiral mode branch, they observed hysteresis in the response amplitude at the beginning of the synchronization regime. More recently, Behara & Sotiropoulos (2016) extended this numerical study by expanding the reduced velocity range to $U^* = 0$–13. They observed that the lock-in regime was $U^* = 5.8$–12.2 for the spiral mode and $U^* = 4.8$–8 for the hairpin mode. The hairpin mode was found to become unstable and merge with the response curve of the spiral mode at $U^* = 9$. They also studied the effect of Reynolds number on VIV at a fixed reduced velocity, $U^* = 9$. They found that the synchronized oscillation persisted up to $Re = 1000$, although the sphere trajectory and wake structures were strongly dependent on the Reynolds number. The spiral wake observed at $Re = 300$ underwent a transition to a hairpin wake in the Reynolds number range $Re = 500$–600. During this transition, the sphere trajectories on the transverse plane changed from circular to elliptic orbits.

In many previous studies of a tethered sphere wake (Williamson & Govardhan 1997; Pregnalato 2003; Govardhan & Williamson 2005), researchers have observed that the transverse oscillation was of higher amplitude than the streamwise oscillation. Even though computational studies have been reported previously on VIV of a sphere allowed to move in all three spatial directions (Behara *et al.* 2011; Behara & Sotiropoulos 2016), surprisingly little effort appears to have been directed towards simulating the reference case of VIV of a sphere free to move only in the transverse direction. Therefore, this is the case considered in the present study. To gain a better insight, two different Reynolds numbers were chosen for this investigation, namely $Re = 300$ and 800. The Reynolds number of 300 was chosen because a static sphere experiences unsteady vortex shedding at $Re = 300$, and, in previous numerical studies, Behara *et al.* (2011) and Behara & Sotiropoulos (2016) observed large-amplitude vibrations at this Reynolds number. The Reynolds number of 800 was chosen since both a static and a tethered sphere show irregular vortex shedding at this Reynolds number (e.g. see Lee *et al.* 2013). Moreover, simulations at $Re = 800$ enable more relevant comparison with experimental studies conduced at higher Reynolds numbers. A mass ratio of $m^* = 2.685$ was chosen for this study, which is equivalent to a reduced mass of $m_r = 1.5$. This is representative of the lower end of mass ratios that have been used for cylinder and sphere VIV experiments in water (e.g. Carberry, Sheridan & Rockwell 2001; Williamson & Govardhan 2004; Govardhan & Williamson 2005; Wong *et al.* 2017; Sareen *et al.* 2018). Wide ranges of reduced velocity were considered to improve the understanding of FIV. In particular, $U^* = 3.5$–100 and 3–50 were chosen at $Re = 300$ and 800 respectively. Finally, very long integration times were used to gain a better understanding of the asymptotic system response, as it was observed that some non-asymptotic states can be maintained for significant times and yet may eventually evolve to different final states.

The structure of the paper is organized as follows: the numerical methods used are presented in § 2; verification and validation of the numerical method and implementation are presented in § 3; the predicted FIVs of a sphere at $Re = 300$

are discussed in § 4; effects of Reynolds number on FIV of a sphere are discussed in § 5 with results obtained at $Re = 800$, including comparisons with previous work; concluding remarks are made in § 6.

2. Numerical approach

The numerical method employed in this study is based on the open-source CFD package OpenFOAM. This package is capable of handling a wide range of flows. It also comes with a built-in dynamic mesh technique that enables the solution of FSI problems (as Ding, Bernitsas & Kim (2013), Habchi *et al.* (2013) and Wu, Bernitsas & Maki (2014) used in their studies). Dynamic mesh techniques are generally expensive since the mesh is deformed according to the solid-body motion during each time step. However, for VIV of a single body, the efficiency of solving the coupled fluid–solid system can be improved by choosing a non-deformable moving mesh, as adopted by Blackburn & Henderson (1996), Leontini *et al.* (2006*a*), Leontini, Thompson & Hourigan (2006*b*) and Leontini, Lo Jacono & Thompson (2013). Therefore, instead of using the built-in dynamic mesh technique, a new solver was developed to treat the coupled fluid–solid system with a non-deformable mesh. This approach is considerably more efficient than the dynamic mesh technique. The FSI system and the FSI solver are discussed in detail in the following two subsections.

2.1. *Governing equations*

Fluid flow was modelled in the moving reference frame attached to the centre of the sphere. This is a non-inertial frame since it accelerates according to the sphere motion. Thus, the fluid momentum equations need to be adjusted accordingly. This can be achieved by adding the acceleration of the sphere to the momentum equation on the right-hand side, acting as a fictitious force in the opposite direction. The fluid is assumed to be incompressible and viscous, while the motion of the sphere is assumed to behave as a spring–mass–damper system. The coupled fluid–solid system can be described by the Navier–Stokes equations, given by (2.1) and (2.2), together with the governing motion of the sphere, given by (2.3),

$$\frac{\partial \boldsymbol{u}}{\partial t} + (\boldsymbol{u} \cdot \nabla)\boldsymbol{u} = -\frac{1}{\rho}\nabla p + \nabla \cdot (\nu \nabla \boldsymbol{u}) - \ddot{\boldsymbol{y}}_s, \tag{2.1}$$

$$\nabla \cdot \boldsymbol{u} = 0, \tag{2.2}$$

$$m\ddot{\boldsymbol{y}}_s + c\dot{\boldsymbol{y}}_s + k\boldsymbol{y}_s = \boldsymbol{f}_l. \tag{2.3}$$

Here, $\boldsymbol{u} = \boldsymbol{u}(x, y, z, t)$ is the velocity vector field in the moving frame, p is the scalar pressure field, ρ is the fluid density, ν is the kinematic viscosity, and $\boldsymbol{y}_s$, $\dot{\boldsymbol{y}}_s$ and $\ddot{\boldsymbol{y}}_s$ are the sphere displacement, velocity and acceleration vectors respectively. In addition, m is the mass of the sphere, c is the damping constant, k is the structural spring constant and $\boldsymbol{f}_l$ is the flow-induced integrated vector force acting on the sphere due to pressure and viscous shear forces acting on the body surface.

2.2. *The fluid–structure solver*

A new fully coupled FSI solver (named vivicoFoam) was developed, based on the 'icoFoam' solver for laminar flows, to solve the coupled fluid–solid system defined by (2.1)–(2.3). This solver employs a predictor–corrector iterative method, which

predicts the solid motion explicitly in the first iteration and then corrects it as necessary through several corrector iterations. Once an approximation to the solid motion is known (from the predictor or a previous corrector step), the Navier–Stokes equations are solved using the PISO algorithm (introduced by Issa 1986). The details of the predictor and corrector iterations at the $(n+1)$th time step are as follows.

In the predictor iteration, initially, the sphere acceleration, $\ddot{\boldsymbol{y}}_s$, is predicted explicitly using stored accelerations at previous time steps, based on third-order polynomial extrapolation,

$$\ddot{\boldsymbol{y}}_s^{(n+1)} = 3\,\ddot{\boldsymbol{y}}_s^{(n)} - 3\,\ddot{\boldsymbol{y}}_s^{(n-1)} + \ddot{\boldsymbol{y}}_s^{(n-2)}. \tag{2.4}$$

Once the sphere acceleration, $\ddot{\boldsymbol{y}}_s$, is known, the Navier–Stokes equations can be solved. However, before proceeding to solve these equations, the sphere velocity, $\dot{\boldsymbol{y}}_s$, and displacement, $\boldsymbol{y}_s$, are estimated by integrating the predicted $\ddot{\boldsymbol{y}}_s$ and estimated $\dot{\boldsymbol{y}}_s$ by a third-order Adams–Moulton method by

$$\dot{\boldsymbol{y}}_s^{(n+1)} = \dot{\boldsymbol{y}}_s^{(n)} + \frac{\delta t}{12}(5\,\ddot{\boldsymbol{y}}_s^{(n+1)} + 8\,\ddot{\boldsymbol{y}}_s^{(n)} - \ddot{\boldsymbol{y}}_s^{(n-1)}) \tag{2.5}$$

and

$$\boldsymbol{y}_s^{(n+1)} = \boldsymbol{y}_s^{(n)} + \frac{\delta t}{12}(5\,\dot{\boldsymbol{y}}_s^{(n+1)} + 8\,\dot{\boldsymbol{y}}_s^{(n)} - \dot{\boldsymbol{y}}_s^{(n-1)}) \tag{2.6}$$

respectively, where δt is the time step. At the end of the predictor step, the Navier–Stokes equations are solved with the predicted $\ddot{\boldsymbol{y}}_s$, and the fluid force exerted on the sphere is calculated for the following corrector iteration.

In the corrector iteration, $\ddot{\boldsymbol{y}}_s$ is corrected with the values of $\boldsymbol{y}_s$, $\dot{\boldsymbol{y}}_s$ and $\boldsymbol{f}_l$ calculated in the predictor or the previous corrector step by

$$\ddot{\boldsymbol{y}}_s^{(n+1)} = -\frac{c}{m}\dot{\boldsymbol{y}}_s^{(n+1)} - \frac{k}{m}\boldsymbol{y}_s^{(n+1)} + \frac{1}{m}\boldsymbol{f}_l^{(n+1)}. \tag{2.7}$$

Then, the correct values of $\dot{\boldsymbol{y}}_s$ and $\boldsymbol{y}_s$ are updated using (2.5) and (2.6) with the corrected $\ddot{\boldsymbol{y}}_s$. Subsequently, the Navier–Stokes equations are solved with the corrected $\ddot{\boldsymbol{y}}_s$, and the fluid force exerted on the sphere is calculated. Several corrector steps are performed until the magnitudes of the fluid force and the solid acceleration converge to within given error bounds.

It should be recalled that the fluid domain is modelled in a moving frame of reference. The motion of this reference frame is acknowledged through the outer domain velocity boundary conditions (except for the outlet boundary). In this study, all of the outer boundaries except for the outlet have velocities prescribed on them. Once the predictor–corrector iterative process is completed, the velocity boundary conditions are updated according to the sphere velocity, $\dot{\boldsymbol{y}}_s$, before proceeding to the next time step.

2.3. *Mesh and domain details*

A uniform flow in the x direction with magnitude U past an elastically mounted sphere of diameter D, restricted to translate in the y axis, was simulated numerically using the newly built FSI solver described above. As shown in figure 1, a cubic domain

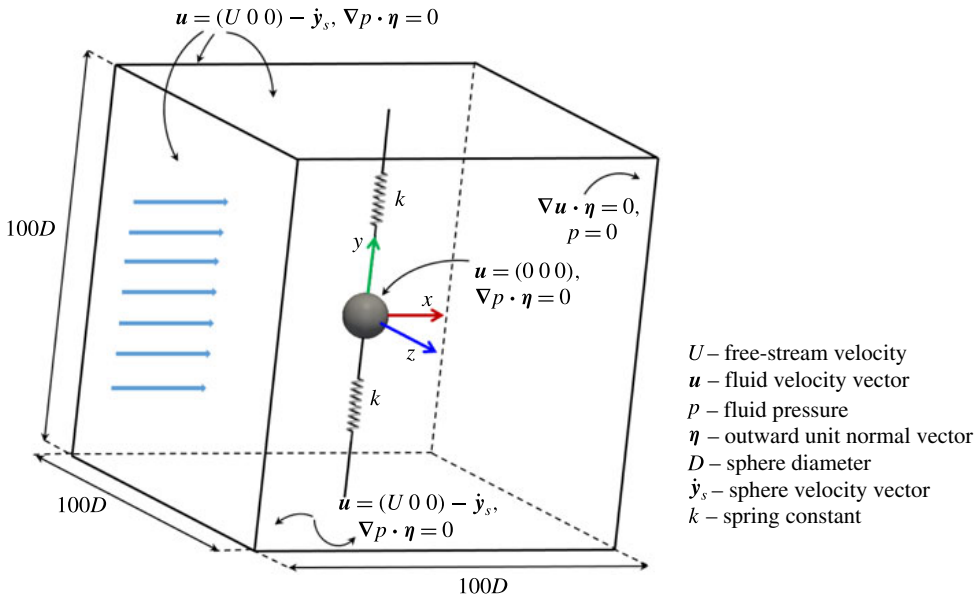

FIGURE 1. (Colour online) Schematic of the computational domain and boundary conditions.

with a side length of $100D$ was chosen for the computational domain with the sphere at its centre. In this study, the sphere motion was assumed to behave as a spring–mass system with zero damping constant to obtain the highest vibration amplitude. In the FSI solver, $\boldsymbol{y}_s$, $\dot{\boldsymbol{y}}_s$, $\ddot{\boldsymbol{y}}_s$ and $\boldsymbol{f}_l$ were treated as vectors with zero x and z components since the sphere motion was restricted to the y direction. At the inlet and sphere boundaries, a Dirichlet boundary condition was prescribed for the velocity, while a zero-gradient Neumann boundary condition was prescribed for the pressure, as shown in figure 1. At the sphere surface, no-slip and no-penetration boundary conditions were applied. At the outlet boundary, the pressure was set to zero while the velocity was prescribed as zero gradient in the surface normal direction.

A block-structured grid was generated using Ansys-ICEM-CFD for the fluid domain, as shown in figure 2. A cubic block, with a side length of $5D$, was placed around the sphere and was decomposed into six square frustums, as shown in figure 2(*b*). In each square frustum, exponentially distributed nodes were assigned in the radial direction to achieve high concentration near the sphere surface (see figure 2*c*). In order to resolve the wake structures behind the sphere, a large number of grid points were assigned in the downstream direction. To examine the sensitivity of the computed solutions to grid refinement (see the next section), four successively finer grids were employed. The first three grids were generated by keeping the number of cells at the sphere surface, N, constant. Grid 1 employed $\simeq$0.79 million cells. In grid 1, the minimum cell thickness in the radial direction from the sphere surface, δl, was $0.011D$. The second grid (grid 2) was generated by decreasing δl to $0.004D$. This yielded $\simeq$1.25 million cells, with approximately 10–16 cells within the boundary layer before flow separation. This was sufficient to resolve the flow in the near wake. However, a third grid (grid 3) was generated by further decreasing δl to $0.002D$ with the same number of cells as grid 2, to determine the effect of δl on the solution. Finally, grid 4 was generated by increasing the number of cells at the sphere surface with $\delta l = 0.004D$ to observe the effect of cell thickness in the tangential direction on the solution. This yielded $\simeq$2.57 million cells. The time step, δt, used for each grid was $0.005D/U$.

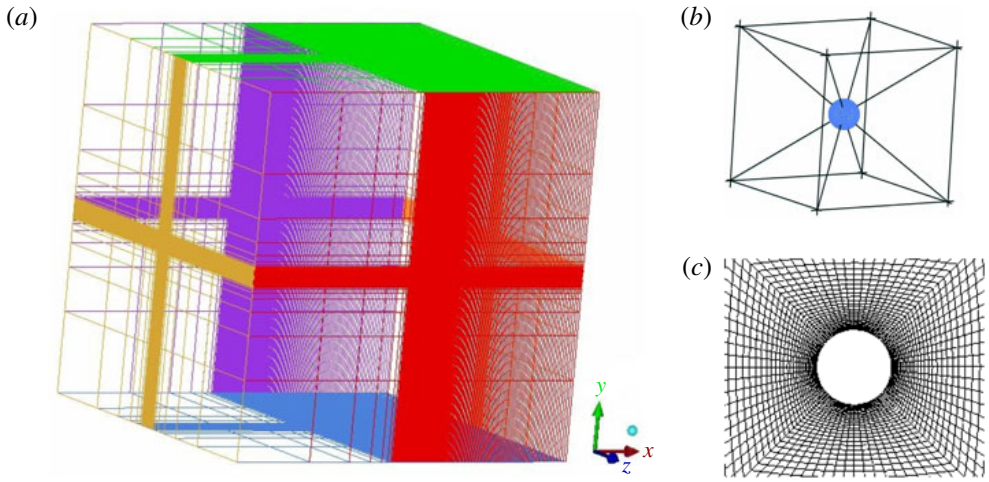

FIGURE 2. (Colour online) The unstructured-grid computational domain: (*a*) isometric view; (*b*) the cubic block placed around the sphere, which was decomposed into six square frustums; (*c*) grid near the sphere surface at the *x*–*y* plane.

Study	$\overline{C}_d$	$\overline{C}_l$	St
Present study	0.665	0.070	0.137
Poon *et al.* (2010)	0.658	0.067	0.134
Giacobello, Ooi & Balachandar (2009)	0.658	0.067	0.134
Kim (2009)	0.658	0.067	0.134
Kim, Kim & Choi (2001)	0.657	0.067	0.137
Constantinescu & Squires (2000)	0.665	0.065	0.136
Johnson & Patel (1999)	0.656	0.069	0.137

TABLE 1. Comparison of computed time-averaged drag coefficient, $\overline{C}_d$, time-averaged lift coefficient, $\overline{C}_l$, and Strouhal number, St, at $Re = 300$ with other numerical studies.

3. Numerical sensitivity and validation studies

This section presents verification and validation studies. The first study aims to verify that the computational domain and mesh are adequate to capture the flow behind a stationary sphere at $Re = 300$ and validates against previous predictions. The second study is undertaken to validate the newly developed FSI solver for VIV studies. Finally, a mesh resolution study for the VIV of a sphere is also presented at the end of this section.

3.1. *Rigid sphere*

Flow past a rigidly mounted sphere was modelled using the non-VIV solver (which formed the basis of the VIV solver) at $Re = 300$. Calculated values for the time-averaged drag coefficient, $\overline{C}_d$, time-averaged lift coefficient, $\overline{C}_l$, and Strouhal number, St, are compared with other studies in table 1. The present results are in close agreement with literature values, generally falling within the narrow ranges of values from accepted benchmark studies (Johnson & Patel 1999; Constantinescu & Squires 2000; Kim *et al.* 2001; Giacobello *et al.* 2009; Kim 2009; Poon *et al.* 2010).

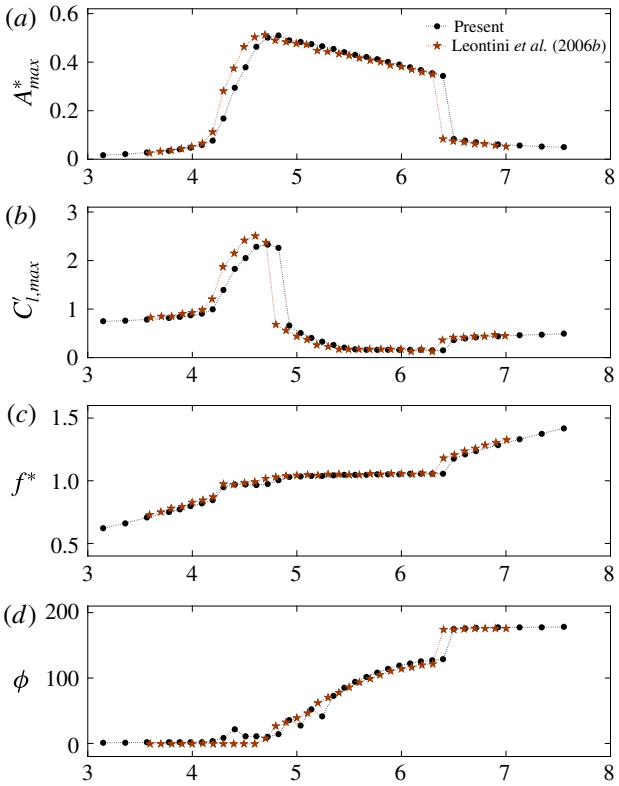

FIGURE 3. (Colour online) Response of an elastically mounted cylinder as a function of reduced velocity: $Re = 200$, $m^* = 10$, $\zeta = 0.01$. (*a*) Maximum oscillation amplitude, A^*_{max}; (*b*) peak lift coefficient, $C'_{l,max}$; (*c*) frequency ratio, $f^* = f/f_n$; (*d*) average phase angle between lift force and cylinder displacement, ϕ.

3.2. *Vortex-induced vibration of a circular cylinder*

To validate the new solver developed for general FSI problems, a set of simulations was conducted on the FIV of a circular cylinder with parameters chosen from Leontini *et al.* (2006*b*). The mass ratio was set to $m^* = 10$ and the damping ratio to $\zeta = 0.01$. (In this case, the cylinder displacement was modelled by a spring–mass–damper system.) The Reynolds number was $Re = 200$ and the reduced velocity range was $3 \leqslant U^* \leqslant 7.5$. Figure 3 compares current predictions for the maximum oscillation amplitude, A^*_{max}, the peak lift coefficient, $C'_{l,max}$, the frequency ratio, $f^* = f/f_n$, and the average phase angle between the lift force and the cylinder displacement, ϕ, with results from Leontini *et al.* (2006*b*); the results obtained are almost identical, with minor differences probably attributable to a slightly different blockage ratio, mesh resolution and/or convergence of the predictor–corrector iteration steps. This study provides confidence in the new solver.

3.3. *Resolution study*

All FSI simulations reported in this work were carried out on grid 2. To demonstrate that this grid was sufficient to resolve the flow in FSI simulations, grid sensitivity analysis was performed for the vibrating sphere case for the following two sets of parameters: $Re = 300$ and $U^* = 7$, and $Re = 800$ and $U^* = 6$, with a sphere

Re	Grid	δl	N	A^*	$\overline{C}_d$	$C'_{d,rms}$	$C'_{l,rms}$	f/f_n
300	grid 1 (0.79 million cells)	$0.011D$	7 350	0.38	0.81	0.05	0.11	0.93
300	grid 2 (1.25 million cells)	$0.004D$	7 350	0.37	0.80	0.05	0.11	0.93
300	grid 3 (1.25 million cells)	$0.002D$	7 350	0.37	0.80	0.05	0.10	0.93
300	grid 4 (2.57 million cells)	$0.004D$	18 150	0.37	0.80	0.05	0.10	0.93
800	grid 1 (0.79 million cells)	$0.011D$	7 350	0.52	0.76	0.12	0.31	0.93
800	grid 2 (1.25 million cells)	$0.004D$	7 350	0.52	0.75	0.12	0.31	0.93
800	grid 3 (1.25 million cells)	$0.002D$	7 350	0.52	0.75	0.12	0.31	0.93
800	grid 4 (2.57 million cells)	$0.004D$	18 150	0.51	0.75	0.12	0.32	0.92

TABLE 2. The sensitivity of the spatial resolution of the flow parameters of VIV of a sphere at $Re = 300$ and $U^* = 7$, and $Re = 800$ and $U^* = 6$ ($m^* = 2.865$ in each case). Here, δl is the minimum thickness of the cells (in the radial direction) on the sphere surface in each grid and N is the number of cells on the sphere surface. The root mean square (r.m.s.) value of the sphere oscillation amplitude, A^*, the time-averaged drag coefficient, $\overline{C}_d$, the r.m.s. values of the fluctuation components of the drag and lift coefficients, $C_{d,rms}$ and $C_{l,rms}$, and the ratio of the vortex shedding frequency to the natural frequency, f/f_n, are listed.

of $m^* = 2.865$. These U^* values were chosen because the sphere showed periodic oscillation with a large amplitude near these values. Table 2 compares the effect of grid refinement on the results for the r.m.s. value of the sphere oscillation amplitude, A^*, the force coefficients (time-averaged drag coefficient, $\overline{C}_d$, r.m.s. values of the fluctuation components of the drag and lift coefficients, $C'_{d,rms}$ and $C'_{l,rms}$) and the frequency ratio, $f^* = f/f_n$. It is noted that for this set of variables, there is less than a 3 % variation in the predictions between grids 1 and 2 over all variables for both $Re = 300$ and 800. Moreover, the results obtained from grids 2–4 are in a good agreement with one another. This suggests that further decrease of δl or increase of N will only affect the predictions weakly. Thus, this observation leads to the conclusion that grid 2 is sufficient for the VIV simulations, and, therefore, this grid was used to obtain all subsequently presented results.

4. Flow-induced vibration of a sphere at $Re = 300$

This section documents and discusses the results obtained for the flow past an elastically mounted sphere allowed to oscillate only along the y direction at a Reynolds number of $Re = 300$ and reduced mass of $m_r = 1.5$ (corresponding to a mass ratio of $m^* = 2.865$) over the reduced velocity range $3.5 \leqslant U^* \leqslant 100$. The Reynolds number of the flow was prescribed through the kinematic viscosity in (2.1) ($\nu = DU/Re$) and the reduced velocity was prescribed through the spring constant in the solid motion equation ($k = 4m\pi^2/U^{*2}$).

4.1. *Sphere response*

Figure 4 shows characteristics of the VIV response of the sphere in the reduced velocity range $3.5 \leqslant U^* \leqslant 100$ in terms of sphere oscillation amplitude, $A^* = \sqrt{2}\,Y_{rms}/D$, mean displacement of the sphere, $\overline{Y}/D$, and frequency ratio, $f^* = f/f_n$, where $Y = \boldsymbol{y_s} \cdot (0\,1\,0)$ is the displacement of the sphere in the y direction, f is the oscillation frequency of the sphere and f_n is the natural frequency of the system calculated

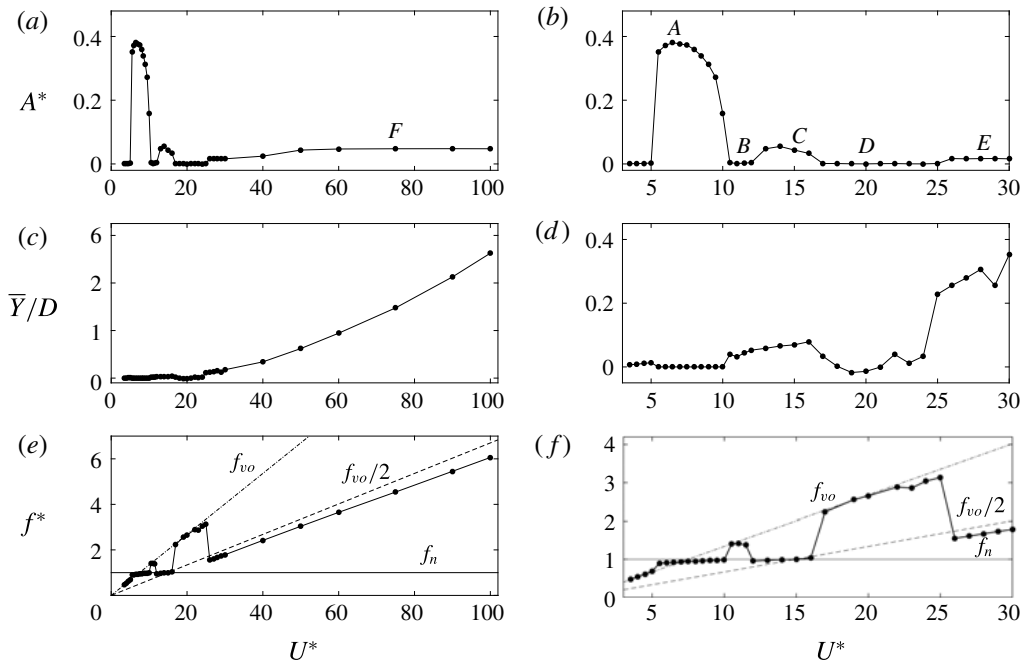

FIGURE 4. Response of an elastically mounted (on the y axis) sphere as a function of the reduced velocity, U^* (calculated without the added-mass effect), at $Re = 300$, $m^* = 2.865$; panels (a,c,e) show the results for $U^* = 3.5$–100 while (b,d,f) show enlarged views for $U^* = 3.5$–30: (a,b) sphere oscillation amplitude, A^*, (c,d) time-averaged non-dimensional sphere displacement, $\overline{Y}/D$, (e,f) oscillation frequency normalized by the system natural frequency, $f^* = f/f_n$. The letters (A, B, C, D, E and F) in (a) mark specific points along the response curve at which the time history of the sphere displacement is displayed in figure 5.

without the added-mass effect. As can be seen from figure 4(a,b), the sphere oscillated significantly, with a maximum oscillation amplitude of approximately $0.4D$, in the reduced velocity range $5.5 \leqslant U^* \leqslant 10$. Within this range, the sphere oscillation frequency was locked in with the vortex shedding frequency and close to the static body vortex shedding frequency, f_{vo}. Moreover, the sphere oscillation frequency was synchronized with the natural frequency of the system (figure 4e,f), confirming that this is a VIV response. This vibration state was designated as branch A.

Figure 4(c,d) displays the variation of the mean position of the sphere with reduced velocity. In the range $3.5 \leqslant U^* \leqslant 5$, where oscillations were very small, the mean position of the sphere was shifted away from its initial position by a small amount. This is consistent with the asymmetric wake of a stationary sphere at $Re = 300$ (e.g. Johnson & Patel 1999; Leweke *et al.* 1999; Ghidsera & Dusek 2000; Thompson, Leweke & Provansal 2001). Furthermore, in this reduced velocity range, the mean displacement of the sphere, $\overline{Y}/D$, increased as the reduced velocity, U^*, increased. However, once the sphere began to oscillate in the reduced velocity range $5.5 \leqslant U^* \leqslant 10$, it oscillated symmetrically about its initial position, yielding a zero time-mean displacement (see figure 4c,d). Moreover, the oscillations observed in branch A were purely sinusoidal, with zero offset (as the time history of sphere displacement, Y/D, shows in figure 5(a) at $U^* = 7$), suggesting that the wake was symmetrical in the oscillation plane.

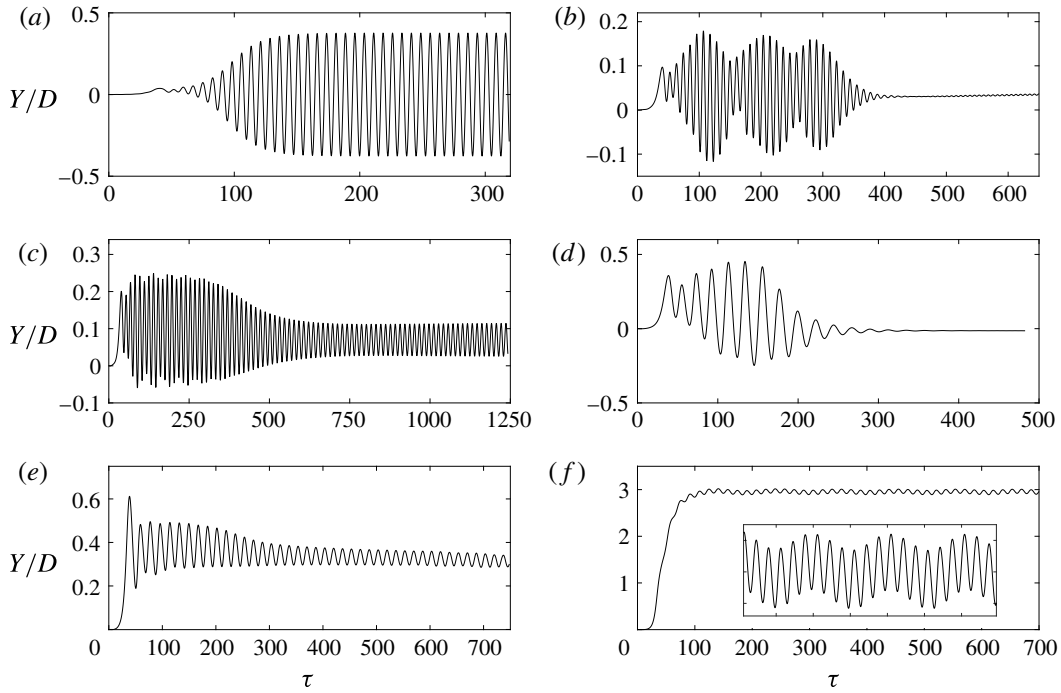

FIGURE 5. Time history of sphere displacement, Y/D, against non-dimensional time, $\tau = tU/D$: (*a*) case *A* at $U^* = 7$, (*b*) case *B* at $U^* = 10.5$, (*c*) case *C* at $U^* = 15$, (*d*) case *D* at $U^* = 20$, (*e*) case *E* at $U^* = 28$ and (*f*) case *F* at $U^* = 75$. See figure 4(*a*,*b*) for the locations of the points *A*–*F* along the sphere response curve.

The time history diagrams in figure 5 show that it takes many oscillation periods to reach the asymptotic system state. For example, in case *A*, the sphere began to oscillate at $\tau \simeq 60$, with the oscillation amplitude reaching its final value at $\tau \simeq 150$, where $\tau = t\,U/D$ is the non-dimensional time. In some cases (see below), the oscillation response can maintain a semi-stable state for many periods prior to relaxing towards the long-time asymptotic state. Hence, care is needed to ensure that the flow is integrated forward in time for long enough to reach the representative long-time system state.

In contrast to the sinusoidal responses observed for $U^* \leqslant 10$, quite different responses were observed for the reduced velocities $U^* > 10$. Furthermore, for each $U^* > 10$ case, varying sphere responses were observed at different time instances. Time histories of the sphere displacement at the points *B*, *C*, *D*, *E* and *F* (marked in figure 4(*a*,*b*) at $U^* = 10.5$, 15, 20, 28 and 75) are shown in figure 5(*b*), (*c*), (*d*), (*e*) and (*f*) respectively. Within the range $U^* \in [10.5\text{–}40]$, initially, the sphere oscillated with a maximum amplitude of approximately $0.15D$, but later the oscillation amplitude decreased greatly. Therefore, all of these cases required simulations over extended times until the solution became stable. In these cases, the time-mean position of the sphere moved away from its initial position by a considerable amount. In addition, over the initial evolution, the oscillation amplitude and the mean position of the sphere varied with the simulation time. Over that initial period, the oscillations were considerably weaker than the purely sinusoidal oscillations observed in branch A.

In the ranges $U^* \in [13\text{–}16]$ and $[26\text{–}100]$, the oscillation amplitude decreased to $\approx 0.05D$ and $0.015D$ respectively after reaching the asymptotic state; see figure 5(*c*,*e*).

However, these vibrations were notably periodic. In particular, the response range $13 \leqslant U^* \leqslant 16$ is designated branch B and the range $26 \leqslant U^* \leqslant 100$ is designated branch C. The sphere oscillation frequencies in both branches were locked in with the vortex shedding frequency. It is not clear that either of these two branches is directly analogous to the response branches observed in higher-Reynolds-number experiments. The sphere oscillation frequency for branch B was approximately equal to the system natural frequency, f_n; see figure 4(*e*,*f*). However, for branch C, the sphere oscillation frequency was not close to the natural frequency of the system, but was close to half of the static body vortex shedding frequency.

Weak initial oscillations in the reduced velocity ranges $U^* \in [10.5–12]$ and $U^* \in [17–25]$ eventually faded away, as shown in figures 5(*b*,*d*), leading to a minimally oscillatory final state. The reduced velocity ranges $U^* \in [3.5–5]$, [10.5–12] and [17–25] are desynchronization regimes where no significant sphere oscillations were observed (points *B* and *D* marked in figure 4*a*,*b*). In those three ranges, except for a few cases, sphere oscillations were observed with a very small amplitude ($\leqslant 0.005D$), and the sphere oscillation frequency was equal to the static body vortex shedding frequency, f_{vo}, as shown in figure 4(*e*,*f*).

In both branches B and C, the time-mean displacement of the sphere increased as the reduced velocity increased (see figure 4*c*,*d*). However, there was not any clear pattern in the mean displacement over the reduced velocity ranges $U^* \in [10.5–12]$ and [17–25], where no oscillations were observed. When the reduced velocity was increased further from 30 to 100, the sphere shifted away from its initial position by a substantial margin and oscillated periodically with an amplitude of approximately $0.05D$ about its new time-mean position, as shown in the time history of sphere displacement at $U^* = 75$ in figure 5(*f*). Moreover, in this regime, the sphere showed a secondary frequency besides the main frequency, as shown in 5(*f*) in the zoomed-in view. For $U^* > 30$, the time-mean displacement of the sphere increased as the reduced velocity increased. At $U^* = 100$, the time-mean position of the sphere migrated to $\sim 5D$ away from its initial position (see figure 4*c*,*e*).

4.1.1. *Comparison with other research studies*

Behara & Sotiropoulos (2016) studied VIV of a sphere that was allowed to move in all three spatial directions for the same Reynolds number with a sphere with a reduced mass of $m_r = 2$. They observed two different hysteretic VIV responses, with different possible states observable at the same reduced velocity. In one case, the sphere moved in a linear path in the transverse plane (*xz* plane) with hairpin-type vortex loops shed behind the sphere. In the other case, the sphere moved in a circular orbit with spiral vortices observed in the wake. Figure 6 compares the amplitude response observed with a sphere of reduced mass $m_r = 2$ for branch A with that of Behara & Sotiropoulos (2016) for their response branch corresponding to linear oscillations for the reduced velocity range $3.5 < U^* < 10$. Here, the sphere response amplitude is observed to be higher when motion is restricted to one DOF (degree of freedom). For the 3-DOF movement, the three orthogonal springs may affect the motion slightly differently from restricted 1-DOF motion aligned with the springs; hence, it is not clear how these two problems exactly relate to each other despite the observed linear motion in a plane in both cases. Despite this, the general amplitude response and lock-in range agree reasonably well, while noting a shift to a slightly higher lock-in range for the current simulations.

The sphere response curves observed for the reduced masses $m_r = 1.5$ and 2 almost lie on top of each other (compare the response curves in figures 4*a* and 6).

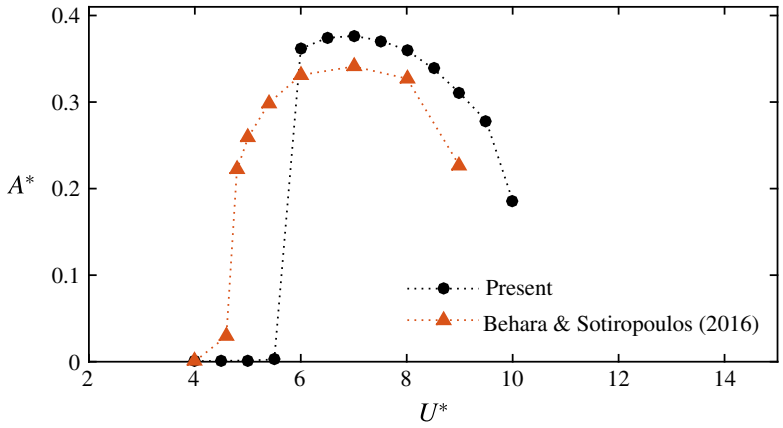

FIGURE 6. (Colour online) Comparison of VIV response for a sphere free to move only in the transverse direction (y only), ●, and free to move in all three spatial directions by Behara & Sotiropoulos (2016) when the sphere is moving in a linear path in the transverse plane (xz plane), ▲ (orange), at a Reynolds number of $Re = 300$ and a mass ratio of $m^* = 3.8197$ ($m_r = 2$).

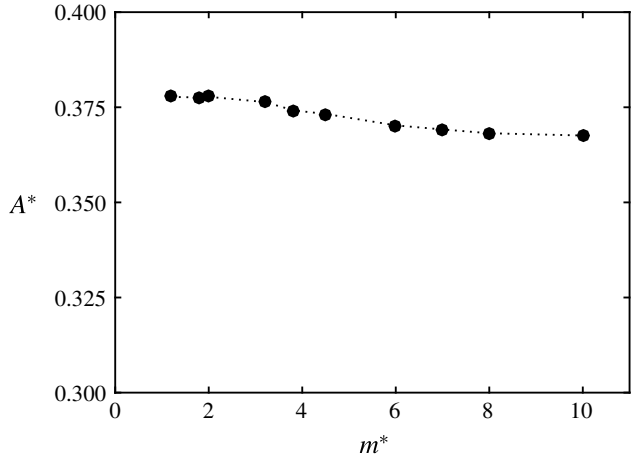

FIGURE 7. Variation of the sphere response amplitude at various mass ratios, at $Re = 300$ and $U^* = 6.5$.

This demonstrates that a small variation in mass ratio does not significantly affect the amplitude response. This was further investigated by varying the mass ratio of the sphere from 1.2 to 10 at a fixed reduced velocity of $U^* = 6.5$, where the peak response occurred (see figure 7). The variation of the sphere response amplitude with mass ratio was less than 2 %. This verifies that there is no significant effect of mass ratio on the sphere peak response amplitude over this mass ratio range, consistent with previous experimental findings for VIV of low-mass-damped spheres and cylinders (Griffin 1980; Govardhan & Williamson 2006).

The highly periodic and large-amplitude vibration observed in branch A resembles the vibration observed over a similar reduced velocity range by Govardhan & Williamson (2005) in their experimental study on tethered spheres at much higher Reynolds numbers. They found that the oscillations of a tethered sphere (xy motion) and a hydroelastic sphere (y only) compared well for similar mass damping parameters.

In this velocity range, they observed two district modes of vibration (modes I and II). In contrast to the clearly distinguishable mode transitions of a circular cylinder, there was a smooth transition between modes I and II for a sphere. These two modes were only clearly distinguishable from the amplitude response curve for spheres with small mass ratios (Jauvtis *et al.* 2001, figure 2). It was even harder to distinguish them from the amplitude response for hydroelastic spheres (Govardhan & Williamson 2005, figure 2*b*). At $Re = 300$, the amplitude response variation is not indicative of two different vibration modes.

For mode I, Govardhan & Williamson (2005) observed an oscillation amplitude of $\approx 0.4D$ for a sphere of mass ratio $m^* = 2.83$ in 2-DOF motion (xy motion); this is similar to the current observations for $m^* = 2.865$ and with 1-DOF motion in the y direction. However, they observed an oscillation amplitude of $\approx 0.8D$ for mode II which was not the case in this study. Indeed, for both modes I and II, they observed that the oscillating frequency of the sphere was close to the natural frequency of the system, consistent with the low-Reynolds-number behaviour here. However, it would be misleading to claim a strong analogy between modes I and II, and branch A, at this low Reynolds number.

4.2. *Force measurements*

This section presents the pressure and viscous force components acting on the sphere in the x, y and z directions. Figure 8 shows the variation with U^* of the mean drag coefficient, $\overline{C}_d$ (the force coefficient in the x direction), the mean lift coefficients in the y and z directions, $\overline{C}_{ly}$ and $\overline{C}_{lz}$ respectively, the mean total lift coefficient, $\overline{C}_l = \sqrt{\overline{C}_{ly}^2 + \overline{C}_{lz}^2}$, and the mean angle of lift, $\overline{\theta}$, where $\theta = \arctan(C_{lz}/C_{ly})$ is the angle between the force coefficients in the y and z directions.

In the reduced velocity range $3.5 \leqslant U^* \leqslant 5$, both $\overline{C}_d$ and $\overline{C}_{ly}$ were constant, consistent with negligible sphere oscillation. Indeed, these values were identical with the corresponding force coefficients of a rigidly mounted sphere at the same Reynolds number. The non-zero mean displacement of the sphere in this reduced velocity range is attributable to the non-zero mean lift. As expected, there was no force component in the z direction over this U^* range. Figure 9 shows the variation of the r.m.s. values of the force coefficients in the x, y and z directions, $C_{d,rms}$, $C_{ly,rms}$ and $C_{lz,rms}$ respectively, with the reduced velocity. Over this range, there were negligible fluctuations of forces in any direction. Therefore, in this non-resonance U^* range, the sphere effectively behaved like a rigidly mounted sphere with no significant oscillatory motion, as discussed previously.

As the sphere began to oscillate at $U^* = 5.5$, the mean drag coefficient, $\overline{C}_d$, suddenly increased by $\approx 30\,\%$ (see figure 8*a*,*b*) from its pre-oscillatory value. Over the reduced velocity range $U^* \in [5.5\text{–}10]$, $\overline{C}_d$ decreased gradually as U^* increased, returning to the non-oscillatory value at the end of the range. A similar behaviour of $\overline{C}_d$ was reported by Behara *et al.* (2011) in their study of VIV of a sphere in 3-DOF. In this velocity range, the mean lift coefficient in the y direction, $\overline{C}_{ly}$, dropped to zero, as shown in figure 8(*c*,*d*). This is consistent with symmetric sphere oscillations observed through its initial position in this regime. However, within this U^* range, the forces in the x and y directions fluctuated with large amplitudes, as shown in figure 9(*a*–*d*) by the r.m.s. values of the fluctuation amplitudes of the force coefficients. This is evidence of the enhancement of sphere oscillations in this regime (branch A). As can be seen from figure 9(*a*–*d*), the r.m.s. values of the drag coefficient and the lift coefficient in

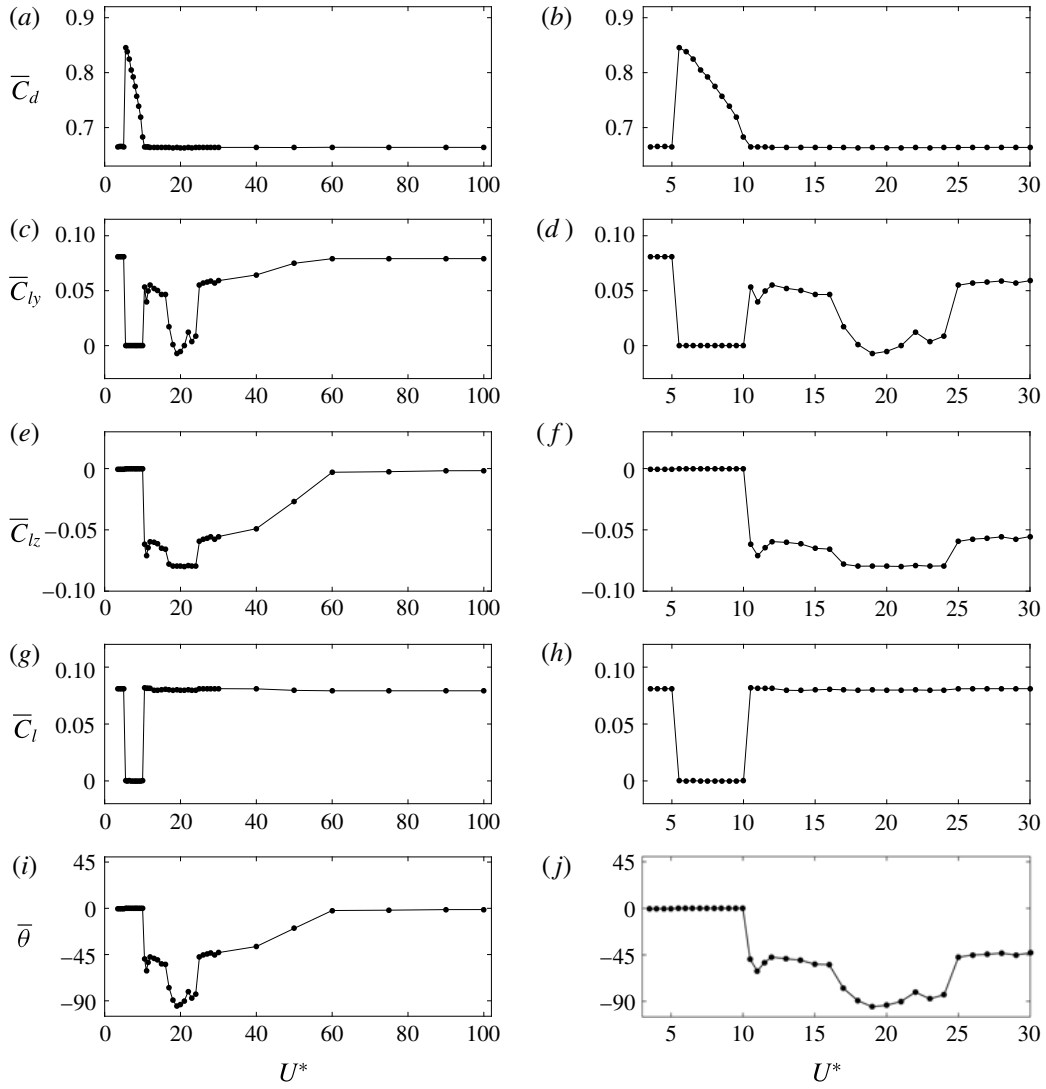

FIGURE 8. Variation of the force coefficients with the reduced velocity; panels (*a*,*c*,*e*,*g*,*i*) show the results for $U^* \in [3.5–100]$ and (*b*,*d*,*f*,*h*,*j*) show enlarged views for $U^* \in [3.5–25]$: (*a*,*b*) mean drag coefficient, $\overline{C}_d$, (*c*,*d*) mean lift coefficient in the y direction, $\overline{C}_{ly}$, (*e*,*f*) mean lift coefficient in the z direction, $\overline{C}_{lz}$, (*g*,*h*) mean lift coefficient, $\overline{C}_l = \sqrt{\overline{C}_{ly}^2 + \overline{C}_{lz}^2}$, and (*i*,*j*) mean lift angle, $\overline{\theta}$, where $\theta = \arctan(C_{lz}/C_{ly})$ is the angle between the lift coefficients in the y and z directions.

the y direction ($C'_{d,rms}$ and $C'_{ly,rms}$ respectively) increased suddenly at $U^* = 5.5$ and then gradually decreased to zero as U^* increased to 10. The analytical solution of the governing motion equation of the sphere (2.3) subjected to a periodic input force shows that the sphere oscillation amplitude is proportional to the fluctuation amplitude of the force, C'_{ly}, and is inversely proportional to the spring constant, $k = 4m\pi^2/U^{*2}$. Therefore, the sphere oscillation amplitude, A^*, is proportional to $C'_{ly} \times U^{*2}$. The exponentially decaying C'_{ly}, as shown in figure 9(*c*,*d*) for increasing U^*, leads to the amplitude response profile shown in figure 4(*a*,*b*), whereby there is a sharp drop of the maximum oscillation amplitude.

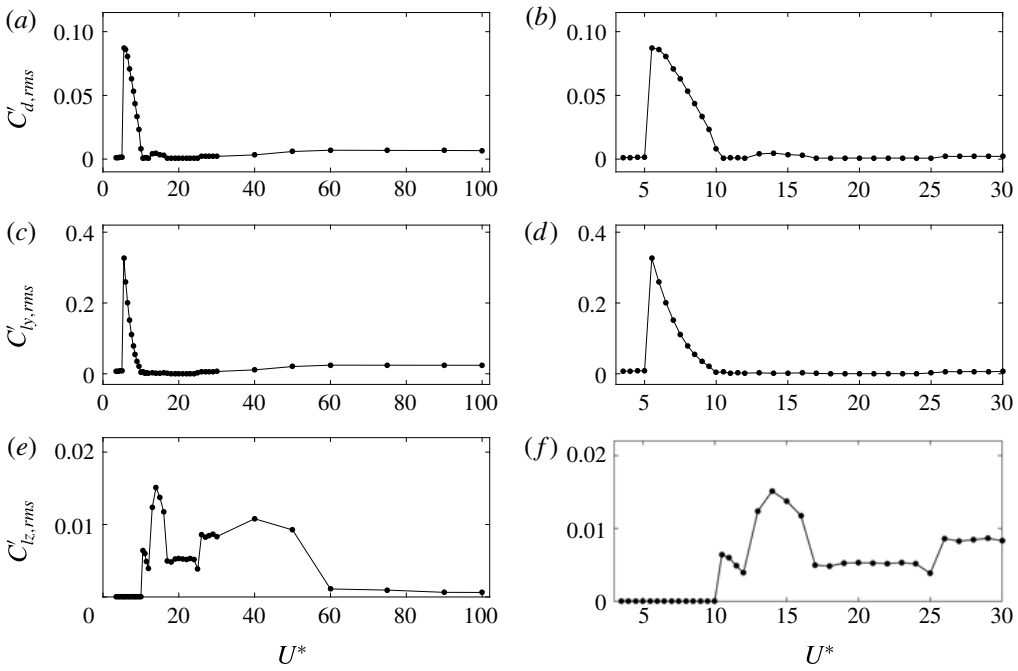

FIGURE 9. Variation of the r.m.s. values of the fluctuation components of the force coefficients with the reduced velocity; panels (*a*,*c*,*e*) show the results for $U^* = 3.5$–100 and (*b*,*d*,*f*) show enlarged views for $U^* = 3.5$–25: (*a*,*b*) r.m.s. of drag coefficient, $C'_{d,rms}$, (*c*,*d*) r.m.s. of lift coefficient in the *y* direction, $C'_{ly,rms}$, (*e*,*f*) r.m.s. of lift coefficient in the *z* direction, $C'_{lz,rms}$.

For the case of $U^* \leqslant 10$, there was no force component in the *z* direction, as expected. However, as U^* increased beyond 10, surprisingly, a force component in the *z* direction was found, indicating that the wake loses mirror symmetry in this range. Figure 10 shows the time histories of the force coefficients in the *y* and *z* directions at the points *A*–*F* marked in figure 4(*a*,*b*). As can be seen, for cases *B*–*E* (in the reduced velocity range $U^* \in [10.5–40]$), a force component in the *z* direction appears gradually with simulation time. The *y* and *z* components of the forces are of the same order of magnitude (see figure 8*c*–*f*). Therefore, the influence of the *z* component of the force is not negligible in this case. If the sphere were to be allowed to move in both the *y* and *z* directions, it might well orbit with an elliptical trajectory. For these reduced velocities, initially, forces in the *y* direction were irregular, with a large oscillation amplitude. However, as the simulation time progressed, forces in the *y* direction were attenuated and the oscillating amplitudes decreased. The behaviour of the forces is consistent with the behaviour of the sphere displacement. The sphere oscillation amplitude decreased as the fluctuation amplitude of the force in the *y* direction decreased. Hence, there was a small oscillation amplitude for vibration branches B and C. However, the force component in the *z* direction diminished with increasing U^* for $U^* \geqslant 26$, in terms of both the mean and the fluctuating amplitude (see figures 8*e*,*f* and 9*e*,*f*). The mean lift force in the *y* direction approached that of a stationary sphere with increasing U^* for $U^* \geqslant 26$.

As figure 8(*c*,*d*) shows, the lift force in the *y* direction was not zero in the vibration branches B ($13 \leqslant U^* \leqslant 16$) and C ($26 \leqslant U^* \leqslant 100$). This non-zero lift force moved the sphere away from its initial position, whereupon vibration in branches B and

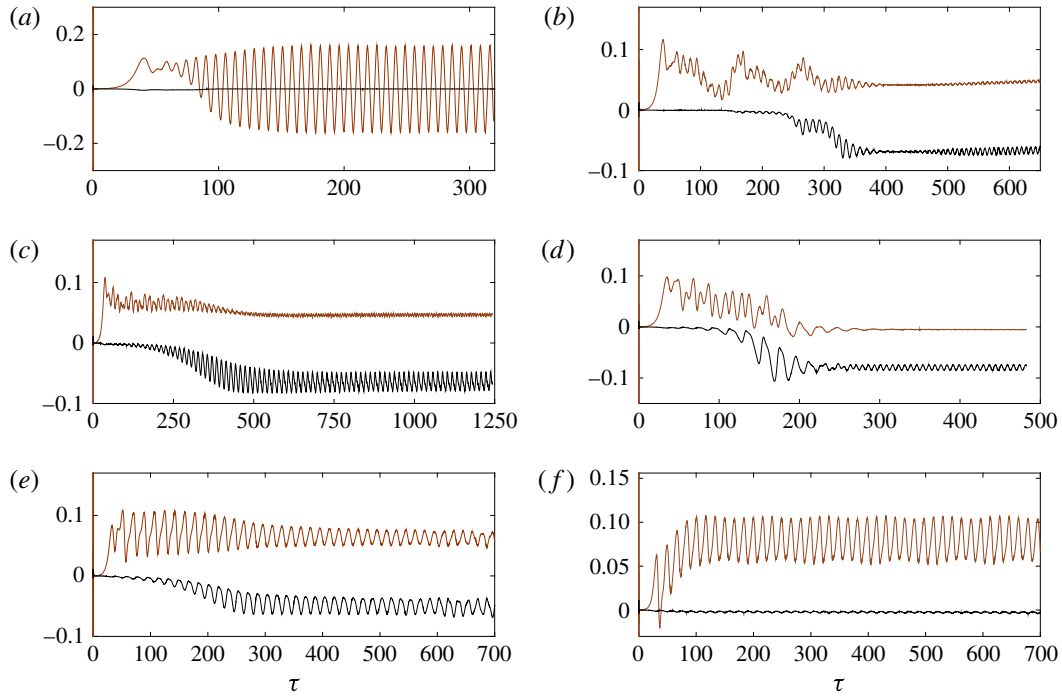

FIGURE 10. (Colour online) Time history of the force coefficients in the y and z directions (C_{ly} and C_{lz} respectively); C_{ly} is shown with the orange colour (light) curves while C_{lz} is shown with the black colour (dark) curves; $\tau = tU/D$ is the non-dimensional time: (a) case A at $U^* = 7$, (b) case B at $U^* = 10.5$, (c) case C at $U^* = 15$, (d) case D at $U^* = 20$, (e) case E at $U^* = 28$ and (f) case F at $U^* = 75$. See figure 4 for the locations of the points A–F on the sphere response curve.

C occurred about this modified position. This may be another reason for the small amplitude of vibrations for these branches. As U^* increased from 26 to 100, the mean displacement of the sphere increased greatly, attaining a value of $5D$ at $U^* = 100$. However, the mean lift force in the y direction increased only to the stationary sphere value. Therefore, the increase in the mean displacement of the sphere can be considered to be due to the effective decrease of the stiffness of the spring as the reduced velocity is increased.

For $U^* > 10$, even though the individual mean lift coefficients in the y and z directions varied with the reduced velocity, the mean value of the total lift coefficient, $\overline{C}_l = \sqrt{\overline{C}_{ly}^2 + \overline{C}_{lz}^2}$, interestingly remained constant and equal to that of a stationary sphere (see figure 8g,h). This indicates that except for branch A, where large-amplitude vibrations were observed, the time-mean of the total lift force was essentially identical to its non-VIV value. The variation of the mean lift angle with the reduced velocity is shown in figure 8(i,j), where the angle of lift, θ, is $\arctan(C_{lz}/C_{ly})$. The mean angle was almost 0° for $U^* \leqslant 10$. It was approximately −45° within the first desynchronization regime and in branch B, and approximately −90° in the second desynchronization regime. At the beginning of branch C, the mean lift angle was approximately −45°, and it approached 0° as the reduced velocity increased, which is consistent with the variation of $\overline{C}_{lz}$ for branch C.

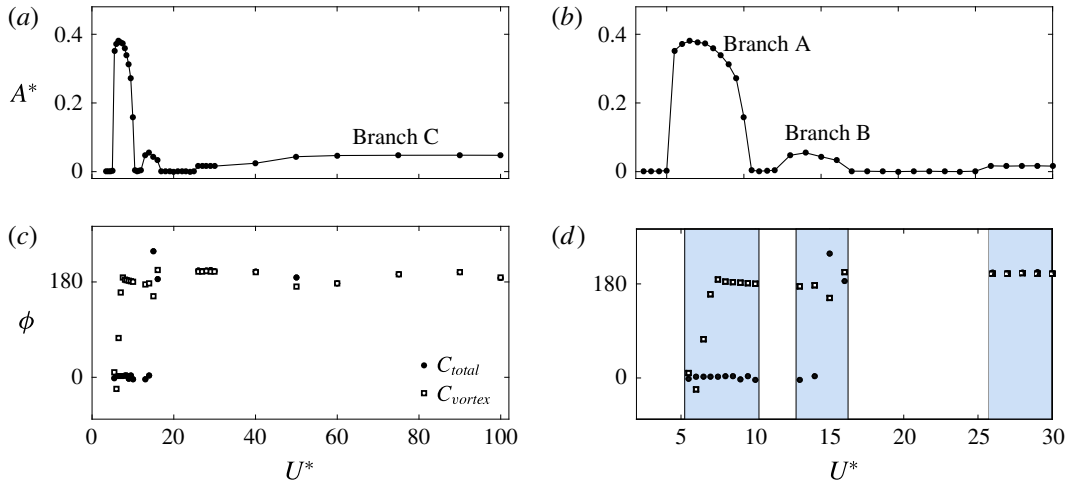

FIGURE 11. (Colour online) Variation of the total phase, C_{total}, and vortex phase, C_{vortex}, with U^*; (*b*) and (*d*) show the zoomed-in view for small U^*.

4.2.1. *Phase between sphere displacement and forces*

As Govardhan & Williamson (2005) discussed, the total fluid force in the y direction, F_{total}, can be split into a potential force component, $F_{potential} = -m_A \ddot{y}(t)$, which arises due to the potential added-mass force, and a vortex force component, F_{vortex}, which is due to the dynamics of vorticity. This recognizes the fact that a flow solution can be constructed as a sum of a potential flow field plus a velocity field associated with vorticity in the flow (see, e.g., Lighthill 1986). Here, m_A is the added mass due to the motion of the sphere. Therefore, the vortex force can be computed from

$$F_{vortex} = F_{total} - F_{potential}. \tag{4.1}$$

Normalization of all forces by $0.5\rho U^2 \pi D^2/4$ gives

$$C_{vortex} = C_{total} - C_{potential}. \tag{4.2}$$

Govardhan & Williamson (2005) observed a shift in vortex phase, ϕ_{vortex}, of 90° in the transition between mode I and mode II. The total phase, ϕ_{total}, only increased slightly over the same U^* range, but it increased towards 180° at the reduced velocity close to the peak amplitude of the mode II range (Govardhan & Williamson 1997, 2005; Jauvtis *et al.* 2001; Sareen *et al.* 2018). Those experiments also show that there is no desynchronized region between modes I and II for small-mass-ratio 1-DOF hydroelastic systems, although this is the case for light ($m^* < 1$) tethered sphere systems. Figure 11 shows the variation of the total phase and vortex phase with the reduced velocity. As can be seen from figure 11(*d*), over branch A, the vortex force gradually increased from 0° to 180° while the total phase stayed at 0°. Therefore, at the beginning of branch A, the force/displacement phasing is consistent with mode I. The increase in total phase does not occur over the range covered by this branch, but instead occurs in branch B; however, this is not to conclude that branch B is analogous to the experimental mode II.

Figure 12 shows the variation of sphere displacement, total force, C_{total}, and vortex force, C_{vortex}, for two periods for branch A at the reduced velocities $U^* = 5$ and

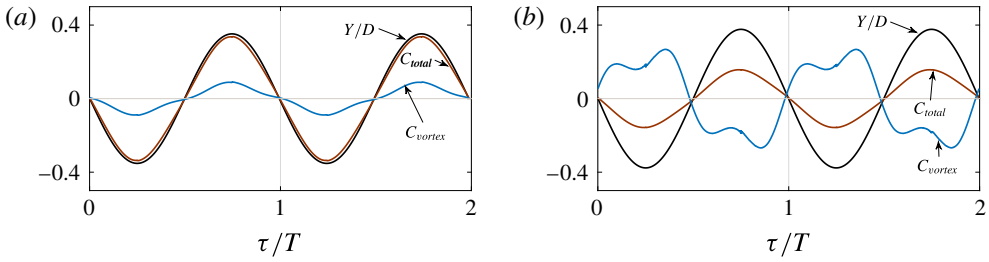

FIGURE 12. (Colour online) Relationship between the total force in the y direction, C_{total}, and the vortex force in the y direction, C_{vortex}, in branch A: (a) at $U^* = 5.5$ (mode I) and (b) at $U^* = 7$ (mode II).

7 respectively. As can be seen, the sphere vibration frequency was locked in with C_{total} as well as with C_{vortex}. As mentioned earlier, there is approximately 180° phase difference between C_{vortex} and Y towards the end of branch A.

As the reduced velocity increased, for branches B and C, ϕ_{vortex} stayed at ∼180° (see figure 11). However, ϕ_{total} suddenly shifted from 0° to 180° within branch B. Indeed, from this point of view, branch B shows some similarities to mode II for light tethered systems, especially as the oscillation frequency follows a $(1/2)f_{vo}$ variation – see figures 4 and 7 of Govardhan & Williamson (2005). Interestingly, branch C also follows this variation but with a difference in vortex and total phase of 180°. On the other hand, mode III, observed in high-mass-ratio higher-Reynolds-number experiments (Jauvtis *et al.* 2001), is locked to the natural frequency of the system, with each oscillation period corresponding to 3–8 vortex shedding periods (Govardhan & Williamson 2005). This is certainly not the case for branch C here, where oscillation occurs at close to the subharmonic of the non-VIV vortex shedding frequency. Thus, branch C and mode III do not appear to be related.

4.3. *Wake structures*

Vortical structures in the wake are depicted using isosurfaces of the second invariant of the velocity tensor (known as the Q-criterion; see Hunt, Wray & Moin 1988). As figure 13 shows, for branch A, two regular streets of hairpin vortices form the wake. This structure resembles those in the wake observed by Govardhan & Williamson (2005) for their mode I and II vibrations using DPIV to extract the vorticity field. The wake also appears identical to the hairpin-type wake observed by Behara *et al.* (2011) for VIV of a sphere with 3-DOF at $Re = 300$; the current study extends the range of reduced velocity considered by an order of magnitude as well as extending the length of the simulations, leading to different evolved states in some cases. The wake observed for a rigidly mounted sphere (shown in figure 14) is modified considerably under vibration of the sphere. Vortex loops are stretched towards positive and negative y directions as the sphere vibrates. In particular, a vortex loop sheds in the positive y direction as the sphere moves to the negative y direction. The evolution of the wake for branch A ($U^* = 7$) over one cycle is shown in figure 15. As can be seen, a vortex loop initiated from the outside sheds like a hairpin and ends from the inside. As a loop is shed, three tails form, one from the tip and two from the sides. Later, these three tails interconnect by creating two small loops. However, as the vortex loop moves further, the connection from the tip disappears and the tail forms a 'U'-shape. The direction of the tail is the same as the direction of the streamlines upstream. The wake

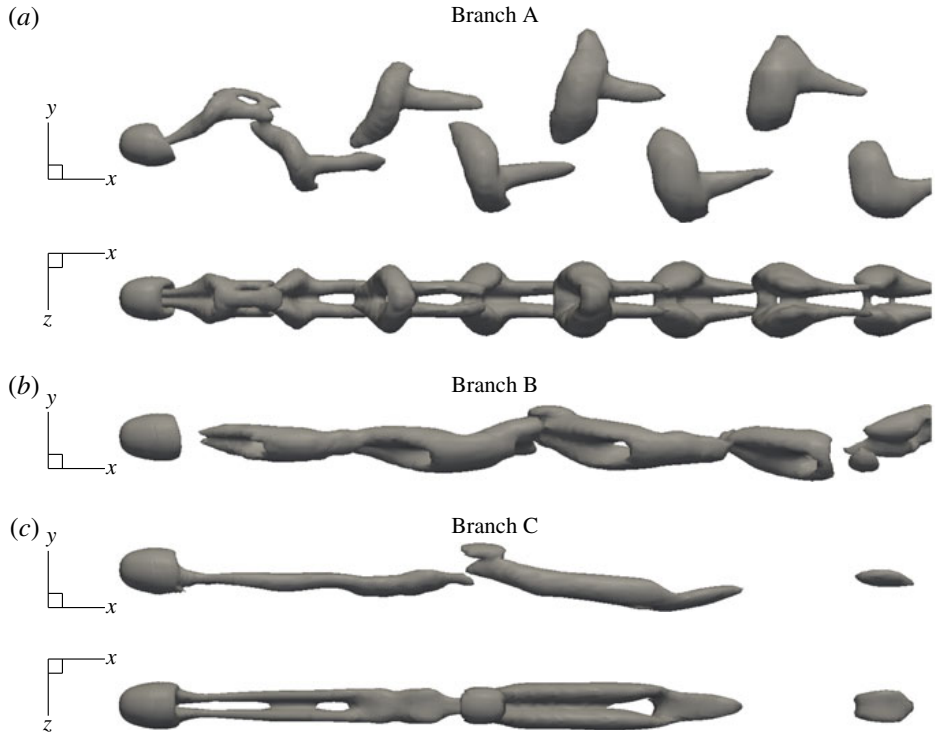

FIGURE 13. Instantaneous wake structures visualized by the Q-criterion ($Q = 0.001$) of branch A (at $U^* = 7$), branch B (at $U^* = 15$) and branch C (at $U^* = 75$) vibrations.

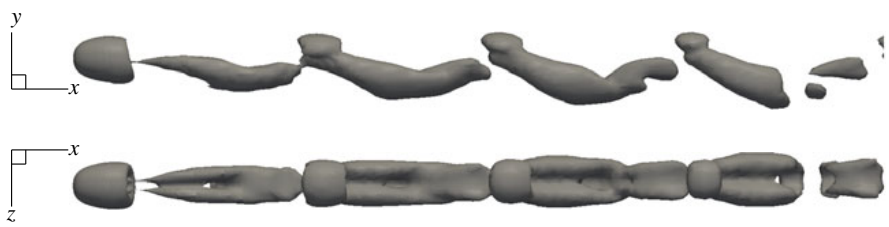

FIGURE 14. Instantaneous wake structures for a rigidly mounted sphere at $Re = 300$.

is symmetric in the xy plane (see also figure 13, branch A in xz plane). The upper and lower vortex streets are equal in strength as the sphere oscillation is symmetric through its initial position.

As figure 13 shows, the wake observed for vibration branch B is quite different. This wake resembles more closely that of a rigidly mounted sphere than the wake for branch A. The orientation of the wake is no longer aligned with the xy plane, as also indicated by the non-zero lift angle shown in figure 9. A lift angle of $\theta \approx 50°$ was found for branch B, and thus the wake for branch B is rotated by an angle of $\approx 50°$. In contrast to the wake for branch A, the loops in the wake for this branch are interconnected and asymmetric.

The wake structures observed in vibration branch C (see figure 13) again more closely resemble the wake structures observed for a rigidly mounted sphere than the wake for branch A. However, the loops are elongated along the x axis, and the non-dimensional shedding frequency is lower than for those structures in branches A and B.

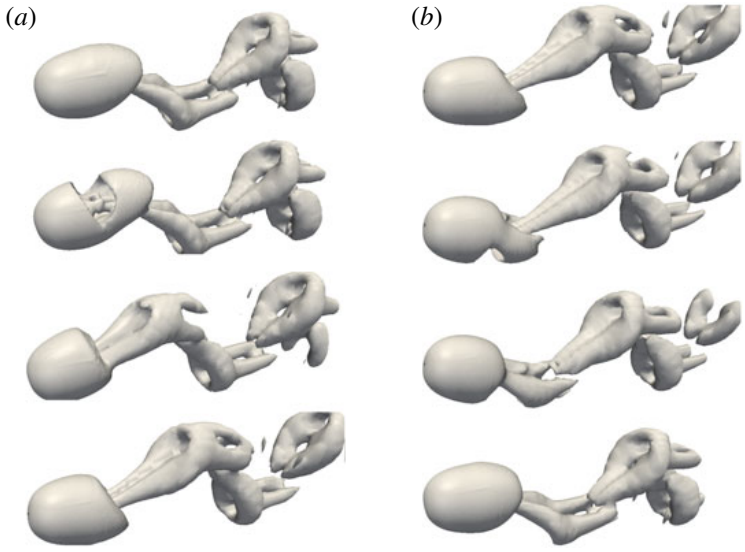

FIGURE 15. Evolution of vortical wake structures behind the sphere with time for the maximum response case of $U^* = 7$. (*a*) The first half of the cycle with the sphere moving downwards, and (*b*) the second half of the cycle with the sphere moving upwards.

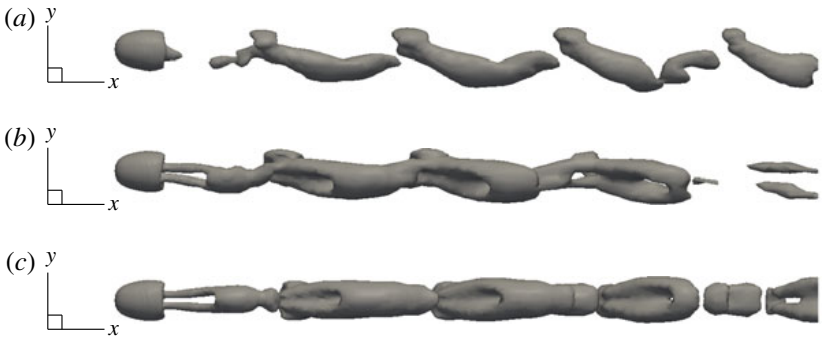

FIGURE 16. Instantaneous wake structures in the *xy* plane in the desynchronization regimes showing rotation of the wake alignment relative to the oscillation direction: (*a*) at $U^* = 4 \in [3.5–5]$, (*b*) at $U^* = 10.5 \in [10.5–12]$, (*c*) at $U^* = 20 \in [17–25]$.

It should be recalled that in this branch, the oscillation frequency is half of the normal shedding frequency. In contrast to the vortical wake structures for branch B, the wake for branch C at higher U^* values has the same orientation as for branch A and is symmetric through the *xy* plane. This is reflected by the lift angle again decreasing at higher reduced velocities. However, the loops are oriented more towards the negative *y* direction, due to the non-zero lift force in the *y* direction.

Figure 16 shows the wake structures observed in the desynchronization regimes where the sphere does not vibrate significantly. In each of these regimes, the wake structures strongly resemble those observed for a rigidly mounted sphere. However, their orientations are different. In the first desynchronization regime, $U^* \in [3.5–5]$, the orientation of the wake is identical to that of the wake of a rigidly mounted sphere. However, in the second and third desynchronization regimes ($U^* \in [10.5–12]$

and [17–25]), the wake has been rotated by angles of $\approx 50°$ and 90°; again, this is consistent with the observed lift angle variation.

Overall, the wake structures observed in branch A are similar to those observed by Govardhan & Williamson (2005) for their mode I and II vibrations and Behara *et al.* (2011) for the hairpin response branch. However, the wake structures observed for branches B and C for the reduced velocity ranges $U^* \in [13–16]$ and [26–100], where the sphere oscillated with a small oscillation amplitude, are different from the wake structures for branch A as well as from the wake structures observed by Govardhan & Williamson (2005) for mode III. This also explains why the vibrations observed in branches B and C are different from the large oscillation amplitudes reported in the experimental studies.

5. Flow-induced vibration of a sphere at $Re = 800$

The investigation of FIV of a sphere was extended by increasing the Reynolds number to $Re = 800$. At $Re = 300$, even though higher reduced velocities were considered, the low-frequency vibration regimes observed by experimental studies with tethered spheres (mode III and IV vibrations investigated by Jauvtis *et al.* (2001)) were not able to be reproduced. Govardhan & Williamson (2005) explained that mode III vibration response occurs for the normalized velocity regime $(U^*/f^*)S = f_{vo}/f = 3$ to 8, where S is the Strouhal number. Furthermore, mode IV vibration appeared after mode III for $(U^*/f^*)S$ approximately greater than 19. However, at $Re = 300$, the highest normalized velocity, $(U^*/f^*)S$, that could be attained was 2 since $f \approx (1/2)f_{vo}$ for higher reduced velocities ($U^* \geqslant 26$). Therefore, to investigate the low-frequency regime and the effect of the Reynolds number in the laminar regime, the Reynolds number of the flow was increased to $Re = 800$. The mass ratio used was again $m^* = 2.865$. Similarly to the $Re = 300$ case, the sphere was restricted to move only in the y direction.

5.1. *Sphere response at* $Re = 800$

Figure 17 shows the characteristics of the FIV response of the sphere at $Re = 800$ over the reduced velocity range $3 \leqslant U^* \leqslant 50$ in terms of the sphere response amplitude, A^*, the time-mean displacement of the sphere, $\overline{Y}/D$, and the frequency ratio, $f^* = f/f_n$. Similarly to the $Re = 300$ case, the sphere suddenly began to oscillate as the reduced velocity increased to a value of 4.5. The sphere vibration amplitude maintained a bell-shaped curve with a highest oscillation amplitude of $\approx 0.6D$ until $U^* = 13$. Then, the oscillation amplitude increased as the reduced velocity increased from $U^* = 14$ to 50, yielding an amplitude of approximately $0.9D$ at $U^* = 50$.

Within the reduced velocity range $U^* = 4.5–13$, the sphere vibrated periodically about its initial position ($\overline{Y}/D = 0$ in this velocity regime; see figure 17*b*). Moreover, the amplitude response varied smoothly within this reduced velocity range. The sphere vibration frequency was synchronized with the vortex shedding frequency. Furthermore, it was identical to the natural frequency of the system ($f^* = f/f_n = 1$; see figure 17*c*). Thus, these are indeed VIVs. This reduced velocity range can be identified as branch A introduced for the simulations at $Re = 300$. Moreover, branch A shows some aspects of behaviour similar to those seen in mode I and II vibrations observed in previous experimental studies. This will be elaborated later in the section discussing force measurements.

In contrast to the smooth amplitude response curve for $U^* = 4.5–13$, the measured r.m.s. amplitudes were scattered, with an overall increasing trend for $U^* \geqslant 14$.

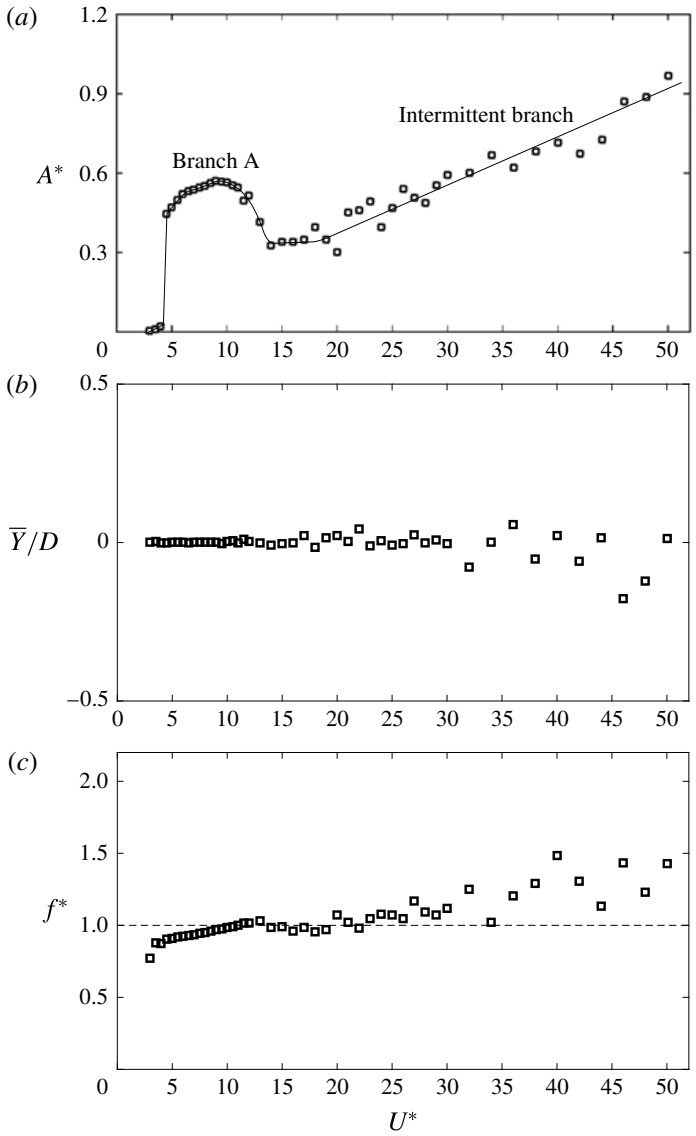

FIGURE 17. Response of an elastically mounted (on y only) sphere as a function of the reduced velocity, U^*, at $Re = 800$ and $m^* = 2.865$: (a) sphere oscillation amplitude, $A^* = \sqrt{2}Y_{rms}/D$, (b) time-averaged non-dimensional sphere displacement, $\overline{Y}/D$, (c) sphere oscillation frequency normalized by the system natural frequency, $f^* = f/f_n$.

This scatter is presumably due to insufficient sampling times for the amplitude signal. Moreover, for reduced velocities $U^* \geqslant 14$, the sphere oscillations were not periodic as at lower reduced velocities. The periodicity of the amplitude response (Govardhan & Williamson 2005) is defined as $\lambda_A = \sqrt{2}Y_{rms}/Y_{max}$, where Y_{max} is the maximum oscillation amplitude observed at each U^*. According to this definition, the periodicity takes values between 0 and 1, with $\lambda_A = 1$ for purely sinusoidal signals. Figure 18 shows the variation of the periodicity of the sphere response with the reduced velocity. As can be seen from figure 18(b), for $U^* = 4.5$–11.5, the sphere response was purely sinusoidal. However, as U^* was increased beyond 12, the sinusoidal nature of the signal decreased and the periodicity of the response dropped dramatically to a value

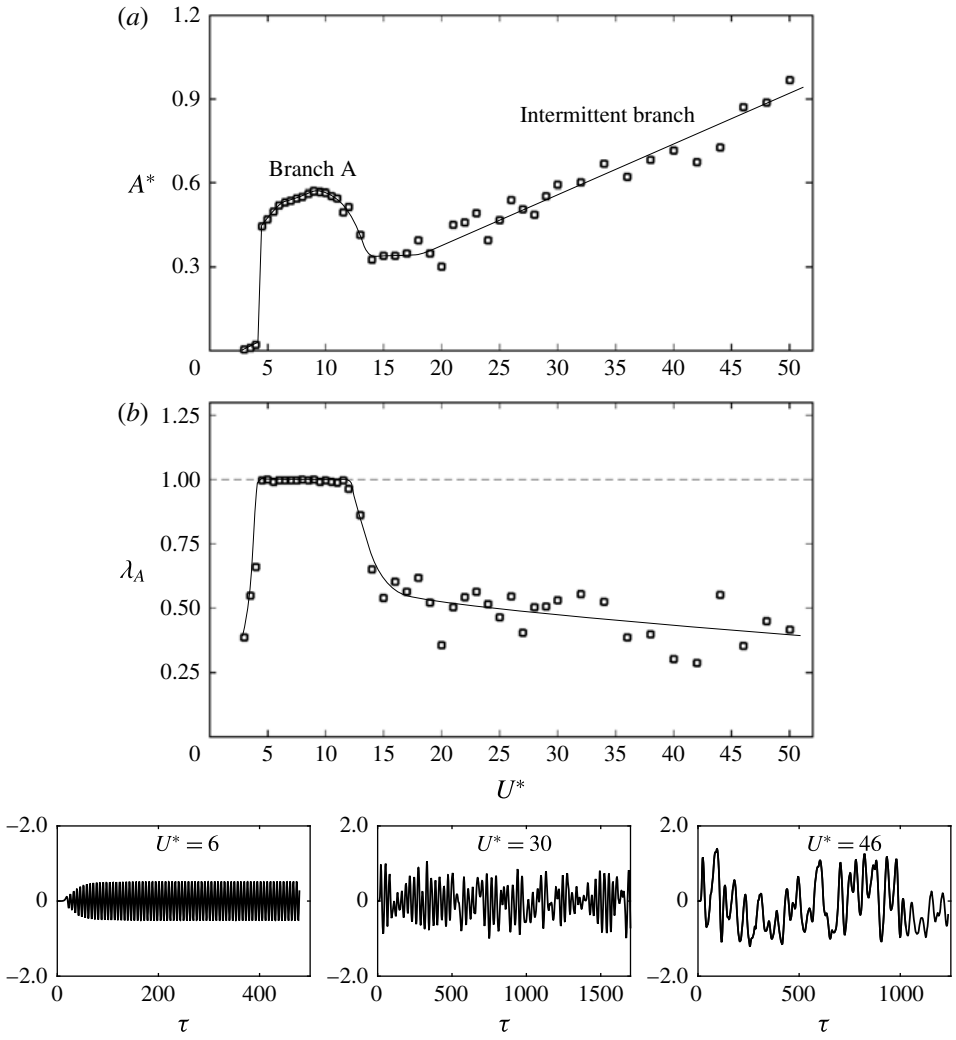

FIGURE 18. Variation of the sphere response amplitude and the periodicity of the response, $\lambda_A = \sqrt{2}Y_{rms}/Y_{max}$, with the reduced velocity, U^*.

of ≈ 0.5 at $U^* = 14$. For $U^* \geqslant 14$, the sphere response was highly aperiodic. However, the periodicity of the response remained close to 0.5, although showing a slightly decreasing trend as the reduced velocity increased from $U^* = 14$. In this regime, the periodicity was also scattered, similarly to the amplitude response. Furthermore, the time-mean position of the sphere was scattered around the initial position of the sphere. These observations indicate that the sphere oscillation response was chaotic for $U^* \geqslant 14$. However, in this regime, the main oscillation frequency component of the sphere was close to the natural frequency of the system, albeit it was not synchronized with the main vortex shedding frequency (see figures 17*c* and 19). Thus, the vibration state in the intermittent branch is not VIV.

The vibrations observed in the intermittent branch resembled the mode IV vibration discovered by Jauvtis *et al.* (2001) with a tethered sphere of $m^* = 80$ for $U^* \geqslant 100$ in wind-tunnel experiments. Even through Jauvtis *et al.* observed mode IV vibration with a high-mass-ratio sphere for very large reduced velocities ($U^* \geqslant 100$), surprisingly, a very similar response was observed with a small-mass-ratio sphere and for quite low

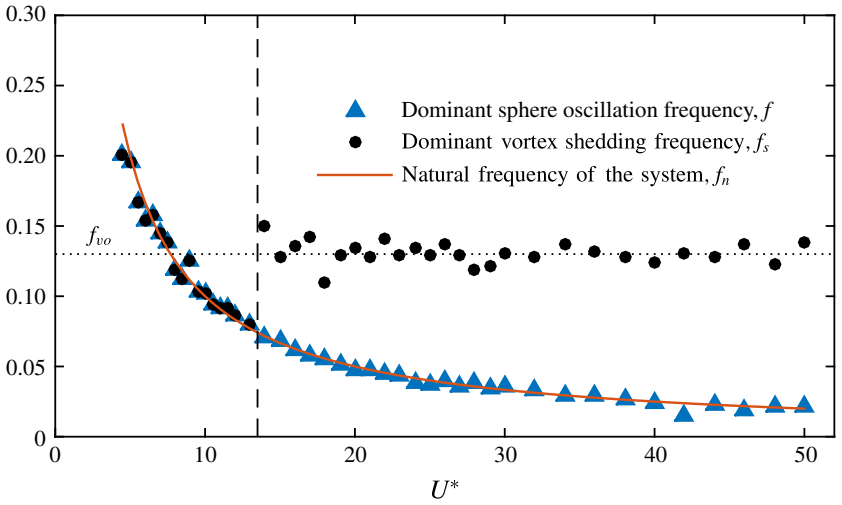

FIGURE 19. (Colour online) Comparison of the dominant sphere oscillation frequency with the dominant vortex shedding frequency and the natural frequency of the system in branch A and the intermittent branch.

reduced velocities ($U^* \leqslant 14$) at $Re = 800$. This may be an effect of zero structural damping, and it seems possible that an increased damping may reduce or even suppress these randomly induced vibrations.

The sphere response at $Re = 800$ was much closer to that observed in experimental studies than the response at $Re = 300$. However, at $Re = 800$, intermittent vibrations (mode IV) were observed directly after the initial vibration response branch without an intervening range of mode III vibration. Again, this may be due to the effect of (zero) damping ratio, mass ratio or even Reynolds number.

Govardhan & Williamson (2005) recognized that the streamwise vortex pair of a sphere creates a lift force analogous to aircraft trailing vortices. As the direction of the streamwise vortices switches according to the two-sided hairpin structures behind the sphere, it creates a periodic lift force that leads to vibration of the sphere and synchronization. Hence, VIV of a sphere (or other such three-dimensional bodies) can occur due to the streamwise trailing vortex pair formed behind it. According to Govardhan & Williamson (2005), all of the first three modes of vibrations (modes I, II and III) occur due to the synchronization of sphere displacement with the vortex force (or streamwise vortex structures). Govardhan & Williamson showed that the sphere vibration phase aligns with the vortex force in mode I and lags in phase with the vortex force in mode II. Moreover, they observed multiple vortex loops shed per sphere vibration cycle in mode III. The mode III vibration state was identified as moment-induced vibration. It is possible that this state may not appear at low Reynolds numbers, or that it requires a higher mass ratio or a non-zero damping to stabilize it. This is difficult to investigate in a numerical parameter study because increase in the mass ratio requires considerably longer integration times to reach an asymptotic state.

The recent experimental study of Sareen *et al.* (2018) investigated the effect of sphere rotation on VIV of a sphere that is free to oscillate in the cross-flow direction. The amplitude responses of the sphere at Reynolds numbers of 300 and 800 are compared with the experimental results of Sareen *et al.* (2018) for the case of a sphere with zero rotation in figure 20. At this point, it worth mentioning that there

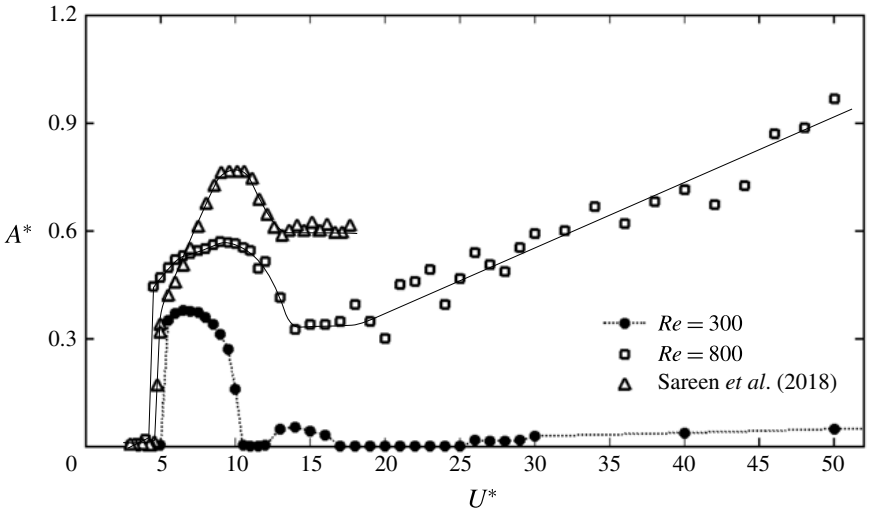

FIGURE 20. Effect of the Reynolds number on the sphere response amplitude: ● at $Re = 300$, □ at $Re = 800$, △ experimental results from Sareen *et al.* (2018) with no sphere rotation, for which the Reynolds number varies between $Re \simeq 5\,000$ and $30\,000$ over this U^* range. (For the latter study, $m^* = 14.2$ and the mass damping parameter $m^*\zeta = 0.0207$.)

is a slight difference between our numerical study and previous experimental studies. In this study, the Reynolds number of the flow was kept constant while varying the spring constant to vary the reduced velocity. However, in experimental studies, the reduced velocity is generally varied by adjusting the flow velocity. Thus, the Reynolds number also varies with the reduced velocity. The Reynolds number in the study by Sareen *et al.* (2018) was varied between 5 000 and 30 000. As can be seen from figure 20, at low reduced velocities ($U^* \leqslant 17$), the peak sphere response amplitude increases with increasing Reynolds number. The shape of the amplitude response curves varies successively from $Re = 300$ to 800 to higher Reynolds numbers. In particular, as the Reynolds number is increased, the transition from mode I to mode II in this branch is relatively clear even at $Re = 800$. At $Re = 300$, there is no indication of mode II response before reaching the end of the branch.

Comparison of the amplitude responses for Reynolds numbers of 800 and 300 shows a higher response amplitude at $Re = 800$ at each reduced velocity. In addition, the range of reduced velocities that show large-amplitude periodic vibration (branch A) is widened as the Reynolds number is increased from $Re = 300$ to 800. Moreover, at higher reduced velocities, the sphere response shows aperiodic intermittent vibrations (mode IV) at $Re = 800$, while it shows periodic vibrations with a very small amplitude at $Re = 300$. Unsurprisingly, these observations show the strong effect of the Reynolds number on FIV.

5.2. *Force measurements at* $Re = 800$

At the beginning of branch A ($4.5 \leqslant U^* \leqslant 13$), where the sphere vibrations are purely sinusoidal, the force components were also sinusoidal, as shown in figure 21(*a*) at $U^* = 6$. Not only the transverse force component in the y direction but also the streamwise force component fluctuated with a significant oscillation amplitude. Moreover, the frequency of the streamwise force was twice the transverse frequency. Therefore, if the sphere were allowed to move in the streamwise direction, it would

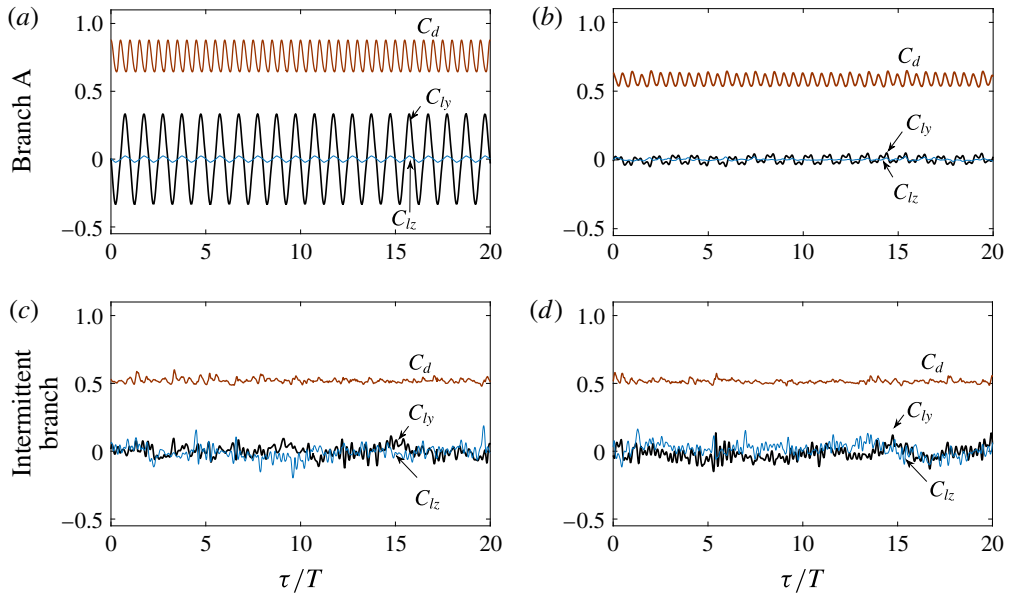

FIGURE 21. (Colour online) The time histories of the drag and lift (in the y and z directions) force coefficients, C_d, C_{ly} and C_{lz} respectively, in branch A (a,b) and the intermittent branch (c,d) for 20 cycles of sphere vibration: (a) $U^* = 6$, (b) $U^* = 12$, (c) $U^* = 30$ and (d) $U^* = 46$.

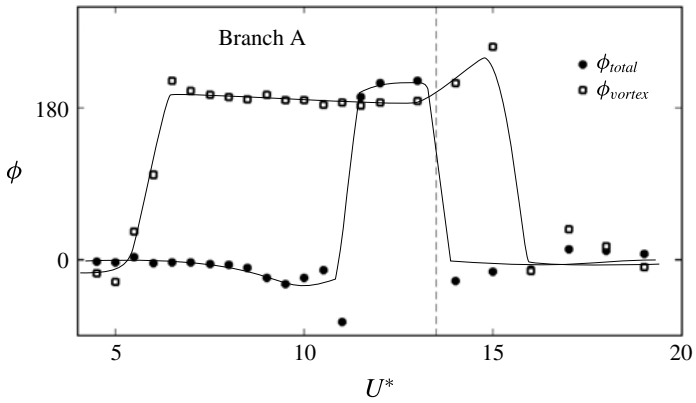

FIGURE 22. Variation of the total and vortex phases (ϕ_{total} and ϕ_{vortex}) with U^* at $Re = 800$ over branch A.

show streamwise vibration with a small oscillation amplitude, as reported in Govardhan & Williamson (2005). In this regime, the force in the z direction oscillated with a negligible amplitude compared with the force in the y direction. Towards the end of this reduced velocity range, the drag and lift forces in the y direction were less sinusoidal, yet still showed a strong periodic component, as shown in figure 21(b) at $U^* = 12$.

In branch A, the displacement signal of the sphere was locked to both the total and the vortex force signals (see figures 23 and 24). Figure 22 shows the variation of the total phase, ϕ_{total}, and the vortex phase, ϕ_{vortex}, with the reduced velocity up to $U^* = 20$. The vortex phase rises up to 180° over the first part of branch A, consistent with the

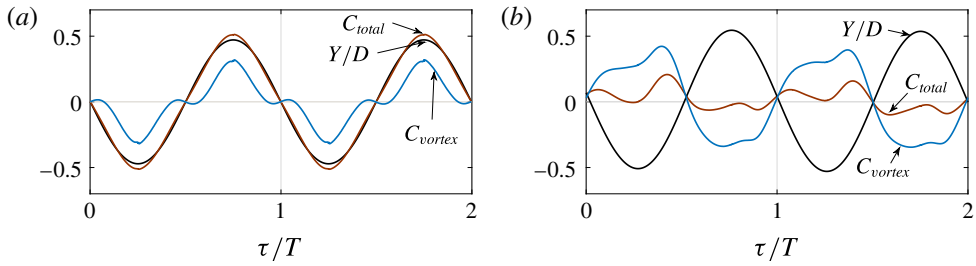

FIGURE 23. (Colour online) The relationship between the total force in the y direction, C_{total}, and the vortex force in the y direction, C_{vortex}, in branch A: (a) at $U^* = 5$ and (b) at $U^* = 12$.

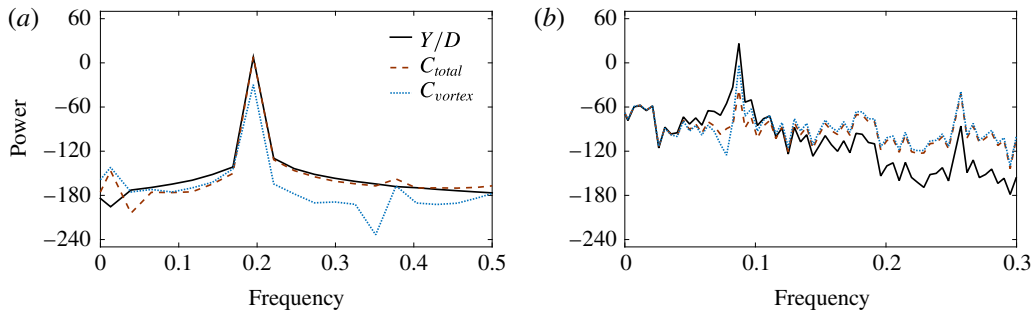

FIGURE 24. (Colour online) Power spectrum of the sphere response, Y/D, total force, C_{total}, and vortex force, C_{vortex}, in branch A: (a) at $U^* = 5$ and (b) at 12.

mode I behaviour seen in experiments (see figure 23a). The total phase rises towards 180° towards the end of the branch, which is also seen experimentally in the mode II region (also see figure 23b). For low-mass-ratio tethered spheres, there is also distinct change in the frequency response across the mode I to mode II transition (Govardhan & Williamson 2005), clearly seen for $m^* = 0.76$, that is not seen here. It is not clear whether this is masked by the higher mass ratio of these simulations, which would mean that any frequency jump would be smaller.

Figure 25 displays the drag and lift (in the y and z directions) force coefficients in terms of time-mean values and r.m.s. of the fluctuating components. Similarly to the $Re = 300$ case, the time-mean drag force coefficient suddenly increases by ≈60 % from its pre-oscillatory value as soon as branch A vibration starts at $U^* = 4.5$ (see figure 25a). This increment decreases with the reduced velocity in the branch A regime and returns to the pre-oscillatory value at the end of the range. Similarly to $\overline{C}_d$, the fluctuation amplitudes of both the drag force and the lift force in the y direction show sudden jumps at the beginning of branch A, and then that increment decreases with increasing U^* over branch A (see figure 25b,d). These observations are consistent with the $Re = 300$ case as well as with the experimental study of Sareen *et al.* (2018).

In branch A, $C_{ly,rms}$ decreases rapidly as the reduced velocity increases. However, as U^* passes beyond 11.5, $C_{ly,rms}$ begins to increase again and asymptotes to a value of 0.06 at the end of the range. Simultaneously, $C_{lz,rms}$ also begins to increase towards the end of branch A and reaches a value of ≈ 0.06. These observations again show a smooth transition between branch A and the intermittent branch.

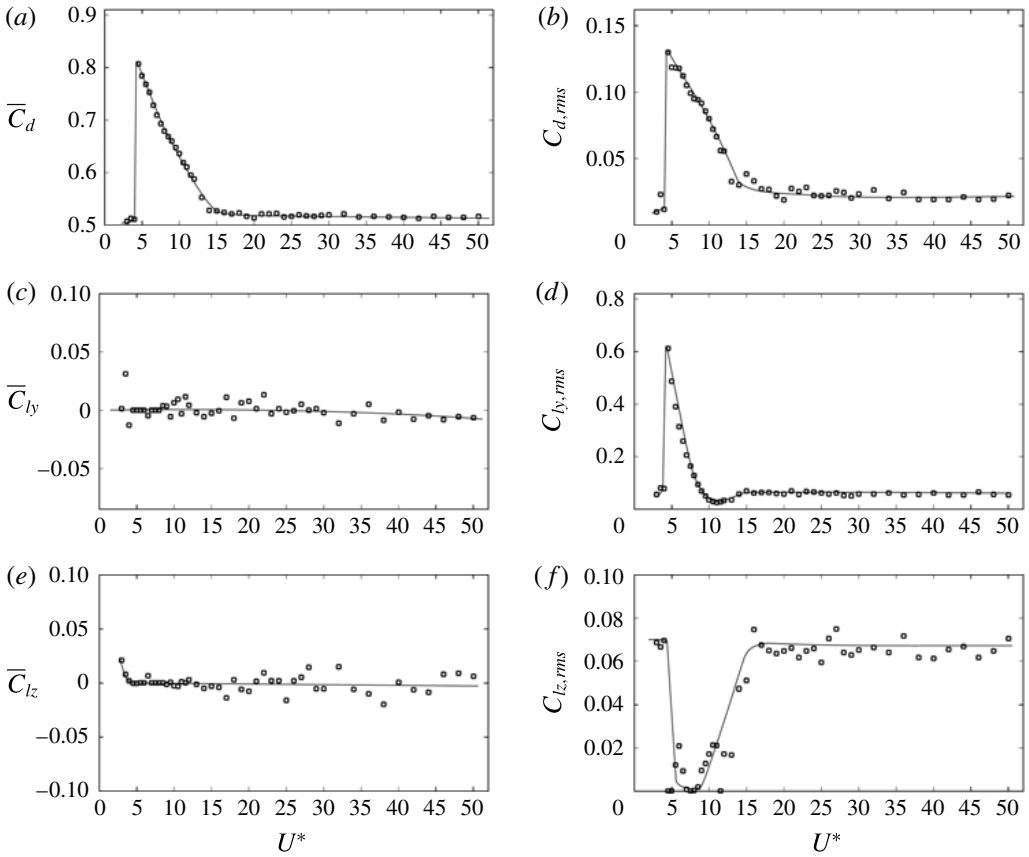

FIGURE 25. Variation of the time-mean force coefficients (*a*,*c*,*e*) and the r.m.s. of the fluctuation components of the force coefficients (*b*,*d*,*f*) in the x, y and z directions with the reduced velocity, U^*, at $Re = 800$. The drag force is measured in the x direction and the lift forces are measured in the y and z directions.

5.2.1. *Intermittent branch*

For the intermittent branch ($U^* \geqslant 14$), no significant variation was observed for either the time-mean or the fluctuation force components with the reduced velocity. The mean drag coefficient, $\overline{C}_d$, was flat at the pre-oscillatory value, while $\overline{C}_{ly}$ and $\overline{C}_{lz}$ were almost zero, as for branch A (see figure 25). All three force components showed a small fluctuation over the intermittent branch. In particular, $C_{d,rms}$ was ≈ 0.02, while both $C_{ly,rms}$ and $C_{lz,rms}$ were ≈ 0.06. The time histories of the forces in the intermittent branch for approximately 20 sphere oscillation cycles are shown in figures 21(*c*) and 21(*d*) at $U^* = 30$ and 46 respectively. As can be seen, the forces were neither periodic nor locked in with the sphere vibration. Therefore, the intermittent vibration branch (mode IV) cannot be described by the classic lock-in theory, but nevertheless represents a response of substantial magnitude. Again, this intermittent response may be enhanced by the zero damping applied to the current set of simulations.

5.3. *Wake structures at* $Re = 800$

As Sakamoto & Haniu (1990) also found, the wake observed for a stationary sphere at $Re = 800$ was irregular in strength and frequency (see figure 26). The wake became regular as soon as the sphere began to vibrate at $U^* = 4.5$. For branch A,

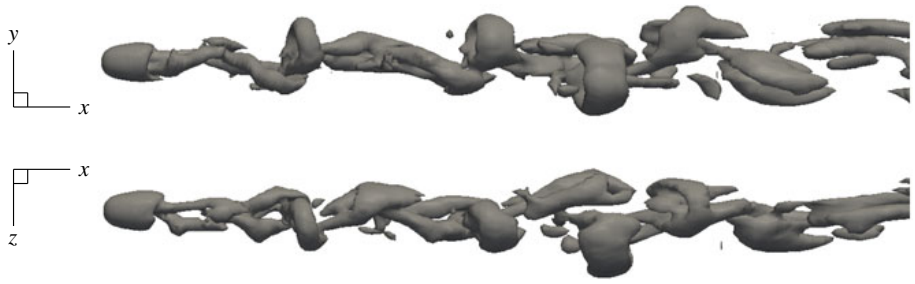

FIGURE 26. Instantaneous wake structure of a stationary sphere at $Re = 800$.

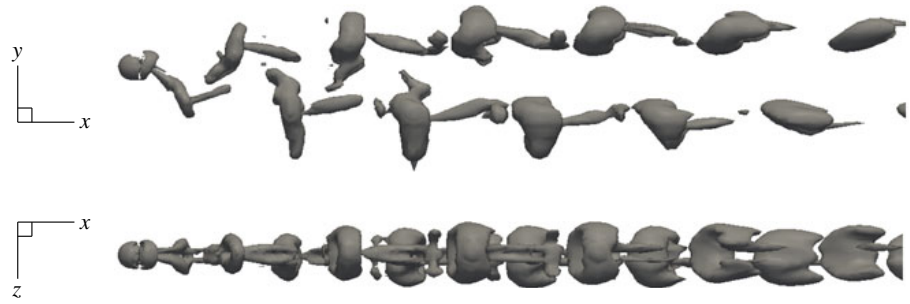

FIGURE 27. Instantaneous wake structure in branch A (depicted at $U^* = 6$) at $Re = 800$.

similarly to the $Re = 300$ case, the wake was formed with two streets of equal strength vortex loops, as shown in figure 27 at $U^* = 6$. The vortical structures were clearly two-sided hairpin loops near the sphere. However, as they moved downstream, the hairpin structures transformed into rings. Similarly to the $Re = 300$ case, a tail was attached to each vortex loop. The vortex loops were slightly twisted in the z direction; this may be due to the small-amplitude periodic force observed to occur in the z direction in this regime. The sphere response and force measurements showed a smooth transition between branch A and the intermittent branch, as discussed in the previous two sections. However, the vortex structures were regular and the vortex shedding frequency was locked in with the sphere vibration frequency until the end of branch A.

In the intermittent branch (mode IV), where the sphere showed intermittent vibration, the wake was irregular in strength and frequency. Several vortex loops were observed during an oscillation cycle. Figure 28 shows wake structures, at five consecutive times during a cycle, observed at $U^* = 30$, for which the sphere vibrated with a large amplitude. In particular, the top wake structure in figure 28 was captured when the sphere was at its lowest point, while the last structure was captured when the sphere next returned to its lowest point. As can be seen, the sphere vibration was not locked in with the vortex shedding. For the intermittent branch, the vortex loop formation appeared to be chaotic, as was the sphere response.

6. Conclusions

The VIV of a sphere restricted to move in a transverse direction (y direction) was studied numerically at $Re = 300$ and 800 over the reduced velocity ranges $U^* \in [3.5–100]$ and [3–50] respectively for a sphere of mass ratio $m^* = 2.865$.

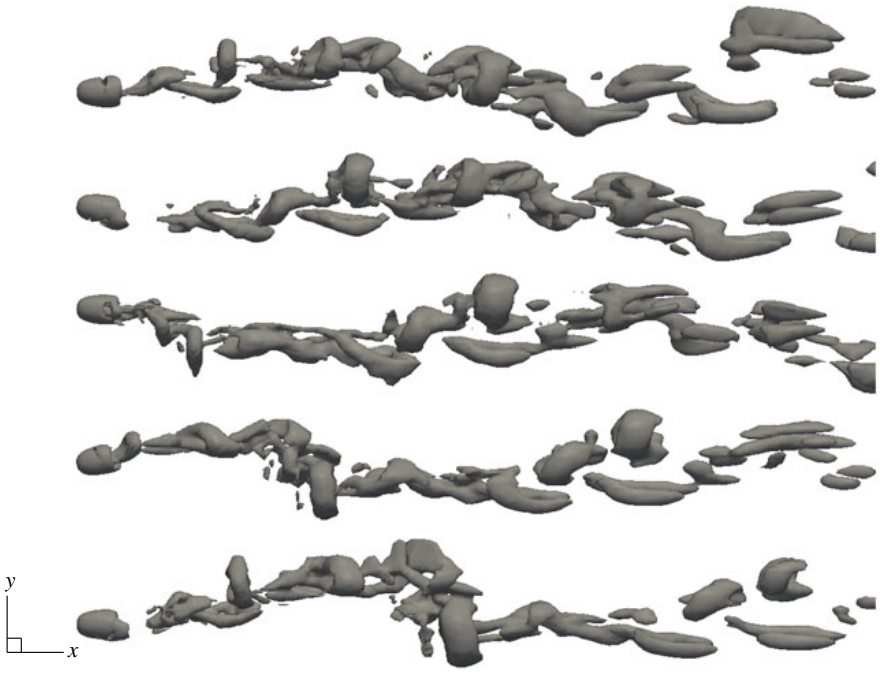

FIGURE 28. Instantaneous wake structures characteristic of the intermittent branch (depicted at $U^* = 30$) and at $Re = 800$ for a sphere starting at its lowest point and moving upwards over four consecutive steps.

It was found that the effect of varying Reynolds number on FIV was significant, with the higher-Reynolds-number simulations showing more similarities with typical higher-Reynolds-number experimental responses.

At $Re = 300$, highly periodic and large-amplitude sphere vibration was observed within the reduced velocity range $U^* \in [5.5–10]$. The sphere response amplitude curve, A^*–U^*, was approximately bell-shaped with a maximum oscillation amplitude of $0.4D$. Over this range, the sphere oscillated at the natural frequency of the system, which also corresponded to the vortex shedding frequency, indicative of VIV. This large-amplitude VIV response was named branch A. This branch showed some similarity to the mode I state observed by Govardhan & Williamson (2005), at least in terms of the jump in vortex phase over the initial part of the branch. The response curve was also similar to that observed by Behara *et al.* (2011) in their numerical investigation of 3-DOF sphere VIV at the same Reynolds number and similar mass ratio ($m^* = 3.8197$) in the reduced velocity range $U^* \in [4–9]$. Indeed, the effect of mass ratio on VIV response amplitude was found to be negligible (less than 2 %) for the range $1.2 \leqslant m^* \leqslant 10$. On increasing the Reynolds number to 800, a similar resonant response was observed within a wider reduced velocity range, $U^* \in [4.5–13]$, but with an increased maximum amplitude of $\sim 0.6D$. Compared with the case of $Re = 300$, the sphere response amplitude was substantially higher and the synchronization regime was wider. Towards maximal response, the total phase also increased, consistent with the switch to mode II observed in experiments. However, no detectable jump in the frequency response was observed across the branch, as observed in low-mass-ratio experiments, where there is a distinct change in the frequency response at the transition.

At both $Re = 300$ and 800, within branch A, a lift coefficient with a large fluctuation amplitude was observed in the direction of sphere motion. The fluctuating lift and

drag coefficients both decreased with increasing reduced velocity. The magnitude of the mean drag coefficient also displayed the same trend as the fluctuating drag coefficient. Two streets of hairpin-type vortex loops were shed behind the sphere as it oscillated, with tails attached to each loop oriented in the streamline direction. This wake structure strongly resembled that observed by Govardhan & Williamson (2005) for mode I and II vibrations, as well as the hairpin-type wake observed by Behara *et al.* (2011).

As the reduced velocity was increased beyond the branch A regime, the sphere response was highly dependent on the Reynolds number. For $Re = 300$, over the reduced velocity ranges $U^* \in [13–16]$ and $[26–100]$, the sphere vibrated at only a small amplitude (one order of magnitude less than seen in branch A). These states were named branches B and C respectively. In branch B, the sphere vibrated periodically at the system frequency. However, its time-mean position moved away from its initial position as a result of the non-zero mean lift force in the y direction due to wake asymmetry. The alignment of the total lift was found to vary from the y direction by $\sim 50°$ as the sphere vibration changed from branch A to branch B. This was matched by a change in the orientation of the vortical structures in the wake. The branch B wake resembled that of a rigidly mounted sphere with interconnected vortex loops. Based on these observations, branch B appears to be different from mode II observed in experimental studies, although there do seem to be similarities to the mode II oscillation.

For branch C, the sphere response was also periodic. However, besides the dominant frequency, the response showed an overlaid long-period oscillation. The dominant sphere vibration frequency was synchronized with the vortex shedding frequency. However, it was not close to the natural frequency of the system, as it was for branches A and B, but instead close to half of the vortex shedding frequency for a stationary sphere. The sphere oscillated about a mean position shifted from its branch A position. The shift increased as the reduced velocity was increased, reaching a value of $5D$ at $U^* = 100$. Physically, this shift can be associated with the reduction of spring stiffness as the reduced velocity is increased. A hairpin-type wake was observed for branch C as well. However, the vortex loops were more stretched in the streamwise direction due to the low frequency of shedding. Moreover, the vortex loops were one-sided.

At $Re = 800$, the sphere was found to vibrate intermittently over the reduced velocity range $U^* \in [14–50]$ immediately after branch A. This vibration state was named the intermittent branch. Even though the sphere response was aperiodic, interestingly, its main vibration frequency component was close to the natural frequency of the system. However, it was not locked in with the vortex shedding frequency, indicating a non-VIV response. The measured r.m.s. sphere response amplitudes were scattered, but with a linear increasing trend over this reduced velocity range. This sphere response resembles the aperiodic mode IV vibration discovered by Jauvtis *et al.* (2001) at higher reduced velocities for a heavy sphere ($U^* > 100$ and $m^* = 80$). There was no sign of mode III occurring prior to the onset of the mode IV vibrations found in previous experimental studies. This may be an effect of the zero-damping ratio, possibly coupled with the lower mass ratio/Reynolds number. In the intermittent branch regime, the time-mean drag coefficient was flat at the pre-oscillatory value while the time-mean lift coefficient was almost zero. A small fluctuation was observed in the lift coefficients for the y and z directions and for the drag coefficient. In the wake, multiple vortices were shed during each sphere oscillation cycle. Moreover, the vortex shedding was irregular in strength and frequency, as for a stationary sphere

at $Re = 800$. Therefore, the generation of this aperiodic vibration appeared to be a random process made possible by the large difference between the system and shedding frequencies.

With these observations, we can conclude that the characteristics of FIV of a sphere are highly dependent on the Reynolds number, particularly at high reduced velocities. At the higher Reynolds number studied of $Re = 800$, the initial oscillatory response branch bore a much stronger similarity to the response observed in the experimental studies of Sareen *et al.* (2018) for a low-mass-damped 1-DOF elastically mounted sphere, but at Reynolds numbers more than an order of magnitude greater. The non-occurrence of mode III oscillations is puzzling, but the zero-system damping may contribute to this. It would be interesting to see how increased damping and mass ratio affect the response in the corresponding reduced velocity range.

Acknowledgements

The support from Australian Research Council Discovery Grants DP150102879 and DP170100275, and computing time available through Merit Project Grants n67 and d71 through the National Computational Infrastructure (NCI) and Pawsey Supercomputing Centre are gratefully acknowledged.

REFERENCES

BEHARA, S., BORAZJANI, I. & SOTIROPOULOS, F. 2011 Vortex-induced vibrations of an elastically mounted sphere with three degrees of freedom at $Re = 300$: hysteresis and vortex shedding modes. *J. Fluid Mech.* **686**, 426–450.

BEHARA, S. & SOTIROPOULOS, F. 2016 Vortex-induced vibrations of an elastically mounted sphere: the effects of Reynolds number and reduced velocity. *J. Fluids Struct.* **66**, 54–68.

BLACKBURN, H. & HENDERSON, R. 1996 Lock-in behavior in simulated vortex-induced vibration. *Exp. Therm. Fluid Sci.* **12** (2), 184–189.

BRÜCKER, C. 1999 Structure and dynamics of the wake of bubbles and its relevance for bubble interaction. *Phys. Fluids* **11** (7), 1781–1796.

CARBERRY, J. J., SHERIDAN, J. & ROCKWELL, D. 2001 Forces and wake modes of an oscillating cylinder. *J. Fluids Struct.* **15** (1), 523–532.

CONSTANTINESCU, G. S. & SQUIRES, K. D. 2000 LES and DES investigations of turbulent flow over a sphere. *AIAA* 2000-0540. American Institute of Aeronautics and Astronautics.

DING, L., BERNITSAS, M. M. & KIM, E. S. 2013 2-D URANS versus experiments of flow induced motions of two circular cylinders in tandem with passive turbulence control for $30\,000 < Re < 105\,000$. *Ocean Engng* **72**, 429–440.

GHIDSERA, B. & DUSEK, J. 2000 Breaking of axisymmetry and onset of unsteadiness in the wake of a sphere. *J. Fluid Mech.* **423**, 33–69.

GIACOBELLO, M., OOI, A. & BALACHANDAR, S. 2009 Wake structure of a transversely rotating sphere at moderate Reynolds numbers. *J. Fluid Mech.* **621**, 103–130.

GOVARDHAN, R. & WILLIAMSON, C. H. K. 1997 Vortex-induced motions of a tethered sphere. *J. Wind Engng Ind. Aerodyn.* **69**, 375–385.

GOVARDHAN, R. & WILLIAMSON, C. H. K. 2006 Defining the modified Griffin plot in vortex-induced vibration: revealing the effect of Reynolds number using controlled damping. *J. Fluid Mech.* **561**, 147–180.

GOVARDHAN, R. N. & WILLIAMSON, C. H. K. 2005 Vortex-induced vibrations of a sphere. *J. Fluid Mech.* **531**, 11–47.

GRIFFIN, O. 1980 Vortex-excited cross-flow vibrations of a single cylindrical tube. *J. Press. Vessel Technol.* **102**, 158–166.

HABCHI, C., RUSSEIL, S., BOUGEARD, D., HARION, J.-L., LEMENAND, T., GHANEM, A., VALLE, D. D. & PEERHOSSAINI, H. 2013 Partitioned solver for strongly coupled fluid–structure interaction. *Comput. Fluids* **71**, 306–319.

HUNT, J. C. R., WRAY, A. A. & MOIN, P. 1988 Eddies, streams, and convergence zones in turbulent flows. In *Studying Turbulence Using Numerical Simulation Databases, 2*. Center for Turbulence Research, Proceedings of the Summer Program.

ISSA, R. I. 1986 Solution of the implicitly discretised fluid flow equations by operator-splitting. *J. Comput. Phys.* **62** (1), 40–65.

JAUVTIS, N., GOVARDHAN, R. & WILLIAMSON, C. H. K. 2001 Multiple modes of vortex-induced vibration of a sphere. *J. Fluids Struct.* **15** (3), 555–563.

JOHNSON, T. A. & PATEL, V. C. 1999 Flow past a sphere up to a Reynolds number of 300. *J. Fluid Mech.* **378**, 19–70.

KIM, D. 2009 Laminar flow past a sphere rotating in the transverse direction. *J. Mech. Sci. Technol.* **23** (2), 578–589.

KIM, J., KIM, D. & CHOI, H. 2001 An immersed-boundary finite-volume method for simulations of flow in complex geometries. *J. Comput. Phys.* **171** (1), 132–150.

LEE, H., HOURIGAN, K. & THOMPSON, M. C. 2013 Vortex-induced vibration of a neutrally buoyant tethered sphere. *J. Fluid Mech.* **719**, 97–128.

LEONTINI, J. S., LO JACONO, D. & THOMPSON, M. C. 2013 Wake states and frequency selection of a streamwise oscillating cylinder. *J. Fluid Mech.* **730**, 162–192.

LEONTINI, J. S., STEWART, B. E., THOMPSON, M. C. & HOURIGAN, K. 2006*a* Predicting vortex-induced vibration from driven oscillation results. *Appl. Math. Model.* **30** (10), 1096–1102; special issue of the 12th Biennial Computational Techniques and Applications Conference and Workshops (CTAC-2004) held at The University of Melbourne, Australia, from 27th September to 1st October 2004.

LEONTINI, J. S., THOMPSON, M. C. & HOURIGAN, K. 2006*b* The beginning of branching behaviour of vortex-induced vibration during two-dimensional flow. *J. Fluids Struct.* **22** (6), 857–864.

LEWEKE, T., PROVANSAL, M., ORMIÈRES, D. & LEBESCOND, R. 1999 Vortex dynamics in the wake of a sphere. *Phys. Fluids* **11**, S12–S12.

LIGHTHILL, J. 1986 Wave loading on offshore structures. *J. Fluid Mech.* **173**, 667–681.

NAUDASCHER, E. & ROCKWELL, D. 2012 *Flow-Induced Vibrations: An Engineering Guide*. Courier Corporation.

PARKINSON, G. 1989 Phenomena and modelling of flow-induced vibrations of bluff bodies. *Prog. Aerosp. Sci.* **26** (2), 169–224.

POON, E. K. W., OOI, A. S. H., GIACOBELLO, M. & COHEN, R. C. Z. 2010 Laminar flow structures from a rotating sphere: effect of rotating axis angle. *Intl J. Heat Fluid Flow* **31** (5), 961–972.

PREGNALATO, C. J. 2003 Flow-induced vibrations of a tethered sphere. PhD thesis, Monash University.

SAKAMOTO, H. & HANIU, H. 1990 A study on vortex shedding from sphere in a uniform flow. *Trans. ASME* **112**, 386–392.

SAREEN, A., ZHAO, J., LO JACONO, D., SHERIDAN, J., HOURIGAN, K. & THOMPSON, M. C. 2018 Vortex-induced vibration of a rotating sphere. *J. Fluid Mech.* **837**, 258–292.

SARPKAYA, T. 2004 A critical review of the intrinsic nature of vortex-induced vibrations. *J. Fluids Struct.* **19** (4), 389–447.

THOMPSON, M. C., LEWEKE, T. & PROVANSAL, M. 2001 Kinematics and dynamics of sphere wake transition. *J. Fluids Struct.* **15**, 575–586.

WILLIAMSON, C. H. K. & GOVARDHAN, R. 1997 Dynamics and forcing of a tethered sphere in a fluid flow. *J. Fluids Struct.* **11** (3), 293–305.

WILLIAMSON, C. H. K. & GOVARDHAN, R. 2004 Vortex-induced vibrations. *Annu. Rev. Fluid Mech.* **36**, 413–455.

WILLIAMSON, C. H. K. & GOVARDHAN, R. 2008 A brief review of recent results in vortex-induced vibrations. *J. Wind Engng Ind. Aerodyn.* **96** (6), 713–735.

WONG, K. W. L., ZHAO, J., LO JACONO, D., THOMPSON, M. C. & SHERIDAN, J. 2017 Experimental investigation of flow-induced vibration of a rotating circular cylinder. *J. Fluid Mech.* **829**, 486–511.

WU, W., BERNITSAS, M. M. & MAKI, K. 2014 RANS simulation versus experiments of flow induced motion of circular cylinder with passive turbulence control at $35\,000 < Re < 130\,000$. *J. Offshore Mech. Arctic Engng* **136** (4), 041802.

WU, X., GE, F. & HONG, Y. 2012 A review of recent studies on vortex-induced vibrations of long slender cylinders. *J. Fluids Struct.* **28**, 292–308.

I've learned that people will forget what you said, people will forget what you did, but people will never forget how you made them feel.

Maya Angelou

5. Flow-induced vibration of a rotating sphere

The rotational motion of a bluff body has a significant impact on the forces applied on it and the wake behind the body, as detailed in § 2.2. In particular, when a solid body is under a transverse rotation, it experiences a lift force (Magnus force) as the wake behind it is deflected to the advancing side due to the body rotation. Although, the Magnus effect was an interesting research topic for centuries, the nature of the vortex-induced vibration of a rotating body is less understood. Only a number of studies have been focused on VIV of a rotating body, and the recent experimental study of Sareen *et al.* (2018*a*) is the only investigation conducted based on a spherical body. Therefore, to enhance the understanding of the correlation between the Magnus effect caused by the sphere rotation and the vortex-induced vibration, a set of simulations was conducted at $Re = 300$ with a sphere of mass ratio $m^* = 2.865$ over the rotation rates $0 \leq \alpha \leq 2.5$. The reduced velocity range $3.5 \leq U^* \leq 11$ was chosen for the study as the sphere showed a periodic VIV response within this range for the zero-rotation case, as described in chapter 4. The content of the chapter is the following article published in the Journal of Fluid Mechanics that reproduced with the permission

Rajamuni, M. M., Thompson, M.C. & Hourigan, K. 2018 Vortex-induced vibration of a transversely rotating sphere. *Journal of Fluid Mechanics* **847** , 786–820.

We found that there is a significant effect of sphere rotation on the vortex-induced vibration. Although the sphere showed synchronized vibrations under a forced rotation, the time-mean position of the sphere was shifted away from the initial position; this was more prominent with increasing U^* as well as with increasing α. The sphere response amplitude was found to decrease globally with increasing rotation rate. In addition, the range of reduced velocities at which the sphere showed synchronized vibration narrowed with increasing α. Importantly, the vortex-induced vibrations were completely suppressed for $\alpha > 1.3$ due to the suppression of vortex shedding, as a result of symmetry breaking of the wake behind the sphere introduced by the Magnus effect. The response amplitude was found to increase with the increasing Reynolds number, indicating that VIV can persist even at higher rotation rates at higher Reynolds number flows, as observed by Sareen *et al.* (2018*a*).

J. Fluid Mech. (2018), *vol.* 847, *pp.* 786–820.
doi:10.1017/jfm.2018.309

Vortex-induced vibration of a transversely rotating sphere

Methma M. Rajamuni[1,†], Mark C. Thompson[1] and Kerry Hourigan[1]

[1]Fluids Laboratory for Aeronautical and Industrial Research (FLAIR), Department of Mechanical and Aerospace Engineering, Monash University, Clayton, Victoria 3800, Australia

(Received 6 September 2017; revised 12 January 2018; accepted 1 April 2018)

The effects of transverse rotation on the vortex-induced vibration (VIV) of a sphere in a uniform flow are investigated numerically. The one degree-of-freedom sphere motion is constrained to the cross-stream direction, with the rotation axis orthogonal to flow and vibration directions. For the current simulations, the Reynolds number of the flow, $Re = UD/\nu$, and the mass ratio of the sphere, $m^* = \rho_s/\rho_f$, were fixed at 300 and 2.865, respectively, while the reduced velocity of the flow was varied over the range $3.5 \leqslant U^* \ (\equiv U/(f_n D)) \leqslant 11$, where, U is the upstream velocity of the flow, D is the sphere diameter, ν is the fluid viscosity, f_n is the system natural frequency and ρ_s and ρ_f are solid and fluid densities, respectively. The effect of sphere rotation on VIV was studied over a wide range of non-dimensional rotation rates: $0 \leqslant \alpha \ (\equiv \omega D/(2U)) \leqslant 2.5$, with ω the angular velocity. The flow satisfied the incompressible Navier–Stokes equations while the coupled sphere motion was modelled by a spring–mass–damper system, under zero damping. For zero rotation, the sphere oscillated symmetrically through its initial position with a maximum amplitude of approximately 0.4 diameters. Under forced rotation, it oscillated about a new time-mean position. Rotation also resulted in a decreased oscillation amplitude and a narrowed synchronisation range. VIV was suppressed completely for $\alpha > 1.3$. Within the U^* synchronisation range for each rotation rate, the drag force coefficient increased while the lift force coefficient decreased from their respective pre-oscillatory values. The increment of the drag force coefficient and the decrement of the lift force coefficient reduced with increasing reduced velocity as well as with increasing rotation rate. In terms of wake dynamics, in the synchronisation range at zero rotation, two equal-strength trails of interlaced hairpin-type vortex loops were formed behind the sphere. Under rotation, the streamwise vorticity trail on the advancing side of the sphere became stronger than the trail in the retreating side, consistent with wake deflection due to the Magnus effect. This symmetry breaking appears to be associated with the reduction in the observed amplitude response and the narrowing of the synchronisation range. In terms of variation with Reynolds number, the sphere oscillation amplitude was found to increase over the range $Re \in [300, 1200]$ at $U^* = 6$ for each of $\alpha = 0.15$, 0.75 and 1.5. The VIV response depends strongly on Reynolds number, with predictions indicating that VIV will persist for higher rotation rates at higher Reynolds numbers.

Key words: aerodynamics, flow–structure interactions

† Email address for correspondence: methma.rajamuni@monash.edu

1. Introduction

A vast amount of research has been dedicated to the understanding of fluid–structure interaction (FSI) because of its practical significance in many fields. For example, fluid flow can induce structural vibration as a result of the formation of alternately shedding vortices into the wake, which is known as flow-induced vibration. If the vibration triggers resonance, then the structure may suffer fatigue or even catastrophic failure. Vortex-induced vibration or VIV is a periodic flow-induced vibration state. VIV can be identified with vibrations that occur through the synchronisation of the structural response with the wake unsteadiness (i.e. vortex shedding) when the frequency is close to the system's natural frequency. The occurrence of VIV can be found for structures such as bridges, chimney stacks, cables, air planes, ground vehicles, submarines and marine vessels, when there is a relative motion between the fluid and the solid structure. Therefore, it is important to study the nature of vortex-induced vibration and its mechanisms as a means for its control.

The fundamentals of VIV have been studied substantially through experimental and numerical research studies focusing on basic geometries, many of which are discussed in the comprehensive reviews of Bearman (1984), Parkinson (1989), Sarpkaya (2004), Williamson & Govardhan (2004, 2008) and Wu, Ge & Hong (2012). Most of these studies were based on cylindrical structures due to their intrinsic engineering importance and due to the simplicity of setting up such models, both experimentally and computationally. For VIV of a cylinder, three distinct branches (initial, upper and lower) have been observed in the vibration amplitude response curve $A^*(U^*)$, where A^* is the non-dimensional vibration amplitude and U^* is the reduced velocity. Govardhan & Williamson (2000) revealed that the first transition involved a jump in the 'vortex phase', related to the changing dynamics of vortex forcing in the transition between $2S$ and $2P$ shedding wake modes; the second transition involved a jump in the 'total phase'.

Compared to VIV of a cylinder, fewer studies have been devoted to developing an understanding of VIV of a sphere, despite the fact that there is an abundance of applications involving spherical bodies. For example, tethered bodies such as buoys, underwater mines, tethered balloons and towed objects behind vessels. A series of experimental studies conducted by Govardhan & Williamson (1997), Williamson & Govardhan (1997), Jauvtis, Govardhan & Williamson (2001) and Govardhan & Williamson (2005) using tethered spheres subject to one or two degrees of freedom (DOF) motion revealed that a sphere also showed a VIV behaviour with a large oscillation amplitude, similar to that of a cylinder. Furthermore, they observed four different modes of vibrations (named modes I–IV) with varying characteristics in terms of sphere oscillation amplitude and phase, and wake structures. The first two modes of oscillation appeared within the reduced-velocity range $5 \lesssim U^* \lesssim 10$. For these two modes, the body oscillation frequency, f, was close to the natural vortex-shedding frequency, f_{vor}, and the system's natural frequency, f_n; this indeed suggested that these two modes of vibration were vortex-induced vibration. A similar observation was reported over the reduced velocity range, $3 \lesssim U^* \lesssim 14$ by Hout, Katz & Greenblatt (2013) and Krakovich, Eshbal & Hout (2013) in their investigations of VIV of a tethered sphere. The sphere response amplitude smoothly transitioned from mode I to mode II, in contrast to the VIV response of a cylinder, which displays discontinuous branches in the amplitude response curve. Govardhan & Williamson (2005) identified that there was a smooth $\sim 90°$ phase difference in vortex phase (the phase between the vortex force and the sphere displacement) between mode I and mode II. In these two modes, they found that two-sided hairpin-type vortex loops

were shedding into the wake as the sphere vibrated. Moreover, there was a change in timing of vortex shedding relative to the sphere motion once it passed from mode I to mode II, which was consistent with their observation of the change in vortex phase.

Following the mode II vibration as the reduced velocity was increased, Jauvtis *et al.* (2001) observed mode III vibration began at a reduced velocity $U^* \sim 20$–40 with heavy spheres of $m^* = 80$ and 940. In contrast to modes I and II, the principal vortex-shedding frequency for mode III vibration was three to eight times higher than the sphere vibration frequency (Jauvtis *et al.* 2001). Therefore, mode III vibration was difficult to explain by classical lock-in theories. However, Govardhan & Williamson (2005) argued that if the body were to be perturbed, it could generate a self-sustaining vortex force that could be sustained over multiple shedding cycles, leading to body vibrations of large amplitudes. They categorised mode III as movement-induced excitation (Naudascher & Rockwell 2012). In this mode of vibration, Govardhan & Williamson (2005) observed that there is an underlying streamwise vortex structure, which is synchronised with the sphere vibration frequency, enabling highly periodic vibration. Consistently, they observed long vortex-loop structures. Subsequently, Jauvtis *et al.* (2001) observed mode IV vibration, at very high reduced velocities ($U^* > 100$). In this mode, the sphere oscillation frequency was not periodic as it was in the first three modes, but interestingly, the vibration frequency was very close to the natural frequency of the system.

Apart from those experimental studies, a few numerical studies have also been reported on VIV of a sphere. Pregnalato (2003) investigated the VIV of a tethered sphere at the Reynolds number 500 with two different mass ratios ($m^* = 0.8$, and 0.082). In that numerical study, he observed modes II–IV vibrations that had been observed in the experimental studies of Jauvtis *et al.* (2001). In the higher mass-ratio case, mode II appeared in the reduced-velocity range, $U^* \approx 5$–10, while modes III and IV appeared for $U^* > 10$. However, for the lower mass-ratio case, mode IV vibration did not appear in the reduced-velocity range studied ($U^* = 0$–20). Therefore, he suspected that there exists a critical mass for mode IV VIV of a sphere to occur. More recently, Lee, Thompson & Hourigan (2008) and Lee, Hourigan & Thompson (2013) investigated the VIV of a neutrally buoyant ($m^* = 1$) tethered sphere, which was constrained to move on a spherical surface. This was a combined numerical and experimental study that covered the Reynolds number range $Re = 50$–12 000. They found there to be seven different broad and relatively distinct sphere oscillation and wake states.

Behara, Borazjani & Sotiropoulos (2011) investigated VIV of a sphere allowing 3 DOF movement at a Reynolds number of 300 and reduced mass of 2, for the reduced-velocity range $4 \leqslant U^* \leqslant 9$. In their study, the sphere showed two different amplitude responses, corresponding to two different wake states at the same reduced velocity. In one case, the sphere moved in a circular orbit with a spiral-type wake shedding behind the sphere. In the other case, the sphere vibrated in a plane with hairpin-type vortex loops shedding behind the sphere. They observed two different amplitude response curves corresponding to each case. The sphere oscillation amplitude was smaller when it moved in a circular orbit compared to the planar state. In addition, they observed hysteresis in the response when the sphere was moving in a circular orbit at the beginning of the synchronisation regime. This study was extended by Behara & Sotiropoulos (2016) by expanding the reduced-velocity range to $0 \leqslant U^* \leqslant 13$, and by varying the Reynolds number of the flow from $Re = 300$ to 1000 for one fixed reduced-velocity case ($U^* = 9$). It was found that the sphere trajectories were strongly dependent on the Reynolds number.

The effect of the rotational motion on bluff bodies has been investigated for centuries. Early research studies carried out by Robins in the eighteenth century (Robins 1972) and Magnus in the nineteenth century (Magnus 1853) revealed that a bluff body experiences a lift force ('Magnus force') when it propagates with a transverse rotation. Later in the twentieth century, researchers investigated the effect of the rotation rate, $\alpha = \omega D/2U$, of a sphere on the drag and lift forces (F_d and F_l), where ω is the angular speed of the sphere, D is the diameter of the sphere and U is the free-stream velocity of the flow. Rubinow & Keller (1961) derived an expression for the lift force acting on a transversely rotating sphere for the Stokes regime ($Re \leqslant 1$ and $\alpha \leqslant 0.01$). They found that the drag force was independent of the rotation rate and that the lift coefficient, $C_l = F_l/(0.5\rho_f U\pi(D/2)^2)$, could be expressed as 2α. Kurose & Komori (1999) considered the flow regimes $1 \leqslant Re \leqslant 500$ and $0 \leqslant \alpha \leqslant 0.25$, and found that both drag and lift forces increased with the rotation rate.

In more recent studies, the effects of transverse rotation on the forces and wake structures behind a sphere were investigated by Giacobello, Ooi & Balachandar (2009) for rotation rates, $\alpha \leqslant 1$, by Kim (2009) for $\alpha \leqslant 1.2$ and by Dobson, Ooi & Poon (2014) for $1.25 \leqslant \alpha \leqslant 3$. All three studies were conducted at $Re = 100$, 250 and 300. At $Re = 100$, they found that the axisymmetric flow present for no sphere rotation became planar symmetric with a double-threaded wake in the presence of rotation up to $\alpha = 3$. At $Re = 250$ and 300, the flow underwent a series of different transitions between 'steadiness' and 'unsteadiness' as the rotation rate was increased. Kim (2009) claimed that the unsteady vortex shedding observed at higher rotation rates (at $Re = 250$ and $\alpha = 1.2$, and at $Re = 300$ and $\alpha = 1$–1.2) was due to the shear-layer instability of the flow. Dobson *et al.* (2014) observed that when $\alpha > 2$, the flow entered a regime different to the shear-layer instability regime; this was named the separatrix regime. Their studies also revealed that the drag force increased up to $\alpha \approx 2$ and then decreased, while the lift coefficient increased up to $\alpha \approx 1.25$ and then became constant. Poon *et al.* (2014) studied the unsteadiness of the flow at $Re = 500$ and 1000 for $0 \leqslant \alpha \leqslant 1.2$ and revealed a new flow regime, the shear-layer stable foci regime, at higher values of α.

A recent experimental study on the flow-induced vibration of an elastically mounted rotating cylinder by Seyed-Aghazadeh & Modarres-Sadeghi (2015) revealed that the synchronisation regime became narrower at higher rotation rates, and oscillations ceased beyond $\alpha = 2.4$. They varied the rotation rate from 0 to 2.6 in the Reynolds number range $350 \leqslant Re \leqslant 1000$. It was observed that cylinder rotation does not significantly influence the oscillation amplitude. As the rotation rate increased at a constant reduced velocity, the vortex-shedding pattern changed from $2S$ to $2P$. Bourguet & Jacono (2014) numerically investigated flow-induced vibration of a transversely rotating cylinder at $Re = 100$. They observed that the peak oscillation amplitude increased with the reduced velocity up to $\alpha = 3.75$. Moreover, the maximum amplitude response of a rotating cylinder was three times higher than the non-rotating case. They also observed that the reduced-velocity range over which the cylinder showed synchronised vibration (synchronisation regime) broadened up to $\alpha = 3.5$, and then narrowed. Vibration was completely suppressed for $\alpha = 4$. They observed two new vortex-shedding patterns at high rotation rates; a $T + S$ pattern (a triplet with a single vortex per cycle) and the U pattern (transverse undulation of the spanwise vorticity layers without vortex detachment).

Despite the fact that rotation greatly influences the oscillatory motion of a sphere, to the authors' knowledge, no experimental or numerical studies have been yet

reported for the flow-induced vibration of a rotating sphere. Therefore, in the present work, the effects of transverse rotation on the vortex-induced vibration of a sphere are investigated by examining the sphere displacement, forces exerted on the sphere and wake structures behind the sphere at $Re = 300$, for rotation rate $0 \leqslant \alpha \leqslant 2.5$ and reduced-velocity range $3.5 \leqslant U^* \leqslant 11$. In addition to that, the effects of Reynolds number on VIV of a rotating sphere are investigated over the Reynolds number range, $300 \leqslant Re \leqslant 1200$ at the rotation rates $\alpha = 0.15$, 0.75 and 1.5 and $U^* = 6$. The structure of this paper is as follows: the next section describes the numerical methods used; the following section presents validation studies performed; the results section presents the sphere response to VIV, reports on the forces exerted on the sphere and documents the wake structures; the effects of Reynolds number on VIV of a rotating sphere are presented in the next section; followed by concluding remarks.

2. Numerical methods

In this study, the widely used open-source computational fluid dynamics (CFD) package OpenFOAM was utilised for the numerical simulations. OpenFOAM enables the solution of a variety of flows including compressible, incompressible, turbulent and multiphase flows. It also facilitates the solution of FSI problems through dynamic grid techniques (Jasak & Tukovic 2010). However, those dynamic grid techniques are highly time consuming due to the deformation of the grid at each time step, which adds a considerable overhead. Therefore, a non-deformable grid was used in this study to improve the efficiency of the solution process. Blackburn & Henderson (1996) and Leontini *et al.* (2006*a*) also used a non-deformable grid by modelling fluid flow in a body-fixed frame. This approach is far more efficient than a dynamic grid technique. In this section, first, the FSI system and FSI solver are discussed in detail in the following two subsections; second, the computational details are provided.

2.1. *Governing equations*

The Newtonian fluid is assumed incompressible and viscous, and modelled in a body-fixed reference frame that is attached to the centre of the sphere. This is a non-inertial reference frame, since the sphere is allowed to move according to the fluid forces acting on it. Therefore, the momentum equation should be corrected to include a term accounting for the acceleration of the frame, which is just the acceleration of the sphere as represented by the last term in (2.1) below. The sphere is assumed to behave as a spring–mass–damper system. Thus, the fluid–solid coupled system can be described by the Navier–Stokes equations, given in (2.1) and (2.2), with the dynamic motion of the sphere described by (2.3):

$$\frac{\partial \boldsymbol{u}}{\partial t} = -(\boldsymbol{u} \cdot \nabla)\boldsymbol{u} - \frac{1}{\rho}\nabla p + \nabla \cdot \nu \nabla \boldsymbol{u} - \ddot{\boldsymbol{y}}_s, \tag{2.1}$$

$$\nabla \cdot \boldsymbol{u} = 0, \tag{2.2}$$

$$m\ddot{\boldsymbol{y}}_s + c\dot{\boldsymbol{y}}_s + k\boldsymbol{y}_s = \boldsymbol{f}_l, \tag{2.3}$$

where $\boldsymbol{u} = \boldsymbol{u}\ (x, y, z, t)$ is the velocity vector field, p is the scalar pressure field, ρ is the fluid density, ν is the kinematic viscosity, $\boldsymbol{y}_s$, $\dot{\boldsymbol{y}}_s$ and $\ddot{\boldsymbol{y}}_s$ are the sphere displacement, velocity and acceleration vectors, respectively, m is the mass of the sphere, c is the damping constant, k is the structural spring constant and $\boldsymbol{f}_l$ is the flow-induced vector force acting on the sphere due to pressure and viscous shear forces.

2.2. *The fluid–structure solver*

Within the OpenFOAM framework, a new solver (named 'vivicoFoam') was developed to solve the fluid–structure coupled system defined by (2.1)–(2.3) for laminar flows. The details of this solver are provided in Rajamuni, Thompson & Hourigan (2018), so only brief details are provided here.

The solver is based on the pressure implicit splitting of operators (PISO) algorithm for solving the unsteady incompressible Navier–Stokes equations (Issa 1986). Within this framework, the coupled fluid–structure system is treated using a third-order predictor–corrector method as described in Rajamuni *et al.* (2018). The flow and structure equations are thus solved in a strongly coupled manner, with convergence determined when the magnitudes of the fluid force and solid acceleration converge to within a prescribed error bound, typically $\epsilon = 0.001$. Tests were performed to ensure that the chosen bound was sufficient to provide converged flow solutions. Typically, the FSI solver required 3 corrector steps. In most cases the number of corrector steps was less than 10 with the upper limit set to 15.

It should be noted that this FSI solver is overall second order in temporal accuracy, despite the fact that the above mentioned FSI algorithm is third-order time accurate. This is because the PISO algorithm itself is of second-order accuracy. It is recalled that the fluid domain was modelled in a moving frame of reference. The motion of this reference frame was taken into the account by adjusting the velocity boundary conditions at the outer domain (except the outlet boundary). In this study, all the outer boundaries except the outlet are treated as defined velocity boundaries. Once the predictor–corrector iterative process is completed, the velocity at these inlet boundaries is updated according to the sphere velocity, before proceeding to the next time step.

2.3. *Computational details*

A uniform flow past a sphere forced to rotate and mounted with elastic supports in the transverse direction was investigated using the FSI solver. As shown in figure 1, the flow is in the x direction, and the sphere is restricted to translate only in the y direction while it rotates about the $-z$ direction with an angular velocity of ω. A cube of $100D$ was chosen for the fluid domain with the sphere at its centre. In this study, the sphere is assumed to translate as a spring–mass system without any damping to obtain the highest vibration amplitude. Moreover, in the FSI solver, $\boldsymbol{y}_s$, $\dot{\boldsymbol{y}}_s$, $\ddot{\boldsymbol{y}}_s$ and $\boldsymbol{f}_l$ are treated as vectors with zero x and z components, since the sphere translation is restricted to the y direction only. At the inlet boundaries, a Dirichlet boundary condition was prescribed for the velocity, while a zero-gradient Neumann boundary condition was prescribed for the pressure, as shown in figure 1. At the sphere surface, no-slip and no-penetration boundary conditions were applied using a rotating wall velocity. A Neumann boundary condition was prescribed for the pressure at the sphere surface. However, the normal pressure gradient at the sphere surface is in general non-zero due to the rotation of the sphere. Therefore, it was calculated by taking the inner product of momentum equation (2.1) and the outward unit normal vector, $\boldsymbol{\eta}$, as follows:

$$\nabla p \cdot \boldsymbol{\eta} = (-(\boldsymbol{u} \cdot \nabla)\boldsymbol{u} + \nabla \cdot \nu \nabla \boldsymbol{u} - \ddot{\boldsymbol{y}}_s) \cdot \boldsymbol{\eta}. \tag{2.4}$$

At the outlet boundary, the pressure was set to zero while the velocity was prescribed as zero gradient in the normal direction.

Figure 2 displays the unstructured grid used for the fluid domain. To achieve high concentration near the sphere, a cube of $5D$ was placed around the sphere. This cube

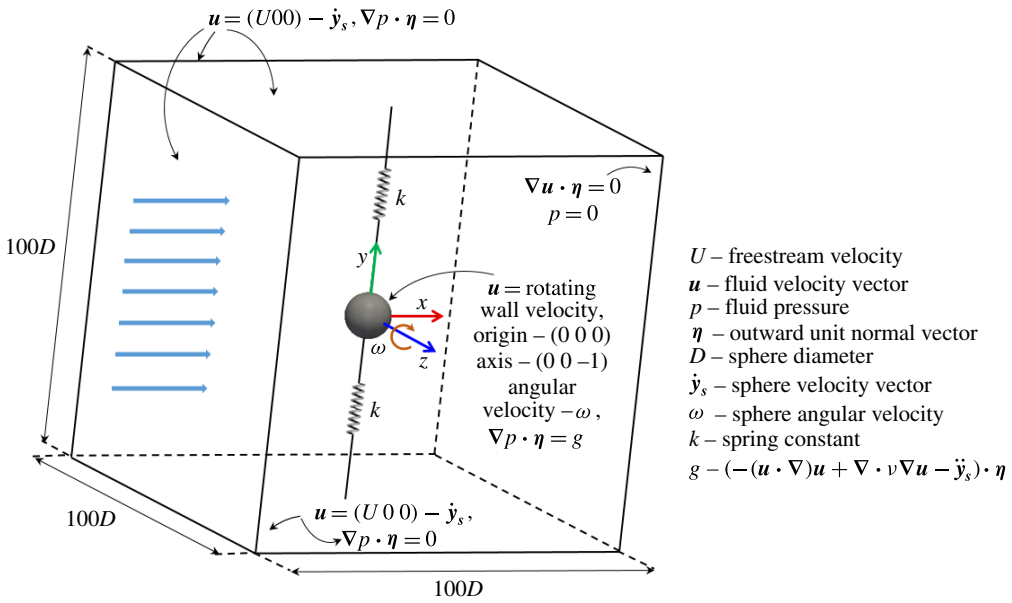

FIGURE 1. (Colour online) Schematic of the computational domain and boundary conditions.

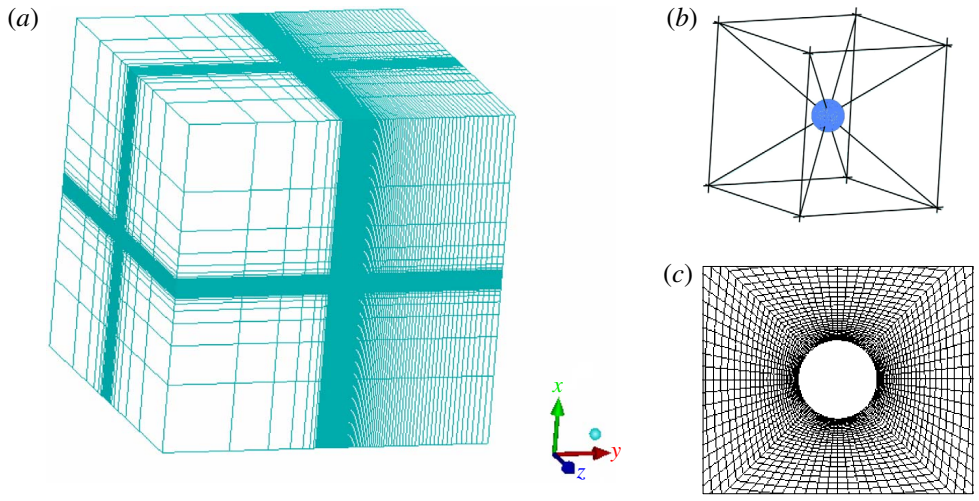

FIGURE 2. (Colour online) The unstructured-grid computational domain: (*a*) isometric view; (*b*) the cubic block placed around the sphere, which was decomposed into six square frustums; (*c*) grid near the sphere surface at *xy* plane.

was decomposed into six square frustum-shaped blocks, as shown in figure 2(*b*). The grid was compressed near the sphere surface by selecting an exponentially distributed cell thickness in the radial direction in each square frustum (see figure 2*c*). A large number of grid points was assigned in the downstream direction to resolve the wake structures. Four finer grids were generated to assess the grid independence analysis (refer to the next section for more details). To optimise the grid generation process, initially, the number of cells on the surface of the sphere, N, was kept constant at 7350. This grid (grid 1) comprised $\simeq$0.79 million cells with a minimum cell

thickness in the radial direction from the sphere surface, δl, of $0.011D$. The second grid was generated by decreasing δl to $0.004D$. This yielded $\simeq$1.25 million cells, with approximately 10–16 cells within the boundary layer. This grid is sufficient to resolve the flow in the near wake. However, two more grids were generated to ensure that the solution was grid independent. In the third grid, δl was further decreased to $0.002D$ by choosing the same number of cells as grid 2. Finally, the fourth grid was generated by increasing N to 18 150 by choosing the same δl as grid 2 to observe the effect of cell thickness in the tangential direction on the solution. The non-dimensional time step, $\delta\tau = \delta t U/D$, used with each grid for all the analyses was 0.005.

3. Numerical sensitivity and validation studies

This section presents two validation studies. The first study aims to display the ability of capturing important physics of the flow past a rigidly mounted and transversely rotating sphere at Reynolds number 300. The second study demonstrates the validation of the newly built FSI solver for vortex-induced vibration studies. Finally, grid independence analyses performed for vortex-induced vibration of a sphere are presented.

3.1. *Transversely rotating rigid sphere*

Flow past a rigidly mounted and transversely rotating (in the $-z$ direction) sphere was investigated at $Re = 300$ for the rotation rates $0 \leqslant \alpha \leqslant 3$. The computed values of the time-mean drag coefficient, $\overline{C}_d$, and the time-mean lift coefficient, $\overline{C}_l$, are compared with other studies in figures 3(*a*) and 3(*b*), respectively. The present results agree well with the results in the literature (Giacobello *et al.* 2009; Kim 2009; Poon *et al.* 2010; Dobson *et al.* 2014). The time-mean lift coefficient increased with increasing α but levelled off at higher rotation rates. The drag coefficient increased with α up to $\alpha \approx 1.75$ and then decreased.

The flow underwent a series of transitions between 'steadiness' and 'unsteadiness' as the rotation rate increased from 0, as shown in table 1. From $\alpha = 0$ to 0.3, the flow was unsteady with vortex shedding. Moreover, the shedding frequency increased as the rotation rate increased. For $\alpha = 0.4$, the flow became steady with a double-threaded wake structure. As α increased further, the flow remained steady until $\alpha = 2$ with a double-threaded wake, except for $\alpha = 1.25$, where the flow was unstable due to the shear-layer instability, as discussed by Kim (2009). For $\alpha \in [2.25, 3]$, the flow became unstable again, but with an asymmetric wake structure having no symmetry at all. Figures 4 and 5 show comparisons of wake structures observed in the present study with Giacobello *et al.* (2009) and Dobson *et al.* (2014) at five rotation rates. The wake structures observed at low rotation rates ($\alpha \in [0, 0.6]$) match well with other research studies; for example, for $\alpha = 0$, 0.3 and 0.5. At higher rotation rates, for example, for $\alpha = 1$ and 1.5, the wake structures observed at the initial stage are similar to those observed by Giacobello *et al.* (2009) and Dobson *et al.* (2014). However, for very long simulation times, the initially unsteady flow became steady with a double-threaded wake structure.

3.2. *Validation: VIV of a cylinder*

A series of simulations was conducted with a rigidly mounted cylinder (non-rotating) to validate the numerical solver developed for the FSI problems by selecting the

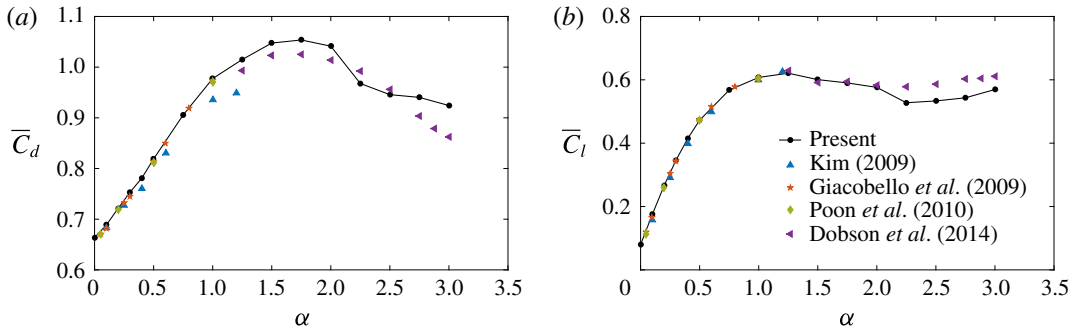

FIGURE 3. (Colour online) Comparison with other numerical studies of computed time-mean drag coefficient, $\overline{C}_d$, and time-mean lift coefficient, $\overline{C}_l$, for flow past a rigidly mounted and transversely rotating sphere at $Re = 300$ for $0 \leqslant \alpha \leqslant 3$.

α	Nature of the flow	Wake structure
[0, 0.3]	Unsteady	Vortex shedding
[0.4, 1]	Steady	Double-threaded wake
1.25	Unsteady	Shear-layer instability
[1.5, 2]	Steady	Double-threaded wake
[2.25, 3]	Unsteady	Asymmetric

TABLE 1. Comparison of the nature of the flow with the rotation rate of flow past a transversely rotating sphere.

study by Leontini, Thompson & Hourigan (2006*b*) as the base case. The mass ratio, damping constant and the Reynolds number of the flow were fixed at $m^* = 10$, $\zeta = 0.01$ and $Re = 200$, respectively, while varying the reduced velocity from $U^* = 3.5$ to 7.1. The oscillation amplitude of the cylinder, A^*, the fluctuation amplitude of the lift coefficient, C_l', the frequency ratio of cylinder vibration to the natural frequency of the system, $f^* = f/f_n$, and the average phase angle between lift force and cylinder vibration, ϕ, were calculated and compared with Leontini *et al.* (2006*b*). The percentage difference calculated for A^*, C_l', f^*, and ϕ are $-8\,\%$, $-8\,\%$, $1.8\,\%$ and $3.6\,\%$, respectively, compared to the results of Leontini *et al.* This study provides validation for the new solver.

3.3. *Resolution studies*

All FSI simulations reported in the next section have been carried out on grid 2. To verify that this grid is fine enough to resolve the flow for FSI simulations, two grid sensitivity analyses were performed; one analysis for the vibrating sphere cases for the parameters, $\alpha = 0$ and $U^* = 7$; a second analysis for the higher rotation rates for the parameters $\alpha = 1.5$ and $U^* = 6$. Both analyses were performed at $Re = 300$ and $m^* = 2.865$ (or $m_r = 1.5$). For the first analysis, $U^* = 7$ was chosen because the sphere showed a maximum oscillation around this value. Table 2 compares the effect of grid refinement for both analyses. In the first analysis ($\alpha = 0$ and $U^* = 7$), the sphere underwent synchronised vibrations. Therefore, the results were tabulated for the sphere oscillation amplitude, A^*, force coefficients (time-mean drag coefficient, $\overline{C}_d$, root-mean-square (r.m.s.) values of the fluctuation components of drag and lift

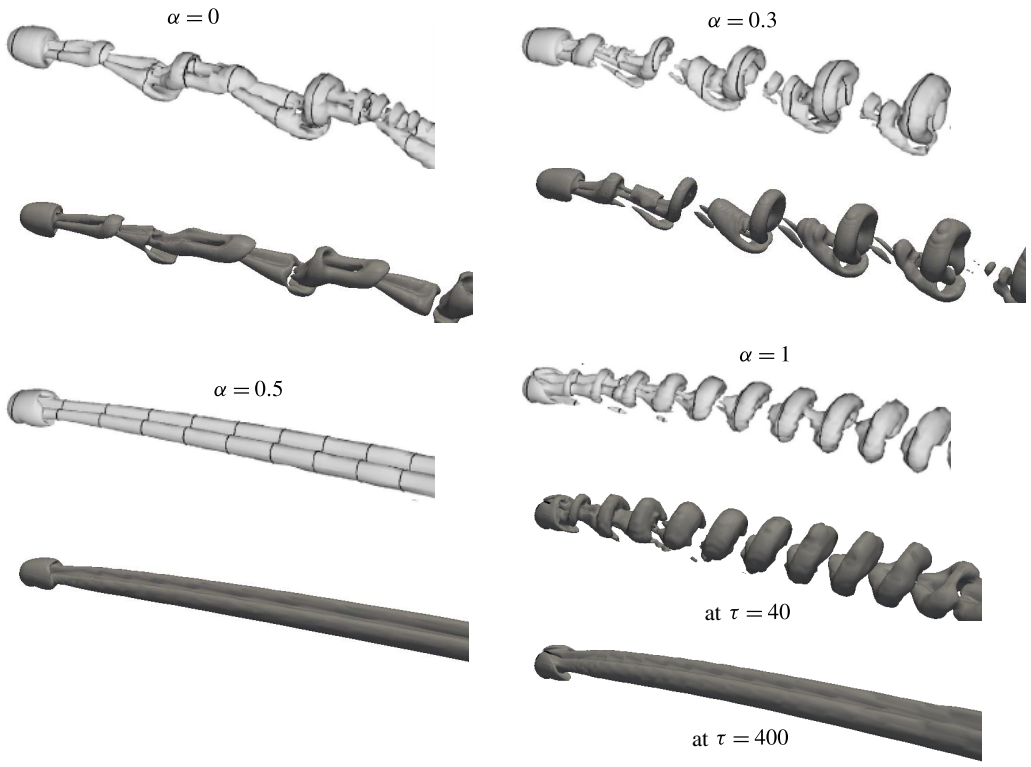

FIGURE 4. Wake structures of a rigidly mounted and transversely rotating sphere for $\alpha = 0$, 0.3, 0.5 and 1. Light grey structures are the results of Giacobello *et al.* (2009); dark structures are the results of the present study identified using the method of Jeong & Hussain (1995) at $\lambda_2 = -5 \times 10^{-4}$. For $\alpha = 1$, the wake structure varied with the time. Initially, the flow was unsteady as shown at $\tau = 40$, but for longer simulation time, the flow became stable with a double-threaded wake structure, as shown at $\tau = 400$, where $\tau = tU/D$ is the non-dimensional time.

coefficients, $C_{d,rms}$ and $C_{l,rms}$), and frequency ratio, $f^* = f/f_n$. In the second analysis ($\alpha = 1.5$ and $U^* = 6$), the flow was steady and the sphere moved to a new position and remained with no vibration. Therefore, the time-mean sphere displacement, $\overline{Y}/D$, time-mean drag and lift coefficients $\overline{C}_d$, and $\overline{C}_l$ were calculated. It is noted that there is less than 1 % variation in the results between grid 1 and grid 2 for both analyses. The results obtained for grids 2–4 agree well with each other. Therefore, for the Reynolds number and rotation rate range of interest, decreasing δl or increasing N further has a negligible effect on the results. Thus, we can conclude that grid 2 is sufficient for all VIV simulations at $Re = 300$, and therefore, this grid was used to obtain all subsequently presented results. As pointed out above, the non-dimensional time step used in these resolution studies and all the other simulations is $\delta\tau = 0.005$. It was verified that reducing the time step by a factor of two, resulted in a less than 1 % change to the key convergence measures discussed above.

4. Effects of transverse rotation on VIV of a sphere

This section presents and discusses the results obtained for flow past an elastically mounted sphere (allowed to translate only in the y direction) forced to rotate about the

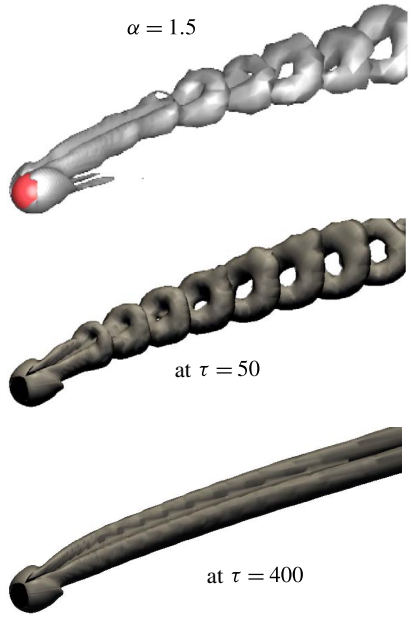

FIGURE 5. (Colour online) Comparison of wake structures of a rigidly mounted and transversely rotating sphere for $\alpha = 1.5$ with Dobson *et al.* (2014) (the dark structure). The light structures are the results of the present study.

			$(\alpha, U^*) = (0, 7)$					$(\alpha, U^*) = (1.5, 6)$		
Grid	δl	N	A^*	$\overline{C}_d$	$C_{d,rms}$	$C_{l,rms}$	f/f_n	$\overline{Y}/D$	$\overline{C}_d$	$\overline{C}_l$
1	$0.011D$	7 350	0.38	0.81	0.05	0.11	0.93	0.15	1.04	0.61
2	$0.004D$	7 350	0.37	0.80	0.05	0.11	0.93	0.14	1.04	0.60
3	$0.002D$	7 350	0.37	0.80	0.05	0.10	0.93	0.14	1.04	0.60
4	$0.002D$	18 150	0.37	0.80	0.05	0.10	0.93	0.14	1.04	0.60

TABLE 2. The sensitivity of the spatial resolution of the flow parameters of vortex-induced vibration of a rotating sphere at $(\alpha, U^*) = (0, 7)$ and $(1.5, 6)$, $Re = 300$ and $m^* = 2.865$ $(m_r = 1.5)$. δl is the minimum thickness of the cells (in the radial direction) at the sphere surface in each grid and N is the number of cells on the sphere surface. The oscillation amplitude of the sphere, A^*, the time-mean sphere displacement, $\overline{Y}/D$, the time-mean drag and lift coefficients, $\overline{C}_d$ and $\overline{C}_l$, the r.m.s. values of fluctuation component of the drag and lift coefficients, $C_{d,rms}$ and $C_{l,rms}$, and the ratio of vortex-shedding frequency to the natural frequency, f/f_n, are listed.

$-z$ direction at the Reynolds number $Re = 300$ and the reduced mass $m_r = 1.5$ (which is equivalent to the mass ratio $m^* = 2.865$) for rotation rates $0 \leqslant \alpha \leqslant 2.5$ and a reduced-velocity range $3.5 \leqslant U^* \leqslant 11$. Non-rotating VIV studies, especially the many studies of circular cylinders but also spheres, show that the amplitude response is not a very strong function of mass ratio, but rather a function of the mass-damping ratio $(m^*\zeta)$, as discussed in the introduction. The choice of a relatively small mass ratio of $m^* \simeq 2.9$ was chosen to ensure a strong VIV response at the Reynolds number made for the first part of this study. While a significantly larger mass ratio may enable modes III and IV to be investigated, this would increase the computational cost significantly,

because a sphere with much higher inertia requires considerably more time to reach an asymptotic oscillatory state. The chosen mass ratio is slightly lower than used by Behara *et al.* (2011) of $m_r = 2$ for their 3-DOF non-rotating sphere VIV studies; however, comparisons of current results with theirs for the same setup (3-DOF VIV) and parameters ($Re = 300$, $m_r = 2$), show a comparable amplitude response curve, and also confirm the relative insensitivity to mass ratio, as discussed in Rajamuni *et al.* (2018).

The non-dimensional rotation rate, α, was prescribed through setting the angular velocity of the sphere, ω, so that ($\alpha = \omega D/(2U)$). This prescribed the velocity boundary condition on the sphere surface, while the reduced velocity was prescribed through setting the spring constant in the solid motion equation by $k = 4m\pi^2/U^{*2}$.

The results are presented in the following three subsections. Initially, the sphere response is discussed with its time-mean position, oscillation amplitude and the frequency of oscillation. Then, the forces exerted on the sphere are given in terms of time-mean values and fluctuation amplitudes. Finally, the behaviour of the flow is analysed through the wake structures observed behind the sphere.

4.1. *Sphere response*

Figure 6 shows the variation of time-mean position of the sphere, $\overline{Y}/D$, with the reduced velocity at each rotation rate, where $Y = \boldsymbol{y_s} \cdot (0\ 1\ 0)$ is the displacement of the sphere in the y direction. As can be seen, $\overline{Y}$ increased monotonically with increasing reduced velocity for each α, except $\alpha = 0$. This is because of the lower effective stiffness of springs at higher reduced velocities. At each reduced velocity, the time-mean position of the sphere, $\overline{Y}$, increased with the rotation rate up to $\alpha = 1$, as expected from the Magnus force applied on the sphere, and this was more prominent as the reduced velocity increased. However, as α increased from 1 to 2.5, $\overline{Y}$ did not increase further; instead it slightly decreased (see the curves with hollow symbols for $\alpha = 1.5$, 2 and 2.5 in figure 6). At a fixed reduced velocity, the variation of $\overline{Y}$ with α agrees well with the trend of the lift coefficient calculated for the transversely rotating and rigidly mounted sphere (see figure 3*b*). The time-mean position of the sphere can be estimated as $\overline{Y}/D = 3\overline{C}_l U^{*2}/(16m^*\pi^2)$ from the time-mean lift coefficient, $\overline{C}_l$, calculated for the transversely rotating and rigidly mounted sphere at each α by considering the time-mean form of the solid motion equation (2.3). The dotted lines in figure 6 represent the estimated $\overline{Y}/D$ at each α. However, the actual values of $\overline{Y}/D$ slightly differ from the estimated values for some ranges of U^* at some rotation rates, especially for $\alpha = 0$. The reason for this deviation is explained later in § 4.2.

Figure 7 displays the effects of transverse rotation on the characteristics of the vortex-induced vibration of a sphere with the oscillation amplitude, $A^* = \sqrt{2}Y_{rms}/D$, and the frequency ratio, $f^* = f/f_n$, over the reduced-velocity range $3.5 \leqslant U^* \leqslant 11$ for $\alpha = 0$–2.5, where f is the frequency of the sphere vibration and f_n is the mechanical natural frequency of the system in the medium without the added-mass contribution. For the non-rotating case ($\alpha = 0$), the sphere showed a relatively large oscillation amplitude ($A^* \simeq 0.4D$) from $U^* = 5.5$ to 10 (see the curve with black dots in figure 7*a*). In this case, at these reduced velocities, the time-mean position of the sphere deviated from the estimated values calculated with the lift force of a rigidly mounted sphere, and remained at its initial position ($\overline{Y} = 0$ for $\alpha = 0$ and $U^* \in [5.5, 10]$, see figure 6). Thus, those oscillations were symmetric through the initial position of the sphere. Furthermore, as can been seen from figure 7(*b*), at those reduced velocities, the frequencies of the sphere displacement and vortex shedding were synchronised and

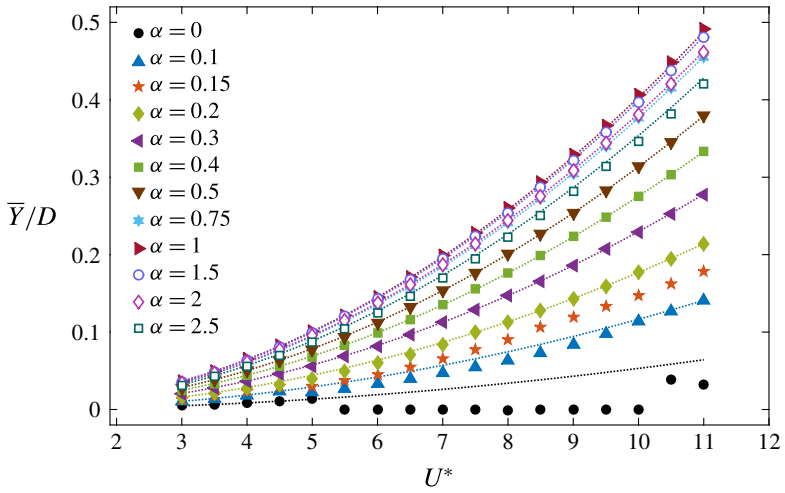

FIGURE 6. (Colour online) Variation of the time-mean position of the sphere, $\overline{Y}/D$, with the reduced velocity, U^*, at each rotation rate: the dotted lines represent the estimated time-mean position of the sphere according to the time-mean lift force, $\overline{C}_l$, calculated for a rigidly mounted sphere at each rotation rate ($\overline{Y}/D = 3\overline{C}_l U^{*2}/(16m^*\pi^2)$).

close to the natural frequency of the system ($f^* \simeq 1$), indicating that these are vortex-induced vibration responses.

For $\alpha = 0$, the sphere began to show large amplitude vibrations suddenly as the reduced velocity increased from 5 to 5.5. A similar observation was reported by Behara *et al.* (2011) and Behara & Sotiropoulos (2016) in their studies on the vortex-induced vibration of a sphere with 3 DOF. The shape of the response curve for $\alpha = 0$ strongly resembles the response curves that they observed. In addition, the response curve for $\alpha = 0$ shows similarities to modes I and II vibration observed by experimental studies on tethered spheres by Govardhan & Williamson (1997), Jauvtis *et al.* (2001) and Govardhan & Williamson (2005). This will be further discussed in the force measurements section.

Interestingly, the sphere response was modified greatly when subjected to a forced rotation. Similar to the non-rotating case, significant vibrations were observed for the rotating cases up to the rotation rate $\alpha = 1$. Importantly, the response amplitude decreased with the increasing rotation rate up to $\alpha = 1$, and it was suppressed for $\alpha \geqslant 1.5$, as shown in figure 7(*a*). Figure 7(*b*) shows that for all the cases for which the sphere vibrated significantly, the vibration frequency was locked in to the vortex-shedding frequency and was close to the system's natural frequency; this again confirms that all of these responses are vortex-induced vibration responses.

The sphere response was further investigated in the range, $\alpha = [1, 1.5]$ at the reduced velocity, $U^* = 6$ which is close to the maximum response. As can be seen from figure 8, the sphere showed synchronised vibrations up to $\alpha = 1.3$. The sphere response amplitude decreased rapidly for small α but was nearly flat in the range, $\alpha \in [1, 1.3]$ and VIV was completely suppressed for $\alpha > 1.4$. The time-mean position of the sphere, $\overline{Y}/D$, shifted away from its initial position with increasing rotation rate up to $\alpha = 1.3$, and for $\alpha \geqslant 1.4$ the time-mean position of the sphere returned back towards the initial position of the sphere for increasing α. The cutoff α for the occurrence of VIV is likely to depend on the Reynolds number, so this cutoff was not further refined over a range of U^*.

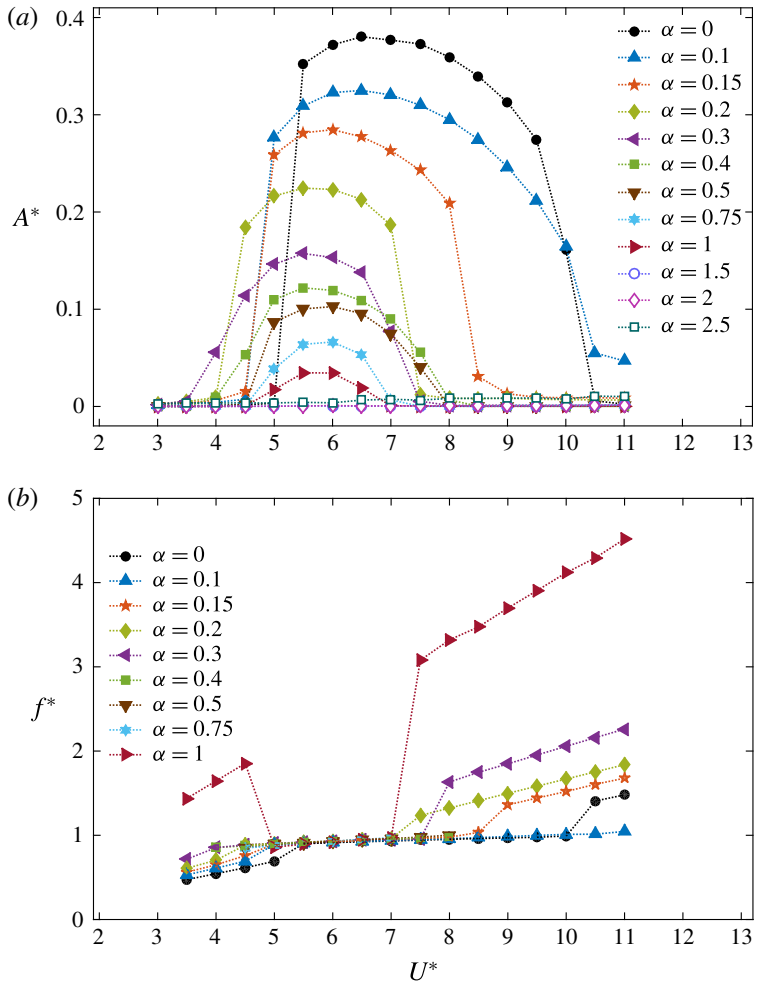

FIGURE 7. (Colour online) The sphere response: (*a*) the variation of the maximum oscillation amplitude, A^*, with the reduced velocity, U^*, at each rotation rate; and (*b*) the frequency ratio $f^* = f/f_n$ for rotation rates and reduced velocities at which the sphere showed a vibrational response.

The amplitude responses appear as approximately bell-shaped curves for each α for $\alpha \leqslant 1$ (see figure 7*a*). Similar to the non-rotating case, the synchronised vibrations began suddenly for $\alpha \leqslant 0.2$. Moreover, the synchronised vibrations ended suddenly for $\alpha = 0.15$ and 0.2. In contrast to lower rotation rates, for higher rotation rates ($\alpha \geqslant 0.3$), the synchronised vibrations appeared and disappeared more gradually at both ends of the synchronised U^* range. The synchronisation regime, which is the reduced-velocity range over which the sphere showed synchronised vibrations, varied with rotation rate. For $\alpha = 0.1$, the synchronisation regime widened to $U^* = 5$–11. However, it generally narrowed as α increased from 0.1, and yielded a narrow synchronisation regime of $U^* = 5$–6.5 for $\alpha = 1$. In addition, the synchronisation regime mostly shifted to the left (to lower reduced velocities) as the rotation rate increased.

Panels 9(*a*) and 9(*b*) show the variation of the maximum oscillation amplitude of the sphere, A^*_{max}, and of the reduced velocity, U^*, at which the maximum oscillation amplitude was observed with the rotation rate, respectively. As can be seen, the maximum oscillation amplitude decreased gradually with increasing rotation rate.

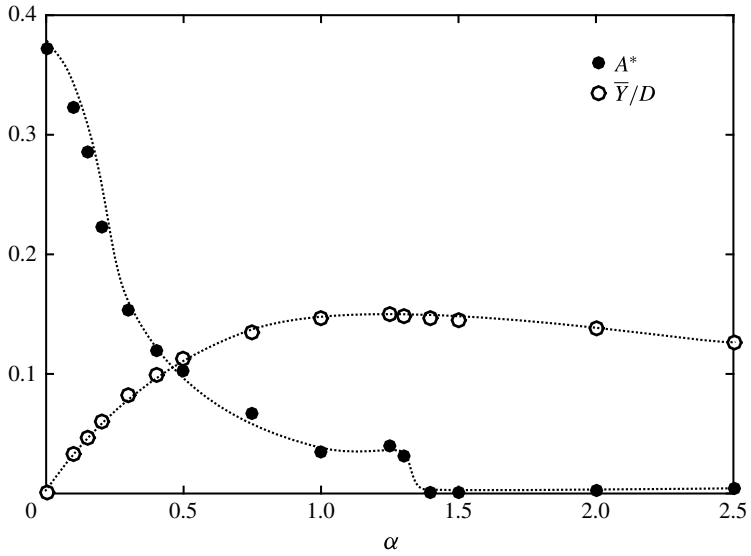

FIGURE 8. Variation of the oscillation amplitude, A^*, and the time-mean position, $\overline{Y}/D$, of the sphere with the rotation rate, α, at the reduced velocity $U^* = 6$.

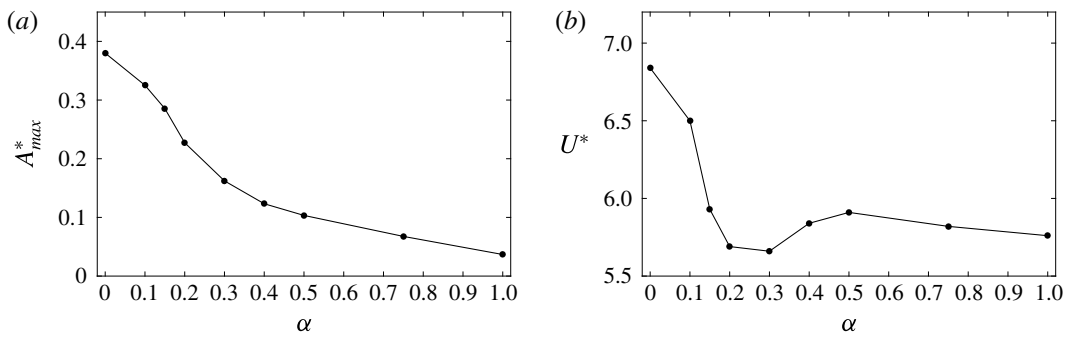

FIGURE 9. Variations of (*a*) the maximum oscillation amplitude of the sphere, A^*_{max}, and (*b*) the reduced velocity at which the sphere showed a maximum oscillation amplitude with the rotation rate, α.

The reduced velocity at which the sphere showed a maximum oscillation amplitude shifted to lower values as α increased from 0 to 0.3. However, it increased and then decreased, as α increased from 0.3 to 1 (see figure 9*b*).

The time history of the sphere displacement is shown in figure 10(*a*) for $\alpha = 0.15$ and in figure 10(*b*) for $\alpha = 0.5$, for five different reduced velocities. At each rotation rate, the sphere vibrated (approximately) sinusoidally in the asymptotic state when in the synchronisation regime. Beyond the synchronisation regime at higher reduced velocities, the sphere initially vibrated significantly, but later, the vibration amplitude decreased substantially (see the time history at $U^* = 8.5$ and 9.5 in figure 10*a*). Moreover, in some cases, the sphere response just beyond the synchronisation regime consisted of two frequencies, as shown in figure 10(*a*) for $\alpha = 0.15$ and $U^* = 8.5$. In this case, the dominant frequency is the natural frequency of the system and the secondary frequency corresponds to the vortex-shedding frequency.

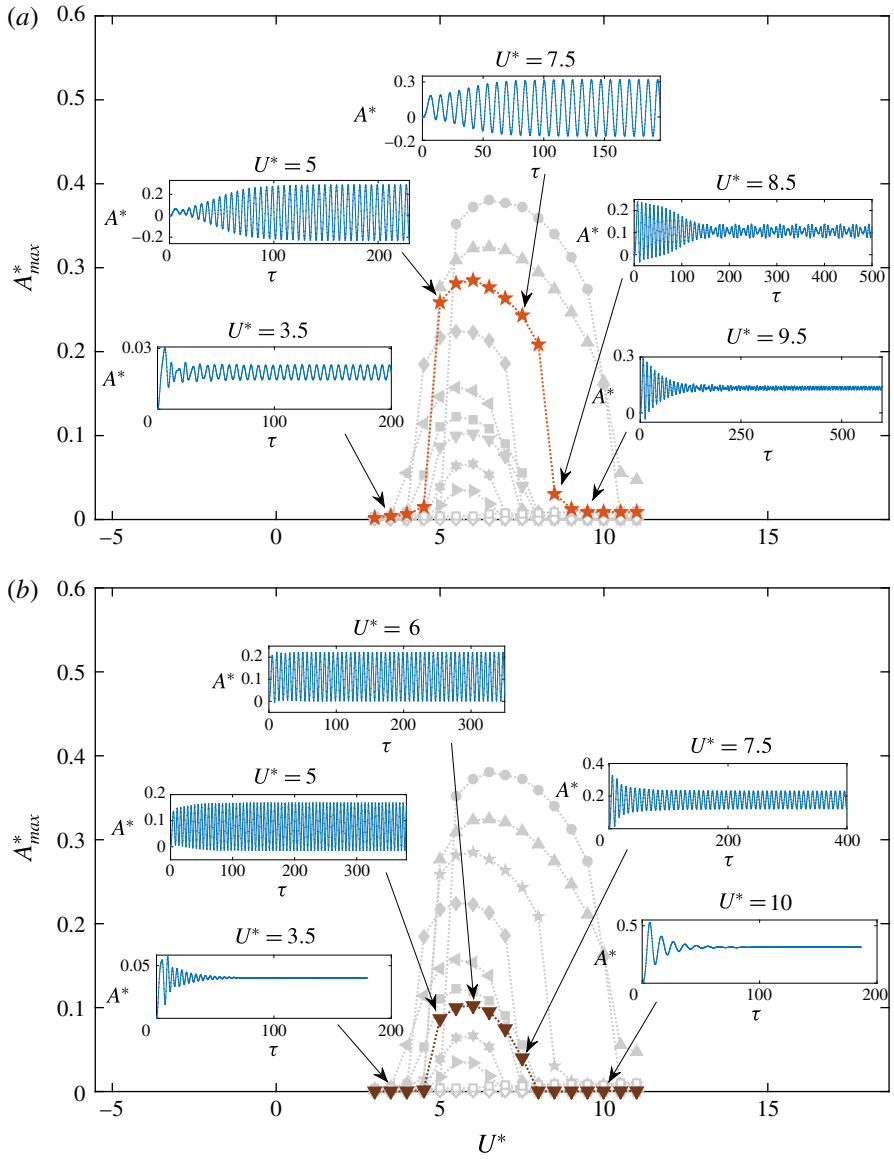

FIGURE 10. (Colour online) Time history of the sphere response (*a*) for $\alpha = 0.15$ and $U^* = 3.5$, 5, 7.5, 8.5 and 9.5; (*b*) for $\alpha = 0.5$ and $U^* = 3.5$, 5, 6, 7.5 and 10.

For $\alpha \leqslant 0.3$, small-scale vibrations were observed outside the synchronisation regimes, as shown in figure 10(*a*) for $\alpha = 0.15$. Interestingly, for $\alpha = 0.4$, 0.5 and 0.75, the vibrations were suppressed outside the synchronisation regime, as shown in figure 10(*b*) for $\alpha = 0.5$. However, for $\alpha = 1$, outside the synchronisation regime, the sphere vibrated with a very small amplitude ($\ll 0.001D$) and a high frequency (see figure 7*b*). In this case, the wake frequency for a non-VIV rotating sphere is approximately a factor of three higher than at lower rotation rates, because the rapid rotation leads to a shear-layer shedding mode. The sphere responses were flat without any oscillations in the steady state for $\alpha = 1.5$ and 2 for all the reduced velocities considered. However, for $\alpha = 2.5$, the sphere oscillated with a small amplitude for all the reduced velocities. As discussed in § 3.1, when the sphere is rigidly mounted

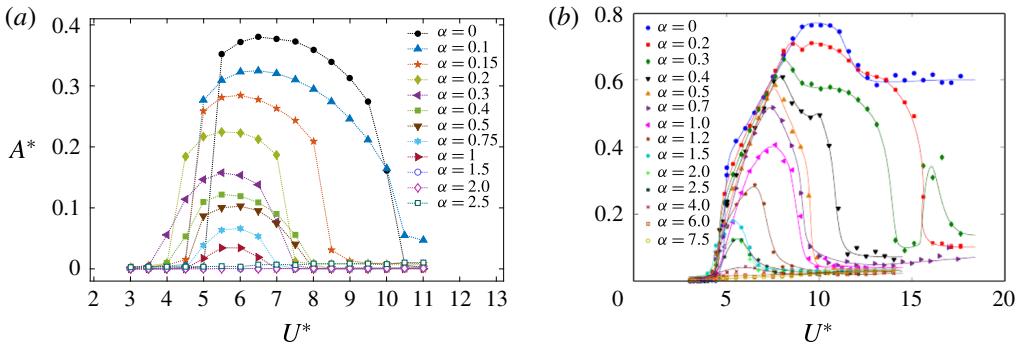

FIGURE 11. (Colour online) The variation sphere response amplitude with reduced velocity at each rotation rate: (*a*) present results of this numerical study at $Re = 300$, (*b*) results of the experimental study of Sareen *et al.* (2018) over the Reynolds number range, $Re = 5000$–$30\,000$.

and with a forced transverse rotation, the flow was unsteady with vortex shedding behind the sphere for $\alpha \leqslant 0.3$; was steady for $0.4 \leqslant \alpha \leqslant 2$, and was unsteady with an irregular wake for $\alpha = 2.5$. Therefore, our observation of the sphere response outside the synchronisation regimes for $\alpha \leqslant 0.75$, and the sphere response for $\alpha \geqslant 1.4$ are consistent with the observation of flow past a rigidly mounted and transversely rotating sphere.

As can be seen from figure 7(*b*), for the cases where the sphere showed small-scale vibrations outside the synchronisation regime ($\alpha = 0$, 0.1, 0.15, 0.2, 0.3 and 1), the vibration frequency of the sphere linearly increased with the reduced velocity. Moreover, the frequency increased with increasing rotation rate. This is consistent with the observation of an increasing vortex-shedding frequency with the rotation rate when the flow is unsteady for a rigidly mounted sphere (Kim 2009).

Bourguet & Jacono (2014) studied the effects of transverse rotation on flow-induced vibration of a cylinder at $Re = 100$ for the rotation rates $\alpha \in [0, 4]$ in the reduced-velocity range $0 \leqslant U^* \leqslant 32$. They observed that when the cylinder was subjected to a forced rotation, it moved to a new position and showed synchronised vibration through this new position for a range of reduced velocities, similar to our observation with a rotating sphere. However, contrary to the decrease in the vibration amplitude we observed for a sphere, they observed an increase in the vibration amplitude for a cylinder with increasing rotation rate, which is also seen in much higher Reynolds number experiments (Wong *et al.* 2017). Moreover, for a rotating cylinder, the synchronisation regime expanded for higher reduced velocities up to $\alpha = 3.5$, and then narrowed, whereas for a rotating sphere it was wider for $\alpha = 0.1$ and then mostly narrowed as α increased. Interestingly, synchronised vibrations were suppressed for higher rotation rates for both the sphere (for $\alpha > 1.3$) and the cylinder (for $\alpha = 4$).

More recently, Sareen *et al.* (2018) investigated the effect of transverse rotation on vortex-induced vibration of a sphere experimentally. They varied the rotation rate over $\alpha \in [0, 7.5]$ and the reduced velocity over $U^* \in [3, 18]$, which corresponds to the Reynolds number range, $Re \in [5000, 30\,000]$. Figure 11 compares our observations of the sphere response amplitude with their observations. Despite the significant difference in Reynolds number, consistent with our predictions, they observed a decrease in the maximum sphere response amplitude and a narrowing of the

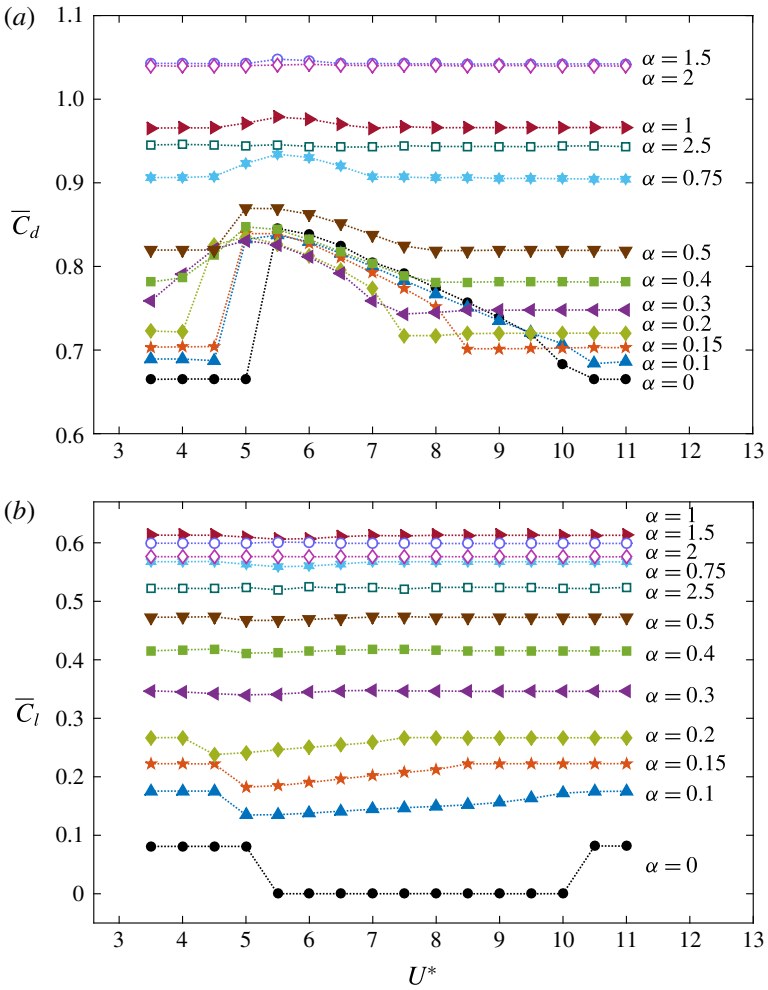

FIGURE 12. (Colour online) Variation of the time-mean (*a*) drag force coefficient, $\overline{C}_d$, and (*b*) lift force coefficient in the y direction, $\overline{C}_{ly}$, with the reduced velocity, U^*, at each rotation rate.

synchronisation regime as the rotation rate increased. However, vortex-induced vibration persisted until $\alpha = 4$ at the higher Reynolds numbers. At the lower Reynolds number ($Re = 300$), the highest rotation rate that showed synchronised vibration was $\alpha = 1.3$.

4.2. *Force measurements*

Figure 12 shows plots of the variation of the time-mean drag and lift coefficients, $\overline{C}_d$ and $\overline{C}_l$, respectively, as functions of the reduced velocity at each rotation rate. The lift coefficient in the z direction was negligible compared to the lift coefficient in the y direction, C_{ly}, for all the cases except $\alpha = 0$ and $U^* \in [10.5, 11]$. Therefore, $\overline{C}_l = \overline{C}_{ly}$ except for $\alpha = 0$ and $U^* \in [10.5, 11]$. Outside the synchronisation regimes, both $\overline{C}_d$ and $\overline{C}_l$ were constant, having the values calculated for a rigidly mounted sphere at each α. However, both $\overline{C}_d$ and $\overline{C}_l$ varied significantly from the values for a rigidly mounted sphere at the reduced velocities for which the sphere showed synchronised vibrations.

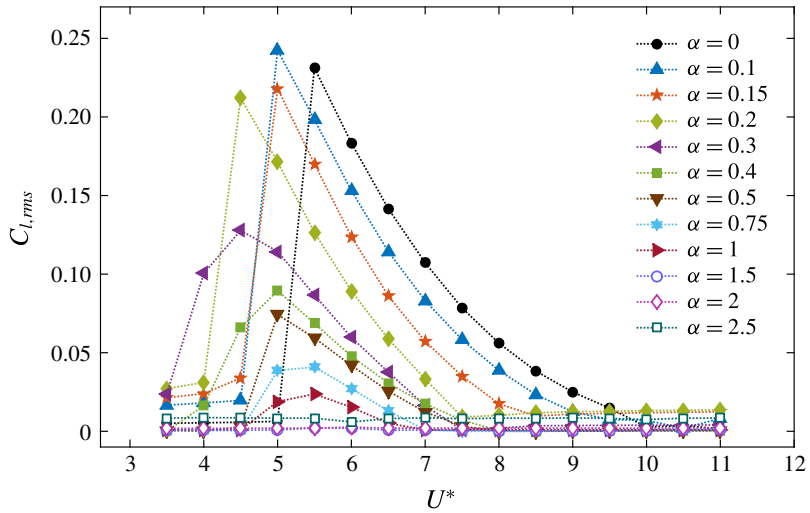

FIGURE 13. (Colour online) Variation of the r.m.s. value of the time-mean lift force coefficient in the y direction over the reduced velocity, U^*, at each rotation rate.

This is consistent with the fact that the time-mean sphere displacement differed from the estimated values based on the lift force of a rigidly mounted rotating sphere in the synchronisation regimes as shown in figure 6 (see § 4.1). At a given reduced velocity, the lift force increased with increasing rotation rate up to $\alpha = 1$, and then decreased, similar to the variation of $\overline{Y}/D$ with α.

For the non-rotating case ($\alpha = 0$), the time-mean lift coefficient dropped down to zero during the synchronisation regime (see the curve with black dots in figure 12*b*). This is consistent with the synchronised vibrations of the sphere being symmetric about the initial position of the sphere for $\alpha = 0$. For the rotating cases, in the synchronisation regimes, $\overline{C}_l$ decreased from the non-oscillatory value, and the decrement reduced, with the increasing α. A similar trend was observed in $\overline{C}_l$ by Bourguet & Jacono (2014) for a rotating cylinder as well.

In the synchronisation regimes, the time-mean drag force, $\overline{C}_d$, increased from its pre-oscillatory value at each rotation rate. There was a sudden increment at the beginning of the synchronisation regime up to $\alpha = 0.2$. For $\alpha = 0$, $\overline{C}_d$ decreased throughout the synchronisation range, asymptoting to its pre-oscillatory value at the end of the range. For $\alpha = 0.1$, 0.15 and 0.2, $\overline{C}_d$ increased slightly, then decreased during the synchronisation regimes and reached the pre-oscillatory value at the end of the regimes. For $0.3 \leqslant \alpha \leqslant 1$, $\overline{C}_d$ increased and decreased gradually, similar to the gradual increase and decrease of the vibration amplitude of the sphere at these rotation rates.

Figure 13 shows the variation of the r.m.s. value of the fluctuation component of the lift force coefficient, C_l', with the reduced velocity, at each rotation rate. Similar to the time-mean components of the forces, the fluctuation components of the forces were also modified in the synchronisation regime at each rotation rate. For $\alpha \leqslant 0.2$, C_l' increased suddenly from 0 to a value of $\simeq 0.22$ at the beginning of the synchronisation regime. Thereafter, C_l' decreased within the synchronisation range and returned to its original value at the end of the range. For $0.3 \leqslant \alpha \leqslant 1$, C_l' increased and then decreased gradually over the synchronisation range. The pattern of variation of C_l' closely matches the pattern of amplitude response (both C_l' and A^* increased

suddenly for $\alpha \leqslant 0.2$ and increased gradually for $0.3 \leqslant \alpha \leqslant 1$). Also, C_l' decreased as the rotation rate increased, similar to the trend of A^* with α.

As discussed by Govardhan & Williamson (2005), the fluid force in the y direction, F_{total}, can be split into a potential force component, $F_{potential} = -m_A\ddot{y}(t)$, which arises due to the potential added-mass force, and a vortex force component, F_{vortex}, from the presence and dynamics of vorticity. This recognises the fact that a flow solution can be constructed as a sum of a potential flow field plus a velocity field associated with vorticity in the flow (e.g. see Lighthill 1986). Here, m_A is the added mass due to the acceleration of the sphere. Therefore, the vortex force can be computed from

$$F_{vortex} = F_{total} - F_{potential}. \tag{4.1}$$

Normalising all forces by $0.5\rho U^2 \pi D^2/4$ gives,

$$C_{vortex} = C_{total} - C_{potential}. \tag{4.2}$$

The phase between the sphere displacement and C_{total} is defined as the total phase, ϕ_{total}, while the phase between sphere displacement and C_{vortex} is defined as the vortex phase, ϕ_{vortex}.

Govardhan & Williamson (2005) observed two distinct modes of vibration (modes I and II) for a non-rotating sphere in the reduced-velocity range $U^* \sim 5$–10. In their study, mode I occurred at the beginning of the synchronisation regime and it smoothly transitioned into mode II as the reduced velocity was increased. They observed that ϕ_{vortex} increased by $\sim 90°$ as the sphere vibration transitioned from mode I to mode II. Moreover, they observed little variation in ϕ_{total} as the mode transitioned from mode I to mode II. Under sphere rotation, a similar behaviour might be expected. Figure 14 shows a comparison of sphere displacement, Y/D, C_{total} and C_{vortex} for two cycles of sphere oscillation for $\alpha = 0$, 0.3 and 0.75 at the beginning of the synchronisation regime (*a*,*c*,*e*) and towards the end of the synchronisation regime (*b*,*d*,*f*). The sphere vibration frequency was locked in to both C_{total} and C_{vortex}, and was phase aligned with C_{total} throughout the synchronisation regime at each α. Moreover, at the beginning of the synchronisation regime, the sphere vibration frequency was phase aligned with C_{vortex}. However, it showed a 180° phase difference with C_{vortex} towards the end of the regime. Nonetheless, under the conditions of zero damping and near sinusoidal forcing, it is not clear this can be taken as an indication of an analogous transition from mode I to mode II.

4.3. *Wake structures*

Vortical structures in the wake are depicted using iso-surfaces of the second invariant of the velocity field (known as the Q-criterion, see Hunt, Wray & Moin (1988) for more details). Figure 15 displays the wake structure observed in the synchronisation regime of the non-rotating case (at $U^* = 6$). As can be seen, two regular symmetrical streets of hairpin vortices form the wake, consistent with the mode I and II wake structure observed by Govardhan & Williamson (2005) in their experimental study of vortex-induced vibration of a tethered sphere. This wake structure was also observed by Behara *et al.* (2011) for VIV of a sphere with 3 DOF at $Re = 300$, when the sphere was undergoing planar oscillations. The vortex streets in the advancing and the retreating sides of the sphere were equal in strength, and the sphere oscillation is symmetric through its initial position.

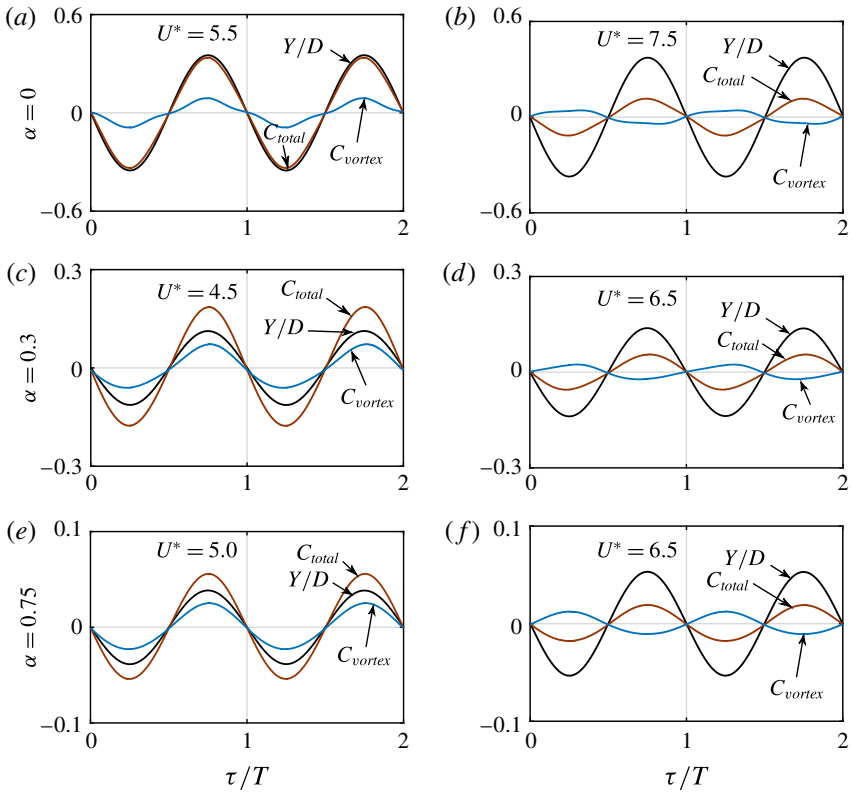

FIGURE 14. (Colour online) Relationship between the time-mean displacement of the sphere, Y/D, the total force in the y direction, C_{total}, and the vortex force in the y direction, C_{vortex}, at $\alpha = 0$, 0.3 and 0.75: (*a*,*c*,*e*) at mode I, and (*b*,*d*,*f*) at mode II.

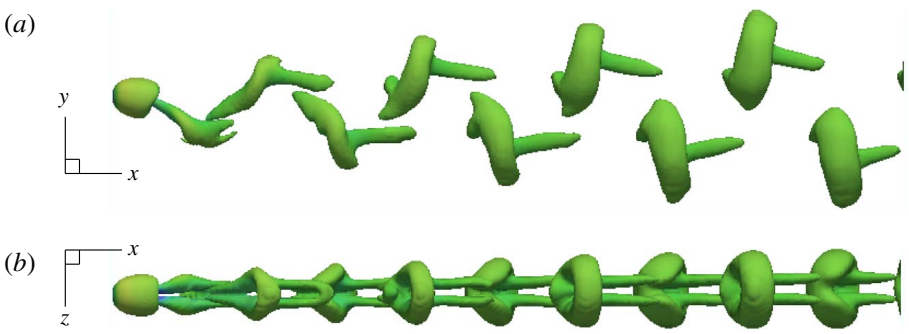

FIGURE 15. (Colour online) Instantaneous wake structures visualised by the Q criterion ($Q = 0.001$) in the synchronisation regime of the non-rotating case at $U^* = 6$.

As discussed in § 3.1, the wake structure of a flow past a rigidly mounted sphere was modified when a rotation was imposed on the sphere. Similarly, various wake structures were observed for an elastically mounted sphere at different rotation rates and at different reduced velocities. Figure 16 shows the wake structures observed at the reduced velocity, $U^* = 6$, at each rotation rate. As a rotation was imposed on the sphere, the wake was deflected to the advancing side (the negative y direction). Moreover, this deflection was more prominent as the rotation rate increased (see

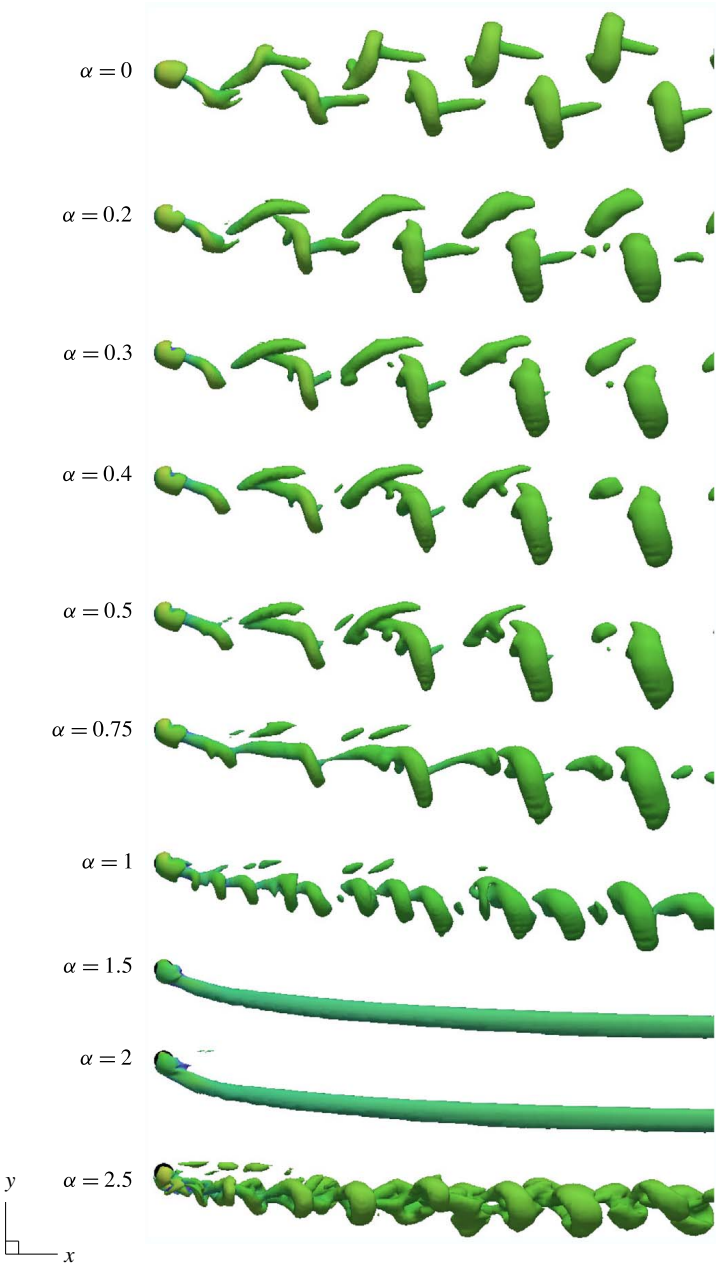

FIGURE 16. (Colour online) Instantaneous wake structures of vortex-induced vibration of a transversely rotating sphere at reduced velocity $U^* = 6$ at each rotation rate. The sphere showed synchronised vibrations up to $\alpha = 1$, and all the synchronisation regimes contained $U^* = 6$. Therefore, the wake structures given for $0 \leqslant \alpha \leqslant 1$ are those in the synchronisation regimes at those rotation rates. The Reynolds number of the flow is $Re = 300$.

figure 16). This is consistent with the lift force applied on the sphere on the retreating side (the positive y direction) due to the Magnus effect.

The wake deflection was quantified by observing the change of the shear strain rate along the sphere surface based on the time-mean velocity field. The wake deflection

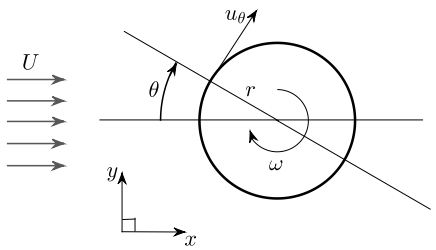

α	Deflection angle, D_θ (deg.)
0.0	0.0
0.1	1.1
0.2	3.7
0.3	6.3
0.4	8.9
0.5	11.5
0.75	19.4
1.0	27.1
1.5	47.2

TABLE 3. Comparison of the phase-averaged wake deflection angle, D_θ, with the rotation rate, α.

angle, D_θ, was defined as the angle at which the shear strain rate in the tangential direction, ϵ_θ, on the sphere surface at the xy plane was zero ($D_\theta = \theta|_{\epsilon_\theta=0}$). This parameter ($\epsilon_\theta$) can be calculated by taking the derivative of tangential velocity, u_θ, in the radial direction, $\mathrm{d}(u_\theta)/\mathrm{d}r$. Therefore, the wake deflection angle, D_θ, was the angle, θ, at which $\mathrm{d}(u_\theta)/\mathrm{d}r = 0$. The variation of the phase-averaged wake deflection angle, D_θ, with the rotation rate is tabulated in table 3. As can be seen, D_θ increased with the rotation rate. This quantifies the observations from visualisations that the deflection was more prominent at higher rotation rates.

The equal strength vortex streets at zero rotation, became unequal as the sphere rotation rate was increased (see figure 16). The vortex street on the advancing side became stronger than the one in the retreating side with increasing rotation rate. The vortex street on the retreating side was greatly weakened for $\alpha = 0.75$, and had largely disappeared for $\alpha \in [1, 1.3]$. This difference in the strength of the vortex streets, which affects the oscillatory forces on the sphere, is consistent with the decrease in the oscillation amplitude as the sphere rotation rate increased.

When the sphere was subjected to a rotation, there was a significant variation in the structure of the wake in the synchronisation regime. The vortex loops on the advancing side were closely spaced hairpin loops. However, the vortex loops on the retreating side deviated from the hairpin type as the rotation rate increased. Moreover, for $0.3 \leqslant \alpha \leqslant 1.3$, the vortex loops on the retreating side near the sphere were attached to the vortex loops on the advancing side that were shed in the previous cycle. However, they separated later as they moved further downstream.

Figures 17 and 18 show the evolution of wakes in the synchronisation regimes (at $U^* = 6$) over a cycle of sphere oscillation for the rotation rates $\alpha = 0$, 0.2, 0.5 and 1. A vortex loop is shed from the retreating side of the sphere as the sphere moved from its apex to its nadir at both $\alpha = 0$ and 0.2 (see figure 17). Another loop is shed from the advancing side half a cycle later. For $\alpha = 0$, the vortex loops were disconnected from each other and formed with a tail. The tail was co-directional with the streamlines upstream. As the loops moved away from the sphere, their shapes changed from a hairpin to a ring shape. In addition to that, the vortex loops on the advancing and the retreating sides are mirror images (with a 180° phase delay) consistent with the symmetric sphere oscillation. However, for $\alpha = 0.2$, in line with the non-zero time-mean lift force applied on the sphere on the retreating side (y direction), a vortex loop on the retreating side is shed weakly compared to the one on the advancing side.

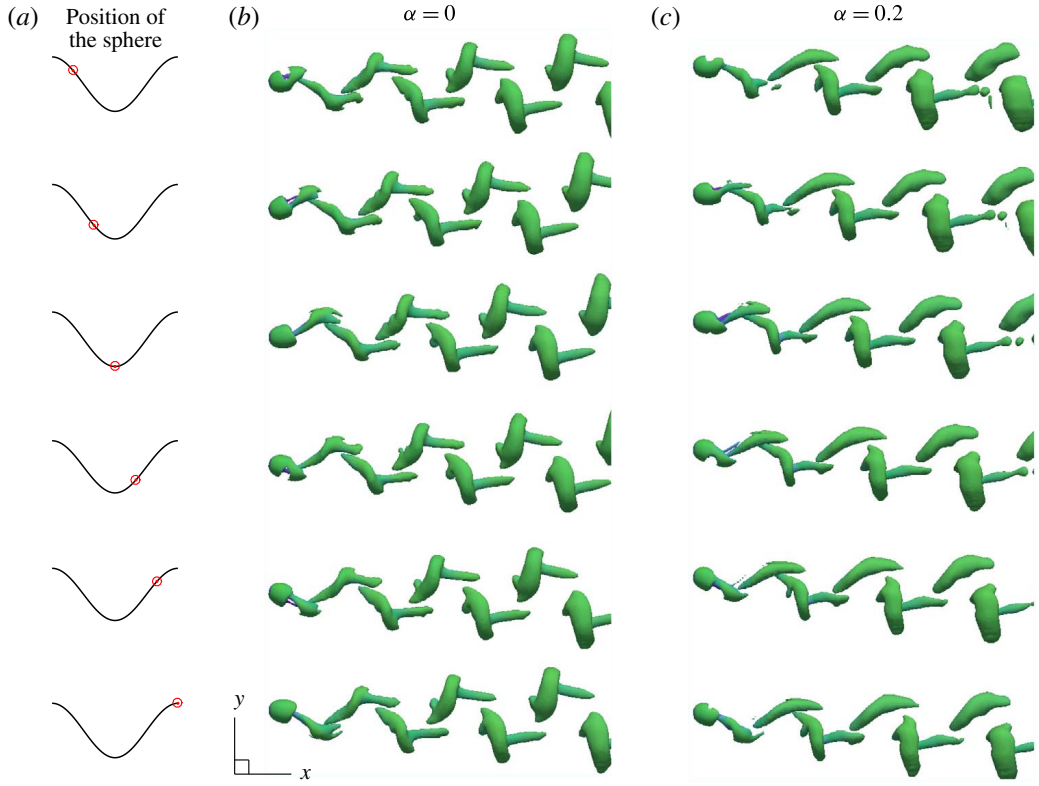

FIGURE 17. (Colour online) Evolution of wake structures for one cycle of sphere oscillation in the synchronisation regimes (at $U^* = 6$) for the rotation rates $\alpha = 0$ and 0.2. The first column displays the position of the sphere by a red 'bullseye' on a cosine wave for one period, while the second and third columns show the instantaneous wake structures observed at each of these positions of the sphere for $\alpha = 0$ and 0.2, respectively.

Moreover, the wake was deflected to the advancing side, and the vortex street on the advancing side was stronger. For $\alpha = 0.5$, a vortex loop on the retreating side was shed far more weakly and appeared only when the sphere was near its nadir (see figure 18). A vortex loop on the advancing side was also modified compared to that at $\alpha = 0$ and its tail had almost disappeared.

On increasing α toward one, vortex loops shed from the retreating side were weak, with the standard sphere wake with long interlacing vortex loops replaced by a different wake structure, with closely spaced loops originating from the boundary layer/shear layer separating from the sphere. This wake structure resembled the wake structure observed by Giacobello *et al.* (2009) and Kim (2009) for the flow past a transversely rotating sphere at $Re = 300$ and $\alpha = 1$. Kim (2009) argued that this unsteadiness was due to the instability of the shear layer caused by rapid rotation. For flow past a transversely rotating rigid sphere at these parameters, we also observed a similar wake structure but only in the initial stage of the simulation as discussed in § 3.1; however, the shedding faded away for long simulation times, and the flow became steady asymptotically. Despite this, when the sphere was allowed to translate in the y direction, the sphere maintained a small amplitude vibration over a narrow reduced velocity range, even after long integration times.

The wake at $\alpha = 1$ and $U^* = 6$ shows vortex loops or hairpins, but the wake frequency is approximately a factor of three higher. Thus at $U^* = 6$, approximately

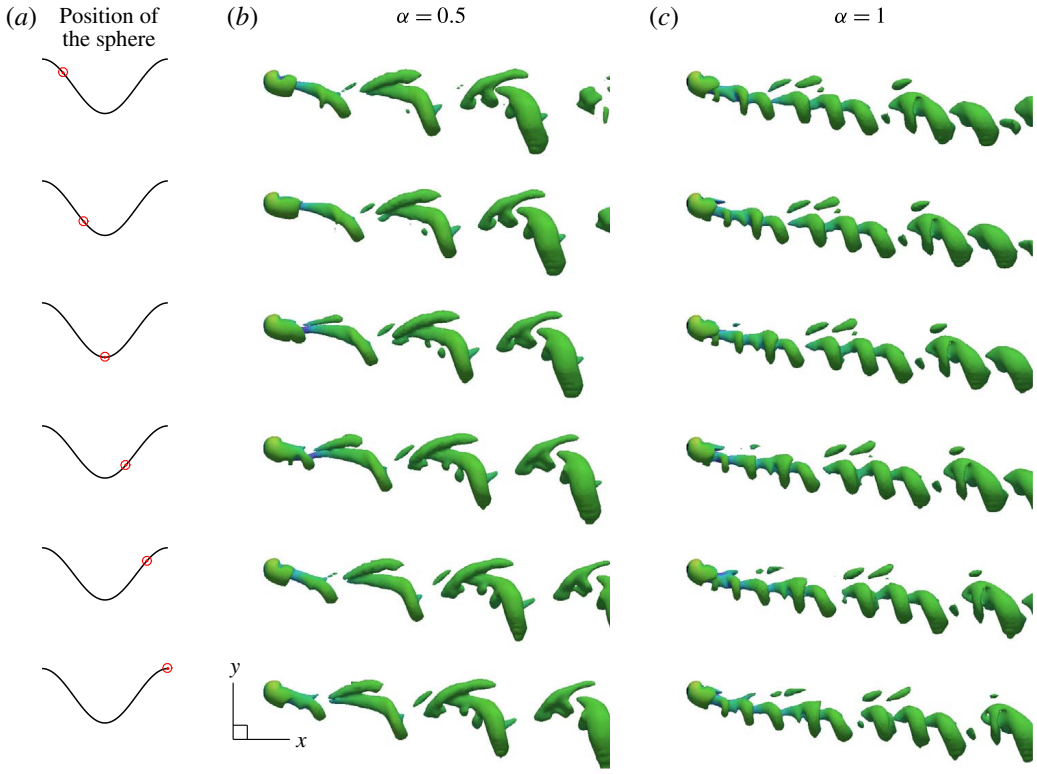

FIGURE 18. (Colour online) Evolution of the wake structures for one cycle of the sphere oscillation in the synchronisation regimes (at $U^* = 6$) for the rotation rates $\alpha = 0.5$ and 1. The first column displays the position of the sphere by a red 'bullseye' on a cosine wave for one period, while the second and third columns show the instantaneous wake structures observed at each of these positions of the sphere for $\alpha = 0.5$ and 1 respectively.

three vortex loops are shed per system oscillation period. However, the shed loops are not identical in the size, nor are they exactly locked to have three shedding periods per vibration period. In this case, the near wake oscillates with the body oscillation at a frequency close to that of a non-vibrating sphere at a lower rotation rate. One possible interpretation is that the natural vortex-shedding instability of the wake, which is suppressed by the development of the shear-layer instability, is still receptive, so that if the sphere is allowed to oscillate at that frequency, that shedding mode can reappear and sustain the oscillation. This study at $\alpha = 1$ was expanded to lower reduced velocities. At $U^* = 2$, where the system frequency matches the shear-layer mode shedding frequency, the body vibration is minimal even through the wake is strongly periodic. In this case, it appears that the timing of the formation and shedding of shear-layer vortices does not lead to positive energy transfer from the fluid to the body, so that large amplitude oscillations do not occur.

A steady wake was observed at the rotation rates $\alpha = 1.5$ and 2 for all the reduced velocities considered, as shown in figure 16 at $U^* = 6$. This confirms that the sphere vibrations were completely suppressed for $\alpha > 1.3$. For $\alpha = 2.5$, an unsteady and asymmetric wake was observed for all the reduced velocities considered, with a structure shown in figure 16 at $U^* = 6$. Even though the flow was unsteady with vortex shedding at this rotation rate, no significant sphere vibration was observed.

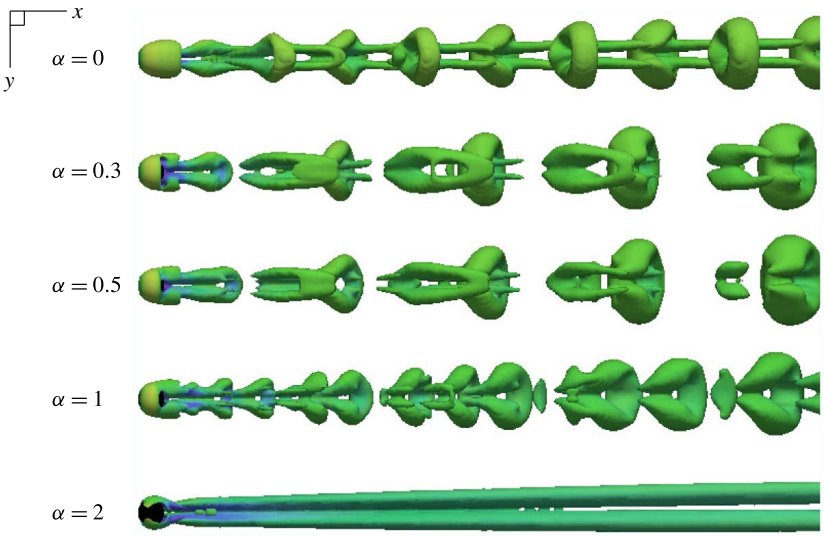

FIGURE 19. (Colour online) Instantaneous wake structures in the xz plane for a transversely rotating sphere at $U^* = 6$ for the rotation rates $\alpha = 0$, 0.3, 0.5, 1 and 2.

Figure 19 shows the wake structures in the xz plane at $U^* = 6$ for the rotation rates $\alpha = 0.1$, 0.3, 1, 2 and 2.5. As can be seen, all the structures observed for $\alpha \leqslant 2$ were mirror symmetric about the xy plane, except the wake at $\alpha = 2.5$.

As discussed in § 3.1, the flow past a transversely rotating rigid sphere showed unsteady vortex shedding for $\alpha \in [0, 0.3]$, and a double-threaded wake for $\alpha \in [0.4, 2]$. When the sphere was allowed to oscillate in the y direction, the sphere showed synchronised vibrations for $\alpha \leqslant 1.3$. At these rotation rates, outside the synchronisation regimes, a few different wake structures were observed, depending on the rotation rate. These different wake states are depicted in figure 20, together with a contour map summarising the oscillation amplitude as a function of U^* and α. The contour map shows the reduction of the oscillation amplitude and narrowing of the synchronisation regime as the rotation rate is increased. Outside the synchronisation regime, for $\alpha \in [0, 0.3]$, unsteady vortex shedding was observed, while for $\alpha \in [0.4, 0.75]$, a steady and a double-threaded wake was found to occur; both states are consistent with rigid sphere wakes at the same rotation rates. However, for $\alpha = 1$, outside the synchronisation regime, an unsteady wake was observed (see figure 20). This wake resembled the wake observed in the initial evolution stage for a rigidly mounted sphere at the same rotation rate, for which the unsteady wake observed in the initial stage transformed into a steady wake in the asymptotic stage. However, given the possibility to oscillate, albeit at very small amplitude, the unsteadiness of the wake persisted.

5. The effect of Reynolds number on VIV of a rotating sphere

The effect of Reynolds number on vortex-induced vibration of a rotating sphere was investigated at three rotation rates, $\alpha = 0.15$, 0.75 and 1.5, by fixing the reduced velocity at $U^* = 6$. These three rotation rates were chosen because at $\alpha = 0.15$ and 0.75, the sphere showed synchronised vibration, whilst at $\alpha = 1.5$, the flow was steady and no sphere vibration was found, but noting that this was not the case in higher Reynolds number experiments (Sareen *et al.* 2018). In addition to that, for flow past

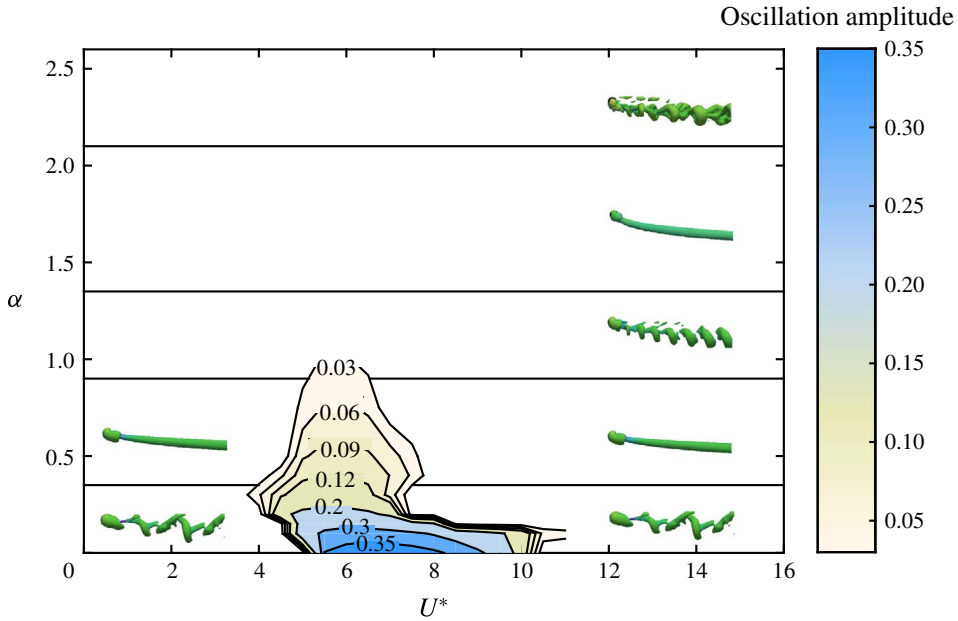

FIGURE 20. (Colour online) Contour plot of the sphere oscillation amplitude, A^*, as a function of the reduced velocity, U^*, and rotation rate, α. The non-synchronisation regime is divided into five regimes according to wake structures.

a rotating sphere, at $Re = 300$, the wake was unsteady with vortex shedding at $\alpha = 0.15$ while the flow was steady at $\alpha = 0.75$. In this investigation, the Reynolds number of the flow was varied from 300 to 1200 while keeping the mass ratio of the sphere fixed at $m^* = 2.865$.

5.1. *Mean displacement, amplitude and forces*

Figure 21 shows the variation of the sphere response amplitude with Reynolds number for $\alpha = 0.15$, 0.75 and 1.5 at $U^* = 6$. At $\alpha = 0.15$ and $Re = 300$, the sphere vibrated synchronously with the vortex-shedding frequency with an amplitude of $\approx 0.3D$. As can be seen from figure 21, at $\alpha = 0.15$, the sphere response amplitude increased with increasing Reynolds number and reached a value of $\approx 0.5D$ at $Re = 1200$. At each of these Reynolds numbers, the sphere vibration was highly sinusoidal. This suggests that even for the non-rotating case, the sphere response amplitude will increase with increasing Reynolds number, which is consistent with the large amplitude response observed in non-rotating sphere VIV experiments (e.g. Govardhan & Williamson 1997, 2005, Jauvtis *et al.* 2001).

Similar to the case of $\alpha = 0.15$, at $\alpha = 0.75$, the sphere vibration amplitude showed an increasing trend with increasing Reynolds number. However, a slight decrement in A^* was observed from $Re = 550$ to 600. The sphere vibration was purely sinusoidal up to $Re = 500$. For $Re \geqslant 550$, even though the sphere response was periodic, it was less sinusoidal. The periodicity of a signal was defined as $\lambda_A = \sqrt{2}Y_{rms}/Y_{max}$ (Jauvtis *et al.* 2001), where Y_{max} is the highest sphere amplitude recorded. According to this definition, λ_A can take values from 0 to 1, with $\lambda_A = 1$ for a purely sinusoidal signal. Figure 22 shows the variation of periodicity of the sphere response with Reynolds number for $\alpha = 0.15$, 0.75 and 1.5. As can be seen, at $\alpha = 0.75$, the periodicity of

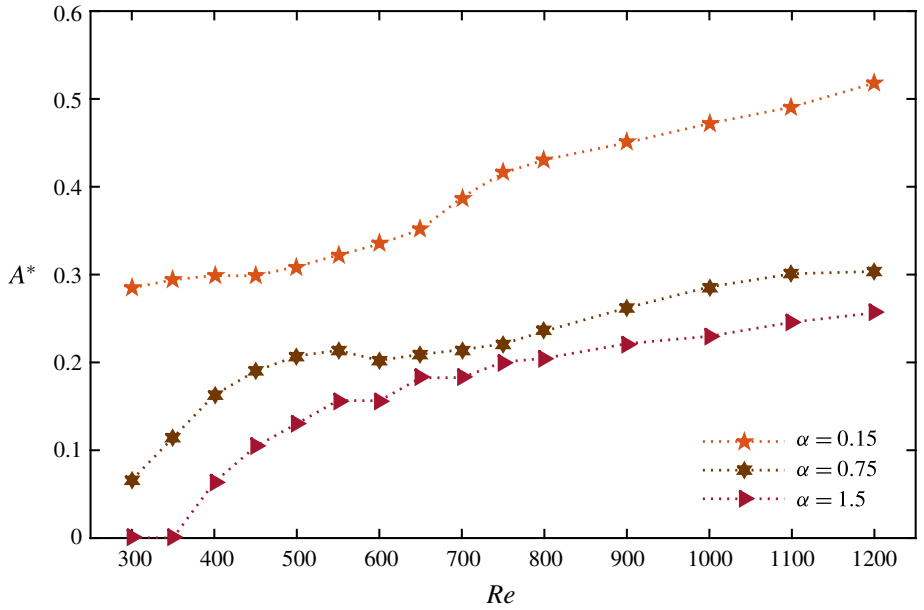

FIGURE 21. (Colour online) Effect of Reynolds number on the sphere response amplitude at the rotation rates, $\alpha = 0.15$, 0.75 and 1.5 at $U^* = 6$.

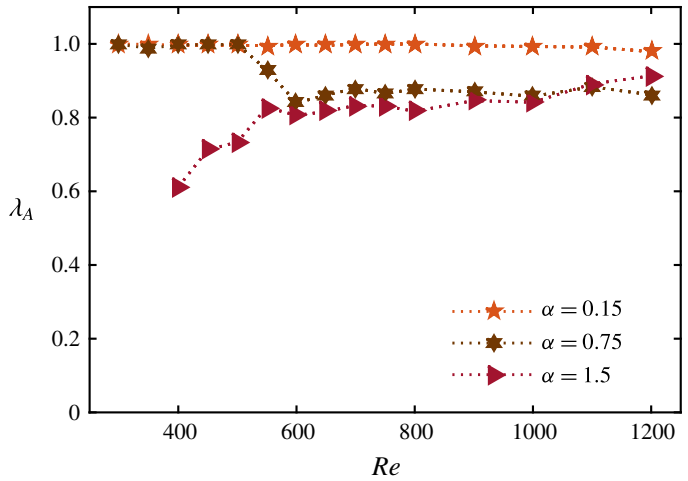

FIGURE 22. (Colour online) Variation of the periodicity of sphere response, λ_A, with Reynolds number at $\alpha = 0.15$, 0.75 and 1.5 for $U^* = 6$.

the signal starts to drop for Re greater than 550. Moreover, λ_A drops to ≈ 0.85 and remains there for $Re \geqslant 600$.

At $\alpha = 1.5$ and $Re = 300$, the flow was steady with no sphere vibration. This behaviour continued at $Re = 350$, as well. However, as the Reynolds number was increased from 400, the sphere started to show synchronised vibration again. The sphere response amplitude increased with the increasing Reynolds number and reached a value of $\approx 0.25D$ at $Re = 1200$. The sphere response was periodic, but was less sinusoidal. The periodicity of the sphere response showed a slight increasing trend with Reynolds number, with values around 0.8 (see figure 22).

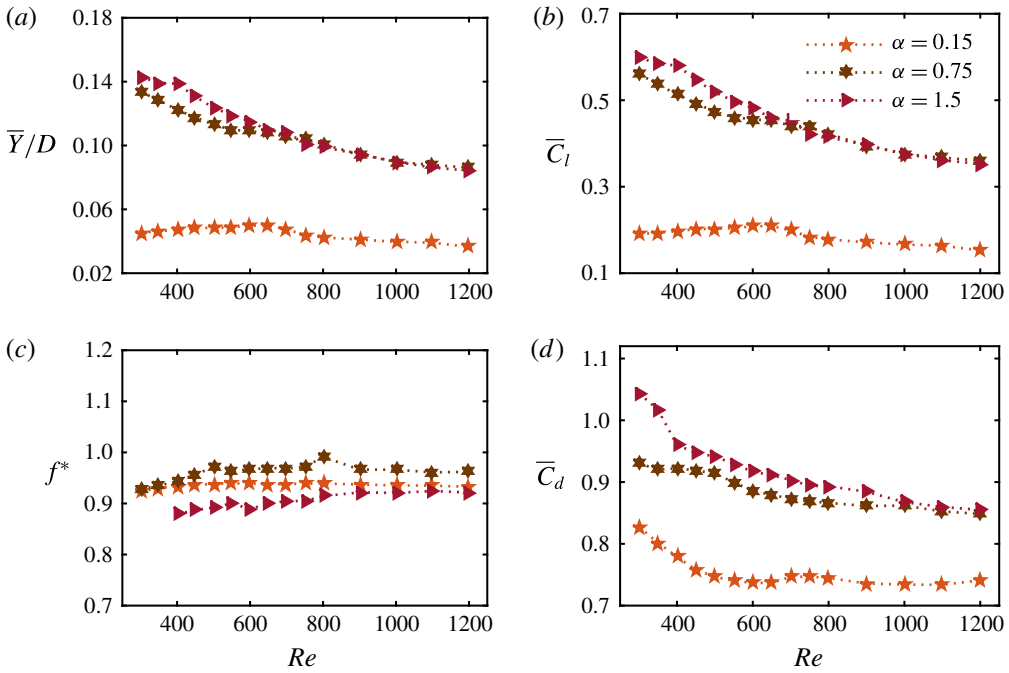

FIGURE 23. (Colour online) Effect of Reynolds number on (*a*) time-mean position of the sphere, (*b*) time-mean lift coefficient, (*c*) frequency ratio and (*d*) time-mean drag coefficient, at the rotation rates $\alpha = 0.15$, 0.75 and 1.5.

At each of the rotation rates and Reynolds numbers considered, the sphere vibration frequency was locked in with the frequency of the lift force (reflecting the vortex shedding). Moreover, the sphere vibration frequency was close to the system's natural frequency ($f^* \approx 1$, see figure 23*c*). Therefore, these vibration states are vortex-induced vibration. From these observations, we can expect that the VIV will occur for even higher rotation rates for higher Reynolds number flows.

Figure 23 shows the variation of the time-mean sphere displacement, the time-mean drag and lift coefficients, and the frequency ratio with Reynolds number for $\alpha = 0.15$, 0.75 and 1.5. As can be seen, at $\alpha = 0.15$, the time-mean position of the sphere, $\overline{Y}/D$, remained almost fixed for all Reynolds numbers considered. However, at $\alpha = 0.75$ and 1.5, $\overline{Y}/D$ decreased with increasing Reynolds number. The time-mean lift coefficient showed an identical trend with the time-mean sphere displacement for all three rotation rates (see figure 23*b*). At $\alpha = 0.15$, the time-mean drag coefficient decreased up to $Re = 600$, and for higher Reynolds numbers it was almost flat (see figure 23*d*). For both $\alpha = 0.75$ and 1.5, $\overline{C}_d$ decreased with increasing Reynolds number.

5.2. *Effect on wake structures*

The vortical structure of the wake was observed using the Q-criterion with a value of $Q = 0.01$. Figure 24 shows the wake structures observed at $\alpha = 0.15$ for $Re = 700$ and 1200; at $\alpha = 0.75$ for $Re = 500$, 900 and 1200; and at $\alpha = 1.5$ for $Re = 900$ and 1200. At $\alpha = 0.15$, two streets of hairpin-type vortex loops were observed at each Reynolds number. However, as the Reynolds number increased, the shape of the vortex loops were modified slightly (e.g. see the difference between the wakes at $Re = 700$ and 1200 in figure 24 at $\alpha = 0.15$). The vortex-shedding frequencies were locked in with the sphere vibrations.

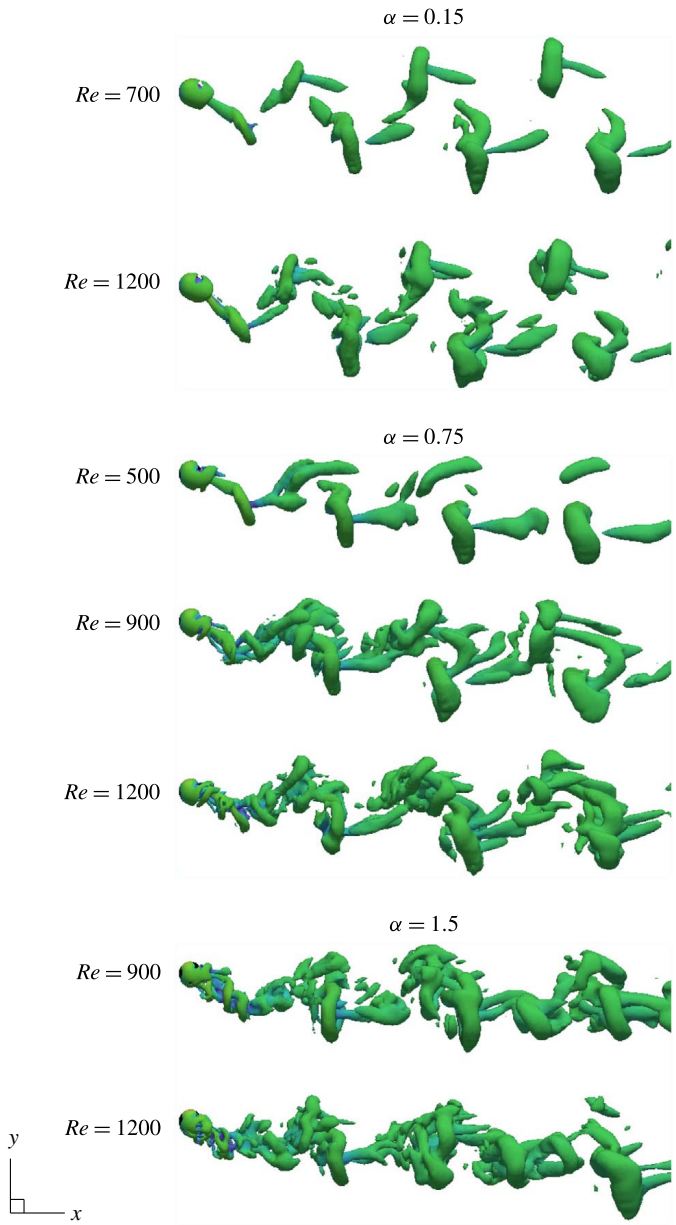

FIGURE 24. (Colour online) Effect of Reynolds number on the wake structures (depicted with $Q = 0.01$) at the rotation rates $\alpha = 0.15$, 0.75 and 1.5. The reduced velocity of the flow is $U^* = 6$ for each case.

As a general comment on these simulations, we would certainly not claim that for the higher Reynolds number cases the chaotic wake structures are fully resolved downstream from the near wake. The main aim of this set of simulations was to properly resolve the near wake through increased spatial resolution, which, together with the larger-scale wake structures, should mainly control the VIV response of the sphere. Further spatial resolution studies were undertaken to confirm that the VIV response was well converged at the highest Reynolds number ($Re = 1200$) and highest rotation rate ($\alpha = 1.5$) considered (see the table 4). As can be seen, there is

Grid	A^*	$\overline{C}_d$	$C_{d,rms}$	$C_{l,rms}$	f/f_n
1	0.26	0.85	0.28	0.30	0.94
2	0.26	0.86	0.27	0.31	0.93
3	0.26	0.85	0.28	0.32	0.93
4	0.26	0.85	0.27	0.31	0.93

TABLE 4. The sensitivity of the spatial resolution of the flow parameters of vortex-induced vibration of a rotating sphere at $(\alpha, U^*) = (1.5, 6)$ and $Re = 1200$ and $m^* = 2.865$ ($m_r = 1.5$). The oscillation amplitude of the sphere, A^*, the time-mean drag coefficient, $\overline{C}_d$, the r.m.s. values of fluctuation component of the drag and lift coefficients, $C_{d,rms}$ and $C_{l,rms}$, and the ratio of vortex-shedding frequency to the natural frequency, f/f_n, are listed.

less than 2 % variation in the amplitude, drag and frequency ratio for the different grids. Thus, grid 2 could be used; however, it was decided to use grid 3 for the higher Reynolds number simulations presented in this section since this grid is more compressed toward the sphere surface.

As discussed above, at $\alpha = 0.75$, the sphere vibration was purely sinusoidal for $Re \in [300, 500]$. In this Reynolds number range, two-sided hairpin-type vortex loops were observed, as shown at $Re = 500$. Compared to the wake at $Re = 300$ shown in figure 16, the wake deflection is smaller and the vortex loops on the retreating side are comparatively stronger at $Re = 500$. This can be attributed to the reduction of the mean lift force at higher Reynolds numbers. In the Reynolds number range, $Re \in [550, 1200]$, the sphere vibration was less sinusoidal ($\lambda_A \approx 0.8$). Indeed, in this range, the wake showed a more turbulent behaviour with shedding of multiple vortex structures per sphere oscillation cycle. However, the dominant vortex-shedding frequency was still synchronised with the sphere vibration frequency (see figure 24 wake for $Re = 900$ and 1200 at $\alpha = 0.75$).

At $\alpha = 1.5$, the sphere showed synchronised vibrations for $Re \in [400, 1200]$. In this Reynolds number range, the sphere vibrations were less sinusoidal. Therefore, similar to $\alpha = 0.75$ at higher Reynolds numbers, multiple vortical structures were shed over a sphere vibration cycle, showing chaotic behaviour. Figure 25 shows the evolution of wake structures over a cycle of sphere vibration in five steps for $\alpha = 1.5$ and $Re = 1200$. Even though multiple vortical structures were shed per sphere oscillation cycle, vortex loops were two sided. In particular, vortex loops were shed from the positive y direction as the sphere moved from its apex to its nadir, and vortex loops were shed from the negative y direction as the sphere moved from its nadir to its apex. Therefore, the dominant vortex shedding frequency was locked in with the sphere vibration frequency.

6. Conclusions

The effects of forced rotation on transverse vortex-induced vibration of a sphere was investigated numerically at Reynolds number 300 with a sphere of mass ratio 2.865 (corresponding to a reduced mass of 1.5). The correlation between the Magnus effect caused by the sphere rotation and the vortex-induced vibration has been analysed over the reduced-velocity range $U^* \in [3.5, 11]$ and rotation rates $\alpha \in [0, 2.5]$. The principal findings of this work can be summarised as follows.

Reduction of the sphere response amplitude with forced rotation. The sphere was found to vibrate, synchronising with the vortex-shedding frequency even subject

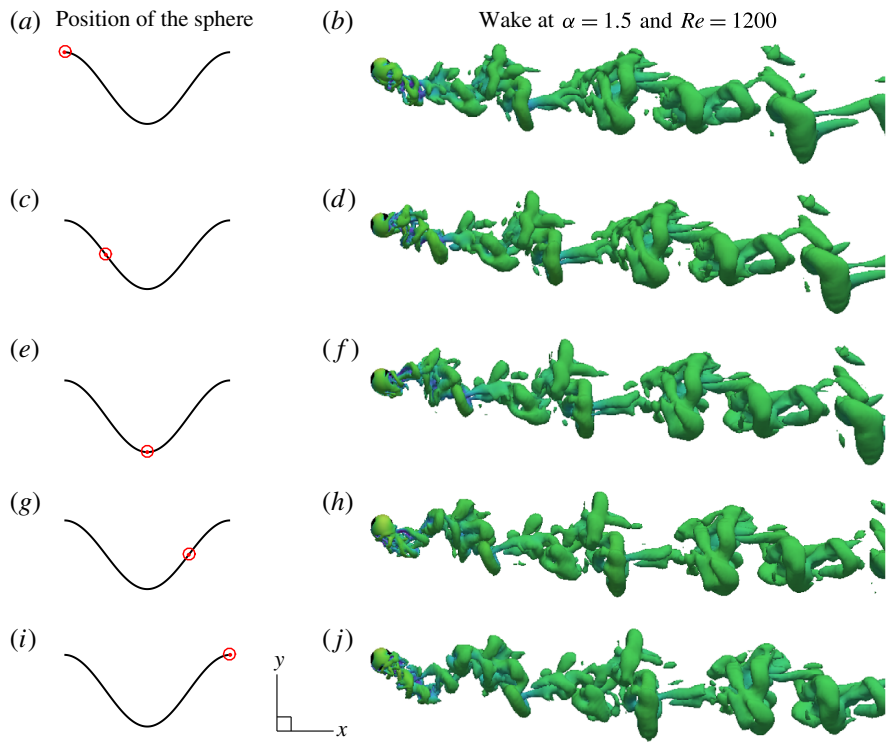

FIGURE 25. (Colour online) Evolution of the wake at $\alpha = 1.5$, $Re = 1200$ and $U^* = 6$ for a cycle of sphere vibration. The left column shows the sphere position in the cycle with a red 'bullseye' on a cosine wave and the right column shows the wake structures observed at corresponding sphere positions.

to an imposed forced rotation. However, the sphere shifted to a new time-mean position for all rotation cases due to the Magnus force generated by the rotation. The sphere showed highly periodic VIV, not only for $\alpha < 0.4$, but also for $0.4 \leqslant \alpha \leqslant 1.3$, i.e. over a range of rotation rates where no vortex shedding was found for a rigidly mounted rotating sphere (at this Reynolds number). Interestingly, the sphere response amplitude, which was $\approx 0.4D$ for the zero rotation case, decreased as the rotation rate increased, and VIV was completely suppressed beyond $\alpha = 1.3$. Simultaneously, the synchronisation range narrowed and moved mostly towards lower values of U^* with increasing rotation rate.

Force coefficients highly modulated in the synchronisation regime. The time-mean lift and drag coefficients were highly modulated as the sphere experienced synchronised vibration. In particular, the time-mean drag force increased while the time-mean lift force decreased from its pre-oscillatory value in the synchronisation regime at each rotation rate. The analysis of phases between sphere displacement and vortex force revealed that, regardless of the rotation rate, the sphere showed similarities to mode I initially and then mode II vibrations identified through total and vortex phase variations.

Symmetry breaking of the wake under forced rotation. In the synchronisation regime of the zero rotation case, two trails of two-sided hairpin loops formed in the wake. Moreover, the vortex trails on the advancing and retreating sides were equal in strength as the sphere oscillation was symmetric about its initial position. These

wake states strongly resemble those of a tethered sphere observed experimentally by Govardhan & Williamson (2005) at much higher Re, for both modes I and II. As a rotation was imposed on the sphere, the wake deflected to the advancing side ($-y$ direction); this was more prominent as the rotation rate increased. With the symmetry breaking of the wake introduced by the Magnus effect, the vortex loops in the vorticity trail from the advancing side became stronger than the vortex loops in the trail from the retreating side. This unevenness of the wake, which affects the oscillatory forces on the sphere, is consistent with the reduction in the amplitude response and narrowing of the synchronisation range at higher rotation rates.

The response amplitude increased significantly as Reynolds number was increased. The effect of Reynolds number on VIV of a rotating sphere was investigated at $U^* = 6$, by increasing Reynolds number incrementally up to $Re = 1200$. As the Reynolds number was increased, the sphere started to show synchronised vibration at higher rotation rates even when there was no VIV at $Re = 300$. In addition, the sphere response amplitude increased generally with the increasing Reynolds number. Therefore, at higher Reynolds numbers, VIV persists for even higher rotation rates and displays a large amplitude response, consistent with experimental studies by Sareen *et al.* (2018).

Based on the above observations, we can draw the following conclusions: vortex-induced vibration persists for a sphere at small rotation rates, but the mitigation/suppression of vortex shedding caused by the Magnus effect as the rotation rate is increased does in fact lead to increased suppression of VIV at higher rotation rates. Moreover, spanning the laminar regime and beyond, the effect of Reynolds number on the VIV response of a rotating sphere is significant.

In terms of future work, it seems worth expanding this study further into the fully turbulent regime where most experiments are conducted. It would also be interesting to examine the response of a heavier sphere at higher reduced velocities, where modes III and IV are observed to occur.

Acknowledgements

The support from Australian Research Council Discovery grants DP130100822, DP150102879 and DP170100275, computing time available through Merit Project grants n67 and d71 through the National Computational Infrastructure (NCI), and the Pawsey Supercomputing Centre are gratefully acknowledged.

REFERENCES

BEARMAN, P. W. 1984 Vortex shedding from oscillating bluff bodies. *Annu. Rev. Fluid Mech.* **16** (1), 195–222.

BEHARA, S., BORAZJANI, I. & SOTIROPOULOS, F. 2011 Vortex-induced vibrations of an elastically mounted sphere with three degrees of freedom at $Re = 300$: hysteresis and vortex shedding modes. *J. Fluid Mech.* **686**, 426–450.

BEHARA, S. & SOTIROPOULOS, F. 2016 Vortex-induced vibrations of an elastically mounted sphere: the effects of Reynolds number and reduced velocity. *J. Fluids Struct.* **66**, 54–68.

BLACKBURN, H. & HENDERSON, R. 1996 Lock-in behavior in simulated vortex-induced vibration. *Exp. Therm. Fluid Sci.* **12** (2), 184–189.

BOURGUET, R. & JACONO, D. L. 2014 Flow-induced vibrations of a rotating cylinder. *J. Fluid Mech.* **740**, 342–380.

DOBSON, J., OOI, A. & POON, E. K. W. 2014 The flow structures of a transversely rotating sphere at high rotation rates. *Comput. Fluids* **102**, 170–181.

GIACOBELLO, M., OOI, A. & BALACHANDAR, S. 2009 Wake structure of a transversely rotating sphere at moderate Reynolds numbers. *J. Fluid Mech.* **621**, 103–130.

GOVARDHAN, R. & WILLIAMSON, C. H. K. 1997 Vortex-induced motions of a tethered sphere. *J. Wind Engng Ind. Aerodyn.* **69**, 375–385.

GOVARDHAN, R. & WILLIAMSON, C. H. K. 2000 Modes of vortex formation and frequency response of a freely vibrating cylinder. *J. Fluid Mech.* **420**, 85–130.

GOVARDHAN, R. N. & WILLIAMSON, C. H. K. 2005 Vortex-induced vibrations of a sphere. *J. Fluid Mech.* **531**, 11–47.

HOUT, R. V., KATZ, A. & GREENBLATT, D. 2013 Time-resolved particle image velocimetry measurements of vortex and shear layer dynamics in the near wake of a tethered sphere. *Phys. Fluids* **25** (7), 077102.

HUNT, J. C. R., WRAY, A. A. & MOIN, P. 1988 Eddies, streams, and convergence zones in turbulent flows. In *Studying Turbulence Using Numerical Simulation Databases*, vol. 2, pp. 193–208. Stanford University.

ISSA, R. I. 1986 Solution of the implicitly discretised fluid flow equations by operator-splitting. *J. Comput. Phys.* **62** (1), 40–65.

JASAK, H. & TUKOVIC, Z. 2010 Dynamic mesh handling in Openfoam applied to fluid-structure interaction simulations. In *Proceedings of the V European Conference on Computational Fluid Dynamics: ECCOMAS CFD 2010, Lisbon, Portugal* (ed. J. C. F. Pereira, A. Sequeira & J. M. C. Pereira), ECCOMAS.

JAUVTIS, N., GOVARDHAN, R. & WILLIAMSON, C. H. K. 2001 Multiple modes of vortex-induced vibration of a sphere. *J. Fluids Struct.* **15** (3), 555–563.

JEONG, J. & HUSSAIN, F. 1995 On the identification of a vortex. *J. Fluid Mech.* **285**, 69–94.

KIM, D. 2009 Laminar flow past a sphere rotating in the transverse direction. *J. Mech. Sci. Technol.* **23** (2), 578–589.

KRAKOVICH, A., ESHBAL, L. & HOUT, R. V. 2013 Vortex dynamics and associated fluid forcing in the near wake of a light and heavy tethered sphere in uniform flow. *Exp. Fluids* **54** (11), 1615.

KUROSE, R. & KOMORI, S. 1999 Drag and lift forces on a rotating sphere in a linear shear flow. *J. Fluid Mech.* **384**, 183–206.

LEE, H., HOURIGAN, K. & THOMPSON, M. C. 2013 Vortex-induced vibration of a neutrally buoyant tethered sphere. *J. Fluid Mech.* **719**, 97–128.

LEE, H., THOMPSON, M. C. & HOURIGAN, K. 2008 Flow around a tethered neutrally-buoyant sphere. In *Proceedings of the XXII International Congress of Theoretical and Applied Mechanics, Adelaide Convention Centre, Adelaide, Australia* (ed. J. Denier, M. Finn & T. Mattner), International Union of Theoretical and Applied Mechanics.

LEONTINI, J. S., STEWART, B. E., THOMPSON, M. C. & HOURIGAN, K. 2006*a* Predicting vortex-induced vibration from driven oscillation results. *Appl. Math. Model.* **30** (10), 1096–1102.

LEONTINI, J. S., THOMPSON, M. C. & HOURIGAN, K. 2006*b* The beginning of branching behaviour of vortex-induced vibration during two-dimensional flow. *J. Fluids Struct.* **22** (6), 857–864.

LIGHTHILL, J. 1986 Wave loading on offshore structures. *J. Fluid Mech.* **173**, 667–681.

MAGNUS, G. 1853 *Über die Abweichung der Geschosse, und: Über eine abfallende Erscheinung bei rotierenden Körpern*, vol. 164. Annalen der Physik.

NAUDASCHER, E. & ROCKWELL, D. 2012 *Flow-induced Vibrations: an Engineering Guide*. Courier Corporation.

PARKINSON, G. 1989 Phenomena and modelling of flow-induced vibrations of bluff bodies. *Prog. Aerosp. Sci.* **26** (2), 169–224.

POON, E. K. W., OOI, A. S. H., GIACOBELLO, M. & COHEN, R. C. Z. 2010 Laminar flow structures from a rotating sphere: effect of rotating axis angle. *Intl J. Heat Fluid Flow* **31** (5), 961–972.

POON, E. K. W., OOI, A. S. H., GIACOBELLO, M., IACCARINO, G. & CHUNG, D. 2014 Flow past a transversely rotating sphere at Reynolds numbers above the laminar regime. *J. Fluid Mech.* **759**, 751–781.

PREGNALATO, C. J. 2003 Flow-induced vibrations of a tethered sphere. PhD, Monash University.

RAJAMUNI, M. M., THOMPSON, M. C. & HOURIGAN, K. 2018 Transverse flow-induced vibrations of a sphere. *J. Fluid Mech.* **837**, 931–966.

ROBINS, B. 1972 *New Principle of Gunnery (of 1742)*. Republished by Richmond Publishing.

RUBINOW, S. I. & KELLER, J. B. 1961 The transverse force on a spinning sphere moving in a viscous fluid. *J. Fluid Mech.* **11** (03), 447–459.

SAREEN, A., ZHAO, J., LO JACONO, D., SHERIDAN, J., HOURIGAN, K. & THOMPSON, M. C. 2018 Vortex-induced vibration of a rotating sphere. *J. Fluid Mech.* **837**, 258–292.

SARPKAYA, T. 2004 A critical review of the intrinsic nature of vortex-induced vibrations. *J. Fluids Struct.* **19** (4), 389–447.

SEYED-AGHAZADEH, B. & MODARRES-SADEGHI, Y. 2015 An experimental investigation of vortex-induced vibration of a rotating circular cylinder in the crossflow direction. *Phys. Fluids* **27** (6), 067101.

WILLIAMSON, C. H. K. & GOVARDHAN, R. 1997 Dynamics and forcing of a tethered sphere in a fluid flow. *J. Fluids Struct.* **11** (3), 293–305.

WILLIAMSON, C. H. K. & GOVARDHAN, R. 2004 Vortex-induced vibrations. *Annu. Rev. Fluid Mech.* **36**, 413–455.

WILLIAMSON, C. H. K. & GOVARDHAN, R. 2008 A brief review of recent results in vortex-induced vibrations. *J. Wind Engng Ind. Aerodyn.* **96** (6), 713–735.

WONG, K. W., ZHAO, J., LO JACONO, D., THOMPSON, M. C. & SHERIDAN, J. 2017 Experimental investigation of flow-induced vibration of a rotating circular cylinder. *J. Fluid Mech.* **829**, 486–511.

WU, X., GE, F. & HONG, Y. 2012 A review of recent studies on vortex-induced vibrations of long slender cylinders. *J. Fluids Struct.* **28**, 292–308.

It is better to be hated for what you are than to be loved for what you are not.

Andre Gide

6. Vortex dynamics and vibration modes of a tethered sphere

Tethered spheres have been extensively used for flow-induced vibration problems of a sphere from the beginning. However, the knowledge of the flow-induced vibration of a tethered sphere at low Reynolds numbers is still lacking in several aspects. As discussed in chapter 4, we observed that the response of an elastically-mounted sphere is highly dependent on the Reynolds number over the range $300 \leq Re \leq 800$. Nevertheless, Govardhan & Williamson (2005) found that FIV was independent of the Reynolds number over the range $2000 < Re < 12000$. Therefore, this computational study focuses on the nature of FIV of a tethered sphere at low to intermediate Reynolds numbers ($500 \leq Re \leq 2000$) with the intention of filling the gap in knowledge. In addition, this chapter gives special attention to the mode III and IV regimes, as the current knowledge on the appearance and characterisation of the modes III and IV vibration states is limited.

The numerical method described in § 3.3 was used for the results presented in this chapter. The *tetheredVivIcoFoam* solver detailed in § 3.3.2 was utilized for the simulations and the calculation of the reduced velocity, as described in § 3.3.4. The chapter begins with a discussion of the results of flow-induced vibration response of a tethered sphere in § 6.1, in terms of the amplitude, periodicity and frequency of the sphere response. The sphere response over the modes I and II ranges are discussed in detail in § 6.2, highlighting the effect of Reynolds number, effect of mass ratio, nature of the wake structures and robustness of the vibration at modes I and II. Following this, results on mode III observed with a heavy sphere are presented in § 6.3. Next, the findings of intermittent burst of vibrations at mode IV are detailed in § 6.4. Finally, the chapter ends with a brief summary and concluding remarks in § 6.5.

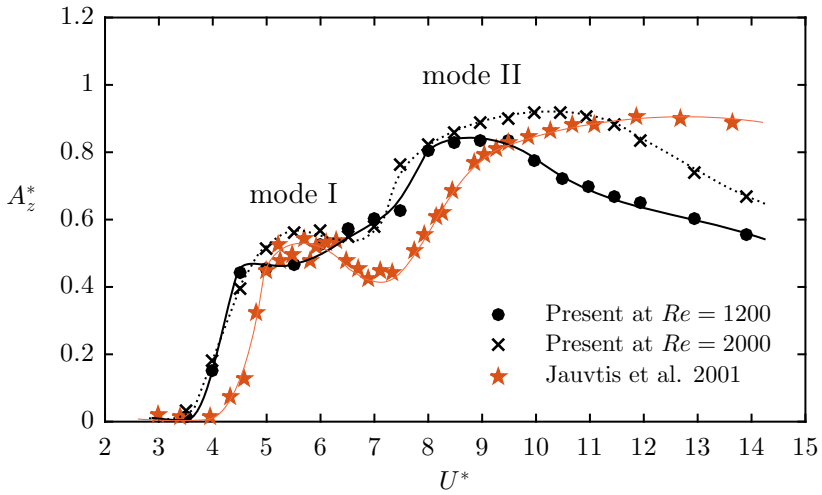

Figure 6.1.: Comparison of the sphere response amplitude, A_z^*, at $Re = 1200$ and 2000 with the experimental results of Jauvtis *et al.* (2001) at higher and varying Reynolds numbers with a sphere of mass ratio, $m^* = 0.8$ over the reduced velocity range, $U^* = [3, 14]$. Consistent with their observations, the first two modes of sphere vibration states were observed.

6.1. FIV response of a tethered sphere

6.1.1. Comparison with other research studies

The flow past a tethered sphere of mass ratio, $m^* = 0.8$, with a tether length of $l^* = 10$ was investigated by fixing the Reynolds number at a particular value. The sphere showed large amplitude modes I and II vibration states at the larger Reynolds numbers investigated, similar to the observation of previous experimental studies. Figure 6.1 compares our results of the sphere vibration amplitude, $A_z^* = \sqrt{2}Z_{rms}/D$, at $Re = 1200$ and 2000 with the experimental results of Jauvtis *et al.* (2001) conducted with a sphere of the same mass ratio, where Z is the sphere displacement in the z direction. As can be seen, the present results match reasonably well with Jauvtis *et al.* Recall that in the experiments, the Reynolds number was not fixed and varied approximately between 2000 and 14 000. Consistent with their observations, the sphere response amplitudes at modes I and II were approximately $0.5D$ and $0.85D$, respectively.

In particular, at this mass ratio, Jauvtis *et al.* (2001) observed two peaks in the amplitude response curve, corresponding to modes I and II. In contrast, at $Re = 1200$, the sphere response amplitude varied smoothly from mode I to mode II without a dip as seen in most of the amplitude response curves of tethered spheres (Jauvtis *et al.* (2001) and Govardhan & Williamson (2005)). However, once the Reynolds number is increased to 2000, the response curve formed a small peak for mode I as observed by Jauvtis *et al.*

(2001). Therefore, if the Reynolds number is further increased, this local peak at mode I is expected to become more prominent. At $Re = 1200$, the highest vibration amplitude occurred around $U^* = 8.5$, and the vibration amplitude decreased beyond this point in contrast to the observation of Jauvtis *et al.* of almost constant amplitude at larger U^* values. However, as the Reynolds number is increased to 2000, the response amplitudes were higher than at $Re = 1200$. Moreover, the response curve was closer to their response curve. Again, if the Reynolds number is further increased, the response curve at mode II is also anticipated to become more similar to the response curve of Jauvtis *et al.* observed at higher and varying Reynolds numbers. These observations show that there is a considerable effect of Reynolds number on the sphere response in this Reynolds number range. Rajamuni *et al.* (2018*a*) (chapter 4) also showed that there is a substantial effect of the Reynolds number on flow-induced vibration of an elastically mounted sphere with 1 DOF in the laminar regime.

Compared to the observation of Jauvtis *et al.* (2001), the predicted response curves look slightly shifted to the left. However, the response that was predicted at $U^* = 4$ is not a periodic response as in mode I, albeit the shedding frequency is locked in to the oscillation frequency. Similar to the results of Jauvtis *et al.*, we also expected mode I to occur around $U^* = 5$ as the static vortex shedding frequency is $f_{vo} \approx 0.2$. Therefore, at $U^* = 4$, the sphere may be in transition from no oscillation to VIV. Nonetheless, we observed mode I vibration at a slightly lower reduced velocity compared to that observed by Jauvtis *et al.* (2001). This difference may be due to the effect of Reynolds number. Note that for the predictions, the Reynolds number was fixed whereas it was allowed to vary with U^* in the experiments.

6.1.2. Nature of the sphere response

To explore the effect of Reynolds number in the laminar regime, another set of simulations was conducted at $Re = 500$ with the same mass ratio and tether length. Figure 6.2 (a) shows a comparison of the sphere response amplitude of $Re = 500$, 1200 and 2000 for the reduced velocity range, $U^* = [3, 32]$. As can be seen, the sphere response amplitude increased globally as the Reynolds number increased over $U^* \in [4.5, 16]$. As discussed earlier, it showed periodic mode I and II vibrations over $U^* \approx [4.5, 7]$ and $[8, 16]$, respectively, at $Re = 1200$ and 2000. At $Re = 500$, a periodic vibration response was found over $U^* = [4.5, 12]$. The response curve took a bell shape with a maximum amplitude of $\approx 0.45D$. At this Reynolds number, modes I and II were not able to be distinguished clearly from the amplitude response curve alone. Govardhan & Williamson (2005) found that mode I occurred around $(U^*/f^*)St = 1$ while mode II occurred in the range of $(U^*/f^*)St \approx [1.4, 2]$. However, if the amplitude is plotted against $(U^*/f^*)St$, both modes I and II responses became clear, even at $Re = 500$, from the range of $(U^*/f^*)St$

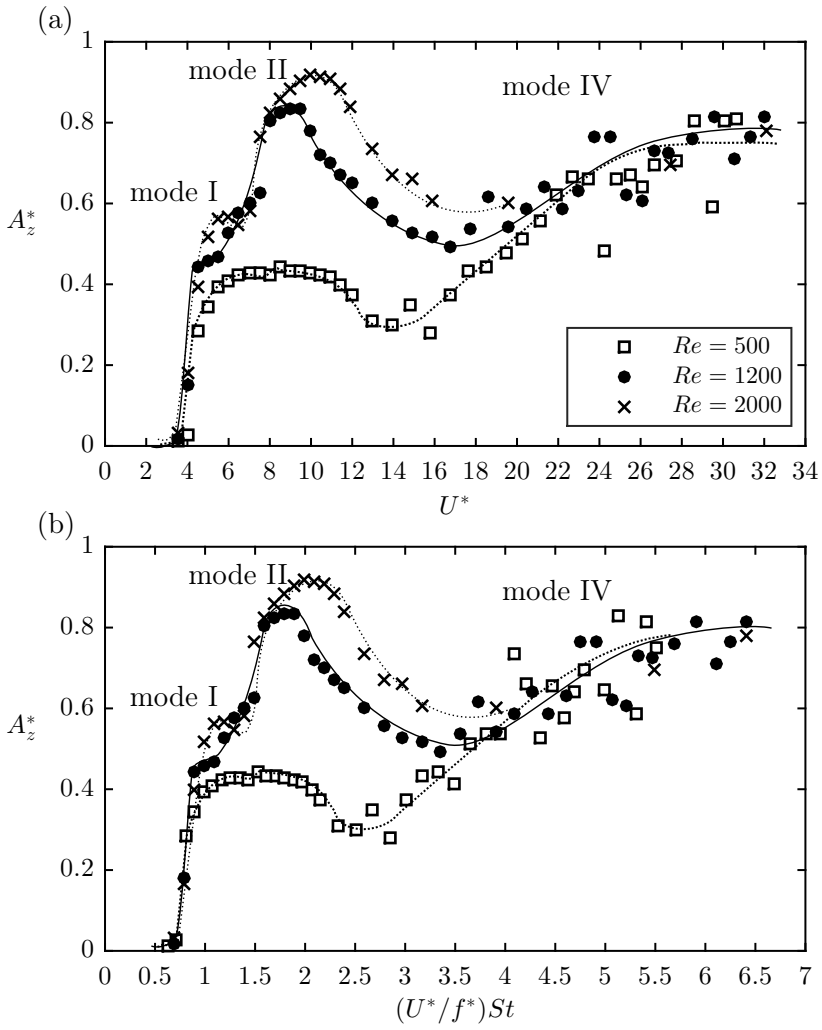

Figure 6.2.: The sphere response curves at $Re = 500$, 1200 and 2000 of a tethered sphere of $m^* = 0.8$: (a) the normalised amplitude, A_z^*, against the reduced velocity, U^*; and (b) plotted against the normalized velocity, $(U^*/f^*)St$.

(see figure 6.2 (b)).

Similar to the $Re = 500$ case, as discussed in chapter 4, we observed bell shaped response curves at $Re = 300$ and 800 with an elastically mounted sphere which were named 'Branch A'. Moreover, the maximum amplitudes we observed at those Reynolds numbers were $\approx 0.4D$ and $0.6D$, respectively. This observation leads to the conclusion that a sphere displays a trend of increasing amplitude globally over $U^* \approx [4, 16]$, as the Reynolds number increased from 300 to 2000, regardless of whether it was an elastically mounted or a tethered sphere.

For $U^* > 16$, the sphere showed an aperiodic response for all three Reynolds numbers. Although the amplitudes were scattered, they showed initially an increasing trend and

then levelling off around $0.8D$ as the reduced velocity increased to 34. We observed a similar behaviour at $Re = 800$ with an elastically mounted sphere for $U^* > 13$, but with a purely increasing trend up to $U^* = 50$ (Rajamuni *et al.* 2018*a*). As we claimed in chapter 4 or Rajamuni *et al.* (2018*a*), this intermittent burst of vibration strongly resembles mode IV vibration discovered by Jauvtis *et al.* (2001) with a heavy sphere of $m^* = 80$ for $U^* > 100$. This begs the question of 'why mode IV is observed just after mode II without an intervening mode III?'. A discussion of this is given in section 6.3.

Williamson & Govardhan (1997) and Govardhan & Williamson (2005) identified that the motion of a tethered sphere is principally in the transverse direction. Consistently, we also observed large amplitude vibrations in the transverse (z) direction compared to the streamwise (x) and lateral (y) directions (see figure 6.3 (a) and 6.4 (a)). For modes I and II regimes, the sphere showed a negligible amplitude in the lateral direction while displaying a small amplitude of $\approx 0.08D$ in the streamwise direction, as shown in figure 6.3 (a) at $Re = 1200$. This is consistent with the observation of Williamson & Govardhan (1997) with a sphere of $m^* = 0.73$ and tether length ratios, $l^* = 8.9$ and 3.8.

The periodicity of the sphere vibration, λ_A, is defined as $\sqrt{2}Z_{rms}/Z_{max}$, where Z_{max} is the maximum amplitude observed at each U^*. According to this definition, λ_A take values from 0 to 1, with $\lambda_A = 1$ representing the most periodic response. For both modes I and II, the sphere vibrations were highly periodic. However, it was more periodic at the peak of mode II compared with the response at mode I (see figure 6.3 (b) and figures 6.5 (a) and (c)). For both modes I and II, the sphere vibrated in synchrony with the vortex shedding frequency, f_s, and was close to the system's natural frequency, as expected (see figure 6.3 (c)). Govardhan & Williamson (1997, 2005) observed for light spheres ($m^* < 1$) across the mode II regime and above that, the dynamic vortex shedding frequency remained between the static body vortex shedding frequency, f_{vo}, and the natural frequency of the system.

As the sphere response curve for $Re = 500$ deviated from the response curve observed at higher Reynolds numbers over the modes I and II regimes ($U^* = [4.5, 12]$), a negligible amplitude was observed in both the streamwise (x) and lateral (y) directions (see figure 6.4 (a)). Vibrations in the transverse (z) directions were highly periodic as in the peak of mode II (figure 6.4 (b)). This is indeed a VIV response ($f = f_s = f_n$). From these observations, we can predict that the response of a tethered sphere collapses well with the response of an elastically mounted sphere of 1 DOF for low Reynolds numbers over the modes I and II regimes.

As the reduced velocity increased beyond $U^* = 12$ (beyond the mode II regime), the periodicity of the sphere response gradually decreased at $Re = 1200$ and reached a value of ≈ 0.5 for the mode IV regime (see figure 6.3 (b)). A similar behaviour was observed at $Re = 500$ as well. However, as U^* was increased, mode IV appeared quickly after

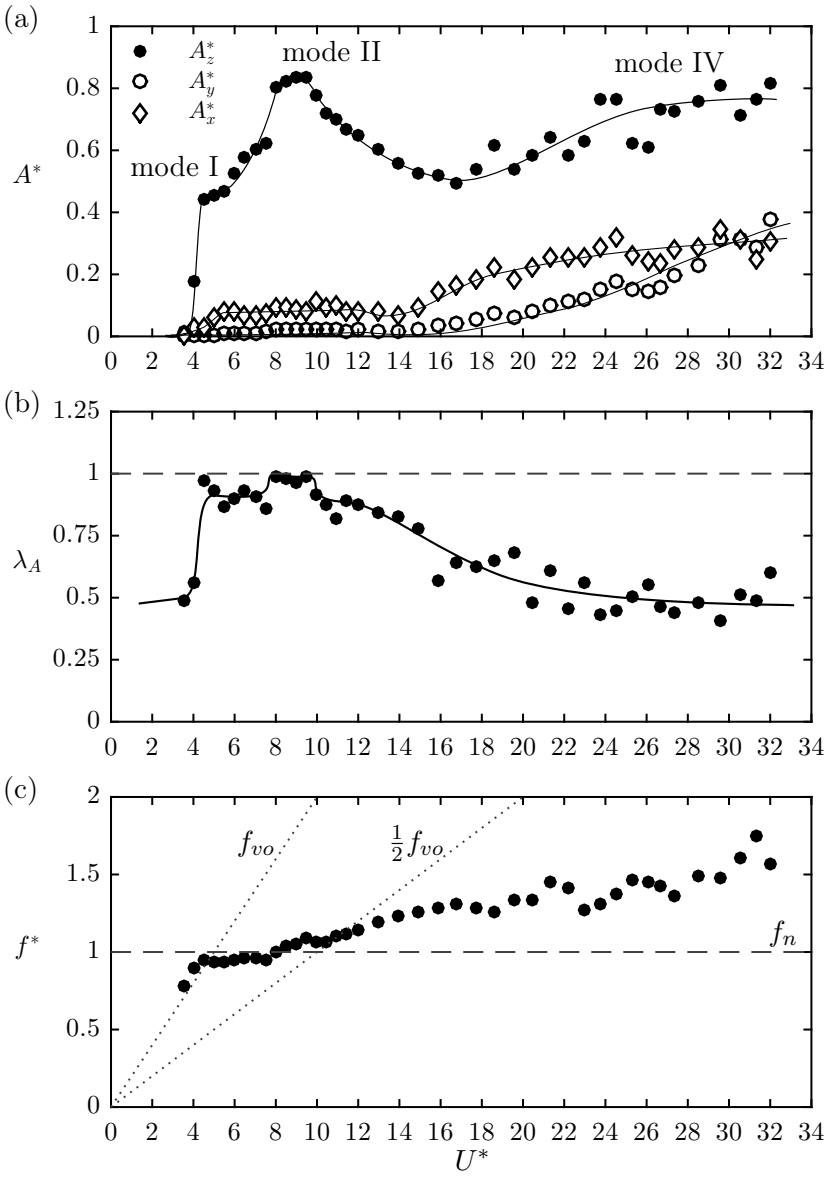

Figure 6.3.: The flow-induced vibration response of a tethered sphere at $Re = 1200$ over the reduced velocity range, $U^* = [3, 32]$: (a) sphere vibration amplitudes A_x^*, A_y^* and A_z^* in the streamwise, lateral and transverse directions, respectively; (b) the periodicity of the sphere vibration, $\lambda_A = \sqrt{2}Z_{rms}/Z_{max}$; and (c) frequency ratio, $f^* = f/f_n$.

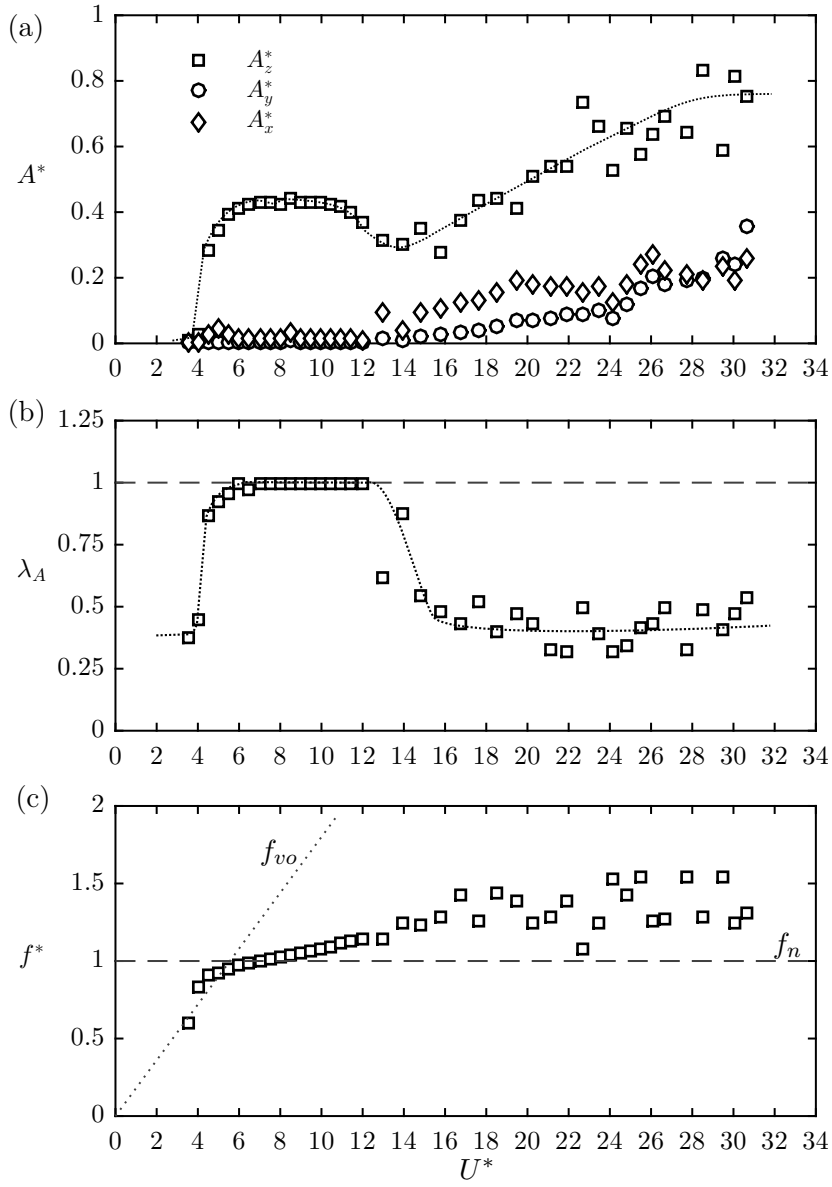

Figure 6.4.: The flow-induced vibration response of a tethered sphere at $Re = 500$ over the reduced velocity range, $U^* = [3, 32]$: (a) sphere vibration amplitude, A^*; (b) the periodicity of the sphere vibration, $\lambda_A = \sqrt{2}Z_{rms}/Z_{max}$; and (c) frequency ratio, $f^* = f/f_n$.

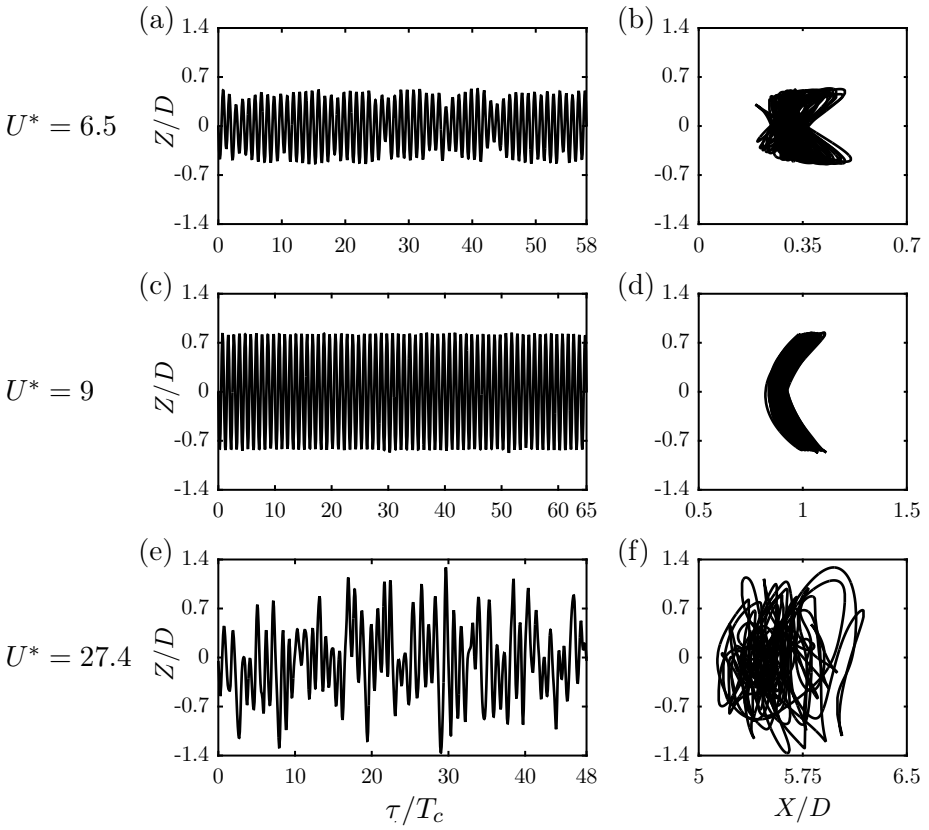

Figure 6.5.: Time histories (first column) and sphere trajectories in the x–z plane (second column) at $Re = 1200$, where $\tau = tU/D$ is the non-dimensional time and T_c is the period. (a) and (b) at $U^* = 5.5$ (mode I), (c) and (d) at $U^* = 9$ (mode II), and (e) and (f) at $U^* = 27.4$ (mode IV).

the periodic vibrations and the periodicity of the response was even lower. The sphere vibration was intermittent in mode IV, as shown in figure 6.5 (e) at $U^* = 27.4$ and it followed a irregular trajectory without a clear pattern as shown in figure 6.5 (f). As λ_A decreased, the sphere displacement in the streamwise and the lateral directions became slightly more significant. The streamwise amplitude was almost a constant value of $\approx 0.3D$ at $Re = 1200$ and $\approx 0.2D$ at $Re = 500$ over mode IV. The lateral amplitude showed a linearly increasing trend as the reduced velocity increased beyond 16 and was almost half the transverse amplitude at the highest reduced velocity considered ($U^* = 32$) at both Reynolds numbers. This shows that the randomness of the signal increases with increasing reduced velocity.

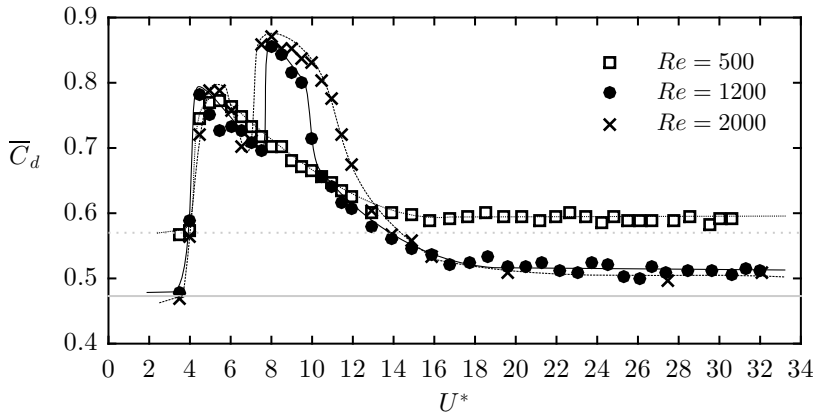

Figure 6.6.: Variation of the time-averaged drag coefficient, $\overline{C}_d$ with the reduced velocity at $Re = 500$, 1200 and 2000. The horizontal grey lines show $\overline{C}_d$ calculated with a stationary sphere at $Re = 500$ (dotted line) and $Re = 1200$ (solid line).

6.1.3. The drag coefficient

Figure 6.6 displays the time-averaged drag coefficient, $\overline{C}_d$, as a function of the reduced velocity for all three Reynolds numbers considered. An increment in $\overline{C}_d$ is observed when it vibrated periodically, as found in previous experimental and numerical studies (Williamson & Govardhan 1997; Gottlieb 1997; Behara *et al.* 2011). At $Re = 500$, as the sphere began to vibrate at $U^* = 4.5$, an $\sim 33\%$ increment of $\overline{C}_d$ was observed from the value for a stationary sphere. Similar to the observation of Rajamuni *et al.* (2018*a*) for their Branch A, this increment then decreased over the synchronization regime. However, they observed a sharp turn at the beginning of the range, while we observed a smooth turn. At both $Re = 1200$ and 2000, $\overline{C}_d$ showed another jump at the beginning of mode II, as Govardhan & Williamson (1997) observed. The increments of $\overline{C}_d$ were $\sim 60\%$ and $\sim 100\%$ at modes I and II, respectively. In the mode IV regime, even larger amplitude vibrations are observed, whereas the drag coefficient hardly changed at all. This is because mode IV is not a VIV response, as discussed in section 6.4.

6.1.4. The layover angle

The time-averaged layover angle, $\overline{\theta}_l$, is defined as the angle of the tether to the lateral direction (vertical). An exponentially increasing trend of $\overline{\theta}_l$ with a slight variation in mode II was observed for all of the Reynolds numbers considered (see figure 6.7). Since the lift force is comparatively small, the layover angle can be estimated from the non-dimensional drag and buoyancy forces as

$$\tan(\overline{\theta}_l) = \frac{C_d}{(1 - m^*)\psi}.$$

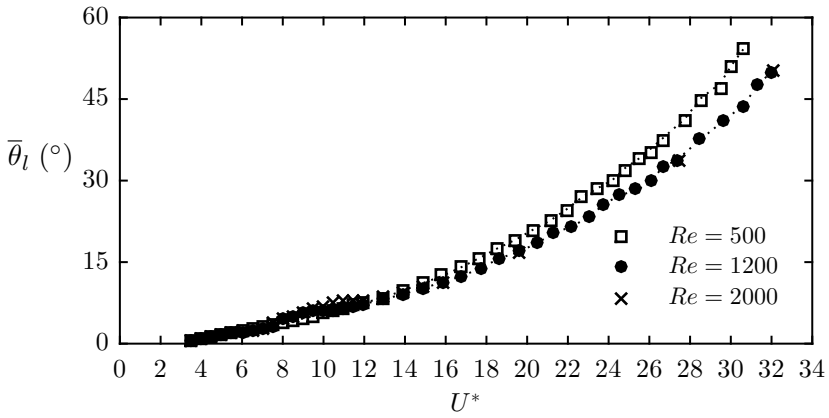

Figure 6.7.: The time-mean layover angle, $\overline{\theta}_l$ (angle of tether from the y direction) as a function of reduced velocity. The dotted lines represent the estimated $\overline{\theta}_l$ from the drag coefficient at each Reynolds number.

As can be seen in figure 6.7, the calculated $\overline{\theta}_l$ is coincident with the estimated values. Note that even though $\overline{C}_d$ is constant over the mode IV regime, $\tan(\overline{\theta}_l)$ increases; this is because $\psi = 4/(3Fr^2)$ is not constant in this numerical study.

From the findings of this study and previous experimental and numerical studies, a brief discussion of the different modes of sphere vibrations is provided in the following three sections.

6.2. Modes I and II

Modes I and II are the only vortex induced vibration responses observed for a sphere out of the four vibration modes found. Mode I response is due to a natural resonance, where the vibration of the sphere is excited when the natural frequency of the system, f_n, is close to the stationary body (non-VIV) vortex shedding frequency. For example, at $Re = 1200$, the vortex shedding frequency of a stationary sphere, f_{vo}, is approximately 0.2, which means that the natural oscillation frequency and the stationary body vortex shedding frequency coincide at $U^* = 5$. As a result of this, mode I was observed close to $U^* = 5$ (see figure 6.3 (a)).

In almost all of the VIV studies, the sphere showed large amplitude periodic vibrations even after the resonance range, and this is known as mode II vibration state. As the sphere is allowed to translate freely, a reduction is observed in the vortex shedding frequency from the value for a static sphere. In this manner, the dynamic shedding frequency deviated from the static shedding frequency and synchronized with the natural frequency (see figure 6.3 (c) and 6.4 (c)). As a result, the sphere showed large amplitude vibration (mode II) after the resonance state.

The mode II response was observed beyond the mode I regime as the reduced velocity was increased. The sphere response amplitude varied smoothly as the vibration state transitioned from mode I to mode II, in contrast with distinct branches observed in the amplitude response curve of an elastically mounted cylinder (1 DOF). The sphere response curve showed a small local peak in mode I for light tethered spheres ($m^* < 1$); for example, the observations of Williamson & Govardhan (1997) at $m^* = 0.729$ with both $l^* = 3.83$ and 8.93 and $m^* = 0.082$ with $l^* = 9.28$, Govardhan & Williamson (1997) at $m^* = 0.26$, and Jauvtis *et al.* (2001) at $m^* = 0.8$, can be given. However, the local peak in mode I is obscured for heavy spheres ($m^* > 1$), especially for elastically mounted spheres as discussed by Govardhan & Williamson (2005). The range of U^* values varies for different modes; mode I is observed for a very short range (within $\sim$ 1–2 U^*) compared with mode II. This is expected as mode I is the result of resonance.

The difference between modes I and II was studied by Govardhan & Williamson (2005) by analysing the phase between sphere oscillation and the fluid forces acting on the sphere. Lighthill (1986) showed that the total fluid force, F_t, can conveniently be split into two components, a 'potential force' component (F_p) related to the potential added mass and a 'vortex force' component (F_v) related to the dynamic vorticity. For a cylinder, Govardhan & Williamson (2000) found a shift in the total phase, ϕ_t (the phase between the sphere displacement and the total force), or the vortex phase, ϕ_v (the phase between the sphere displacement and the vortex force), as the vibration state transitions from one branch to another. Analogously, Govardhan & Williamson (2005) observed a shift in the vortex phase, while the total phase remains almost constant, as the sphere

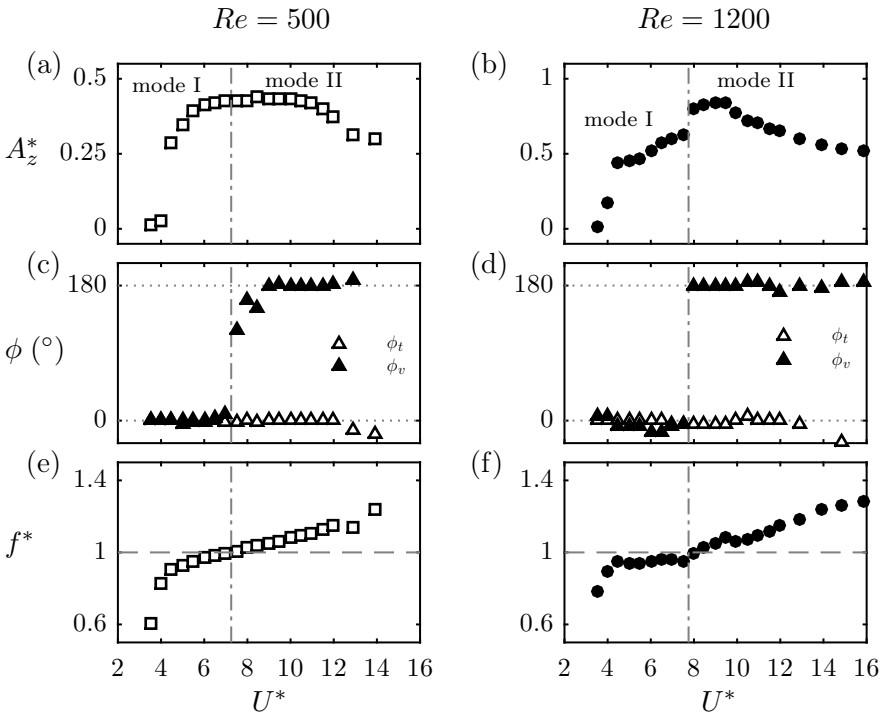

Figure 6.8.: Variation of the total phase, ϕ_t, and vortex phase, ϕ_v, over modes I and II regimes ((c) and (d)). The first column is for $Re = 500$ and the second column is for $Re = 1200$. The last row shows that the frequency ratio crosses the $f^* = 1$ line as the vortex phase shifts from 0° to 180°.

transitions from mode I to mode II. In a similar fashion, we found that the vortex phase shifted from 0° to 180° as the vibration state transitioned from mode I to mode II, while the total phase remained at $\approx 0°$, as shown in figure 6.8 (c) and (d) for $Re = 500$ and 1200, respectively.

For an elastically mounted cylinder, Govardhan & Williamson (2000) argued that a sudden shift in total or vortex phase can be expected as the body oscillation frequency passes the natural frequency of the system (or the frequency ratio crosses the $f^* = 1$ line). Consistent with this argument, we observed that the shift in ϕ_v occurs as the frequency ratio crosses the $f^* = 1$ line (see figure 6.8 (e) and (f)). In addition to this, they discussed that for a purely sinusoidal response with zero damping ratio, the total or vortex force can only be either phase aligned or be 180° out of phase with the body vibration. That discussion related to an elastically mounted cylinder. The motion of a tethered sphere has no damping effect (see equation 3.27). Therefore, if the sphere response is periodic, we can predict that ϕ_t and ϕ_v can be either 0° or 180° in a similar way. Consistently, we observed that ϕ_t and ϕ_v was mostly either 0° or 180°.

The response amplitude of mode II was found to be higher than the amplitude of

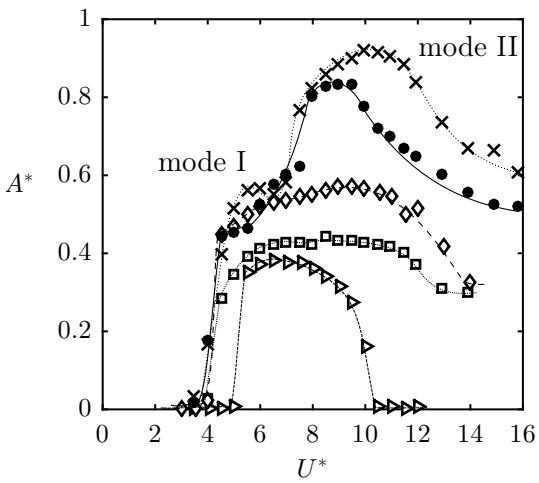

Figure 6.9.: The amplitude response curves at different Reynolds number at the modes I and II regimes: ▷ at $Re = 300$ of Rajamuni *et al.* (2018*a*) with an elastically mounted sphere of $m^* = 2.865$; □ at $Re = 500$; ◇ at $Re = 800$ of Rajamuni *et al.* (2018*a*) with an elastically mounted sphere of $m^* = 2.865$; • at $Re = 1200$; and × at $Re = 2000$.

mode I (for some cases, approximately twice the amplitude of mode I) by experimental studies at higher Reynolds numbers. We also observed a similar behaviour at $Re = 1200$ and 2000. However, for $Re < 1000$, the amplitude of mode II was observed to be similar to that of mode I (present results at $Re = 500$ and Rajamuni *et al.* (2018*a*) at $Re = 300$ and 800). Therefore, the effect of Reynolds number on the amplitude of mode II is not negligible in the laminar regime.

6.2.1. Effect of Reynolds number

Govardhan & Williamson (2005) showed that the effect of Reynolds number is negligible for the VIV of a sphere over a range of $Re \in [2000, 12000]$ with help of the Griffin plot and the tether length ratio. However, the effect of Reynolds number is significant over $Re \in [300, 2000]$. Figure 6.9 plots the sphere predicted responses together with the results of Rajamuni *et al.* (2018*a*) with elastically mounted spheres at five different Reynolds numbers over modes I and II regimes. As can be seen, the response amplitude increases globally with the Reynolds number. This effect is more significant over the mode II regime than the mode I regime. In addition, the mode II regime widened as the Reynolds number increased in this range. Mode II appears to be more sensitive to the Reynolds number.

6.2.2. Effect of mass ratio

Govardhan & Williamson (2005) studied the effect of mass ratio on the sphere re-

sponse and found that the response amplitude increased and the synchronization regime widened as the mass ratio decreased over the range $m^* \in [2.8, 198.4]$. For light spheres ($m^* < 1$), once the sphere reached its maximum amplitude (in mode II) by diverging from the usual decreasing trend, a levelling-off trend was observed in experiments. For example, Williamson & Govardhan (1997) at $m^* = 0.729$, Govardhan & Williamson (2005) at $m^* = 0.45$, and Jauvtis *et al.* (2001) at $m^* = 0.8$. However, in this numerical study, we observed a decreasing trend of amplitude after the maximum amplitude at $m^* = 0.8$. This difference with the experiments is most probably due to the effect of Reynolds number. We showed that the effect of Reynolds number is higher in the mode II regime. Therefore, if Re was increased further, there is an expectation that there will be a levelling-off trend toward the end of mode II. In addition, for light spheres and mode II, the shedding frequency was slightly higher than the natural frequency of the system.

6.2.3. Wake structure

The vortical structures of the wake were visualised with an iso-surface of the Q criterion (the second invariant of the velocity tensor) introduced by Hunt *et al.* (1988). The wake structures observed in modes I and II regimes are shown in figure 6.10. As can be seen, at $Re = 500$, two trails of hairpin vortices form the wake in both modes I and II regimes. These wake structures strongly resemble the wakes observed by Govardhan & Williamson (2005) for modes I and II, and by Rajamuni *et al.* (2018*a*) for their Branch A. Two hairpin loops were shed per sphere oscillation cycle and these loops were disconnected and two-sided. Furthermore, each vortex loop was accompanied by a tail. These hairpin loops were symmetric through the x–z plan as expected. Govardhan & Williamson (2005) explained that the two streamwise vortex loops associated with the orientation of the hairpin loops create a lift force similar to the vertical lift force associated with aircraft trailing 'tip vortices'. As the hairpin loops are two sided, the lift force is periodic and hence the sphere is excited to vibrate.

As the Reynolds number is increased, small-scale structures begin to appear in the wake. In mode I, the underlying wake structure was only slightly modified, continuing to show two strong hairpin loops per oscillation cycle, along with smaller scale structures. However, in mode II, the wake was modified further. Multiple loops were observed per oscillation cycle in the higher Reynolds number cases. Moreover, those loops were mostly connected with each other.

6.2.4. Dynamic Mode Decomposition (DMD)

For further examination of the wake, and to identify the dominant wake modes, DMD was performed based on the methods presented in § 3.4. The nature of the wake of mode

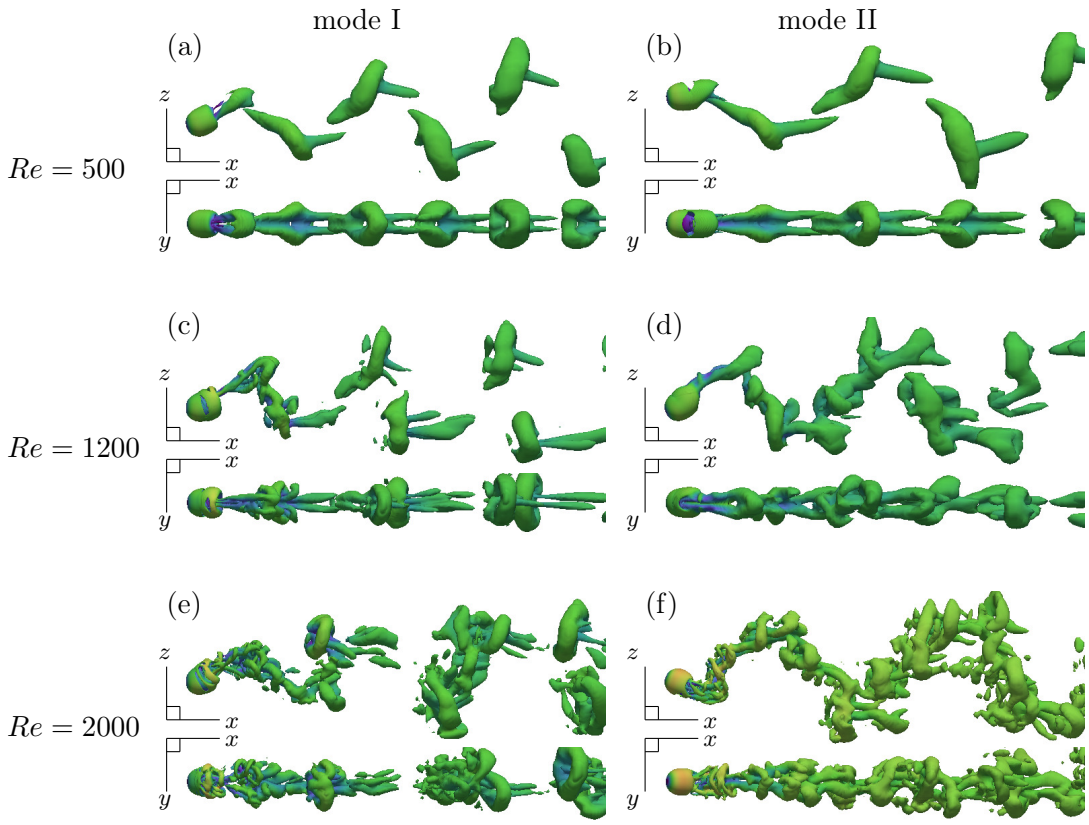

Figure 6.10.: Wake structures in modes I and II at $Re = 500$, 1200, and 2000 visualized with iso-surface of Q at 0.01. Flow from left to right.

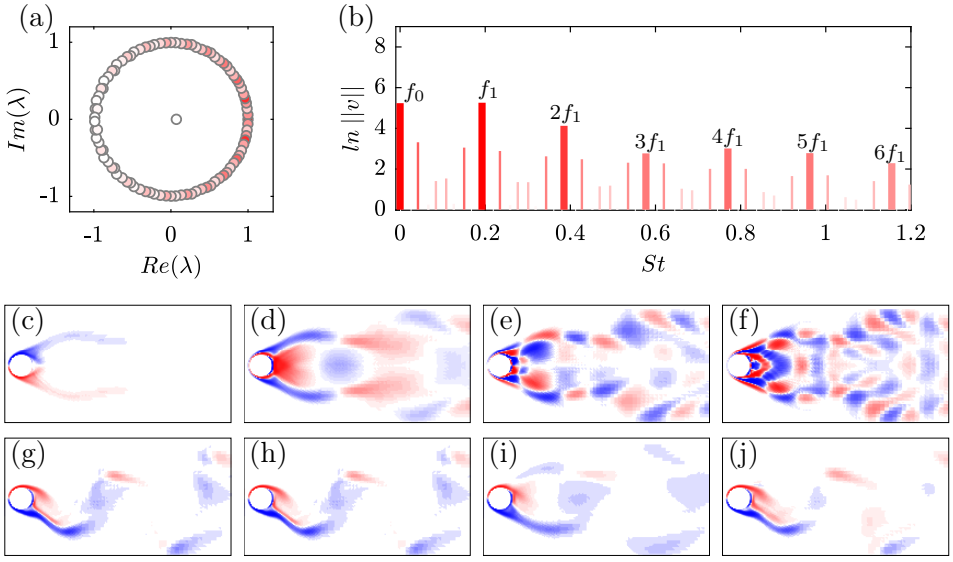

Figure 6.11.: Results of DMD analysis of $2D$ velocity field over 10 oscillation cycles of Mode I at $Re = 500$; (a) plot of eigenvalues of the Companion matrix; (b) frequency spectrum; (c)-(f) Dynamic modes, KM, (visualized by vorticity field) correspond to frequencies, f_0, f_1, $2f_1$, and $3f_1$, respectively; (g) Actual vorticity field; (h)-(j) reconstruction of vorticity field using all KMs, the dominant KM (f_0+f_1), and the dominant KM and its higher order harmonics $(f_0+f_1+2f_1+3f_1+4f_1+5f_1+6f_1)$, respectively.

I ($U^* = 5.5$) was studied at $Re = 500$ using the $2D$ velocity field (on x-z plane) over 10 oscillation cycles with 23 snapshots per cycle. As figure 6.11 (a) shows, the plot of eigenvalues of the Companion matrix, C lies in a unit circle, indicating a periodic wake. Moreover, the frequency, f_1, of the dynamic mode with the highest magnitude was identical to the oscillation frequency of the sphere, as expected. The sphere oscillation was not purely sinusoidal in this case; therefore, the frequency spectrum contained other frequencies besides the dominant frequency and its higher order harmonics (see figure 6.11 (b)). The vorticity field was used to visualize the Koopman modes, KMs, and to compare the reconstruction using these modes with the actual field (see figure 6.11 (c)–(j)). The reconstruction with all modes, shown in (h), is identical to the actual field shown in (g), providing some validation to the analysis. The dominant KM has captured the main features of the field (see figure 6.11 (i)). Moreover, when its higher order harmonics are also used it looks much closer to the actual field – compare (j) and (g).

The DMD analysis of $2D$ velocity field of mode II ($U^* = 9$) at $Re = 1200$ over 24 oscillation cycles with 48 snapshots per cycle was performed and results are presented in figure 6.12. The plot of eigenvalues of the Companion matrix provides evidence of a highly periodic wake. The sphere oscillation is purely sinusoidal in mode II. Inferred

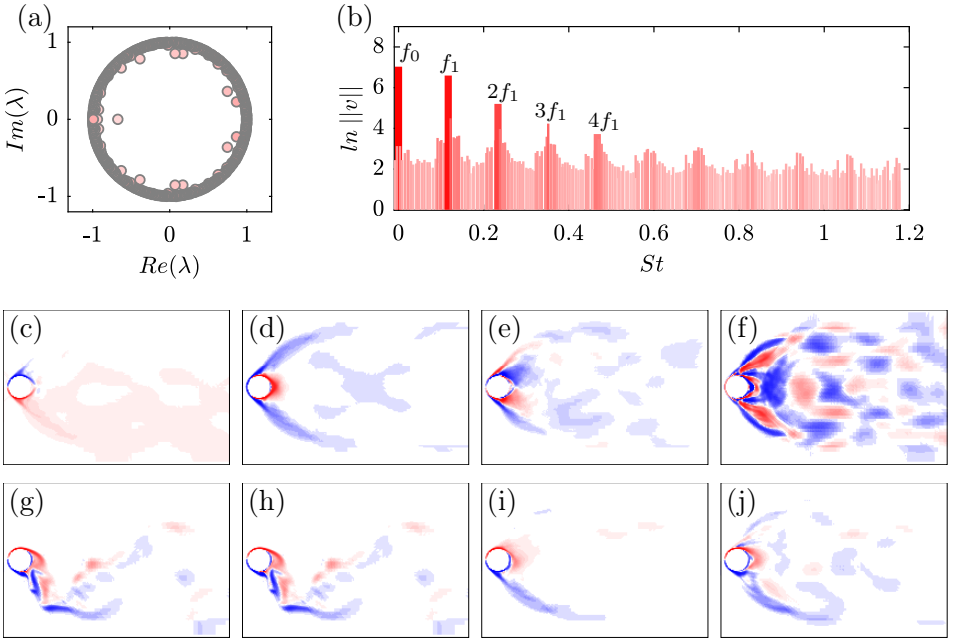

Figure 6.12.: Results of DMD analysis of $2D$ velocity field over 24 oscillation cycles of Mode II at $Re = 1200$; (a) plot of eigenvalues of the Companion matrix; (b) frequency spectrum; (c)-(f) Dynamic modes, KM, (visualized by vorticity field) correspond to frequencies, f_0, f_1, $2f_1$, and $3f_1$, respectively; (g) actual vorticity field; (h)-(j) reconstruction of vorticity field using all of the KMs, only the dominant KM $(f_0 + f_1)$ and the dominant KM and its higher order harmonics $(f_0+f_1+2f_1+3f_1+4f_1)$, respectively.

from this, the frequency spectrum in mode II for $Re = 500$ contained only the dominant frequency and its higher-order harmonics, as shown in figure 6.13 (b). However, as Re was increased to 1200, the frequency spectrum was dense with other frequencies, showing the effect of Reynolds number (see figure 6.12 (b)). Nevertheless, the underlying streamwise vortex structure observed for with the dominant KM (see figure 6.12 (i)) was synchronized with the sphere oscillation, so the sphere showed large amplitude mode II vibrations. This was also clearly visible from the iso-surfaces of the Q when $3D$ velocity fields were used for the analysis as shown in figure 6.14 for both modes I and II.

6.2.5. Robustness of modes I and II

Earlier, we showed that mode II is quite sensitive to the Reynolds number for $Re \in [300, 2000]$. In addition, mode II also appears sensitive to disturbances and other factors. For example, the experimental study of Sareen *et al.* (2018*a*) and the computational study of Rajamuni *et al.* (2018*b*) found that the mode II response weakens if even weak rotation (in the transverse direction) is imposed on the sphere. In particular, they observed a considerable reduction in the maximum oscillation amplitude and a

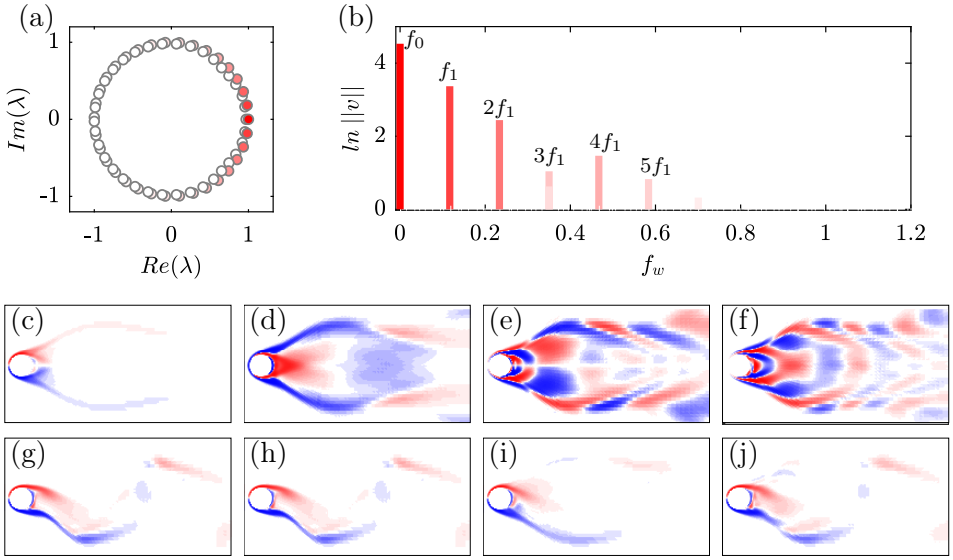

Figure 6.13.: Results of DMD analysis of $2D$ velocity field over 10 oscillation cycles of Mode II at $Re = 500$; (a) plot of eigenvalues of the Companion matrix; (b) frequency spectrum; (c)-(f) Dynamic modes, KM, (visualized by vorticity field) correspond to frequencies, f_0, f_1, $2f_1$, and $3f_1$, respectively; (g) Actual vorticity field; (h)-(j) reconstruction of vorticity field using all KMs, the dominant KM (f_0+f_1), and the dominant KM and its higher order harmonics ($f_0 + f_1 + 2f_1 + 3f_1 + 4f_1 + 5f_1$), respectively.

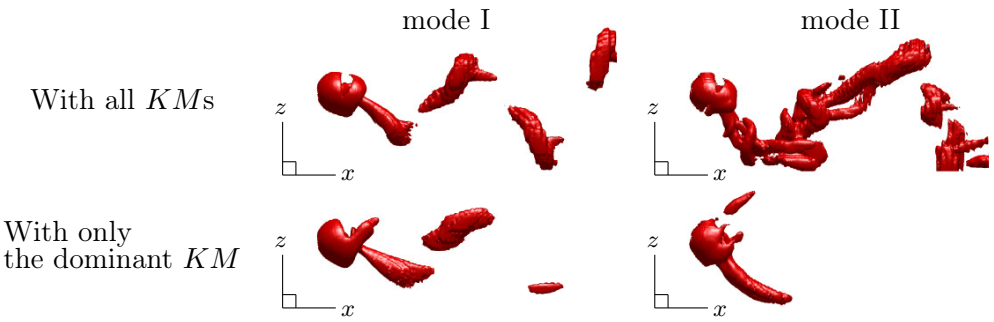

Figure 6.14.: Iso-surfaces of the wake at modes I and II reconstructed from all of the KMs (first row) and with only the dominant KM (second row). The dominant KM has captured the main feature of the flow.

narrowing of the synchronization regime. Furthermore, Sareen *et al.* (2018*b*) identified that the proximity of the sphere to the free surface greatly influences mode II. From these observations, we can conclude that mode I is more robust than mode II. Perhaps this is unsurprising as mode I is the primary resonant response.

6.3. Mode III

After the mode II regime, Jauvtis *et al.* (2001) discovered another periodic vibration state, namely mode III. It was an unexpected finding that was first observed with a sphere of $m^* = 28$ with water channel experiments. To study this mode further, they performed a set of wind tunnel experiments with a tethered sphere of $m^* = 80$ for a wide range of U^*. Mode III was found to occur after a desynchronization regime for a broad range of U^* from 20 to 40. They repeated this set of experiments with a larger tunnel to check whether it was an experimental artifact. Mode III was evident even with the larger tunnel. In addition to that, it was observed with a sphere of $m^* = 940$. The sphere response was remarkably periodic and the vibration amplitudes were almost the same as for mode II. Not only tethered spheres, but also elastically mounted spheres, showed mode III vibrations, but without a desynchronization regime; for example, this was found by Govardhan & Williamson (2005) with $m^* = 53.7$ and Sareen *et al.* (2018*a*) with $m^* = 14.2$.

As a consequence of the high mass ratio in previous experiments, the oscillation frequency of mode III was identical to the system's natural frequency. Nevertheless, it was difficult to explain the existence of mode III, since the principal vortex shedding frequency is 3 to 8 times higher than the oscillation frequency. Govardhan & Williamson (2005) observed multiple small-scale structures in the wake of mode III. There was no clear association between vortex shedding and full or half wave-length of the sphere vibration.

Mode III is not possible to explain with the classic lock-in theories and such a vibration state does not exist for the case of cylinder free vibration. Govardhan & Williamson (2005) argued that the flow must create a forcing on the body at this low frequency, sufficient to deliver a net energy transfer to the body motion. They measured the streamwise vorticity using DPIV and found a two-sided chain of trailing vortex pairs that is locked-in with the sphere frequency. With this observation, they claimed that there is a net positive energy transfer in the vibration over a cycle, enabling the highly periodic mode III. A tethered or an elastically mounted sphere is intrinsically unstable. Govardhan & Williamson (2005) argued that if the sphere is perturbed in the transverse direction, it can generate a self-sustaining vortex force to enhance the body vibration, to possibly a large amplitude. In the mode III regime, the sphere is highly likely to be perturbed as its wake is naturally responsive to low-frequency disturbances (Brücker 2001). Hence, Govardhan & Williamson (2005) concluded that mode III is an example of 'Movement induced vibration', categorized by Naudascher & Rockwell (2012).

Compared to the first two vibration modes, mode III has been little examined; only a couple of studies have reported it, and its nature is not well understood yet. Therefore, further investigation is presented in this chapter. We attempt to enhance the under-

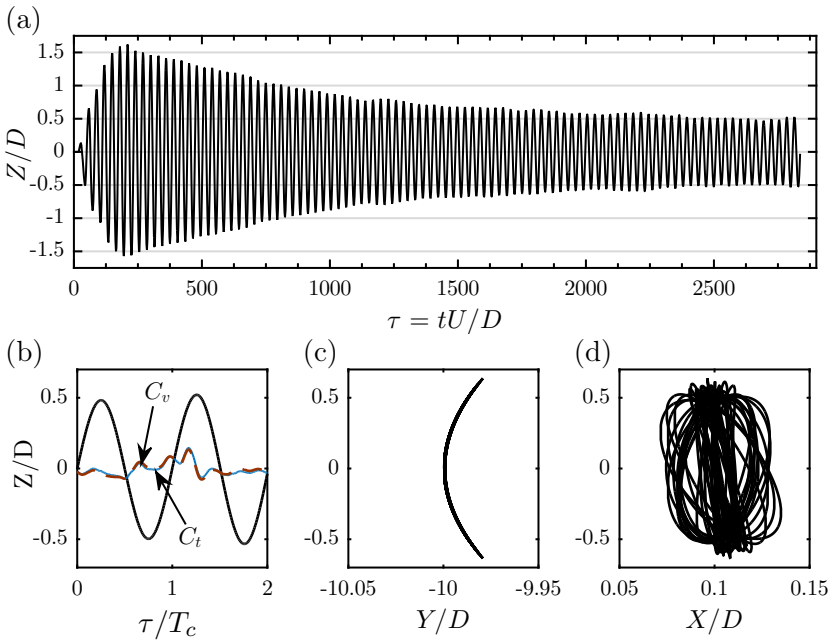

Figure 6.15.: The sphere response at $m^* = 80$, $U^* = 30$ and $Re = 1200$: (a) time history; (b) sphere displacement together with total and vortex force coefficients, C_t and C_v, respectively; (c) and (d) trajectory of the sphere in y-z and x-z planes, respectively, at the asymptotic state.

standing of mode III, through some previous experimental observations together with selected simulations.

We observed that the mode III state appears only with heavy spheres. In particular, Jauvtis *et al.* (2001) found mode III for spheres of $m^* = 28$, 80 and 940, while Govardhan & Williamson (2005) observed it for spheres of $m^* = 11.7$, 31.1, 53.7 and 75, and Sareen *et al.* (2018*a*) for a sphere of $m^* = 14.2$. From this, we can hypothesis that mode III arises only for high inertia systems (heavy spheres). We intended to check this hypothesis with a sphere of higher mass ratio. Unfortunately, simulations are very costly for higher mass ratio cases, since it takes a very long time to reach the asymptotic state. Therefore, only a couple of runs were feasible.

6.3.1. Present results at mode III

At $m^* = 0.8$ and $Re = 1200$, intermittent mode IV vibrations were observed for $U^* \in [16, 32]$ just after mode II, without a trace of mode III. To study the possibility of mode III being excited, we performed a simulation with a sphere of $m^* = 80$ at $U^* = 30$ and $Re = 1200$. This U^* was chosen since mode III emerged predominantly for the reduced velocity range, $U^* \in [20, 40]$, in earlier experimental studies. Figure 6.15 (a) shows the

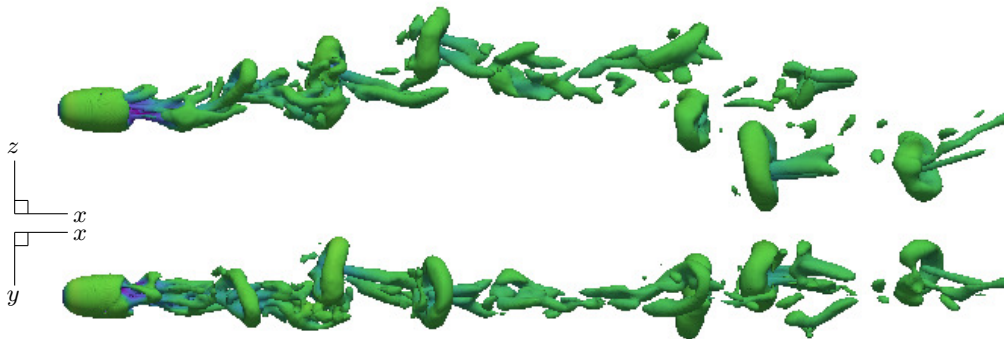

Figure 6.16.: Wake observed in mode III ($Re = 1200$, $m^* = 80$, $l^* = 10$ and $U^* = 30$) visualised with iso-surface of $Q = 0.001$. Flow from left to right.

time history of the sphere displacement in this case. As can be seen, the sphere vibration has become fairly periodic from intermittent vibration as the mass ratio increased to 80. The sphere response amplitude converged to a value of $\approx 0.5D$ after a long transient period. The sphere vibration is highly periodic. Moreover, its frequency coincides with the system's natural frequency, as expected at this high mass ratio. However, neither the total nor vortex forces were periodic, and those forces were small in magnitude with a high frequency (see figure 6.15 (b)). As seen in previous experimental studies, the vortex shedding frequency was higher than the sphere frequency; for this case, it was approximately six times higher. Thus, this is essentially a mode III response. Figure 6.16 shows the wake structure observed. Figures 6.15 (c) and (d) show the sphere trajectory in y–z and x–z planes. Its displacement in the streamwise (x) and lateral (y) directions were negligible compared to the displacement in the transverse (z) direction. However, the streamwise frequency is the same as the transverse frequency, in contrast to modes I and II, for which the streamwise frequency is double the transverse frequency.

6.3.1.1. Dynamic Mode Decomposition

The wake of mode III was investigated with DMD using the velocity field over 10 sphere oscillation cycles, with 48 snapshots per cycles. As figure 6.17 (a) shows, eigenvalues of the Companion matrix lie mainly on the unit circle, indicating a strong periodicity of the wake. Additionally, the dominant frequency of the wake, identified from the frequency spectrum shown in figure 6.17 (b), $f_1 = 0.0335$, is identical to the sphere oscillation frequency. Even though a number of small loops were shed per oscillation cycle, the wake displays a long wavelength structure in the downstream direction corresponding to the sphere oscillation. Figure 6.18 (a) and (b) show the iso-surfaces of Q of the reconstructed field with all of the KMs and only the dominant KM pair, respectively. The reconstruction with only the dominant KM pair consists of long vortical structures, similar to the observation of Govardhan & Williamson (2005). These long structures

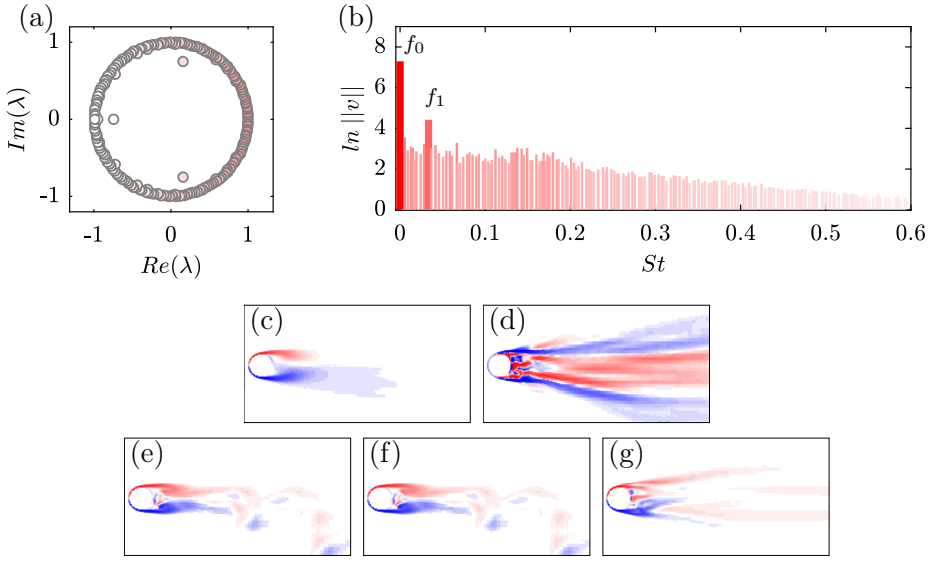

Figure 6.17.: Results of DMD analysis of $2D$ velocity field over 10 oscillation cycles of Mode III at $Re = 1200$; (a) plot of eigenvalues of the Companion matrix; (b) frequency spectrum; (c) and (d) Dynamic modes, KM, (visualized by vorticity field) correspond to frequencies, f_0 and f_1, respectively; (e) Actual vorticity field; (f) and (g) reconstruction of vorticity field using all KMs and the dominant KM $(f_0 + f_1)$, respectively.

Figure 6.18.: Iso-surface of Q at mode III; (a) using all KMs and (b) only the dominant KM conjugate pair.

were also visible in the $2D$ vorticity field (see figure 6.17 (d)). The frequency spectrum was dense with several frequencies, showing the effect of Reynolds number.

6.3.1.2. Response at higher reduced velocities

To compare with the results of Jauvtis *et al.* (2001) at higher U^* values, two more simulations were performed at $U^* = 70$ and 150. After mode III, they have observed a desynchronization regime for the U^* range of $\approx [40, 100]$ and then mode IV vibration for $U^* > 100$ with a sphere of $m^* = 80$. Consistent with their results, we observed a small-scale vibration at $U^* = 70$ and mode IV at $U^* = 150$ (see figure 6.19).

As the mass ratio increased from 0.8 to 80, mode III vibration was predicted before

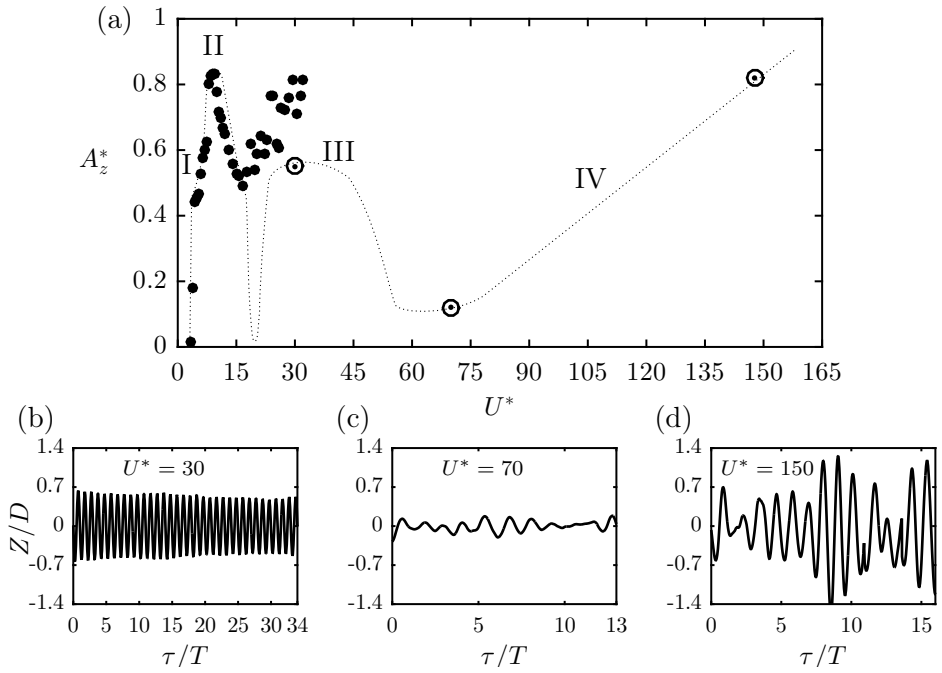

Figure 6.19.: The sphere response at $m^* = 80$ and $Re = 1200$. (a) Comparison of the response amplitudes for $m^* = 80$ calculated for $U^* = 30$, 70, and 150 denoted by $\odot$ with the amplitude of $m^* = 0.8$ denoted by $\bullet$. The dotted line shows the expected response amplitude curve for $m^* = 80$. (b), (c) and (d) show the time histories at $m^* = 80$ for $U^* = 30$, 70, and 150, respectively.

mode IV and the ranges of these modes match well with the experimental result of Jauvtis *et al.* (2001). From these observations it is evident that mode III is essentially a moment-induced vibration, as Govardhan & Williamson (2005) explained. The self-excitation initiated by the sphere wake pattern in this low frequency regime becomes regular most likely as a result of the high inertia of the system. If the mass ratio is too small then the sphere motion may not become regular and will show random vibration (mode IV), as observed at $m^* = 0.8$. The mode III state can be identified as an unstable state that can only appear for high inertia spheres. Moreover, mode III appears quite sensitive to disturbances. For example, Sareen *et al.* (2018*a*) observed a mode III type of response for $U^* > 14$ for an elastically mounted sphere with zero-rotation. However, when a rotation was imposed on the sphere, mode III was no longer observed. Mode III seems weaker than mode II. As a result, we can conclude that mode III is likely to be disappear if a continual disturbance is applied on the system.

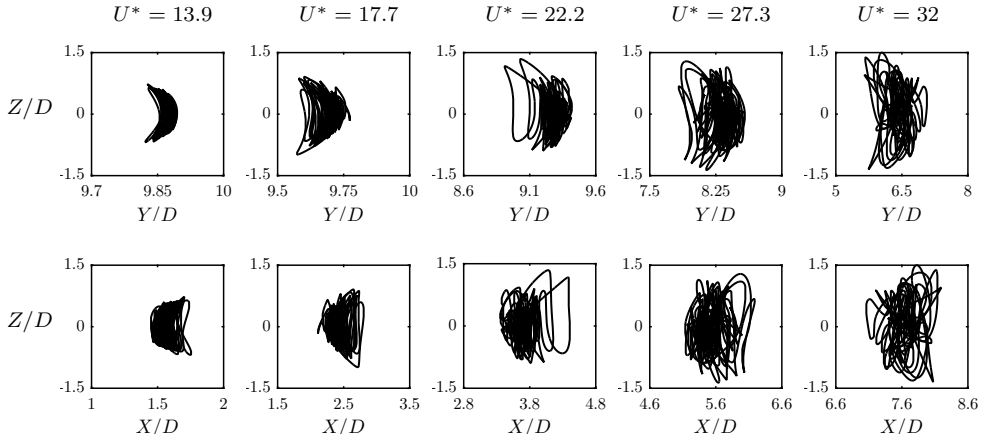

Figure 6.20.: Sphere trajectories in mode IV and $Re = 1200$. First row in y-z plane and second row in x-z plane at $U^* = 13.9$, 17.7, 22.2, 27.3, and 32.

6.4. Mode IV

Jauvtis *et al.* (2001) observed intermittent bursts of large amplitude vibration (mode IV) after the mode III regime with a sphere of $m^* = 80$ for $U^* > 100$. The periodicity of mode IV was found to be $\lambda_A = 0.5$ compared to the highly periodic first three modes ($\lambda_A = 1$). They found that the sphere vibration frequency remained very close to the system's natural frequency throughout the range of velocity up to at least $U^* = 300$. Jauvtis *et al.* argued that mode IV cannot be a VIV response as the vortex shedding frequency is much higher than the sphere frequency and there is no correlation between those two frequencies.

Rajamuni *et al.* (2018*a*) also observed mode IV type aperiodic vibration in their numerical study at $Re = 800$, and called it the Intermittent Branch. It was observed immediately following their periodic Branch A for $U^* > 14$ up to $U^* = 50$ with a sphere of $m^* = 2.685$. In mode IV, Rajamuni *et al.* found that the r.m.s. of the oscillation amplitude linearly increased with increasing U^*, similar to the observation of Jauvtis *et al.* (2001). It was quite surprising how can a small-mass-ratio sphere could show mode IV response for relatively low reduced velocities. Rajamuni *et al.* (2018*a*) conjectured that it may be an effect of zero structural damping. Moreover, they argued that an increased damping may reduce or even suppress these intermittent vibrations.

Mode IV type intermittent response was observed in this numerical study with a tethered sphere of $m^* = 0.8$ at all three Reynolds numbers considered. In particular, the sphere showed mode IV at $Re = 500$ for $U^* > 14$ and at $Re = 1200$ for $U^* > 16$. For this mass ratio, mode IV appeared immediately after mode II without an intervening mode III, as Rajamuni *et al.* (2018*a*) observed with an elastically mounted sphere.

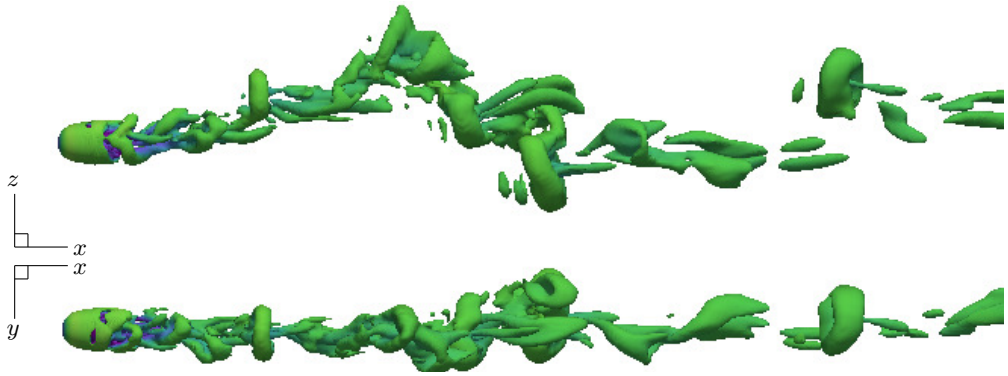

Figure 6.21.: Wake structure observed in mode IV ($Re = 1200$, $m^* = 0.8$, $l^* = 10$, and $U^* = 30$) visualised with iso-surfaces at $Q = 0.001$. Flow from left to right.

Figure 6.20 shows the trajectories of the sphere at five different U^* values in both x–z and y–z planes at $Re = 1200$. In contrast to the first three modes, the sphere showed significant motion in the streamwise and the lateral directions as well. As can be seen, the regularized trajectory observed at $U^* = 13.9$ (mode II) became irregular as the sphere transitioned to mode IV. Moreover, the sphere followed a random trajectory with a large amplitude in the transverse (z) direction. However, the dominant sphere oscillation frequency was close to the system's natural frequency. In this mode, no increment was found in the time-mean drag coefficient (figure 6.6) and the fluctuation force components were small in magnitude. There was no correlation between forces and the sphere vibration. In addition, the wake was irregular in strength and frequency with several vortex loops formed per oscillation cycle (see figure 6.21).

For a static sphere, Brücker (2001) measured broad low frequencies for the streamwise vortex formation. Therefore, the motion of the sphere seems to originate from the wake pattern of the sphere even in the mode IV regime. The sphere is likely to exhibit a random motion than rather a periodic motion at this higher reduced velocities since the flow speed is comparatively higher. As discussed in the previous section, when the mass ratio increased from 0.8 to 80, mode III appeared before mode IV. Here, we can see that the inertia of the sphere plays a major roll in this low frequency regime. When the inertia is high, then it tends to show mode III characteristics before mode IV, but when it is low, it shows mode IV behaviour.

For light spheres, modes III or IV were not observed experimentally due to experimental limitations (Jauvtis *et al.* (2001)). The maximum U^* considered in those experiments was $U^* \approx 20$. They observed mode II with a constant amplitude up to the highest U^* value they considered. Mode II might be continued even for larger U^* values. Since mode IV is a irregular motion, it is likely to appear for light spheres in the turbulent regime.

6.5. Summary

Compared to cylindrical bodies, only a few studies have focused on investigating the flow-induced vibration of spherical bodies. Therefore, this numerical study aims to further enhance knowledge of FIV of tethered spheres, with special attention on the different modes of sphere vibration discovered in previous experimental studies. Three sets of simulations were conducted for a tethered sphere of mass ratio $m^* = 0.8$ and length ratio $l^* = 10$ by fixing the Reynolds number at $Re = 500$, 1200 and 2000. The sphere response was investigated over the reduced velocity range $U^* \in [3, 32]$. The major findings of this study can be summarised as follows.

The effect of Reynolds number on the mode I and II responses is substantial. The sphere showed periodic mode I and II vortex-induced vibration responses at each Reynolds number. For $Re = 500$, by deviating from the previous experimental studies, the sphere showed a constant amplitude of $\approx 0.45D$ over both modes I and II regimes ($U^* = [4.5, 12]$). The sphere response amplitude increased as the Reynolds number was increased, especially in the mode II regime. Moreover, the amplitude response curve showed a clear transition between modes I and II for both $Re = 1200$ and 2000. The sphere response was closer to that seen in previous experimental studies as the Reynolds number was increased. As expected, the resonance response (mode I) appeared near the normalized velocity $(U^*/f^*)St = 1$, while mode II appeared in the range $(U^*/f^*)St \in [1.4, 2.4]$ for each Reynolds number, which is consistent with the (experimental) findings of Govardhan & Williamson (2005). The current predictions and the results of Rajamuni *et al.* (2018*a*) for their branch A at $Re = 300$ and 800, observed with an elastically mounted sphere, led to the conclusion that the sphere response amplitude increases globally with the Reynolds number over the range $Re = [300, 2000]$ in modes I and II regimes. Moreover, the effect of Reynolds number is greater on mode II than mode I. The mode I response appears more robust than the mode II response, as it corresponds to the natural resonance. Two-sided hairpin loops were observed in the wake of these two modes. Moreover, two loops were shed on opposite sides of the sphere per oscillation cycle. However, for $Re = 1200$ and 2000, in mode II multiple loops were observed over an oscillation cycle.

The mode III response is excited under the condition of high inertia of the system. At each Reynolds number, as the reduced velocity was increased, the sphere switched to a mode IV-type irregular response immediately after the periodic mode II response without passing through an intervening mode III regime. In previous experimental studies, mode III has only been found for heavy spheres. Therefore, a few simulations were conducted by increasing the mass ratio of the sphere to $m^* = 80$ at $Re = 1200$, for further investigation. At $U^* = 30$, on increasing the mass ratio from 0.8 to 80, the random motion of the sphere became fairly periodic, consistent with a mode III

response. In the wake, multiple vortex loops were observed per oscillation cycle as seen in previous experiments. Govardhan & Williamson (2005) argued that mode III is a movement induced vibration which is excited as a result of the initial perturbation of the sphere occurring due to its wake pattern. We found that the sphere can only have a sustainable periodic motion if it has enough inertia, in this low-frequency range. Finally, mode III can be identified as an unstable vibration state that is only excited for large-mass-ratio spheres.

The sphere motion is irregular in mode IV. A tethered sphere of $m^* = 0.8$ showed mode IV oscillations for $U^* > 14$ for $Re = 500$ and for $U^* > 16$ for the other two Reynolds numbers. The motion of the sphere was highly irregular in this mode. Interestingly, the sphere motion was mainly in the transverse direction. However, its motion was non-negligible in the other two directions. The r.m.s of the transverse amplitude showed an increasing and then levelling-off trend, as the reduced velocity was increased over the mode IV regime. For $m^* = 80$, mode IV was found to occur after mode III for very large reduced velocities ($U^* = 150$), consistent with observation of Jauvtis *et al.* (2001). The onset of mode IV shifts to higher U^* values as the mass ratio is increased. The irregularity of the motion in mode IV is presumably a result of the considerable difference between the wake forcing frequency and the natural system frequency.

If you judge people, you have no time to love them.

Mother Teresa

7. Conclusions and future scopes of research

7.1. Conclusions

In this thesis, we have examined the nature of the flow-induced vibration of a sphere. The dynamic behaviour of the sphere, forces applied on it and the wake structures behind the body were investigated for both elastically-mounted and tethered spheres. In addition, the effects of imposed transverse rotation on the flow-induced vibration of a sphere were also studied. The main findings of the thesis are summarised below.

FIV of an elastically-mounted sphere

First, we explored the FIV of an elastically-mounted sphere for the classic case, where the sphere motion was constrained to move in a direction transverse to the freestream. Numerical simulations were conducted at Reynolds numbers 300 and 800 over the reduced velocity ranges $3.5 \leq U^* \leq 100$ and $3 \leq U^* \leq 50$, respectively, with a sphere of mass ratio $m^* = 3.865$.

A highly periodic vortex-induced vibration response (named as Branch A) was observed at lower reduced velocities. At $Re = 300$, the sphere vibrated with a maximum amplitude of $0.4D$ over the reduced velocity range $5.5 \leq U^* \leq 10$. The amplitude response curve, $A^* - U^*$, for Branch A was approximately bell-shaped with a single peak, similar to the response curve of Behara *et al.* (2011) and Behara & Sotiropoulos (2016) with a $3 - DOF$ sphere. This response curve did not exhibit a clear partition between modes I and II. Nevertheless, we observed that the vortex phase switches from $\backsim 0°$ to $\backsim 180°$, indicating a partition of Branch A into modes I and II.

On increasing the Reynolds number to 800, the response amplitude of the Branch A increased substantially (maximum amplitude $\backsim 0.6D$). Moreover, the response curve showed more similarities to that observed in experimental studies at higher and varying Reynolds numbers in the modes I and II regimes. Compared to the $Re = 300$ case, the range of reduced velocities that showed synchronised vibrations was also widened at $Re = 800$.

In one oscillation cycle, two hairpin loops were shed into the wake from the opposite side of the sphere, creating two trails of vortex loops behind the sphere. These vortex trails were of equal strength, as the sphere oscillation was symmetric about its

initial position. This wake structure strongly resembles that observed by Govardhan & Williamson (2005) for mode I and II vibrations and hairpin type wakes observed by Behara *et al.* (2011).

At higher reduced velocities, the sphere response at $Re = 800$ was entirely different from that at $Re = 300$. At $Re = 800$, the sphere showed intermittent bursts of vibrations for $U^* > 16$. This aperiodic response was named the Intermittent Branch, and it strongly resembles the mode IV vibration state identified by the experimental study of Jauvtis *et al.* (2001) with a higher mass ratio sphere for very high reduced velocities ($U^* > 100$). At $Re = 300$, the sphere showed small scale vibrations through a new time-mean position over the ranges $U^* \in [13,\ 16]$ and $[26,\ 100]$, which were named as Branch B and C, respectively. These observations led to the conclusion of that *the flow-induced vibration of a sphere is strongly dependent on the Reynolds number in the range of* $300 \leq Re \leq 800$*, especially at higher reduced velocities.*

Effects of transverse rotation of VIV

Secondly, we explored the nature of the vortex-induced vibration response Branch A, when the sphere is under a forced rotation in the transverse direction. A Reynolds number of 300 was chosen for this study. Numerical simulations were conducted over the reduced velocity range $3.5 \leq U^* \leq 11$ and rotation rates $0 \leq \alpha \leq 2.5$, to study the correlation between the Magnus effect caused by the sphere rotation and the vortex-induced vibration.

The sphere showed vortex induced vibration response even under a forced rotation. However, it vibrated through a new time-mean position with a smaller amplitude, compared with the zero-rotation case. Interestingly, the sphere response amplitude decreased with increasing rotation rate, and the VIV was completely suppressed beyond $\alpha = 1.3$. Concurrently, the synchronisation regime narrowed, and mostly moved toward lower U^* values, with increasing rotation rate. This indicates that *the sphere rotation has a comparatively larger impact on mode II than on mode I.*

When a rotation was imposed on the sphere, the wake deflected to the advancing side due to the Magnus effect; this was more prominent as the rotation rate increased. With this symmetry breaking of the wake, the vortex loops in the trail from the advancing side were stronger than the loops in the trail from the retreating side. This unevenness of the wake, which affects the oscillatory forces applied on the sphere, appeared to be associated with the reduction of the sphere amplitude at higher rotation rates. From these observations, we can conclude that *vortex-induced vibration can only persist at small rotation rates, and the dominating Magnus effect at higher rotating rates cause suppression of VIV, as a result of the suppression of vortex shedding.*

The effects of Reynolds number on the VIV of a rotating sphere was studied at the reduced velocity of 6, over the Reynolds number range $300 \leq Re \leq 1200$. The sphere

response amplitude increased significantly as the Reynolds number was increased at all three rotation rates considered. Thus, at higher Reynolds numbers, VIV will persist for even higher rotation rates with a larger amplitude. With this observation, we can conclude that *the VIV of a sphere is strongly dependent on the rotation rate, reduced velocity and Reynolds number, which span the laminar regime and beyond.*

Vibration modes of a tethered sphere

Finally, we studied the flow-induced vibration of a tethered sphere. Three sets of numerical simulations were conducted at $Re = 500$, 1200, and 2000 with a sphere of mass ratio 0.8 and a tether length ratio of 10 to enhance the understanding of different modes of sphere vibration.

The sphere showed periodic modes I and II VIV responses at each Reynolds number. The amplitude response curve at $Re = 500$ looked similar to that observed with an elastically-mounted sphere in the first study at $Re = 300$, but with slightly higher amplitudes (maximum amplitude of $\backsim 0.45D$). The sphere response amplitude increased progressively with increasing Reynolds number, especially in the mode II regime. Moreover, at higher Reynolds numbers, the sphere response curves were closer to those seen in previous experimental studies. The mode I response appeared to be more robust than the mode II response, as it corresponds to the natural resonance. Together with the results from the first study, we can conclude that *in mode I and II regimes, the sphere response amplitude increases globally with the Reynolds number over the range* $300 \leq Re \leq 2000$*, regardless of the mounting method of the sphere. Moreover, the effect of Reynolds number is greater on mode II than mode I.*

A mode III type response was not observed with this small mass ratio sphere. In previous experimental studies, mode III has only appeared with a heavy sphere. Therefore, a few simulations were conducted by increasing the mass ratio to 80 at $Re = 1200$. At $U^* = 30$, the sphere showed periodic mode III response when $m^* = 80$, which was mode IV type aperiodic response with $m^* = 0.8$. For mode III, the wake showed a strong synchrony with the sphere oscillation even though multiple vortex loops were observed per oscillation cycle, as seen in previous experimental studies. Therefore, *mode III can be identified as an unstable vibration state that is only excited for high inertia systems.*

For $m^* = 0.8$, as U^* increased beyond the periodic mode II regime, the sphere showed mode IV type intermittent bursts of vibration at all three Reynolds numbers, similar to that seen in $Re = 800$ in our first study. In this mode, the motion of the sphere was highly irregular. But, the sphere motion was mainly in the transverse direction. For $m^* = 80$, mode IV was found to occur after mode III for very large reduced velocities, consistent with the observation of Jauvtis *et al.* (2001). Thus, we can conclude that *the onset of mode IV shifts to higher U^* values as the mass ratio is increased.*

7.2. Future scopes of research

This thesis examined the nature of flow-induced vibration of a sphere by varying the parameters such as Reynolds number, reduced velocity, mass ratio and the rotation rate over wide ranges in the parameter space. However, there remains scope for future work as listed below:

1. Flow past a stationary sphere becomes unsteady with the onset of vortex shedding beyond $Re \simeq 270$. The smallest Reynolds number used in FIV problems of a sphere is 300. It will be interesting to know the lowest Reynolds number of the flow at which a sphere will be excited to vibrate.

2. Only a few FIV problems of the sphere have been conducted with elastically mounted spheres, and most of these studies constrained the sphere motion to lie in the transverse direction. Behara *et al.* (2011) and Behara & Sotiropoulos (2016) conducted the only studies on the VIV of a sphere with $3-DOF$ motion. They have observed two distinct sphere responses at the same reduced velocities at $Re = 300$. The majority of the results they presented are at $Re = 300$ by varying U^* in the modes I and II regimes. Therefore, it will be interesting to investigate the nature of flow-induced vibration response with a $3-DOF$ sphere at higher Reynolds numbers over a broad range of reduced velocities. In addition, one can also explore the nature of flow-induced vibration when the sphere motion is restricted to lie in the streamwise direction.

3. The effects of mass ratio on the flow induced vibration response of a sphere over low to intermediate Reynolds number range have been less examined. Therefore, the study of FIV of a sphere can be extended by broadening the mass ratio to higher values.

4. FIV problems of the sphere at higher Reynolds numbers ($Re > 2000$) have only been studied experimentally. The numerical study of FIV of a sphere with elastic support or supported with a tether can be extended to higher Reynolds number flows by introducing turbulent modelling.

5. The flow-induced vibration of a sphere close to the free surface will be another interesting research study which has more practical applications.

6. We examined the effect of sphere rotation on vortex-induced vibration of a sphere at $Re = 300$. In this case, VIV was found to suppressed beyond $\alpha = 1.3$. Moreover, we found that the effect of the Reynolds number is significant over the range spanning from low to moderate Reynolds numbers. Therefore, it will be interesting

to investigate the effects of rotational motion of the sphere on the FIV at higher Reynolds numbers.

7. The vortex-induced vibration of a rotating sphere was studied for the classic case, where the sphere motion is restricted in the transverse direction. It will be interesting to study the nature of the problem when the sphere is allowed to move in all three directions.

8. We investigated the effect of imposed transverse rotation on VIV of a sphere. It will be interesting to investigate the effect of the streamwise rotation on VIV of a sphere.

9. The effect of sphere rotation has only been investigated over the modes I and II regimes. This study can also extend to higher reduced velocities, which the sphere exhibit modes III and IV type vibrations.

References

Achenbach, E. 1974 Vortex shedding from spheres. *Journal of Fluid Mechanics* **62** (02), 209–221.

Aoki, K., Kinoshita, Y., Nagase, J. & Nakayama, Y. 2003 Dependence of aerodynamic characteristics and flow pattern on surface structure of a baseball. *Journal of Visualization* **6** (2), 185–193.

Barkla, H. M. & Auchterlonie, L. J. 1971 The Magnus or Robins effect on rotating spheres. *Journal of Fluid Mechanics* **47** (03), 437–447.

Bearman, P. W. 1984 Vortex shedding from oscillating bluff bodies. *Annual Review of Fluid Mechanics* **16** (1), 195–222.

Behara, S., Borazjani, I. & Sotiropoulos, F. 2011 Vortex-induced vibrations of an elastically mounted sphere with three degrees of freedom at Re = 300: hysteresis and vortex shedding modes. *Journal of Fluid Mechanics* **686**, 426–450.

Behara, S. & Sotiropoulos, F. 2016 Vortex-induced vibrations of an elastically mounted sphere: The effects of Reynolds number and reduced velocity. *Journal of Fluids and Structures* **66**, 54–68.

Blackburn, H. & Henderson, R. 1996 Lock-in behavior in simulated vortex-induced vibration. *Experimental Thermal and Fluid Science* **12** (2), 184–189.

Blevins, R. D. 1977 *Flow-induced vibration*.

Bourguet, R. & Jacono, D. L. 2014 Flow-induced vibrations of a rotating cylinder. *Journal of Fluid Mechanics* **740**, 342–380.

Brücker, C. 1999 Structure and dynamics of the wake of bubbles and its relevance for bubble interaction. *Physics of Fluids (1994-present)* **11** (7), 1781–1796.

Brücker, C. 2001 Spatio-temporal reconstruction of vortex dynamics in axisymmetric wakes. *Journal of Fluids and Structures* **15** (3-4), 543–554.

Clift, R., Grace, J. R. & Weber, M. E. 2005 *Bubbles, drops, and particles*. Courier Corporation.

Constantinescu, G. S. & Squires, K. D. 2000 *LES and DES investigations of turbulent flow over a sphere*. American Institute of Aeronautics and Astronautics.

Coulombe-Pontbriand, P. & Nahon, M. 2009 Experimental testing and modeling of a tethered spherical aerostat in an outdoor environment. *Journal of Wind Engineering and Industrial Aerodynamics* **97** (5), 208–218.

Davies, J. M. 1949 The aerodynamics of golf balls. *Journal of Applied Physics* **20** (9), 821–828.

Dennis, S. C. R. & Walker, J. D. A. 1971 Calculation of the steady flow past a sphere at low and moderate Reynolds numbers. *Journal of Fluid Mechanics* **48** (04), 771–789.

Dgheim, J., Abdallah, M., Habchi, R. & Zakhia, N. 2012 Heat and mass transfer investigation of rotating hydrocarbons droplet which behaves as a hard sphere. *Applied Mathematical Modelling* **36** (7), 2935–2946.

Ding, L., Bernitsas, M. M. & Kim, E. S. 2013 2-d urans vs. experiments of flow induced motions of two circular cylinders in tandem with passive turbulence control for 30,000< re< 105,000. *Ocean Engineering* **72**, 429–440.

Dobson, J., Ooi, A. & Poon, E. K. W. 2014 The flow structures of a transversely rotating sphere at high rotation rates. *Computers & Fluids* **102**, 170–181.

Eshbal, L., Krakovich, A. & Hout, R. V. 2012 Time resolved measurements of vortex-induced vibrations of a positively buoyant tethered sphere in uniform water flow. *Journal of Fluids and Structures* **35**, 185–199.

Feng, C. C. 1968 The measurement of vortex induced effects in flow past stationary and oscillating circular and d-section cylinders. PhD thesis, University of British Columbia.

Ghidersa, B. & Dušek, J. 2000 Breaking of axisymmetry and onset of unsteadiness in the wake of a sphere. *Journal of Fluid Mechanics* **423**, 33–69.

Giacobello, M., Ooi, A. & Balachandar, S. 2009 Wake structure of a transversely rotating sphere at moderate Reynolds numbers. *Journal of Fluid Mechanics* **621**, 103–130.

Goff, J. E. & Carré, M. J. 2010 Soccer ball lift coefficients via trajectory analysis. *European Journal of Physics* **31** (4), 775.

Gottlieb, O. 1997 Bifurcations of a nonlinear small-body ocean-mooring system excited by finite-amplitude waves. *Transactions-American Society of Mechanical Engineers Journal of Offshore Mechanics and Arctic Engineering* **119**, 234–238.

Govardhan, R. & Williamson, C. H. K. 1997 Vortex-induced motions of a tethered sphere. *Journal of Wind Engineering and Industrial Aerodynamics* **69**, 375–385.

Govardhan, R. & Williamson, C. H. K. 2000 Modes of vortex formation and frequency response of a freely vibrating cylinder. *Journal of Fluid Mechanics* **420**, 85–130.

Govardhan, R. & Williamson, C. H. K. 2002 Resonance forever: existence of a critical mass and an infinite regime of resonance in vortex-induced vibration. *Journal of Fluid Mechanics* **473**, 147–166.

Govardhan, R. N. & Williamson, C. H. K. 2005 Vortex-induced vibrations of a sphere. *Journal of Fluid Mechanics* **531**, 11–47.

Gushchin, V. A., Kostomarov, A. V., Matyushin, P. V. & Pavlyukova, E. R. 2002 Direct numerical simulation of the transitional separated fluid flows around a sphere and a circular cylinder. *Journal of Wind Engineering and Industrial Aerodynamics* **90** (4-5), 341–358.

Habchi, C., Russeil, S., Bougeard, D., Harion, J., Lemenand, T., Ghanem, A., Della Valle, D. & Peerhossaini, H. 2013 Partitioned solver for strongly coupled fluid–structure interaction. *Computers & Fluids* **71**, 306–319.

Harleman, D. R. F. & Shapiro, W. C. 1960 The dynamics of a submerged moored sphere in oscillatory waves. *Coastal Engineering Proceedings* **1** (7), 41.

Horowitz, M. & Williamson, C. H. K. 2010 The effect of Reynolds number on the dynamics and wakes of freely rising and falling spheres. *Journal of Fluid Mechanics* **651**, 251–294.

Hout, R. V., Krakovich, A. & Gottlieb, O. 2010 Time resolved measurements of vortex-induced vibrations of a tethered sphere in uniform flow. *Physics of Fluids* **22** (8), 087101.

Hunt, J. C. R., Wray, A. A. & Moin, P. 1988 Eddies, streams, and convergence zones in turbulent flows. In *Studying Turbulence Using Numerical Simulation Databases, 2*.

Issa, R. I. 1986 Solution of the implicitly discretised fluid flow equations by operator-splitting. *Journal of Computational Physics* **62** (1), 40–65.

Jauvtis, N., Govardhan, R. & Williamson, C. H. K. 2001 Multiple modes of vortex-induced vibration of a sphere. *Journal of Fluids and Structures* **15** (3), 555–563.

Johnson, T. A. & Patel, V. C. 1999 Flow past a sphere up to a Reynolds number of 300. *Journal of Fluid Mechanics* **378**, 19–70.

Johnson, W. 1986 The Magnus effect—early investigations and a question of priority. *International Journal of Mechanical Sciences* **28** (12), 859–872.

Jones, D. A., Clarke, D. B., Science, D. & Division, T. O. A. M. P. 2008 Simulation of the flow past a sphere using the fluent code Includes bibliographical references.

Kang, S., Choi, H. & Lee, S. 1999 Laminar flow past a rotating circular cylinder. *Physics of Fluids* **11** (11), 3312–3321.

Kawaguti, M. 1955 The critical Reynolds number for the flow past a sphere. *Journal of the Physical Society of Japan* **10** (8), 694–699.

Khalak, A. & Williamson, C. H. K. 1999 Motions, forces and mode transitions in vortex-induced vibrations at low mass-damping. *Journal of Fluids and Structures* **13** (7), 813–851.

Kim, D. 2009 Laminar flow past a sphere rotating in the transverse direction. *Journal of Mechanical Science and Technology* **23** (2), 578–589.

Kim, D. & Choi, H. 2002 Laminar flow past a sphere rotating in the streamwise direction. *Journal of Fluid Mechanics* **461**, 365–386.

Kim, J., Choi, H., Park, H. & Yoo, J. Y. 2014 Inverse Magnus effect on a rotating sphere: when and why. *Journal of Fluid Mechanics* **754**.

Kim, J., Kim, D. & Choi, H. 2001 An immersed-boundary finite-volume method for simulations of flow in complex geometries. *Journal of Computational Physics* **171** (1), 132–150.

Kurose, R. & Komori, S. 1999 Drag and lift forces on a rotating sphere in a linear shear flow. *Journal of Fluid Mechanics* **384**, 183–206.

Lambert, C. M. 2002 Dynamics modeling and conceptual design of a multi-tethered aerostat system. PhD thesis, University of Victoria.

Lee, H., Hourigan, K. & Thompson, M. C. 2013 Vortex-induced vibration of a neutrally buoyant tethered sphere. *Journal of Fluid Mechanics* **719**, 97–128.

Lee, H., Thompson, M. C. & Hourigan, K. 2008 Vortex-induced vibrations of a tethered sphere with neutral buoyancy. *XXII ICTAM, Adelaide* pp. 25–29.

Leontini, J. S., Lo Jacono, D. & Thompson, M. C. 2013 Wake states and frequency selection of a streamwise oscillating cylinder. *Journal of Fluid Mechanics* **730**, 162–192.

Leontini, J. S., Stewart, B. E., Thompson, M. C. & Hourigan, K. 2006*a* Predicting vortex-induced vibration from driven oscillation results. *Applied Mathematical Modelling* **30** (10), 1096 – 1102, special issue of the 12th Biennial Computational Techniques and Applications Conference and Workshops (CTAC-2004) held at The University of Melbourne, Australia, from 27th September to 1st October 2004.

Leontini, J. S., Thompson, M. C. & Hourigan, K. 2006*b* The beginning of branching behaviour of vortex-induced vibration during two-dimensional flow. *Journal of Fluids and Structures* **22** (6), 857–864.

Leweke, T., Provansal, M., Ormieres, D. & Lebescond, R. 1999 Vortex dynamics in the wake of a sphere. *Physics of Fluids* **11** (9), S12–S12.

Lighthill, J. 1986 Wave loading on offshore structures. *Journal of Fluid Mechanics* **173**, 667–681.

Maccoll, J. W. 1928 Aerodynamics of a spinning sphere. *The Aeronautical Journal* **32** (213), 777–798.

Magarvey, R. H. & Bishop, R. L. 1961 Transition ranges for three-dimensional wakes. *Canadian Journal of Physics* **39** (10), 1418–1422.

Magarvey, R. H. & MacLatchy, C. S. 1965 Vortices in sphere wakes. *Canadian Journal of Physics* **43** (9), 1649–1656.

Magnus, G. 1853 *Über die Abweichung der Geschosse, und: Über eine abfallende Erscheinung bei rotierenden Körpern*, , vol. 164. Annalen der Physik.

Masliyah, J. H. & Epstein, N. 1970 Numerical study of steady flow past spheroids. *Journal of Fluid Mechanics* **44** (03), 493–512.

Mi, L. & Gottlieb, O. 2015 Asymptotic model-based estimation of a wake oscillator for a tethered sphere in uniform flow. *Journal of Fluids and Structures* **54**, 361–389.

Mi, L. & Gottlieb, O. 2016 Nonlinear dynamics and internal resonances of a planar multi-tethered spherical aerostat in modulated flow. *Meccanica* **51** (11), 2689–2712.

Mi, L. & Gottlieb, O. 2017 Nonlinear dynamics and bifurcations of a spherical multi-tethered lighter-than-air system in uniform and modulated flow. *Procedia Engineering* **199**, 717–722.

Mittal, R. 1999 A Fourier-Chebyshev spectral collocation method for simulating flow past spheres and spheroids. *International Journal for Numerical Methods in Fluids* **30** (7), 921–937.

Mittal, R., Wilson, J. J. & Najjar, F. M. 2002 Symmetry properties of the transitional sphere wake. *AIAA Journal* **40** (3), 579–582.

Mittal, S. & Kumar, B. 2003 Flow past a rotating cylinder. *Journal of Fluid Mechanics* **476**, 303–334.

Morsi, S. A. & Alexander, A. J. 1972 An investigation of particle trajectories in two-phase flow systems. *Journal of Fluid Mechanics* **55**, 193–208.

Muto, M.and Tsubokura, M. & Oshima, N. 2012 Negative Magnus lift on a rotating sphere at around the critical Reynolds number. *Physics of Fluids* **24** (1), 014102.

Natarajan, R. & Acrivos, A. 1993 The instability of the steady flow past spheres and disks. *Journal of Fluid Mechanics* **254**, 323–344.

Naudascher, E. & Rockwell, D. 2005 *Flow-Induced Vibrations, An Engineering Guide*. Dover Publications.

Naudascher, E. & Rockwell, D. 2012 *Flow-induced vibrations: an engineering guide*. Courier Corporation.

Niazmand, H. & Renksizbulut, M. 2003 Surface effects on transient three-dimensional flows around rotating spheres at moderate Reynolds numbers. *Computers & Fluids* **32** (10), 1405–1433.

Oesterlé, B. & Dinh, T. B. 1998 Experiments on the lift of a spinning sphere in a range of intermediate Reynolds numbers. *Experiments in Fluids* **25** (1), 16–22.

Ormières, D. & Provansal, M. 1999 Transition to turbulence in the wake of a sphere. *Physical Review Letters* **83** (1), 80.

Parkinson, G. 1989 Phenomena and modelling of flow-induced vibrations of bluff bodies. *Progress in Aerospace Sciences* **26** (2), 169 – 224.

Pearlman, H. G. & Sohrab, S. H. 1997 Diffusion flame extinction and viscous hydrodynamics around rotating porous spheres with surface blowing. *Combustion and Flame* **108** (4), 419–441.

Poon, E., Iaccarino, G., Ooi, A. S. H. & Giacobello, M. 2009 Numerical studies of high Reynolds number flow past a stationary and rotating sphere. In *Proceedings of the 7th International Conference on CFD in the Minerals and Process Industries*.

Poon, E. K. W., Ooi, A. S. H., Giacobello, M. & Cohen, R. C. Z. 2010 Laminar flow structures from a rotating sphere: effect of rotating axis angle. *International Journal of Heat and Fluid Flow* **31** (5), 961–972.

Poon, E. K. W., Ooi, A. S. H., Giacobello, M. & Cohen, R. C. Z. 2013 Hydrodynamic forces on a rotating sphere. *International Journal of Heat and Fluid Flow* **42**, 278–288.

Poon, E. K. W., Ooi, A. S. H., Giacobello, M., Iaccarino, G. & Chung, D. 2014 Flow past a transversely rotating sphere at Reynolds numbers above the laminar regime. *Journal of Fluid Mechanics* **759**, 751–781.

Pregnalato, C. J. 2003 *Flow-induced vibrations of a tethered sphere*. PhD, Monash University.

Provansal, M., Leweke, T. & Schouveiler, L.and Guébert, N. 2003 3d oscillations and vortex-induced vibrations of a tethered sphere in a flow parallel to the thread. *Proceedings of PSFVIP-4, Chamonix, France* **35**.

Rajamuni, M. M., Aulisa, E. & Ghosh, B. K. 2014 Optimal control problems in binocular vision. *IFAC Proceedings Volumes* **47** (3), 5283 – 5289, 19th IFAC World Congress.

Rajamuni, M. M., Thompson, M. C. & Hourigan, K. 2018*a* Transverse flow-induced vibrations of a sphere. *Journal of Fluid Mechanics* **837**, 931–966.

Rajamuni, M. M., Thompson, M. C. & Hourigan, K. 2018*b* Vortex-induced vibration of a transversely rotating sphere. *Journal of Fluid Mechanics* **847**, 786–820.

Robin, B. 1972 *New Principle of Gunnery (of 1742)*. Republished by Richmond Publishing Co Ltd.

Roos, F. W. & Willmarth, W. W. 1971 Some experimental results on sphere and disk drag. *AIAA Journal* **9** (2), 285–291.

Rowley, C. W., Mezić, I., Bagheri, S., Schlatter, P. & Henningson, D. S. 2009 Spectral analysis of nonlinear flows. *Journal of Fluid Mechanics* **641**, 115–127.

Rubinow, S. I. & Keller, J. B. 1961 The transverse force on a spinning sphere moving in a viscous fluid. *Journal of Fluid Mechanics* **11** (03), 447–459.

Sakamoto, H. & Haniu, H. 1990 A study on votex shedding from sphere in a uniform flow. *Transactions of the ASME* **112**, 386–392.

Sakamoto, H. & Haniu, H. 1995 The formation mechanism and shedding frequency of vortices from a sphere in uniform shear flow. *Journal of Fluid Mechanics* **287**, 151–171.

Salem, M. B. & Oesterle, B. 1998 A shear flow around a spinning sphere: numerical study at moderate Reynolds numbers. *International Journal of Multiphase Flow* **24** (4), 563–585.

Sareen, A., Zhao, J., Lo Jacono, D., Sheridan, J., Hourigan, K. & Thompson, M. C. 2018*a* Vortex-induced vibration of a rotating sphere. *Journal of Fluid Mechanics* **837**, 258–292.

Sareen, A., Zhao, J., Sheridan, J., Hourigan, K. & Thompson, M. C. 2018*b* Vortex-induced vibrations of a sphere close to a free surface. *Journal of Fluid Mechanics* **846**, 1023–1058.

Sarpkaya, T. 2004 A critical review of the intrinsic nature of vortex-induced vibrations. *Journal of Fluids and Structures* **19** (4), 389–447.

Schmid, P. J. 2010 Dynamic mode decomposition of numerical and experimental data. *Journal of Fluid Mechanics* **656**, 5–28.

Schmid, P. J. 2011 Application of the dynamic mode decomposition to experimental data. *Experiments in Fluids* **50** (4), 1123–1130.

Schmid, P. J. & Sesterhenn, J. L. 2008 Dynamic mode decomposition of numerical and experimental data .

Schouveiler, L. & Provansal, M. 2002 Self-sustained oscillations in the wake of a sphere. *Physics of Fluids* **14** (11), 3846–3854.

Seyed-Aghazadeh, B. & Modarres-Sadeghi, Y. 2015 An experimental investigation of vortex-induced vibration of a rotating circular cylinder in the crossflow direction. *Physics of Fluids (1994-present)* **27** (6), 067101.

Shi-Igai, H. & Kono, T. 1969 Study on vibration of submerged spheres caused by surface waves. *Coastal Engineering in Japan* **12**, 29–40.

Stokes, G. G. 1851 *On the effect of the internal friction of fluids on the motion of pendulums*, , vol. 9. Pitt Press Cambridge.

Tabata, M. & Itakura, K. 1998 A precise computation of drag coefficients of a sphere. *International Journal of Computational Fluid Dynamics* **9** (3-4), 303–311.

Tanaka, T., Yamagata, K. & Tsuji, Y. 1990 Experiment of fluid forces on a rotating sphere and spheroid. In *Pro. 2nd KSME-JSME Fluids Engineering Conference*, , vol. 1, p. 366.

Taneda, S. 1956 Experimental investigation of the wake behind a sphere at low Reynolds numbers. *Journal of the Physical Society of Japan* **11** (10), 1104–1108.

Taneda, S. 1957 Negative Magnus effect. *Reports of Research Institute for Applied Mechanics* .

Taneda, S. 1978 Visual observations of the flow past a sphere at Reynolds numbers between 10e4 and 10e6. *Journal of Fluid Mechanics* **85** (1), 187–192.

The-OpenFOAM-Foundation 2018 Openfoam v6 user guide. https://cfd.direct/openfoam/user-guide.

Thompson, M. C., Leweke, T. & Provansal, M. 2001 Kinematics and dynamics of sphere wake transition. *Journal of Fluids and Structures* **15** (3–4), 575 – 585.

Tomboulides, A. G. & Orszag, S. A. 2000 Numerical investigation of transitional and weak turbulent flow past a sphere. *Journal of Fluid Mechanics* **416**, 45–73.

Tomboulides, A. G., Orszag, S. A. & Karniadakis, G. E. 1993 Direct and large eddy simulations of axisymmetric wakes. *AIAA Paper* **546**.

Torobin, L. B. & Gauvin, W. H. 1960 Fundamental aspects of solids-gas flow: Part iv: The effects of particle rotation, roughness and shape. *The Canadian Journal of Chemical Engineering* **38** (5), 142–153.

Tsuji, Y., Morikawa, Y. & Mizuno, O. 1985 Experimental measurement of the Magnus force on a rotating sphere at low Reynolds numbers. *Journal of Fluids Engineering* **107** (4), 484–488.

White, B. R. & Schulz, J. C. 1977 Magnus effect in saltation. *Journal of Fluid Mechanics* **81** (03), 497–512.

Wieselsberger, C. V. 1922 Weitere feststellungen uber die gesetze des flussigkeits und luftwiderstandes. *Physik Zeitschrift* **23**, 219–224.

Williamson, C. H. K. & Govardhan, R. 1997 Dynamics and forcing of a tethered sphere in a fluid flow. *Journal of Fluids and Structures* **11** (3), 293 – 305.

Williamson, C. H. K. & Govardhan, R. 2004 Vortex-induced vibrations. *Annual Review of Fluid Mechanics* **36**, 413–455.

Williamson, C. H. K. & Govardhan, R. 2008 A brief review of recent results in vortex-induced vibrations. *Journal of Wind Engineering and Industrial Aerodynamics* **96** (6), 713–735.

Williamson, C. H. K. & Roshko, A. 1988 Vortex formation in the wake of an oscillating cylinder. *Journal of Fluids and Structures* **2** (4), 355–381.

Wong, K. W. L., Zhao, J., Jacono, D. L., Thompson, M. C. & Sheridan, J. 2017 Experimental investigation of flow-induced vibration of a rotating circular cylinder. *Journal of Fluid Mechanics* **829**, 486–511.

Wu, J. S. & Faeth, G. M. 1993 Sphere wakes in still surroundings at intermediate Reynolds numbers. *AIAA Journal* **31** (8), 1448–1455.

Wu, W., Bernitsas, M. M. & Maki, K. 2014 RANS simulation versus experiments of flow induced motion of circular cylinder with passive turbulence control at 35,000<Re< 130,000. *Journal of Offshore Mechanics and Arctic Engineering* **136** (4), 041802.

Wu, X., Ge, F. & Hong, Y. 2012 A review of recent studies on vortex-induced vibrations of long slender cylinders. *Journal of Fluids and Structures* **28**, 292–308.

You, C. F., Qi, H. Y. & Xu, X. C. 2003 Lift force on rotating sphere at low Reynolds numbers and high rotational speeds. *Acta Mechanica Sinica* **19** (4), 300–307.

Zhao, J., Jacono, D. L., Sheridan, J., Hourigan, K. & Thompson, M. C. 2018 Experimental investigation of in-line flow-induced vibration of a rotating circular cylinder. *Journal of Fluid Mechanics* **847**, 664–699.

Zhao, M., Cheng, L. & Lu, L. 2014 Vortex induced vibrations of a rotating circular cylinder at low Reynolds number. *Physics of Fluids (1994-present)* **26** (7), 073602.

A. Samples of OpenFOAM *controlDict* and *forceCoeffs* files

An OpenFOAM *controlDict* file

File: /home/rajamunr/Sphere/free-su...2000/h2/u50/system/controlDict Page 1 of 1

```
/*-------------------------------*- C++ -*----------------------------------*\
| =========                 |                                                 |
| \\      /  F ield         | OpenFOAM: The Open Source CFD Toolbox           |
|  \\    /   O peration     | Version:  2.3.1                                 |
|   \\  /    A nd           | Web:      www.OpenFOAM.org                      |
|    \\/     M anipulation  |                                                 |
\*---------------------------------------------------------------------------*/
FoamFile
{
    version     2.0;
    format      ascii;
    class       dictionary;
    location    "system";
    object      controlDict;
}
// * * * * * * * * * * * * * * * * * * * * * * * * * * * * * * * * * * * * * //

application             icoFoam;

startFrom               startTime;

startTime               150;

stopAt                  endTime;

endTime                 2000;

deltaT                  0.005;

writeControl            runTime;

writeInterval           10;

purgeWrite              0;

writeFormat             ascii;

writePrecision          6;

writeCompression        off;

timeFormat              general;

timePrecision           6;

runTimeModifiable       false;

functions
{
   #include "forceCoeffs"
}

// ************************************************************************* //
```

An OpenFOAM *forceCoeffs* file

File: /home/rajamunr/Sphere/free-su...2000/h2/u50/system/forceCoeffs Page 1 of 1

```
/*--------------------------------*- C++ -*----------------------------------*\
| =========                 |                                                 |
| \\      /  F ield         | OpenFOAM: The Open Source CFD Toolbox           |
|  \\    /   O peration     | Version:  2.3.1                                 |
|   \\  /    A nd           | Web:      www.OpenFOAM.org                      |
|    \\/     M anipulation  |                                                 |
\*---------------------------------------------------------------------------*/
FoamFile
{
    version     2.0;
    format      ascii;
    class       dictionary;
    object      forceCoeffs;
}
// * * * * * * * * * * * * * * * * * * * * * * * * * * * * * * * * * * * * * //
forces
{
    type                forces;
    functionObjectLibs  ( "libforces.so" );
    outputControl       timeStep;
    outputInterval      1;
    patches             ( "SPHERE.*" );
    pName               p;
    UName               U;
    rhoName             rhoInf;
    log                 true;
    CofR                (0 0 0);
    rhoInf              1000;
}


forceCoeffs
{
    type                forceCoeffs;
    functionObjectLibs  ( "libforces.so" );
    outputControl       timeStep;
    outputInterval      1;

    patches             ( "SPHERE.*" );
    pName               p;
    UName               U;
    rhoName             rhoInf;
    log                 true;

    liftDir             (0 1 0);
    dragDir             (1 0 0);
    CofR                (0 0 0);
    pitchAxis           (0 1 0);

    magUInf             1.00;
    rhoInf              1000;
    lRef                1;  // Dimeter of the sphere
    Aref                0.78539816339;  // frontal area
}

//************************************************************************//
```

B. PISO algorithm used in icoFoam solver

This algorithm states the steps of solving Navier-Stokes equations for the time step $(n+1)$ with the values of $\mathbf{u}$ and p at previous time step (n) for two corrector steps.

Let the superscripts *,**,*** denote intermediate field values obtained during the spitting process. A semi discrete form of the momentum equation 3.1 can be given as

$$\frac{\mathbf{u}^* - \mathbf{u}^n}{\Delta t} = -A'\mathbf{u}^* + H'(\mathbf{u}^*) - \nabla p^n, \tag{B.1}$$

where $-A'\mathbf{u}^*$ and $H'(\mathbf{u}^*)$ represents the diagonal and non-diagonal elements of discretized convection and diffusion terms, respectively. This equation can rearranges as,

$$A\mathbf{u}^* = H(\mathbf{u}^*) - \nabla p^n, \tag{B.2}$$

with $A = 1/\Delta t + A'$ and $H(\mathbf{u}^*) = H'(\mathbf{u}^*) + \mathbf{u}^n/\Delta t$.

Predictor step: Solve the momentum equation given in B.2 for the first intermediate value of the velocity field $(\mathbf{u}^*)$ with previous values of pressure $(p^n\ )$ and velocity $(\mathbf{u}^n)$. This $\mathbf{u}^*$ in general will not satisfy the zero divergence condition (given in 3.2).

First corrector step: A new velocity field $(\mathbf{u}^{**})$ together with a corresponding new pressure field (p^*) are now considered such that the zero-divergence condition

$$\nabla \cdot \mathbf{u}^{**} = 0 \tag{B.3}$$

is met. For this, the momentum equation B.2 is taken as

$$A\mathbf{u}^{**} = H(\mathbf{u}^*) - \nabla p^*. \tag{B.4}$$

Here, non-diagonal terms of the convection and diffusion terms have treated explicitly $(H(\mathbf{u}^*))$; we will see the reason shortly. Equation B.4 and B.3 are used to derive the pressure equation

$$\nabla\left(\frac{\nabla p^*}{A}\right) = \nabla \cdot \left(\frac{H(\mathbf{u}^*)}{A}\right). \tag{B.5}$$

Then the pressure equation is solved for p^* with velocity field found in the predictor step $(\mathbf{u}^*)$, and afterwards equation B.4 is solved for $\mathbf{u}^{**}$.

Second corrector step: A new velocity field ($\mathbf{u}^{***}$) together with its corresponding new pressure field (p^{**}) are formulated such that the zero-divergence condition

$$\nabla \cdot \mathbf{u}^{***} = 0. \tag{B.6}$$

The momentum equation B.2 is taken as semi explicit form as

$$A\mathbf{u}^{***} = H(\mathbf{u}^{**}) - \nabla p^{**}, \tag{B.7}$$

The corresponding pressure equation is therefore

$$\nabla \left(\frac{\nabla p^{**}}{A} \right) = \nabla \cdot \left(\frac{H(\mathbf{u}^{**})}{A} \right) \tag{B.8}$$

Solving equation B.8, p^{**} can be found. Then $\mathbf{u}^{***}$ can be found from equation B.7. Finally, take $\mathbf{u}^{***}$ as $\mathbf{u}^{n+1}$ and p^{**} as p^{n+1}.

C. The OpenFOAM *icoFoam.C* file

File: /home/rajamunr/OpenFOAM/OpenF...compressible/icoFoam/icoFoam.C

```
/*-------------------------------------------------------------------------*\
  =========                 |
  \\      /  F ield         | OpenFOAM: The Open Source CFD Toolbox
   \\    /   O peration     |
    \\  /    A nd           | Copyright (C) 2011-2015 OpenFOAM Foundation
     \\/     M anipulation  |
-------------------------------------------------------------------------------
License
    This file is part of OpenFOAM.

    OpenFOAM is free software: you can redistribute it and/or modify it
    under the terms of the GNU General Public License as published by
    the Free Software Foundation, either version 3 of the License, or
    (at your option) any later version.

    OpenFOAM is distributed in the hope that it will be useful, but WITHOUT
    ANY WARRANTY; without even the implied warranty of MERCHANTABILITY or
    FITNESS FOR A PARTICULAR PURPOSE.  See the GNU General Public License
    for more details.

    You should have received a copy of the GNU General Public License
    along with OpenFOAM.  If not, see <http://www.gnu.org/licenses/>.

Application
    icoFoam

Description
    Transient solver for incompressible, laminar flow of Newtonian fluids.

\*-------------------------------------------------------------------------*/

#include "fvCFD.H"
#include "pisoControl.H"

// * * * * * * * * * * * * * * * * * * * * * * * * * * * * * * * * * * * * * //

int main(int argc, char *argv[])
{
    #include "setRootCase.H"
    #include "createTime.H"
    #include "createMesh.H"

    pisoControl piso(mesh);

    #include "createFields.H"
    #include "initContinuityErrs.H"

    // * * * * * * * * * * * * * * * * * * * * * * * * * * * * * * * * * * * * * //

    Info<< "\nStarting time loop\n" << endl;

    while (runTime.loop())
    {
        Info<< "Time = " << runTime.timeName() << nl << endl;

        #include "CourantNo.H"

        // Momentum predictor

        fvVectorMatrix UEqn
        (
            fvm::ddt(U)
          + fvm::div(phi, U)
          - fvm::laplacian(nu, U)
        );
```

```
        if (piso.momentumPredictor())
        {
            solve(UEqn == -fvc::grad(p));
        }

        // --- PISO loop
        while (piso.correct())
        {
            volScalarField rAU(1.0/UEqn.A());

            volVectorField HbyA("HbyA", U);
            HbyA = rAU*UEqn.H();
            surfaceScalarField phiHbyA
            (
                "phiHbyA",
                (fvc::interpolate(HbyA) & mesh.Sf())
              + fvc::interpolate(rAU)*fvc::ddtCorr(U, phi)
            );

            adjustPhi(phiHbyA, U, p);

            // Non-orthogonal pressure corrector loop
            while (piso.correctNonOrthogonal())
            {
                // Pressure corrector

                fvScalarMatrix pEqn
                (
                    fvm::laplacian(rAU, p) == fvc::div(phiHbyA)
                );

                pEqn.setReference(pRefCell, pRefValue);

                pEqn.solve(mesh.solver(p.select(piso.finalInnerIter())));

                if (piso.finalNonOrthogonalIter())
                {
                    phi = phiHbyA - pEqn.flux();
                }
            }

            #include "continuityErrs.H"

            U = HbyA - rAU*fvc::grad(p);
            U.correctBoundaryConditions();
        }

        runTime.write();

        Info<< "ExecutionTime = " << runTime.elapsedCpuTime() << " s"
            << "  ClockTime = " << runTime.elapsedClockTime() << " s"
            << nl << endl;
    }

    Info<< "End\n" << endl;

    return 0;
}


// ************************************************************************* //
```

D. vivIcoFoam algorithm

The steps of 'vivIcoFoam' algorithm, which solves fluid-solid coupled system (Navier-Stokes equations, 3.3 and 3.4 together with the solid motion equation, 3.5) are given below for the time step $(n+1)$ with the values of $\mathbf{u}$, p, $\boldsymbol{y_s}$, $\dot{\boldsymbol{y}}_{\boldsymbol{s}}$, and $\ddot{\boldsymbol{y}}_{\boldsymbol{s}}$ at the previous time steps, n, $n-1$ and $n-2$.

Step 01: Initializations.
Read the *solidMotionData* file in the *system* directory and the *boundarytToUpdate* file in the *constant* directory of the case. Declare variables, and perform initializations required to update the boundary conditions and to write the output data. Calculate the dimensional parameters of the solid motion equation given in equation 3.5 according to the user defined non-dimensional parameters.

Step 02a: Predict the solid acceleration, $\ddot{\boldsymbol{y}}_{\boldsymbol{s}}$.
Predict the solid acceleration, $\ddot{\boldsymbol{y}}_{\boldsymbol{s}}^{(n+1)}$, using a polynomial extrapolation as shown in equation 3.6. Then, estimate the solid velocity, $\dot{\boldsymbol{y}}_{\boldsymbol{s}}^{(n+1)}$, and displacement, $\boldsymbol{y}_{\boldsymbol{s}}^{(n+1)}$, using equations 3.7 and 3.8, respectively.

Step 02b: Correct the solid acceleration, $\ddot{\boldsymbol{y}}_{\boldsymbol{s}}$.
Correct the value of $\ddot{\boldsymbol{y}}_{\boldsymbol{s}}^{(n+1)}$ by solving the equation 3.9. Then, update the values of $\dot{\boldsymbol{y}}_{\boldsymbol{s}}^{(n+1)}$ and $\boldsymbol{y}_{\boldsymbol{s}}^{(n+1)}$ using equations 3.7 and 3.8, respectively.

Step 03: Solve fluid equations using PISO algorithm.
PISO algorithm discussed in Appendix B was modified to solve Navier-Stokes equations 3.3 and 3.4. Each form of momentum equations in PISO algorithm in Appendix B, needs to include the solid acceleration term in the right. Thus, equation B.2, B.4, and B.7 become;

$$A\mathbf{u}^{*} = H(\mathbf{u}^{*}) - \nabla p^{n} + \ddot{\boldsymbol{y}}_{\boldsymbol{s}}^{(n+1)}, \tag{D.1}$$

$$A\mathbf{u}^{**} = H(\mathbf{u}^{*}) - \nabla p^{*} + \ddot{\boldsymbol{y}}_{\boldsymbol{s}}^{(n+1)}, \tag{D.2}$$

and

$$A\mathbf{u}^{***} = H(\mathbf{u}^{**}) - \nabla p^{**} + \ddot{\boldsymbol{y}}_{\boldsymbol{s}}^{(n+1)}, \tag{D.3}$$

respectively. Due to the new term in the momentum equation, pressure equation also needs to modify accordingly. Thus, equation B.5 and B.8 become

$$\nabla\left(\frac{\nabla p^*}{A}\right) = \nabla\cdot\left(\frac{H(\mathbf{u}^*) + \ddot{\boldsymbol{y}}_{\boldsymbol{s}}^{(n+1)}}{A}\right) \tag{D.4}$$

and

$$\nabla\left(\frac{\nabla p^{**}}{A}\right) = \nabla\cdot\left(\frac{H(\mathbf{u}^{**}) + \ddot{\boldsymbol{y}}_{\boldsymbol{s}}^{(n+1)}}{A}\right). \tag{D.5}$$

Step 04: Calculate the new forces exerted on the sphere.
With $\mathbf{u}^{n+1}$ and p^{n+1} found from the PISO algorithm, calculate fluid forces exerted on the sphere, $\boldsymbol{f}_{\boldsymbol{l}}^{(n+1)}$.

Step 05: Iterate step 02b to step 04 until fluid forces and solid velocity converge.
Proceed to the next iteration (to step 02b) with the newly calculated fluid forces, $\boldsymbol{f}_{\boldsymbol{l}}^{(n+1)}$. When it completed step 04, calculate the relative errors of fluid forces ($e_f^{(i+1)}$) and solid acceleration ($e_s^{(i+1)}$) at $(i+1)^{th}$ iteration by,

$$e_f^{(i+1)} = \frac{|\boldsymbol{f}_{\boldsymbol{l}}^{(i)} - \boldsymbol{f}_{\boldsymbol{l}}^{(i+1)}|}{|\boldsymbol{f}_{\boldsymbol{l}}^{(i+1)}|} \tag{D.6}$$

and

$$e_s^{(i+1)} = \frac{|\ddot{\boldsymbol{y}}_{\boldsymbol{s}}^{(i)} - \ddot{\boldsymbol{y}}_{\boldsymbol{s}}^{(i+1)}|}{|\ddot{\boldsymbol{y}}_{\boldsymbol{s}}^{(i+1)}|}. \tag{D.7}$$

Brake the iterative loop if both $e_f^{(i+1)}$ and $e_s^{(i+1)}$ are less than the desired error tolerance. If none of the convergence criteria is met, then continue until it reaches the maximum number of iterations.

Step 06: Update the boundary conditions, write motion data to a file and proceed to the next time step.
Once the iterative process is over, update the boundary conditions and write the solid motion data ($\boldsymbol{y}_{\boldsymbol{s}}$, $\dot{\boldsymbol{y}}_{\boldsymbol{s}}$ and $\ddot{\boldsymbol{y}}_{\boldsymbol{s}}$) and force coefficients in all three direction to a csv file called *solidMotionData-0.csv*. Then, proceed to the next time step.

E. Files used to compile the *vivIcoFoam* solver

vivicoFoam.C

```
/*-------------------------------------------------------------------------*\
  =========                 |
  \\      /  F ield         | OpenFOAM: The Open Source CFD Toolbox
   \\    /   O peration     |
    \\  /    A nd           | Copyright (C) 2011-2013 OpenFOAM Foundation
     \\/     M anipulation  |
-------------------------------------------------------------------------------
License
    This file is part of OpenFOAM.

    OpenFOAM is free software: you can redistribute it and/or modify it
    under the terms of the GNU General Public License as published by
    the Free Software Foundation, either version 3 of the License, or
    (at your option) any later version.

    OpenFOAM is distributed in the hope that it will be useful, but WITHOUT
    ANY WARRANTY; without even the implied warranty of MERCHANTABILITY or
    FITNESS FOR A PARTICULAR PURPOSE.  See the GNU General Public License
    for more details.

    You should have received a copy of the GNU General Public License
    along with OpenFOAM.  If not, see <http://www.gnu.org/licenses/>.

Application
    vivicoFoam

Description
    Transient solver for incompressible, laminar flow of Newtonian fluids interact
with an elastically-mounted solid body. This is a modification of icoFoam solver
developed for flow-induced vibration problems.

    To calculate the dynamics of the solid motion, necessary parameters (mass,
spring constant, and damping constant) are calculated according to the mass ratio,
damping ratio and reduced velocity. Those are needed to be given in a dictionary
called solidMotionData inside the system folder.

    The solidMotionData dictionary contains the data about the solid motion and
numerical methods.

    Example
    \verbatim
    massRatio           2;      // m* value
    zeta                0;      // damping ratio
    reducedVelocity     6;      // U* = 5.2
    D                   1;      // Diameter of the sphere
    CS                  2;      // 2 for cylinder and 3 for sphere
    L                   1;      // If a cylinder, Length of the cylinder
    Uinf                1;      // Upstream velocity
    dispFreedom         2;      // 1 for restrict on transverse direction
    numericalODEMethod  1;      // Numerical method of solving solid motion: 1-
backward Eular, 2-trapezoidal, 3-impson's
    coupleIterate       15;     // How many iterations for coupled system.
    rho                 1000;   // fluid density
    stopcriterion       0.001;  // tolerence to stop the iterative method
    underRelaxationPara 1;      // 1- for no under relaxation
    \verbatim

    Boundary condition can be applied according to the motion restriction (1D-
transverse direction, 2D or 3D).  In the constant directory, the
'boundaryToUpdate' dictionary provides the patch names which needs to be updated
in each time step. For a 2D mesh 'type' can be 1,2, or 3: 1- inlet only, 2: inlet,
top an bottom, 3- inlet, top, bottom, front, and back patches.  The patch names
should match with your other dictionaries.

    Example
    \verbatim
```

```
    type            1;     //  0 for no, 1 for inlet only, 2 for 2D, 3 for 3D
    patch1          inlet;
    patch2          top;
    patch3          bottom;
    patch4          front;
    patch5          back;
    patch6          outlet;
    patch7          hole;  // the patch7 should be the solid
    \endverbatim


\*---------------------------------------------------------------------------*/

#include "fvCFD.H"
#include "IOmanip.H"
#include "forces.H"                     // To calculate the forces on solid
#include "fixedGradientFvPatchFields.H" // To get the pressure gradient at solid
#include <iostream>
#include <fstream>

int main(int argc, char *argv[])
{
    argList args(argc, argv);
    #include "createTime.H"
    #include "createMesh.H"
    #include "createFields.H"
    #include "initContinuityErrs.H"
    #include "readsolidMotionData.H"    // Read the solid motion data

     // * * * * * * * * * * * * * * * * * * * * * * * * * * * * * * * * * * * * //

    Info<< "\nStarting time loop\n" << endl;
    #include "initializeToSolidMotion.H"// Initializations for ode solver
    #include "initilizeToWrite.H"       // Initialize to write data

    while (runTime.loop())
    {
        #include "initilizeToUpdateBC.H"
        #include "readPISOControls.H"
        #include "CourantNo.H"

        Info<< "Time = " << runTime.timeName() << nl << endl;

        // ************************************************************************//

        scalar ite_ = 0;
        for (int iterate=0; iterate<maxIte_; iterate++)
        {
            #include "SolveODE.H"

             // Change to the synchronized mode once the solid started to vibrate
            if (mag(s0next_) > 0.001 && synchronized_== false)
            {
                synchronized_ = true;
            }

             // Update the acceleration BC of the frame and higher order BC of p
            #include "UpdateAccelarationBC.H"
            #include "ChangePressureBConSphere.H"

            fvVectorMatrix UEqn         // Solve fluid equations
            (
                    fvm::ddt(U)
                + fvm::div(phi, U)
                - fvm::laplacian(nu, U)
            );


            solve(UEqn == -fvc::grad(p) - ddy);     // ddy- frame acceleration

             // PISO loop
            for (int corr=0; corr<nCorr; corr++)
            {
                volScalarField rAU(1.0/UEqn.A());
                volVectorField HbyA("HbyA", U);
                HbyA = rAU*UEqn.H();
                surfaceScalarField fphi = fvc::interpolate(rAU*ddy) & mesh.Sf();
                                                // Surface scalar field of ddy
                surfaceScalarField phiHbyA
                (
                "phiHbyA",
                  (fvc::interpolate(HbyA) & mesh.Sf())
                + fvc::interpolate(rAU)*fvc::ddtCorr(U, phi)
                - fphi                          // Frame acceleration
                );
```

```
            adjustPhi(phiHbyA, U, p);

            for (int nonOrth=0; nonOrth<=nNonOrthCorr; nonOrth++)
            {
                fvScalarMatrix pEqn
                (
                fvm::laplacian(rAU, p) == fvc::div(phiHbyA)
                );
                pEqn.setReference(pRefCell, pRefValue);
                pEqn.solve();

                if (nonOrth == nNonOrthCorr)
                {
                    phi = phiHbyA - pEqn.flux();
                }
            }

            #include "continuityErrs.H"
            U = HbyA - rAU*fvc::grad(p) - rAU*ddy;
            U.correctBoundaryConditions();
        }

        #include "readforcedict.H"      // To calculate forces on solid surface

        forces f("forces", U.db(), forceCoeffsDict.subDict("forces"));
        f.calcForcesMoment();
        liftforce_ =  (f.forceEff() & liftDir_);
        totalforce_ =  f.forceEff();
        fCoeall_ = totalforce_/(0.5*rho_*Uinf_*Uinf_*Aref_);

        if (dispFreedom_ == 1 || runTime.timeOutputValue() < 5)
        {
            totalforce_ =liftforce_*liftDir_;
        }
        FlNext_ = totalforce_;
        Info << " Calculated fluid forces  " << FlNext_ << nl << endl;

         // Termination of the FSI iterative process
        if (iterate !=0)
        {
            Abserror_ = mag(Flold_ - FlNext_);
            Relerror_ = Abserror_/mag(FlNext_);
            Abserrors2_ = mag(s2next_ - s2old_) ;
            Relerrors2_ = Abserrors2_/mag(s2next_);

             // Write convergence errors to a file for
debugging
            #include "writeConvergenceError.H"
             if (runTime.outputTime())
             {
                 #include "writeLastMotionData.H"
             }

              // Terminate if the the error is less than the tolerance limit

             if ((Relerror_ < Fepsi_ ) && (Relerrors2_ < Fepsi_ ))
             {
                 ite_ = iterate;
                 break;
             }

              // Terminate if the relative error of forces do not change
             if (iterate >1)
             {
                 errorratio_ = Abserror_/Abserrorold_;
                 if (errorratio_ <= 1+0.25 && errorratio_ >= 1-0.25 &&
Abserror_< 5 )
                 {
                     ++errorcon_;
                 }
                 if (errorcon_>=5)
                 {
                     errorcon_=0;
                     ite_ = iterate;
                     break;
                 }
             }
         }
```

```
        // Terminate if driven oscillation or no-oscillation mode
        if (iterate == 0 && (mode_==2 || mode_ ==3 ))
        {
            ite_ = iterate;
            break;
        }
        // Terminate if the solid has not synchronized
        if (synchronized_ == false && iterate == 1 )
        {
            ite_ = iterate;
            break;
        }

        // Save motion data for the calculations of the next iteration
        Flold_ = FlNext_;
        s2old_ = s2next_;
        Abserrorold_ = Abserror_;
        ite_ = iterate;
    }

    // Save the solid motion data for next time step
    s2last2_ = s2last_;
    s2last_ = s2now_;
    s2now_ = s2next_;
    s1last_ = s1now_;
    s1now_ = s1next_;
    s0last_ = s0now_;
    s0now_ = s0next_;

    #include "writeSolidDis.H"  // Write the solid displacement data to a file
    #include "updateBC.H"       // Update BC at inlet boundaries

    runTime.write();
    Info<< "ExecutionTime = " << runTime.elapsedCpuTime() << " s"
        << "  ClockTime = " << runTime.elapsedClockTime() << " s"
    }   << nl << endl;

    Info<< "End\n" << endl;
    return 0;
}

// ************************************************************************* //
```

createFields.H

```
// * * * * * * * * * * * * * * * * * * * * * * * * * * * * * * * * * * * * * * * * * //
    Info<< "Reading transportProperties\n" << endl;

    IOdictionary transportProperties
    (
        IOobject
        (
            "transportProperties",
            runTime.constant(),
            mesh,
            IOobject::MUST_READ_IF_MODIFIED,

            IOobject::NO_WRITE
        )
    );

    dimensionedScalar nu
    (
        transportProperties.lookup("nu")
    );


    Info<< "Reading field p\n" << endl;
    volScalarField p
    (
        IOobject
        (
            "p",
            runTime.timeName(),
            mesh,
            IOobject::MUST_READ,
            IOobject::AUTO_WRITE
        ),
        mesh
    );


    Info<< "Reading field U\n" << endl;
    volVectorField U
    (
        IOobject
        (
            "U",
            runTime.timeName(),
            mesh,
            IOobject::MUST_READ,
            IOobject::AUTO_WRITE
        ),
        mesh
    );

     // The accelaration of the reference, ddy
    volVectorField ddy
    (
        IOobject
        (
            "ddy",
            runTime.timeName(),
            mesh,
            IOobject::MUST_READ,
            IOobject::AUTO_WRITE
        ),
        mesh
    );

#   include "createPhi.H"

   label pRefCell = 0;
   scalar pRefValue = 0.0;
   setRefCell(p, mesh.solutionDict().subDict("PISO"), pRefCell, pRefValue);

// * * * * * * * * * * * * * * * * * * * * * * * * * * * * * * * * * * * * * * * * * //
```

readsolidMotionData.H

```
// * * * * * * * * * * * * * * * * * * * * * * * * * * * * * * * * * * * * * * * * * //

    Info<< "Reading solid motion data \n" << endl;

    IOdictionary solidMotionData
    (
        IOobject
        (
            "solidMotionData",
            runTime.system(),
            mesh,
            IOobject::MUST_READ_IF_MODIFIED,
            IOobject::NO_WRITE
        )
    );

    scalar massRatio_;          // Mass ration
    scalar zeta_;               // Zeta
    scalar Ustar_;              // U* without added mass effect
    scalar D_;                  // Diameter of the sphere or cylinder
    scalar CS_;                 // Sphere or sylinder; 2-cylinder, 3-sphere
    scalar Uinf_;               // Free stream velocity of the fluid
    scalar dispFreedom_;        // DOF of solid; defalt 3D, set 1 for 1D
    scalar maxIte_;             // Maximum number of iterations of FSI solver
    scalar IntegrationMethod_;  // Integration method of ODE solver; default 3rd
order AM
    scalar rho_;                // Fluid density
    scalar Fepsi_;              // Error tolerance
    scalar alpha_;              // Under relaxation parameter
    scalar mode_;               // Vibration mode; 1- elastically mounted, 2-
driven oscillation, 3- no oscillation
    scalar ymax_;               // In driven oscillation, maximum amplitude
    scalar yfrequency_;         // In driven oscillation, frequency

solidMotionData.lookup("massRatio") >> massRatio_;
solidMotionData.lookup("zeta") >> zeta_;
solidMotionData.lookup("reducedVelocity") >> Ustar_;
solidMotionData.lookup("D") >> D_;
solidMotionData.lookup("CS") >> CS_;
solidMotionData.lookup("Uinf") >> Uinf_;
solidMotionData.lookup("dispFreedom") >> dispFreedom_;
solidMotionData.lookup("maxNoOfIterations") >> maxIte_;
solidMotionData.lookup("IntegrationMethod") >> IntegrationMethod_;
solidMotionData.lookup("rho") >> rho_;
solidMotionData.lookup("stopcriterion") >> Fepsi_;
solidMotionData.lookup("underRelaxationPara") >> alpha_;
solidMotionData.lookup("osillationMode") >> mode_;
solidMotionData.lookup("maximumDispalcement") >> ymax_;
solidMotionData.lookup("osillationFrequency") >> yfrequency_;

// * * * * * * * * * * * * * * * * * * * * * * * * * * * * * * * * * * * * * * * * * //
```

initilizeToUpdateBC.H

```
// * * * * * * * * * * * * * * * * * * * * * * * * * * * * * * * * * * * * * * //
// initialisation to update the boundary conditions
   scalar mType_;

   IOdictionary boundaryToUpdate
   (
       IOobject
       (
           "boundaryToUpdate",
           runTime.constant(),
           mesh,
           IOobject::MUST_READ,
           IOobject::NO_WRITE
       )
   );

   boundaryToUpdate.lookup("type") >> mType_;

   word patch1_; // inlet
   word patch2_; // top
   word patch3_; // bottom
   word patch4_; // front
   word patch5_; // back
   word patch6_; // outlet
   word patch7_; // solid
   boundaryToUpdate.lookup("patch1") >> patch1_;
   boundaryToUpdate.lookup("patch2") >> patch2_;
   boundaryToUpdate.lookup("patch3") >> patch3_;
   boundaryToUpdate.lookup("patch4") >> patch4_;
   boundaryToUpdate.lookup("patch5") >> patch5_;
   boundaryToUpdate.lookup("patch6") >> patch6_;
   boundaryToUpdate.lookup("patch7") >> patch7_;
   label patchID1_ = mesh.boundaryMesh().findPatchID(patch1_);
   label patchID2_ = mesh.boundaryMesh().findPatchID(patch2_);
   label patchID3_ = mesh.boundaryMesh().findPatchID(patch3_);
   label patchID4_ = mesh.boundaryMesh().findPatchID(patch4_);
   label patchID5_ = mesh.boundaryMesh().findPatchID(patch5_);
   label patchID6_ = mesh.boundaryMesh().findPatchID(patch6_);
   label patchID7_ = mesh.boundaryMesh().findPatchID(patch7_);

// * * * * * * * * * * * * * * * * * * * * * * * * * * * * * * * * * * * * * * //
```

SolveODE.H

```
/*-------------------------------------------------------------------------*\
  =========                 |
  \\      /  F ield         | OpenFOAM: The Open Source CFD Toolbox
   \\    /   O peration     |
    \\  /    A nd           | Copyright (C) 2011-2013 OpenFOAM Foundation
     \\/     M anipulation  |
-------------------------------------------------------------------------------
License
    This file is part of OpenFOAM.

    OpenFOAM is free software: you can redistribute it and/or modify it
    under the terms of the GNU General Public License as published by
    the Free Software Foundation, either version 3 of the License, or
    (at your option) any later version.

    OpenFOAM is distributed in the hope that it will be useful, but WITHOUT
    ANY WARRANTY; without even the implied warranty of MERCHANTABILITY or
    FITNESS FOR A PARTICULAR PURPOSE.  See the GNU General Public License
    for more details.

    You should have received a copy of the GNU General Public License
    along with OpenFOAM.  If not, see <http://www.gnu.org/licenses/>.

Class
    Foam::ODESystem

Description
    solve the solid motion by Backward Eular, or Trapezoidal Method, or
    two-step simpson's methos.


\*-------------------------------------------------------------------------*/

#ifndef SolveODE_H
#define SolveODE_H


// * * * * * * * * * * * * * * * * * * * * * * * * * * * * * * * * * * * * * //

scalar massf_ = 0; // Mass of the fluid

 // Create the ODE system
if (CS_ != 2 && CS_ !=3 )
{
        Info << "\n Error: The shape of the solid is undifined. \n Plese set the
value of CS in the system dictionary, solidMotionData directory to 2 for a
cylinder and 3 for a sphere \n";
}

 // Claculate the mass of the fluid according to the shape of the solid
if (CS_ == 2)   // cylinder
{
    scalar L_(readScalar(solidMotionData.lookup("L")));
        massf_ = rho_*constant::mathematical::pi*pow(D_/2.0,2)*L_;
}
if (CS_ == 3)   // Sphere
{
        massf_ = rho_*(4.0/3.0)*constant::mathematical::pi*pow(D_/2.0,3);
}

scalar m_ = massRatio_*massf_;
 // Structural damping constant
scalar c_ = 4.0*constant::mathematical::pi*m_*zeta_*1.0/Ustar_;
 // Structural spring constant
scalar k_ = 4.0*pow(constant::mathematical::pi,2)*m_*pow(1.0/Ustar_,2);
scalar deltat = runTime.deltaTValue();
```

```
scalar t = runTime.timeOutputValue();

for (int i=0; i<3; i++)
{
        if (dispFreedom_ != 1 || (dispFreedom_ == 1 && i==1))
        {
                if (mode_ == 1) // Elastically mounted sphere/cylinder
                {
                         // The predictor step
                        if (iterate == 0)
                        {
                                s2next_[i] = 3.0*s2now_[i] - 3.0*s2last_[i] +
s2last2_[i];
                        }
                         // The foifirst corrector step
                if (iterate == 1)
                        {
                                s2next_[i] = -(k_/m_)*s0next_[i] - (c_/m_)*s1next_
[i] + (1.0/m_)*FlNext_[i];
                        }
                         //  The other corrector steps with under relaxation
                        if (iterate != 0 && iterate != 1)
                        {
                                s2next_[i] = -(k_/m_)*s0next_[i] - (c_/m_)*s1next_
[i] + (1.0/m_)*FlNext_[i];
                                s2next_[i] = s2old_[i] + alpha_*(s2next_[i] -s2old_
[i]);
                        }

                     // dThe default integration method is 3rd order Adams Moulton
                        s1next_[i] = s1now_[i] + deltat*(5.0*s2next_[i] +
8.0*s2now_[i] - s2last_[i])/12.0;
                        s0next_[i] = s0now_[i] + deltat*(5.0*s1next_[i] +
8.0*s1now_[i] - s1last_[i])/12.0;

                        if (IntegrationMethod_ == 2) // Backward Eular
                        {
                                s1next_[i] = s1now_[i] + deltat*s2next_
[i];
                                s0next_[i] = s0now_[i] + deltat*s1next_[i];
                        }

                        if (IntegrationMethod_ == 3) // Trapizoidal rule
                        {
                                s1next_[i] = s1now_[i] + deltat*(s2next_[i] +
s2now_[i])/2.0;
                                s0next_[i] = s0now_[i] + deltat*(s1next_[i] +
s1now_[i])/2.0;
                        }
                }

                if (mode_ == 2) // Driven osillation
                {
                        s0next_[i] = ymax_*Foam::cos
(2.0*constant::mathematical::pi*yfrequency_*t);
                        s1next_[i] = -
ymax_*2.0*constant::mathematical::pi*yfrequency_*Foam::sin
(2.0*constant::mathematical::pi*yfrequency_*t);
                        s2next_[i] = -ymax_*pow
(2.0*constant::mathematical::pi*yfrequency_,2)*Foam::cos
(2.0*constant::mathematical::pi*yfrequency_*t);
                }
                if (mode_ == 3) // No osillation
                {
                        s0next_[i] = 0.0;
                        s1next_[i] = 0.0;

                        s2next_[i] = 0.0;
                }

        }
}


#endif

// * * * * * * * * * * * * * * * * * * * * * * * * * * * * * * * * * * * * * //
```

UpdateAccelarationBC.H

```
   // * * * * * * * * * * * * * * * * * * * * * * * * * * * * * * * * * * * * * //

  if ( patchID1_ == -1 ||  patchID2_ == -1 ||patchID3_ == -1 || patchID4_ == -1 ||
  patchID5_ == -1 || patchID6_ == -1 || patchID7_ == -1)
  {
          FatalError << "patch not found!" << exit(FatalError);
  }

      ddy.boundaryField()[patchID1_] == s2next_;
      ddy.boundaryField()[patchID2_] == s2next_;
      ddy.boundaryField()[patchID3_] == s2next_;
      ddy.boundaryField()[patchID4_] == s2next_;
      ddy.boundaryField()[patchID5_] == s2next_;
      ddy.boundaryField()[patchID6_] == s2next_;
      ddy.boundaryField()[patchID7_] == s2next_;
      ddy =  dimensionedVector("myddy", dimAcceleration, s2next_);

   // * * * * * * * * * * * * * * * * * * * * * * * * * * * * * * * * * * * * * //
```

ChangePressureBConSphere.H

```
 // * * * * * * * * * * * * * * * * * * * * * * * * * * * * * * * * * * * * * //
 // Initialize to update pressure gradient at solid boundary

if ( p.boundaryField()[patchID7_].type() ==
fixedGradientFvPatchVectorField::typeName )
{
        fixedGradientFvPatchScalarField& Upatch7_ =
        refCast<fixedGradientFvPatchScalarField>(p.boundaryField()[patchID7_]);

         // Calculate the pressure gradient at solid boundary based on the velocity
        surfaceVectorField pgrad_(fvc::interpolate(-ddy + fvc::laplacian(nu, U) -
fvc::   iv(phi,U)));
        vectorField pgradSolid_ = pgrad_.boundaryField()[patchID7_];
        vectorField n = mesh.boundary()[patchID7_].nf();
        scalarField NormalpgradSolid_ = pgradSolid_ & n;
        Upatch7_.gradient() = NormalpgradSolid_;
}

 // Calculate the pressure gradient at the inlet boundary
 surfaceVectorField pgradall_(fvc::interpolate(fvc::laplacian(nu, U) - fvc::div
(phi,U)));

 // Initialize to update pressure gradient at inlet boundary
if ( p.boundaryField()[patchID1_].type() ==
fixedGradientFvPatchVectorField::typeName )
{
        fixedGradientFvPatchScalarField& Upatch1_ =
        refCast<fixedGradientFvPatchScalarField>(p.boundaryField()[patchID1_]);
        vectorField pgradinlet_ = pgradall_.boundaryField()[patchID1_];
        vectorField ninlet = mesh.boundary()[patchID1_].nf();
        scalarField Normalpgradinlet_ = pgradinlet_ & ninlet;
        Upatch1_.gradient() = Normalpgradinlet_; //- update the pressure gradient
}

 // Initialize to update pressure gradient at the top boundary
if ( p.boundaryField()[patchID2_].type() ==
fixedGradientFvPatchVectorField::typeName )
{
        fixedGradientFvPatchScalarField& Upatch2_ =
        refCast<fixedGradientFvPatchScalarField>(p.boundaryField()[patchID2_]);
        vectorField pgradtop_ = pgradall_.boundaryField()[patchID2_];
        vectorField ntop = mesh.boundary()[patchID2_].nf();
        scalarField Normalpgradtop_ = pgradtop_ & ntop;
        Upatch2_.gradient() = Normalpgradtop_; //- update the pressure gradient
}
```

```
 // Initialize to update pressure gradient at the bottom boundary
if ( p.boundaryField()[patchID3_].type() ==
fixedGradientFvPatchVectorField::typeName )
{
        fixedGradientFvPatchScalarField& Upatch3_ =
        refCast<fixedGradientFvPatchScalarField>(p.boundaryField()[patchID3_]);
        vectorField pgradbottom_ = pgradall_.boundaryField()[patchID3_];
        vectorField nbottom = mesh.boundary()[patchID3_].nf();
        scalarField Normalpgradbottom_ = pgradbottom_ & nbottom;
        Upatch3_.gradient() = Normalpgradbottom_; //- update the pressure gradient
}
 // Initialize to update pressure gradient at the front boundary
if ( mType_ == 3 && p.boundaryField()[patchID4_].type() ==
fixedGradientFvPatchVectorField::typeName )
{
        fixedGradientFvPatchScalarField& Upatch4_ =
        refCast<fixedGradientFvPatchScalarField>(p.boundaryField()[patchID4_]);
        vectorField pgradfront_ = pgradall_.boundaryField()[patchID4_];
        vectorField nfront = mesh.boundary()[patchID4_].nf();
        scalarField Normalpgradfront_ = pgradfront_ & nfront;
        Upatch4_.gradient() = Normalpgradfront_; //- update the pressure gradient
}

 // Initialize to update pressure gradient at the back boundary
if ( mType_ == 3 && p.boundaryField()[patchID5_].type() ==
fixedGradientFvPatchVectorField::typeName )
{
        fixedGradientFvPatchScalarField& Upatch5_ =
        refCast<fixedGradientFvPatchScalarField>(p.boundaryField()[patchID5_]);
        vectorField pgradback_ = pgradall_.boundaryField()[patchID5_];
        vectorField nback = mesh.boundary()[patchID5_].nf();
        scalarField Normalpgradback_ = pgradback_ & nback;
        Upatch5_.gradient() = Normalpgradback_; //- update the pressure gradient
}

 // * * * * * * * * * * * * * * * * * * * * * * * * * * * * * * * * * * * * * * * * //
```

readforcedict.H

```
// * * * * * * * * * * * * * * * * * * * * * * * * * * * * * * * * * * * * * * * * //
// Initialize for force calculationse

   vector liftDir_;
   scalar liftforce_;
   vector totalforce_;
   scalar magUInf_;
   scalar Aref_;

   IOdictionary forceCoeffsDict
   (
       IOobject
       (
           "forceCoeffs",
           runTime.system(),
           mesh,
           IOobject::MUST_READ,
           IOobject::AUTO_WRITE,
                 true
       )
   );

forceCoeffsDict.subDict("forceCoeffs").lookup("liftDir") >> liftDir_;
forceCoeffsDict.subDict("forceCoeffs").lookup("Aref") >> Aref_;

// * * * * * * * * * * * * * * * * * * * * * * * * * * * * * * * * * * * * * * * * //
```

writeConvergenceError.H

```
 // * * * * * * * * * * * * * * * * * * * * * * * * * * * * * * * * * * * * * * * * * //
 // Data on the current processor

scalar Af = Abserror_;
scalar Rf = Relerror_;
scalar As2 = Abserrors2_;
scalar Rs2 = Relerrors2_;

 // Sync data to the master (in this, I will get the max)
reduce(Af, maxOp<scalar>());
reduce(Rf, maxOp<scalar>());
reduce(As2, maxOp<scalar>());
reduce(Rs2, maxOp<scalar>());

 // We will now get the master to write to the file

if (Pstream::master())
{
        OFstream& errorFile = *errorPtr;
     errorFile
        << runTime.timeName() << " , "<< iterate <<" , "<<  Af <<" , "<< Rf << " ,
"<< As2 << " , "<< Rs2 << endl;
}

 // * * * * * * * * * * * * * * * * * * * * * * * * * * * * * * * * * * * * * * * * * //
```

writeLastMotionData.H

```
 // * * * * * * * * * * * * * * * * * * * * * * * * * * * * * * * * * * * * * * * * * //

IOdictionary lastMotionDict
   (IOobject
    ("lastMotionData",
            runTime.system(),
            runTime)
    );
 lastMotionDict.add<vector>("s0now", s0next_);
 lastMotionDict.add<vector>("s0last", s0now_);
 lastMotionDict.add<vector>("s1now", s1next_);
 lastMotionDict.add<vector>("s1last", s1now_);
 lastMotionDict.add<vector>("s2now", s2next_);
 lastMotionDict.add<vector>("s2last", s2now_);
 lastMotionDict.add<vector>("s2last2", s2last_);

 static_cast<regIOobject*>(&lastMotionDict)->write();

 // * * * * * * * * * * * * * * * * * * * * * * * * * * * * * * * * * * * * * * * * * //
```

writeSolidDis.H

```
// * * * * * * * * * * * * * * * * * * * * * * * * * * * * * * * * * * * * * * * * * //

     // Data on the current processor
    vector s0 = s0next_;
    vector s1 = s1next_;
    vector s2 = s2next_;
    scalar iter = ite_;
    vector fl = fCoeall_;

     // Sync data to the master (in this, I will get the max)
    reduce(s0, maxOp<vector>());
    reduce(s1, maxOp<vector>());
    reduce(s2, maxOp<vector>());
    reduce(iter, maxOp<scalar>());
    reduce(fl, maxOp<vector>());

    // Write solid displacement, solid velocity, solid acceleration, number of
iterations, and fluid forces
    if (Pstream::master())
    {
        OFstream& myOutFile = *myOutFilePtr;
        myOutFile
            << runTime.timeName() << " , "<< s0[0]<<" , "<< s0[1] <<" , "<< s0[2]
<< " , "<< s1[0] << " , "<< s1[1] << " , "<< s1[2] << " , "<< s2[0]<< " , "<< s2
[1]<< " , "<< s2[2] << " , " << iter << " , "<< fl[0]<< " , "<< fl[1]<< " , "<< fl
[2] <<  endl;
    }

// * * * * * * * * * * * * * * * * * * * * * * * * * * * * * * * * * * * * * * * * * //
```

F. Additional files required for a FIV simulation

system/solidMotionaData

```
/*-------------------------------*- C++ -*----------------------------------*\
| =========                 |                                                 |
| \\      /  F ield         | OpenFOAM: The Open Source CFD Toolbox           |
|  \\    /   O peration     | Version:  2.3.1                                 |
|   \\  /    A nd           | Web:      www.OpenFOAM.org                      |
|    \\/     M anipulation  |                                                 |
\*---------------------------------------------------------------------------*/
FoamFile
{
    version     2.0;
    format      ascii;
    class       dictionary;
    object      solidMotionData;
}

// * * * * * * * * * * * * * * * * * * * * * * * * * * * * * * * * * * * * * //


massRatio           3.8197; // Mass ratio, m*
zeta                0.0;    // Damping ratio
reducedVelocity     3.5;    // Reduced velocity, U* w/o added mass
D                   1;      // Diameter of the sphere
CS                  3;      // Cylinder/Sphere, 2- cylinder and 3- sphere
L                   1;      // If a cylinder, Length of the cylinder
Uinf                1;      // Upstream velocity
rho                 1000;   // Fluid density
dispFreedom         1;      // 1- restrict motion on the lift direction.
maxNoOfIterations   50;     // Maximun number of iterations
stopcriterion       0.001;  // Tolarence to stop the iterative process
underRelaxationPara 1;      // Under relaxation, 1- no under relaxation
osillationMode      3;      // 1-elastically mounted, 2-force diven, 3- no
osillation
maximumDispalcement 0.4;    // Maximum dispacement, if forced oscillation
osillationFrequency 0.195;  // Osillation frequency, if forced oscillation
IntegrationMethod   1;      // Integration method used. Defaul- Adams Moulton, 2-
Backward Eular, 3- Trapizoidal rule.

// * * * * * * * * * * * * * * * * * * * * * * * * * * * * * * * * * * * * * //
```

system/lastMotionaData

```
/*-------------------------------*- C++ -*----------------------------------*\
| =========                 |                                                 |
| \\      /  F ield         | OpenFOAM: The Open Source CFD Toolbox           |
|  \\    /   O peration     | Version:  2.3.1                                 |
|   \\  /    A nd           | Web:      www.OpenFOAM.org                      |
|    \\/     M anipulation  |                                                 |
\*---------------------------------------------------------------------------*/
FoamFile
{
    version     2.0;
    format      ascii;
    class       dictionary;
    location    "system";
    object      lastMotionData;
}
// * * * * * * * * * * * * * * * * * * * * * * * * * * * * * * * * * * * * * //

s0now           ( 0 0.113035 0 );

s0last          ( 0 0.1131 0 );

s1now           ( 0 -0.0129737 0 );

s1last          ( 0 -0.012904 0 );

s2now           ( 0 -0.0138929 0 );

s2last          ( 0 -0.0139706 0 );

s2last2         ( 0 -0.0140492 0 );


// * * * * * * * * * * * * * * * * * * * * * * * * * * * * * * * * * * * * * //
```

constant/boundaryToUpdate

```
/*-------------------------------*- C++ -*----------------------------------*\
| =========                 |                                                 |
| \\      /  F ield         | OpenFOAM: The Open Source CFD Toolbox           |
|  \\    /   O peration     | Version:  2.3.1                                 |
|   \\  /    A nd           | Web:      www.OpenFOAM.org                      |
|    \\/     M anipulation  |                                                 |
\*---------------------------------------------------------------------------*/
FoamFile
{
    version     2.0;
    format      ascii;
    class       dictionary;
    object      boundaryToUpdate;
}

// * * * * * * * * * * * * * * * * * * * * * * * * * * * * * * * * * * * * * //

    type        3; // 0- no, 1- inlet only, 2- 2D (inlet, top, bottom), 3- 3D
(first 5 patches)

    patch1      INFLOW;
    patch2      TOP;
    patch3      BOTTOM;
    patch4      FRONT;
    patch5      BACK;
    patch6      OUTFLOW;
    patch7      SPHERE; // The patch7 should be the solid (cylinder/sphere)


// * * * * * * * * * * * * * * * * * * * * * * * * * * * * * * * * * * * * * //
```